Development and Optimisation of 3D Printed Compliant Joint Mechanisms for Hypermobile Robots

by

Andrew Robert Barber

Submitted in accordance with the requirements
for the degree of Doctor of Philosophy.

The University of Leeds

School of Mechanical Engineering

August 2017

The candidate confirms that the work submitted is his/her own, except where work which has formed part of jointly authored publications has been included. The contribution of the candidate and the other authors to this work has been explicitly indicated below. The candidate confirms that appropriate credit has been given within the thesis where reference has been made to the work of others.

The work in Chapter 6 of the thesis has appeared in publication as follows:

"Development and Characterisation of a Multi-material 3D Printed Torsion Spring", *Proc. TAROS*, (2015) 44-49. Springer, Cham.

A. Barber, P. Culmer and J. H. Boyle

I was responsible for the literature research, experimental design and implementation and data analysis, as well as writing the paper The contribution of the other authers was high level guidence and proof reading, and assistance in data analysis.

Abstract

Hypermobile robots are an area of robotics that are often used as exploratory robots, but have facets that feature in other areas of the field. Hypermobile robots are robots that feature multiple body segments or modules, with joints between each. These robots are often used for exploratory purposes due to being able to maintain contact with the ground due to their flexible bodies. Wormbot was a hypermobile robot developed at the University of Leeds, which used a locomotion gait based on that of a *Caenorhabditis elegans* nematode worm, otherwise known as *C.elegans*. This movement pattern is reliant on compliance; a mechanism where the joints are slightly sprung and comply to the environment. The next iteration of Wormbot needs to be reduced in size, which would also require a new actuation and compliance system.

This thesis describes the process of investigating a method of compliance to be used in the next version of Wormbot, while utilising the multi-material 3D printing capabilities available at the University. 3D printing provides quick manufacturing, allowing for fast changes to made to prototype components if required.

During the process of this research, two 3D printed compliant actuation systems were produced; a pneumatic bellow and a Series Elastic Element (SEE) to be used in tandem with a servo motor. Both methods were tested to analyse their performance. The bellow was produced to utilise the capabilities of multi-material printing to strengthening suspected weak areas of the actuator. However, the performance of the bellow was unsatisfactory, failing twice in two actuation tests tests due to the device breaking. The SEE on the other hand, designed with two stiffer plates and a rubber-like spring element in the middle, initially proved to be reliable and repeatable in performance, with potential to behave linearly to a set spring constant. These results were acquired by performing rotational step response tests and fitting a spring-damper model to the results. However, issues with the plastic material were discovered when it was found to deform much more than anticipated, behaving in a similar manner to an additional spring element, complicating the model. Simulation work to explore the potential for using different spring constants of joint compliance in varying environments was also explored. This involved testing a virtual Wormbot in a range of environments while altering joint compliance. These simulations revealed that softer joints allow for favourable performance in constricting environments, while stiffer joints lend themselves more to quicker movement.

Acknowledgements

Firstly, I would like to thank my supervisor, Dr. Jordan Boyle, for his support throughout this project. His enthusiasm and guidance has been invaluable, and he has always been on hand to provide advice when required and needed, in everything from direction and composure when an experiment hasn't gone as planned, to advising me I should probably take a day off after knee surgery. I would also like to extend my gratitude to Dr. Peter Culmer, Prof. Anne Neville and Prof. Abbas Dehghani-Sanij, who have all been on hand to provide advice, encouragement and moral support along the way. You have all made this possible and thank you for this opportunity.

I would also like to thank the Technicians within the Mechanical Engineering Department. I would specifically like to thank Graham Brown and Tony Wiese, who have always been on hand for their skills with 3D printing and component testing respectively.

Next, to those who have been part of office 332a during my time at Leeds, as well as those who I have come to know from around the department, thank you. There are not many who have the stamina to put up with my incessant ramblings about Cricket and my ceaseless puns, but somehow you've done it. I have found it amazing how a group with such a wide net of personalities, from reletively sane to... lets say the other end of the spectrum... can form such an amazing group of friends. I look forward to our many years of friendship ahead.

I would like to thank my Mum, Dad, Sister and Brother-in-Law for their backing throughout the project, always checking that I was maintaining my sanity. Finally, I cannot thank my girlfriend, Amy, enough for her unrelenting support. Along the way, she has always been there to support me whatever the situation, whether it be to listen to me complain or remind me that I need to eat. I couldn't have done this without her.

Contents

List of Figures

List of Tables

Chapter 1

Introduction

1.1 Background

Robotics has worked its way into many facets of modern life, from manufacture to medicine, from education to entertainment. One of the advantages the field can offer is its ability to achieve the things we cannot, from minimally invasive surgical technologies to bomb disposal robotics. There are numerous other areas to analyse but this report is focussed more on the exploration side of Robotics.

Exploration robotics is a rather broad term that can encompass many areas. The military could require robotics to survey an area before or during combat, analysing it for potential hazards, advantageous positions and enemy and/or hostage positions. A charity such as the British Red Cross could use a robot for investigating natural disaster sites, such as tsunami and earthquake areas, to search for survivors in rubble or to find potential structural instabilities in weakened buildings where it is too dangerous or cramped for people to enter. There are many other applications within the field too, including deep sea excavation points and exploring archaeological sites.

In 2013, Jordan Boyle published a paper describing his development at the University of Leeds into Wormbot; a hypermobile robot designed to physically implement his work on a neural control algorithms of the nematode worm *C.elegans* [26]. The robot supported work into accurately mapping the nematode worms movement pattern. The robot managed to achieve forward movement and move itself around obstacles. However, the robot has plenty of room to development. Along with downscaling the large size of the robot, one of these areas in particular is the application of the joint mechanism, which needed to be more powerful. This however would need to be able to incorporate joint compliance [28].

Compliant joints allow for a certain level of rotation flexibility. This means if, in the case of hypermobile robots, a robot was to collide with the environment, the joint would be able to deflect to the environment. This can be used as a way of protecting the robot or surroundings, but also in this instance they are used to help provide proprioceptive feedback, providing information on the position of the robots joints. This information in turn is used to help the robot navigate the environment. Using compliant joints generally in hypermobile robotics can greatly decrease the complexity of sensing how the body is reacting to the terrain [39].

This research project aims to experiment with producing compliant actuation methods for a smaller version of Wormbot, with an emphasis on exploring the capabilities of modern manufacturing techniques to aid research. This research will utilise multi-material 3D printing to produce flexible actuators as well as components to use alongside non compliant actuators, while also using simulation packages to examine the effectiveness of compliant systems within different environments.

1.2 Aims and Objectives

1.2.1 Aim

To explore the potential of producing compliant actuation systems using 3D printing for hypermobile robots and to analyse the effect of varying levels of compliance for the future development of hypermobile robotics.

1.2.2 Objectives

- Perform a critical literature review of snake and worm-like robots to identify:
    - Capabilities of the current solutions.
    - Promising design features and areas for improvement.
    - Candidate actuator technologies.
    - Potential compliance solutions.
- Develop simple theoretical models to evaluate the suitability of candidate actuator technologies and select the two best options for further investigation.

- Produce prototype compliant mechanisms based on the theoretical models previously presented.
- Analyse how varying levels of compliance within different environments effect the performance of hypermobile robots.
- Investigate the potential to produce compliant actuation methods according to simulated Wormbot analysis.

1.3 Contribution to the Field

While there are a number of hypermobile robots that have been developed, the modern capabilities of multi-material 3D printing are under-utilised in the field. With modern 3D printing techniques and materials, the range of possibilities is vastly increased. The work detailed within this thesis investigates whether multi-material 3D printing can aid the production, quality and repeatability of compliant actuation methods. This is achieved by creating two actuators that utilise both solid plastic and rubber-like materials printed into the same component.

Furthermore, simulations are undertaken to explore the potential of altering the level of compliance within Wormbot. Using a number of varying environments, it will be investigated whether performance can be improved by altering how compliant the joints of the robot are.

1.4 Thesis Structure

Chapter 2 will provide a literature review of the previous version of Wormbot, as well as a range of other hypermobile robots, actuator technologies and compliance methods. Chapter 3 will discuss a range of potential actuation methods for hypermobile robots, taking size and power among other facets into consideration. A potential 3D printed pneumatic solution for compliant actuation will be developed and tested in Chapter 4. After this, Chapter 5 will use simulation software to investigate the effects of varying levels of joint compliance within hypermobile robots when used in a range of environments. Chapter 6 will then describe the process of producing a 3D printed Series Elastic Element (SEE) to use as another method of providing compliant actuation, from proof of concept to developing SEEs to specification. Finally, Chapter 7 will discuss the results of the research and any future work that should be considered.

Chapter 2

Literature review

2.1 Introduction

This Chapter provides a brief overview of the developments in hypermobile robotics, reviewing methods and assessing strengths and weaknesses. This will start with looking at non-wheeled hypermobile robots, followed by machines with wheels and tracks, and then robots without locomotion, intended to be used as manipulators. Focus will then be pointed at the actuators, giving a guide to what options are available for joint movement, looking at a range of solutions including pneumatics, smart actuators and motors. This will take size, power and efficiency into consideration, as well as ability to employ compliance within the system, a facet that is important project, as explained in Chapter 2.2.3. Finally, these will be assessed and some of the more promising design concepts will be identified.

2.2 Hypermobile Robots

2.2.1 Introduction

The field of hypermobile and snake-like robotics started in the 1940s with analytical research on snakes, but has taken a leap forward in the last 20 years [60]. Hypermobile robots have a wide range of potential applications, including exploration, search and rescue and endoscopy among others. There are also numerous ways in which these are implemented, whether it be with wheels, tracks or body propulsion (assuming the robot is one which can travel, as certain end effectors/ manipulators do not travel but can be included under the heading of Hypermobile robots) as well as many variants on the numbers of degrees of freedom (DOF). In order to make the most of the possibilities this area provides, one must first explore the existing applications to determine what is most effective, a task previously performed by Granosik, Hirose, Hopkins, Liljebäck and Webster amongst others [38, 46, 47, 60, 90].

2.2.2 The Original Wormbot

The first of the robots that will be discussed is the Wormbot developed at the University of Leeds [28], shown in Figure 2.1. The programming of the robot allows it to replicate the forwards locomotion of the nematode worm *C.elegans*. The physical robot in question is constructed of 13 connected segments with 12 joints, each powered by a geared DC motor with a pulley system. Springs between the segments provide worm-like compliance since the motors themselves cannot provide this.

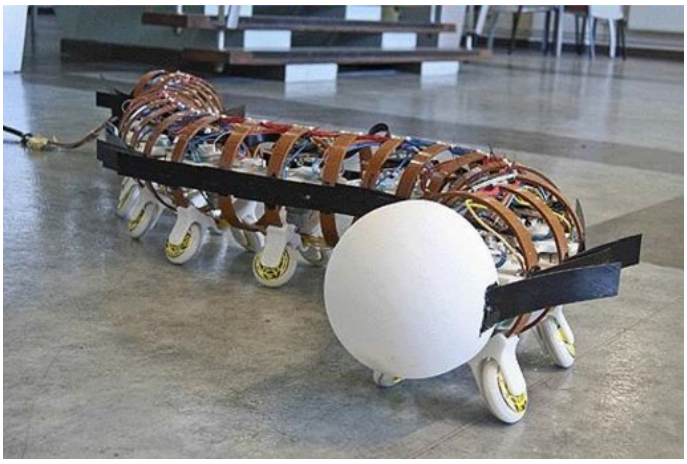

Figure 2.1: Wormbot features 13 segments, each with 2 passive wheels to facilitate forward motion. The black strips allow for smooth contact with objects [28].

Compliance was found to be a vital component to the way *C.elegans* moves and this, in part, is due to the requirement of proprioceptive feedback [27]. To understand this, a brief description of the gait of *C.elegans* is required. *C.elegans* uses a single gait to travel through all environments [25, 26]. In this gait, if the length of the body is broken up into segments, a single segment of the body is either moving in one direction or the other. To calculate this, each segment takes into consideration it's position and the position of a number of segments in front and behind. This is one of the facets that contributes the it's recognisable gait. However, this proprioceptive feedback is dependant on stretch receptors [27]. These are receptors that communicate whether the bending of the body has been influenced by the surrounding environment. This effects how the segments move to overcome the potential object or resistance to movement. To achieve this in Wormbot, compliant torsion spring elements within the joints are utilised, with rotary potentiometers acting as the stretch receptors [28].

The method by which Wormbot travels is generally as desired for this project, though a number of modifications would need to be made for it to be used outside laboratory conditions. The system would require a stronger form of actuation as the mechanism used proved to be underpowered. Furthermore, the large size of the original robot could make it difficult to fit between objects in tighter environments, so a new model would need to be reduced in size. This would lead to a redesign of the method of compliance. Additionally, the passive wheels on each segment would need to be removed as these could get caught on rubble or other parts of the environment. This, in turn, could require the development of a skin that could allow the Wormbot to move itself forward (i.e. provide more friction laterally than lengthways). Alternatively, wheels that are less open to the environment could be used, examples of which can be seen later. It would be desirable if the robot could also be waterproof, considering the harsh environment in which the robot might be used. Placing wheels around the circumference of the robot, or removing the wheels entirely and implementing the skin could also allow the robot to function upside down. An improved Wormbot may also need to be able to move in three dimensions as opposed to two, to allow it to navigate rubble.

2.2.3 Body Motion Powered

The ACM series of robots have been developing for many years under Shigeo Hirose, who built his first snake robot back in 1972 [46]. Over the years the series of hypermobile robots have developed in many different ways. One example of this was with the ACM-R1 [36]. Experiments were performed to find out how angle of curvature affected the properties of movement. It was found that using larger turning angles in the sine wave motion meant the robot could climb steeper inclines, which holds uses when travelling over uneven terrain [36]. Both the ACM-III and the ACM-R1 used wheels positioned in the joints of the robot instead of in the middle of each segment to make it less likely for wheels to collide, increasing body flexibility. Later units such as the ACM-R3 however used wheels which were positioned across each segment to simplify the design [46]. This is shown in Figure 2.2. The ACM-R3 aimed to reduce the chance of wheel collision with a method that had other advantages [68]. Wheels were arranged at 90° to the adjacent segments, as this is the axis in which the joint can bend. This makes it less likely for wheels to collide and allows the robot to work in three dimensions, as well as run on all sides. This can be seen in Figure 2.3. This concept was also used in the ACM-R4, though when updated to the ACM-R4.2, this wheel arrangement was replaced with more standard wheel arrangement [53]. This was due to the 90 ° arrangement reducing space for larger wheels for greater purchase and requiring more components for operation, increasing weight.

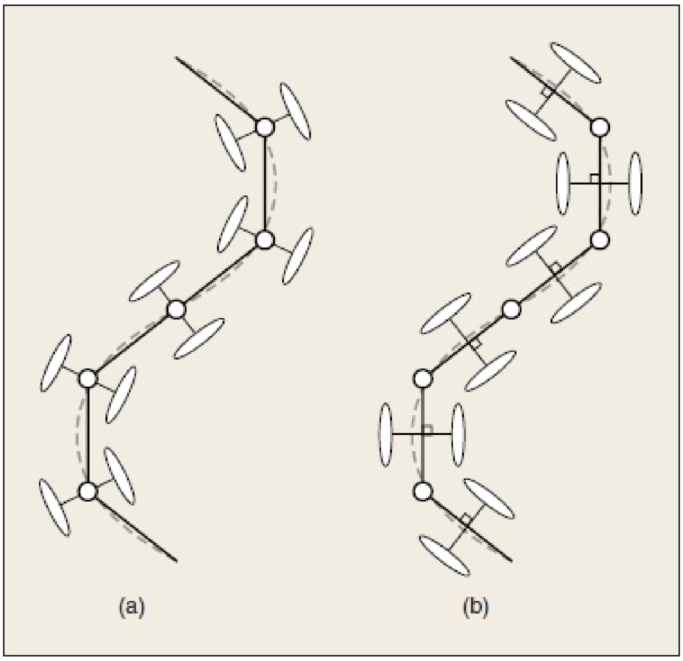

Figure 2.2: Wheel layout in (a) ACM-III (b) ACM-R3. Note the position has altered from corner wheels to being mounted mid-segment [46].

The ACM-R5s (Figure 2.4) actuated joints have two DC motors in each joint for rotation in two degrees of freedom (DOF), allowing for three dimensional movement in each joint instead of alternating the DOF from joint to joint [46]. One motor imparts lateral rotation on the joints in a similar fashion to the Wormbot, while the other pitches the joint up and down. Additionally, with ACM-R5 being completely water-tight and with the addition of fins on the outside of each segment, it is not only able to swim, but able to swim under water as well as on the surface. Each fin also had a small passive wheel on the end which facilitates movement on land. Having these fins positioned evenly round each segment also means that the ACM-R5 is invertible. Furthermore, ACM-R5 is tetherless so its travel distance is not hindered by being connected to a static power pack. However, it was not clear from the literature whether the robot would be able to travel across rubble and uneven surfaces that may occur in a disaster area; something the ACM-R3 claimed to be able to do [68]. Finally, while this robot can be made shorter than the Wormbot (2m

Figure 2.3: ACM-R3, with its striking wheel layout [46].

long) and its predecessor the ACM-R3 (1.755m long) with its modular design, the robot was still quite large with a typical 8 segments and overall length of 1.44m.

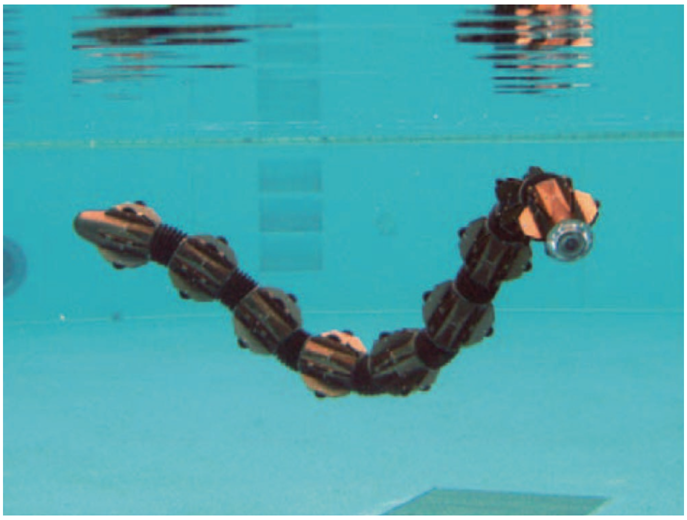

Figure 2.4: ACM-R5 also features passive wheels, but has 6 equally spaced around each segment to make it invertible. It also has the ability to travel in 3 DOF which aids in its ability to swim [46].

The issue of size was addressed by small ACM, which was 0.65m in length [95]. However, this robot lacked wheels, contributing to it having difficulty in forward locomotion using undulatory motion, though it travelled by using a sidewinding gait, travelling 90° to the direction ACM-R5 travels. However, imagining this robot working with wheels to allow forward motion is not unfeasible. The team behind this robot also developed a new joint that allowed greater flexibility. Using two motors, rotating input arms A and B on Figure 2.5(a), the joint could achieve rotation on 4 different axes by using a series of lever arms and gears. Two motors rotating together resulted in rotation around the pitch axis, wheras motors working in opposition created rotation around the yaw axis. As can be seen in Figure 2.5(b), by operating two joints with each motor, the number of axes of rotation is doubled. This meant that the robot would be able to achieve as much movement as possible without requiring space for additional motors, making miniaturization much easier.

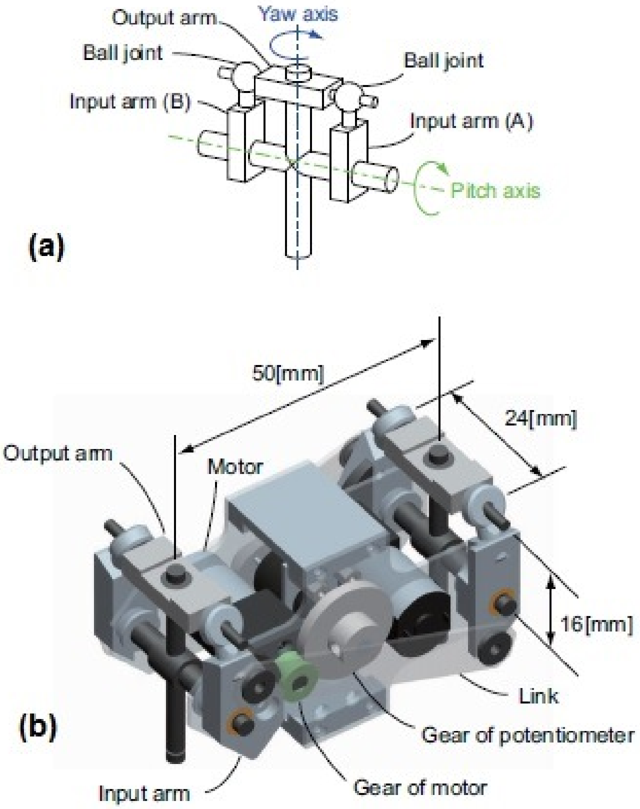

Figure 2.5: (a) One end of joint mechanism. Motor input at A and B. Motors working in opposition rotate the joint. Motors working in the same direction will lift or drop the segment [95]. (b) The whole joint for small ACM. Due to the design any movement imparted by the motors on one side is mirrored on the other, doubling the rotation [95].

German researchers Rainer Worst and Ralf Linneman developed snake robot GMD-SNAKE in 1996 using a similar actuation method to Wormbot [92]. Each joint has drive motors which bend the joint using pulley strings. There are 2 sets of these to allow vertical actuation as well as horizontal. While this creation doesn't use springs to add compliance to the system, each segment does use rubber pieces between segments in the framework which could perform a similar role. Furthermore, the robot requires no wheels to assist in moving itself forward. However this makes it hard to envisage how the snake produces the lateral friction required for this locomotion method [48]. This could explain why the second version had active wheels located around each segment to improve locomotion efficiency [51]. More robots using active wheels and similar locomotion will be discussed in Chapter 2.2.4.

Another robot that moves in a similar fashion to the Wormbot was designed by Dr Gavin Miller [65,66]. Miller has made many versions but this review will focus primarily on S5, as later versions were either experimental or not presented with enough information. Controlling the bending of the snake's segments are 64 servos, connected to 42 batteries. While this robot appears to be very long and have a relatively large cross section (though the previous version is smaller, its cross sections are larger), its gait is very smooth due to the high number of segments [65]. Additionally, it has the advantage of being tetherless. However it lacks the ability to operate upside down as it relies on each segment having a wheel. The S7 version does not need a wheel due to a redesigned shell although, as stated previously, details of this design are very limited. The S5 produced promising results with its smooth gait, though it could not sidewind. This was assumed to be due to the scaling up effects from previous models that could sidewind (additional weight for example), as well as having a large heavy head module. Additionally, this robot has not been designed for use on or under water, or on rough terrain. Due to these reasons it is unlikely to be suitable for a search and rescue application at this time.

Researchers at the Shenyang Institute of Aeronautical Engineering have built a snake robot called "Perambulator II" [96]. It uses the same style of sinusoidal motion as ACM-R5, but the joints are more complex, allowing for 3 DOF as opposed to the ACM-R5s 2 DOFs. It is argued that this allows the robot to navigate more complex terrains. The perambulator also uses rollers instead of wheels, which allow for smoother and more efficient movement when rolling laterally in its "twist" locomotion gait. These would be less efficient if the robot was required to swim, but the robot was not built for this application. It is also shorter than the ACM-R5 by approximately 0.4m at a length of 1.2m, but has a larger cross-sectional area, which could hinder its ability in narrow channels. Furthermore, the maximum speed of 0.1m/s is quite slow.

A few years later, at Shenyangs Institute of Automation (SIA), a group of engineers worked together to produce an amphibious snake robot [97]. In comparison with ACM-R5, each joint in the SIA has three motors and they are all placed in one side of the joint, instead of two motors shared between both sides. Each segment has 8 wheels with each of these positioned towards the end of the fin to propel the robot forward more efficiently, as seen in Figure 2.6. Finally the robot is waterproofed using bellow-like extendible joint casing, two aluminium sealing rings and o-rings on each segment, allowing flexibility along with water resistance. As a collective result, the SIA robot is shorter by about half a metre than the ACM-R5. Both robots are relatively light, though considering the SIA robot is tethered and the ACM-R5 is not, the latter is more efficient as it carries its own power source. The SIA robot uses a number of original gaits for travelling that the ACM-R5 does not, but most of these do not increase upon the effectiveness of the ACM-R5 and many of them are ineffective, or even damaging, in water [97].

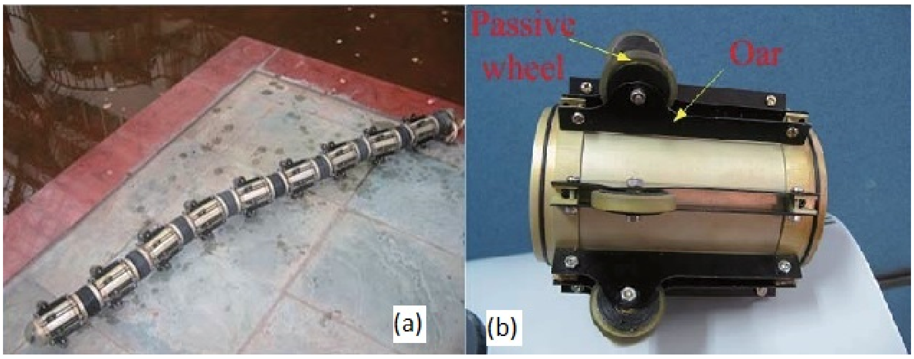

Figure 2.6: (a) Amphibious snake robot [97]. (b) Segment and fin, with wheels positioned towards one end of the fin for more efficient propulsion [97].

Slim Slime was a robot that was produced in 2000 and, like Millers S5, relied on body movement alone for propulsion. It was developed with the ability to move each joint in 3 DOF [71]. This is achieved by having 3 bellows placed equidistantly around the joint module, each supplied with air by a central main pipe. When these bellows are activated, they expand in length. A set of springs are used in opposition to ensure the robot will always return to its contracted state. Another useful trait is that Slim slime has the ability to alter its gait to perform differently (e.g. to gain a higher driving force, greater speed etc) by altering the frequency and amplitude of the propulsion wave (lower amplitudes lead to quicker progression, whilst higher amplitudes lead to a greater driving force).

The team behind the Slim Slime Robot (SSR) changed direction with the second version's propulsion method [18, 19]. Instead of having 3 bellows per joint, it has just one central bellow, with the direction controlled by 3 evenly spaced bridles, or pulleys. This has led to the cross section of the robot resembling a triangle. This, in turn, may have led to the change in movement style. Instead of the robot using a sinusoidal wave to move, the second SSR crawls using longitudinally travelling body wave. The robot is still quite cumbersome, being 270mm long and the robot is still slow are just under 0.05m/s.

At Carnegie Mellons's Biorobotics laboratory, one of the projects that has been undertaken is on, at first sight, a simpler hypermobile robot, where each joint only has one degree of freedom, like the ACM-R3 [94]. To achieve a greater range of movement, the modules orientation is rotated 90° in relation to the adjacent modules. In this method, the robot sacrifices some flexibility for a cheaper, simpler and potentially more robust design. This is because each joint does not need to have as many motors or gears to control it. The group also worked on lowering the current draw from the servo motors. This was performed by using power regulators that could increase the running voltage up to 4.8 times the rated voltage of the original servos, meaning thinner wires can be used and the system can handle voltage fluctuations better [94]. Finally the team behind the creation worked on using different skins and "compliances" as they are referred to by the authors, or material pads (Figure 2.7). They discussed how skins can be used to protect against the environment, but can hinder movement and create heating problems. They also discussed how the material pads cannot protect against the environment but can be used to increase friction between the robot and surfaces. Additionally, this could be viewed as an alternative to using springs or spring-like components within a joint mechanism to allow a robot to comply to surroundings.

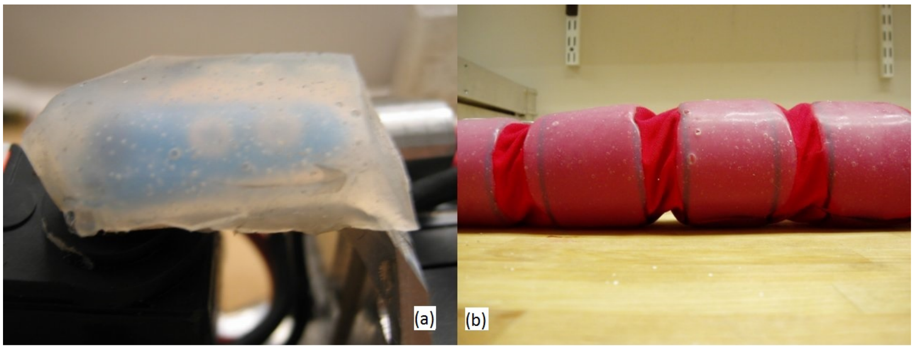

Figure 2.7: (a) Example of module "compliance" [94]. (b) Example of robot skin [94].

In a later version, known as Unified Snake (US), the pads option was used to help the robot have enough grip for tasks such as climbing trees [93]. US kept the same design structure as its predecessor, which assisted in keeping it small (910mm long and, more importantly, 51mm in diameter), so it could access more hard to reach areas. The US also has the ability to conserve energy using a joint brake. This means that power to the motors can be turned off with the joint staying in a stationary position when the brake is applied. This brake is operated using shape memory alloys (SMAs). This can either be actively operated, or automatically applied if power is unexpectedly lost. The brake increases the holding torque from 1.3Nm to 6.8Nm. While US proves a design such as this can be effective, there are still a few issues. Firstly the brake can be slow to release. Secondly, the robot is still tethered. If power was to be contained within the robot, it can be assumed that the size of the modules would need to increase.

SnakeFighter Anna Konda from the ROBOTNOR Centre for Advanced Robotics in Trondheim, Norway, was a snake robot that was designed to be used to fight fires in hard to reach, dangerous areas such as large vehicle accidents in tunnels, using a pressurised water supply feeding through the centre of the robot [59]. Water is also used in the actuation system of the robot, which relies on hydraulic pistons to control each joint. This makes use of a cheap and easy to access actuation power supply, though it still limits where the robot can operate. Due to size constraints all the hydraulic valves and components had to be custom built, which will have added cost to the build, though these components will have been built to a good quality as they are able to work under very high pressures (1450PSI/ 100Bar). This also means the pistons can impart a large force on the joints, which will be necessary considering the 70Kg weight of the robot. Unfortunately, the robot is not able to move forward using a sinusoidal gait due to the lack of lateral friction created from the skin panels, but they are strong and they protect force sensors underneath. The robot uses type of hinge called a cardan joints to add strength to the joints as well (Figure 2.8).

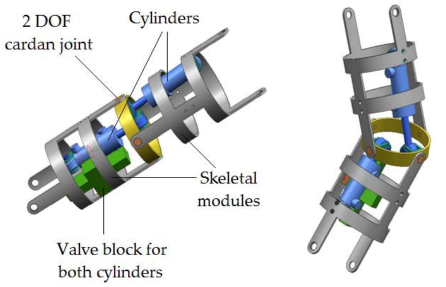

Figure 2.8: CAD model of Anna Konda segments with cardan joint, giving additional structure to the system [59].

The developers took a slightly different approach to their robot KULKO's locomotion

[58]. At a glance, the design of the robot isnt too dissimilar to others in the field; it uses two servo motors to achieve 2 DOF per joint and it performs gaits that are performed by other robots too. However, when travelling in a traditional sinusoidal wave method, Kulko relies on obstacles around it to move forward, pushing off the terrain with the side of its body. To assist in this, it has the ability to measure the force being applied to the body wall in a feedback loop. This approach would be unsuitable for a number of applications, as not all terrains provide the obstacles this robot requires for forward propulsion. Furthermore, in some circumstances, the robot may create further damage if it applies a force to an unstable object.

Crespi and Ijspeert of the Biologically Inspired Robotics Group (BIRG) based in Lausanne, Switzerland contributed Amphibot II to the world of hypermobile robots [33]. The actuation method is similar to many existing robots in that motors are used for controlling joints, but each module can function by itself because it had its own power supply, encoder and control circuitry. This not only means that the system is tetherless, but the number of modules is not limited by power constraints and can be adapted to many different shapes and sizes. Using similar segments, salamander and fish robots have also been created [33, 34]. The robot can swim and, due to low robot density, floats just below the surface of water when swimming. It also has the majority of the weight of each module positioned as low as possible to increase stability. The salamander version of this robot also uses a 25cm fin at the rear of the robot to increase swimming speed, though this could potentially hinder movement on land. Amphibot III has been created with a smaller tail fin which is responsible for the latter versions improved performance [76]. Amphibot III also possesses sprung joints. One advantage of these is that it could allow for a level of joint compliance, similar to Boyle's Wormbot [28]. Additionally, the robots have limited passive movement vertically which proves useful for small undulations but the authors state is a problem for outdoor environments, as it may mean they can't move over larger inclines, hills and other objects [34].

Bayraktaroglu created a hypermobile robot which moves forward through sinusoidal movement but, unlike most other snake like robots, does not require passive wheels [23]. However the robot is dependent on obstacles in the environment to propel itself forward, similarly to the previously mentioned "Kulko". This makes the robot very useful in small confined spaces and channels or terrain with lots of close objects, but not for open areas. In these situations, the robot must move in an"inchworm" fashion after being positioned on its side. This demonstrates that, while hypermobile robots do not require passive wheels to be able to move in a visually similar fashion to snakes, eels etc., a difference in force acting laterally and longitudinally on the robot must be created. It would be unlikely for every environment that a search and rescue robot was put in to include the necessary objects for this. Therefore it would be wise to have some method of producing it on board the robot, though care would have to be taken to avoid said method catching on rubble or other hazards.

This is backed up by research performed by a group which developed a similar robot [29]. Brunete et al developed a snake-like robot for small pipe inspection in 2006. Like Bayraktaroglu, the group from Madrid made a hypermobile robot without wheels, but on a much smaller scale. However the problem of having enough friction for sinusoidal movement was still apparent. Brunete said, “Serpentine Locomotion is more suitable to negotiate bends and for straight stretches when the friction between the robot and the pipe is strong enough” [29]. It is stated that this robot would be able to cope with certain sections of piping, where friction from the pipe can be built up, but whether this could be achieved in other environments is unknown. However, later work from the author suggests updated versions of the robot used different types of modules (modules for extension, rotation and other motion types) to achieve good functionality [30].

An alternative bio-inspired method of locomotion for a worm robot is peristalsis, in which sections of the body alternately contract and then expand as the next section along contracts, resulting in a movement not too dissimilar to the inchworm method. This process allows the robot to crawl forward with no lateral displacement in a similar fashion to an inchworm gait. Peristalsis is used as the only mode of locomotion in Meshworm, produced by a group at MIT [81]. The robot in question uses Shape Memory Alloys (SMAs) to replicate the effect of two different sets of muscles. One set are arranged radially and cause parts of the body to contract, while the other set are arranged longitudinally to control the direction in which the worm travels. Meshworm has proved to be very robust, as it will still work after being stepped on or hit with a mallet. This would be highly advantageous in disaster situations, such as an earthquake, where there is a threat of falling rubble. It is also very small (around 200mm unloaded) and light. Additionally, it is untethered which further lends itself to search and rescue applications. However, it is quite slow in comparison to the previously discussed robots and it is unknown whether it would function in a wet environment.

2.2.4 Wheeled and Tracked Robots

Hypermobile robots do not always use bio-inspired locomotion methods. For example, powered wheels are often used to good effect. The first of these was the Koryu (KR) series from the Tokyo Institute of Technology [45]. This robot would be considered obsolete by todays standards as it is very large and incredibly heavy (KR-II is 3.3m long, 1.08m high, 0.46m wide and 320kg) but it had a number of original ideas for its time. It was able to stay balanced and continue moving on inclines and on uneven terrain due primarily to two innovative solutions. The first of these was the ability to move segments in the Z axis using a linear actuator between them. The second was the use of only one wheel per segment. This sounds unstable at first, but they were arranged so that the wheels on adjacent segments alternated sides. Thus, if every segment with a right side wheel is positioned higher than ones with left side wheels, the KR-II can move across an incline while keeping its body level.

Snake-like hypermobile robots have the potential to be useful in many different applications besides search and rescue. For example, the MAKRO series of robots was designed for inspecting sewers [80]. It uses active wheels for propulsion, but also has powered joints with 3 DOF (2 rolling, 1 yawing) to help navigate pipes. Later versions of the robot included a casing that improved robustness to the point where it became “water and explosion proof” [85]. One problem with the MAKRO is that it only has wheels on the underside, meaning if the robot flipped over it could become stuck. This is an acceptable limitation in sewers but could prove a problem should the robot be in an environment where it could get lodged on uneven surfaces.

Another locomotion strategy that is similar to wheels is the use of tracks. One of the problems that is caused by using wheels is that rubble can get caught between the wheels and prevent movement. Tracks reduce the risk of this happening as the continuous track belt does not allow rubble or debris to get stuck as easily as with wheels. One group of hypermobile robots that utilise this approach is the Souryu series [20]. Souryu V (Figure 2.9(a)), for example, has two main attributes that set it apart. The first is the use of a mono-tread track, unlike its predecessors which had a track on either side of the body. The advantage of a mono-tread is, as can be seen in Figure 2.9(c) that the robot cannot become beached on uneven terrain that is positioned between tracks. The other innovative technique that is used in the Souryu V is its turning mechanism, seen in Figure 2.9(b) and (d). Due to the mono-tread design, a hinged joint cannot be used to connect adjacent segments. Therefore, Souryu V utilises four elastic rods positioned in pairs on either side of the tread. These can be shortened or lengthened to allow the robot to travel around corners or head up or down. With these being elastic rods, they bend around the tracks as well. A solid bar used in this way could catch on the corner of the mono-tread, causing damage. Using this system, the Souryu V can climb a step that is 440% of its own height. The Souryu-V is shown in Figure 2.9.

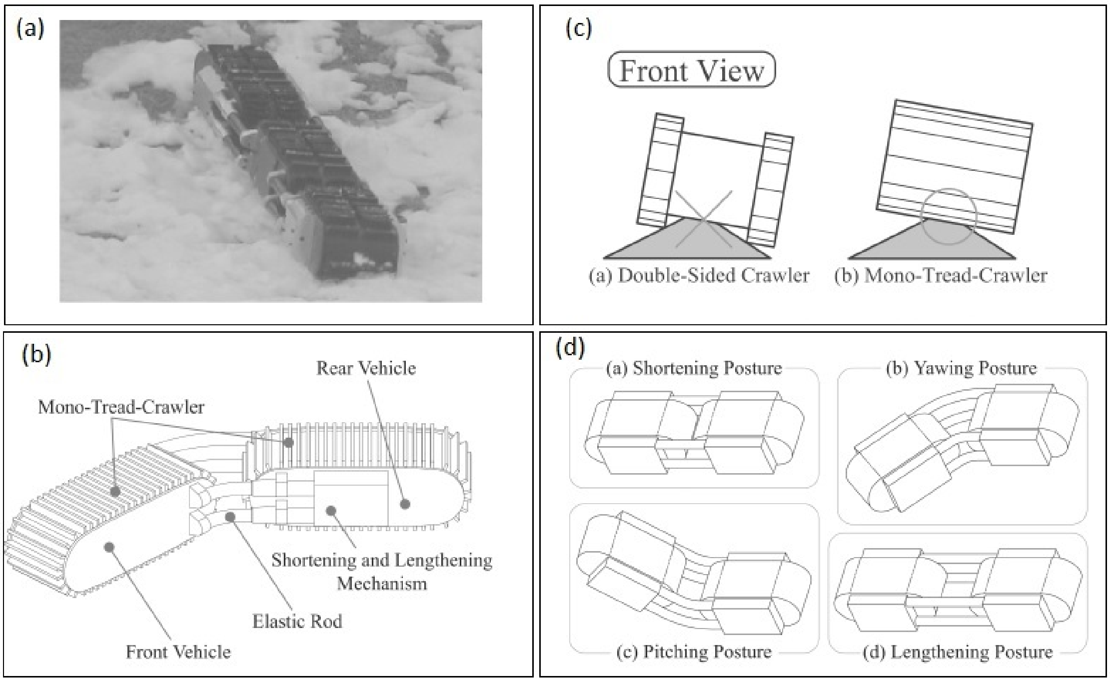

Figure 2.9: (a) Souryu-V in use [20]. (b) Diagram of Souryu-V [20]. (c) Diagram showing the advantage of using a mono-tread [20]. (d) Diagram showing steering mechanism of Souryu-V [20].

Another group that has tried to solve the beaching problem (Figure 2.10) is the team behind the MOIRA series of robots at Universities of Kyoto and Kobe [44]. The philosophy that is applied is that to increase the efficiency of a tracked robot, one must keep the proportion of surface area used for propulsion high. This is known as the Propulsion Ratio [39] and is shown in equation (2.1).

$$K_{PR} = \frac{A_P}{A_P + A_I} \tag{2.1}$$

K_{PR} is the Propution Ratio, A_P is surface area that provides propulsion and A_I is the surface area that is inert. Therefore $A_P + A_I$ is the total surface area of the robot. The original MOIRA, which had 2 thin tracks on each of 4 sides had a K_{PR} of 0.56, meaning 44% of the robots surface was inert and thus a potential beaching point. To combat this and other problems, MOIRA 2 was changed from a square cross section to a rectangular one to provide more stability. After this, tracks were only placed on the 2 longer sides. Finally the joints were made smaller and the segments longer to increase the K_{PR} to 0.9. The other point of note on the MOIRA 2 is that the joints are pneumatic. The robot performed well in tests, showing high mobility, but it was let down by being tethered, with the umbilical catching on debris [44].

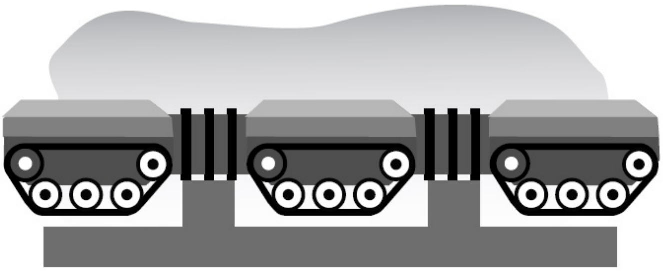

Figure 2.10: Diagram of beaching. Note where the ground meets the robot. Tracks are not in contact with ground leading to the robot becoming stuck [44].

Following on from the Meshworm introduced earlier, another hypermobile robot produced by MIT is the Omni-Tread collection of robots [39, 41, 42]. This series started off with the Omnipede, a mobile robot using simplified legs. The team behind it recognised problems with this form of propulsion, such as a low propulsion ratio and the legs becoming stuck on rough terrain. This lead to the group deciding to use tracks in future developments, which in turn lead to the development of the Omni-tread and eventually the OT-4. In having tracks on all four sides of its square cross-section, it resembles MOIRA; but OT-4 differs in that its joints are powered by 4 pneumatic bellows each. The advantage of using bellows is that they have a power to weight ratio greater than electric actuators and, while hydraulics have an even greater power to weight ratio, pneumatics are more reliable and cost less to maintain [39]. Due to this, OT-4 is able to complete a wide range of tasks, including moving across open trenches 52% of its length. However, one problem with OT-4 is that it is not autonomous and requires three operators at a time.

Another novel idea concerning hypermobile robots was presented by Zhang et al. from the University of Hamburg [98]. Their robot, the JL-I has the ability to separate into three independent robots to perform distributed activities and then couple back together to reform the hypermobile robot. The robot can function either as three separate parts or as one entity. The connectors on each segment also allow for rotation in 3 DOF at the joint

Figure 2.11: OT-4 controls its joint movement via four bellows per joint, which are flat when unactuated to save space and to reduce the risk of them becoming caught on foreign objects [42].

when connected to another segment. All this together allows for a very versatile robot that can get out of many situations. One problem with the system though is that, compared to other robots built at the same time, the segments are quite large (cross section = 150mm x 250mm) and the system as a whole is heavy (21kg).

Returning to the idea of the Propulsion Ratio, unless there is a ratio of 1, there is still a chance, however small, that a hypermobile robot could still get stuck on a protruding piece of terrain [50]. A team at the Okayama University of Science therefore developed of mono-tread robot, WORMY, that has no spaces between segments and thus achieves a very high propulsion ratio. As shown in Figure 2.12, this is achieved by having one flexible rubber track belt stretched over a chain of segments which extend and shorten the length of each side of the robot. The robot turns via the use of pulley belts running along each segment. Through this method, the robot can turn in three DOF. Additionally these pulleys can help maintain rigidity throughout the body, thus helping it to bridge gaps 46% of its body length. One potential problem is the size of the robot, with a cross section of 200mm x 200mm compared to OT-4s 82mm x 82mm, possibly preventing it from navigating certain obstacles. However it isnt unreasonable to think it could be made smaller.

The Souryu team developed a method of bending similar to that of WORMY's for their later works [88]. However, in comparison to WORMY, more recent Souryus had

Figure 2.12: WORMY features 1 single track that is positioned round the whole robot to avoid it becoming beached [50].

advantages and disadvantages. Souryu VII, VIII and IX all had a much smaller cross section (the largest being IXs 162mm x 96mm in comparison to WORMYs 200mm x 200mm) so it could fit into smaller spaces. However, Souryu could get stuck in small channels, partly due to its short body, but potentially also due to its lack of ability to rotate in the roll axis. A roll joint was therefore added in Souryu IX. The team behind Souryu took another change in approach to later versions. Instead of using treads, Souryu VII, VIII and IX use an asymmetrical wheel layout, similar to the layout of the KR-II. Suzuki argues that this is preferable as a wheeled robot is easier to water proof than a tracked one due to the sliding parts used in treads. Additionally, the asymmetrical wheel layout allows for a tighter turning circle then a traditional wheel base layout, as there is less chance of wheels close to each other on one side interfering with each other.

Nagase, of Ryukoko University in Japan, came up with an original propulsion method for a robot [69]. The method required a worm gear system inside the robot, which inches forward a series of belts that are used for propulsion (Figure 2.14). This is not the first time screw-like locomotion has been used for propulsion [8] but it is rare to find such a device driving tracks. In tests the method proved successful, though there are a number of potential issues. First, the robot is slow at 0.022m/s. Second, if something gets caught in the crawler belts, it could have a damaging effect on the internal workings of the robot. Finally, the robot cannot steer, though this could be solved by having a number of these attached together and using active joints to direct the segments.

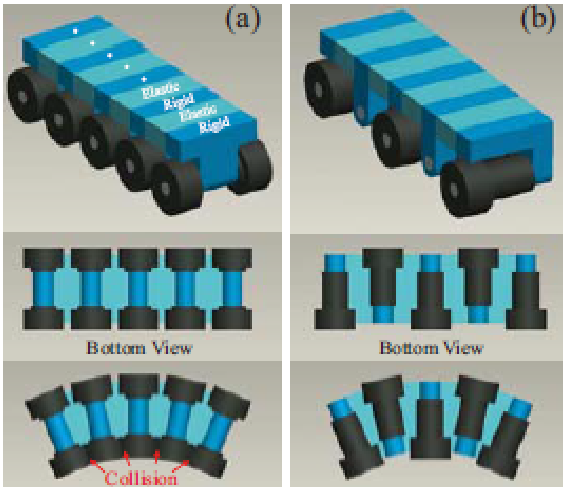

Figure 2.13: (a) Standard symmetrical whhel layout. (b) Asymmetrical wheel layout used in Souryu VII, VIII and IX [88].

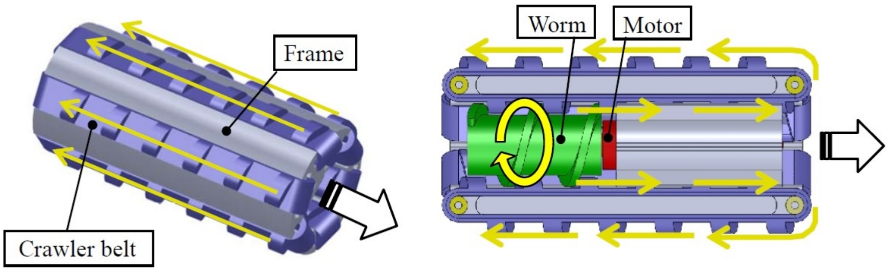

(a) Overview (b) Section

Figure 2.14: Cylindrical crawler robot uses a screw to drive the tracks [69].

2.2.5 Stationary Robots

Inspiration for hypermobile robots is not constrained to snakes and worms. Other animals can provide useful ideas as well, such as elephants [43] or octopuses [57]. The inspiration from a snakes body and an octopus arm lead to Lis flexible robot arm [57]. Each segment has 12 holes equidistant around the edge. With varying lengths of pulleys acting through the holes, the robot can bend at three different points with 2 DOF (with 4 wires acting per section). Li reports that the robot is accurate to control and simpler to use in comparison to other continuum robots. This approach has also been adopted by other projects, including a ureteroscope by [56]. This approach is less well suited to a mobile robot however, because all motors and gears would have to be positioned on one end segment, which could prove harder to move due to its increased weight. This would be more of a problem if more sections, and thus more motors, were to be used. Another issue would be that the wires could be subject to significant wear. Therefore, strong wire and a non-abrasive casing would have to be used. Additionally, a strong casing would be useful to prevent any damage to the mechanism from the environment.

Hannan and Walker built a continuum robot manipulator [43] based on an elephants trunk with the same principle of movement to that of Li's robot, shown in Figure 2.15. Hannan made the argument that the pulleys dont need to be connected to each joint. It is possible to, for example, connect to every third segments and you can move all three previous joints with just one actuation instead of using three individual actuators. However, while this makes for a simpler system to operate, the machine in question may lose out on extra flexibility that may be useful for certain situations, such as navigating small, winding channels. Another idea implemented in this design is that the trunk will always revert to its original shape when unactuated because there are springs attached between each segment. Whilst this means no counter-actuation will be needed for movement, the force required to move each joint will need to be greater than it would have been otherwise.

Laschi and his team in Pisa, Italy, worked on building a prototype of a robotic arm, seen in Figure 2.16 [54] based on that of an octopus, in a similar fashion to Li. The Italian creation however was design to mimic the physiology of the octopus arm much more accurately, using longitudinal and transverse muscles to make the prototype extend and shorten as well as bend. Future versions of this are intended to use Electro Active Polymers (EAPs) as the artificial muscles. While the arm they created has the ability to move in many degrees of freedom, the design is quite complicated and currently may be difficult to control or build on a smaller scale.

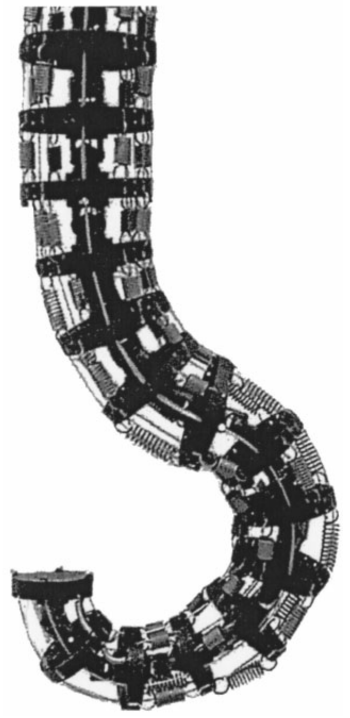

Figure 2.15: Elephant's trunk manipulator, which actuates groups of joints instead of each one individually [43].

Figure 2.16: Octopus based robotic arm [54].

SMAs have also been used in flexible arm robots. One of the advantages with SMAs is that they require very little space in comparison to a servo or a motor. This was fully utilised by a team based in Yamagata, Japan [67]. They designed an active guide wire that could be used in catheter placement, with the idea being that the guide wire could assist in positioning it around corners. One issue was that an SMA will not revert into its original state when current is removed without a restorative force, though this was partly resolved in the guide wire device by positioning a spring, or bias coil, around the SMA to revert the wire to its default straight position after being deflected.

2.3 Actuators

2.3.1 Introduction

As discussed in Section 2.2, hypermobile robots have been produced for over 20 years. Over this period of time, the development of new technologies and design concepts means many different methods of actuation have been tried. These, broadly speaking, can be split into three groups; electric motors, hydraulics/ pneumatics and smart materials. Within these groups there are many further variants on these methods of actuation. In this section, the specific methods in which these robots joints are actuated will be analysed and compared. This will be performed by analysing surveys from other authors as well as drawing conclusions from technical and performance data.

2.3.2 Overview

Comparing actuator types for hypermobile robots is not new. Granosik [39] completed a table of data to compare the approximate performance statistics of electric motors, hydraulics and pneumatics, as shown in Table 2.1.

From this it is clear that the suitability of different types of actuator depends on which of these characteristics are most important. For example, electric motors and power systems are generally efficient, very precise and easy to pack and store in small spaces, all of which are important features for self-contained small robots. However they have a lower power to weight ratio (a view supported by Kingsley) and are less durable than other methods used in the field [49]. Hydraulics, according to Table 2.1, would be perfect for a machine requiring a very high force output, but they are relatively unreliable and are costly to repair. Reliability is an important characteristic for most areas of robotics, not just hypermobile robots. Additionally, the additional weight of fluid within the system could increase the weight of the whole robot. This could explain the the low number of

Table 2.1: Key parameters of different actuators [39]

Drive type performance compared	**Electric**	**Hydraulic**	**Pneumatic**
Efficiency * [%]	50-55	30-35	15-25
Power to weight ratio [W/kg]	25-150	650	300
Force to cross section area [N/cm2]	0.3-1.5	2000	100
Durability [cycles]	$5\text{-}9\text{x}10^5$	$6\text{x}10^6$	$>10^7$
Stiffness [kN/mm]	10-120	30	1
Overload ratio [%]	25	50	50-150
Linear movements ranges [m]	0.3-5	0.02-2	0.05-3
Linear velocity [m/s]	0.001-5	0.002-2	0.05-30
Positioning precision [mm]	0.005	0.1-0.05	0.1
Reliability (relative)	Normal	Worse	Better
Maintenance costs (relative)	Normal	Higher	Lower
Unfavourable feature(s)	Electric hazard, magnetic disturbances, heating	Leakages, difficulties with energy transmission	Noisy
Favourable feature(s)	Easy energy transmission, storage		Safety

hydraulic actuators in the previously analysed robots. Pneumatics on the other hand are very reliable, cheap to repair, durable and still fairly powerful. Therefore, despite being less efficient than hydraulics, pneumatics are much more common in this field. While the table is useful, it only gives a general overview of the field, so more specific details must be analysed before choosing the optimum actuator.

2.3.3 DC/ Electric Motors

Motors are by far the most common form of actuation in hypermobile robots, with a large proportion of the robots reviewed in Chapter 2.2 using electric motors as the primary source of joint movement. Most of these use a combination of motor and gear box to achieve the optimum balance between torque and speed.

- The MAKRO uses three motors per joint (two for roll DOF and one yaw DOF). To achieve the torque required at the joint, MAKRO uses harmonic gears to dramatically reduce the speed of the motor and increase the torque [80].

- The WORMY robot uses pulleys to control the steering of the body. Each of the pulleys uses a motor to power it, with worm gears to reduce the output speed [50].

- Wright's US robot uses only one motor per joint, changing the axis of rotation for alternating segments. The gearbox for this robot uses three compound gears to get a gear reduction of 401:1 [93].

The use of a gearbox in such a robot is vital when powered by a motor. This is because a lot of motors bought for this size of application spin far too quickly for joint movement (the motor for the US robot spins at 11,500 RPM) and don't produce enough torque. Using a gearbox benefits in two ways. They reduce speed to usable levels and increase the torque, which is a much more desirable attribute than speed when controlling a joint for hypermobile robots. However, using different gears can have varying effects on the performance of a robot. For example, using a chain of compound gears could take up a large amount of space in comparison to other methods, such as a planetary gearbox. Additionally, with an efficiency loss at each gear connection, a long chain of gears could lead to an inefficient system. Worm gears can achieve a large reduction of speed between the two gears, requiring fewer stages and hence saving space. Worm gears are also useful for increasing system torque but are not back-drivable, which could limit joint compliance. Harmonic drives however can also be used in high torque systems and are back-drivable.

Another design feature that is often used with motors in hypermobile robots is the use of pulleys [57]. The advantage of pulleys is that it avoids the need to have motors positioned along the body of a hypermobile robot. This can lead to a robot being narrower and more nimble. The motors required to operate the pulleys are sometimes positioned at one or both ends of the robot, which could cause problems when creating a mobile robot. A few mobile robots manage to make use of pulleys however, including WORMY [50] and Souryu IX [88]. WORMY only has one motor at either end controlling bending via pulleys in the robot (one motor for up/down, one motor for left/right]. Therefore, there is no need for a larger module at the end of the body. This does mean that the robot would not be able to travel forward purely by body movement, as there would not be enough actuated degrees of freedom to create the sinusoidal body motion required. This is not a problem for the WORMY robot as the primary method of propulsion comes from the large tread around the body.

Motors are commonly used in hypermobile robots for a number of reasons. Firstly, there are such a wide range of motors available that suitable motors for most applications are easy to find and can be adapted relatively easily with gearboxes if need be. They are also, as previously discussed, easy to use and take up less space than pneumatic and hydraulic systems [49]. Additionally, electric servo motors offer very accurate position control which could be useful for precisely navigating rubble and other obstacles [39]. However, this is not a necessity for a robot based on *C.elegans* as the movement of the nematode worm is not a precise movement [26]. Motion is only controlled by a section moving in one direction or the other, not precision movement to a set point, as discussed in Chapter 2.2.2. The price of this is that motors and servos are generally inferior to hydraulic and pneumatic methods when it comes to power to weight ratio. According to Granosik, motors have a shorter lifespan than hydraulics and pneumatics in terms of number of cycles [39].

2.3.4 Pneumatics & Hydraulics

2.3.4.1 Pistons

Out of the robots analysed previously in the report, the only example to use pneumatic pistons to drive joint movement was the MOIRA2 [44]. It uses an arrangement of two cylinders, both positioned above and either side of the joint fulcrum (Figure 2.17). This arrangement allows two actuators to move the joint in two degrees of freedom. Use of both pistons working in opposition allows the joint to yaw left and right, while both pistons working together pitches the joint up and down.

Haraguchi provides little technical data about the pistons but the robot performed well during tests, successfully navigating various types of rubble and displaying good dexterity. However, Kinsgley pointed out a few points to take note of when using pneumatic cylinders [49]. Pistons are often well suited to “bang bang” operation, in which the actuator moves quickly between the fully extended and fully retracted positions. However, fine position control can be difficult to achieve, partly due to the problem of stiction between the moving parts, though Liljebäck does not state this as a problem for Anna Konda, though this was using hydraulic pistons which present their own problems [59]. Haraguchi will have found a way to cope with position control but did not state whether stiction was a problem in operation. Additionally, pistons are relatively heavy and much lighter actuation options are available.

2.3.4.2 Air Muscles

Air muscles (also known as braided pneumatic actuators or McKibben artificial muscles) are a lighter alternative to pneumatic cylinders, being constructed from less dense and less rigid materials. The two main components of an artificial air muscle are a bladder

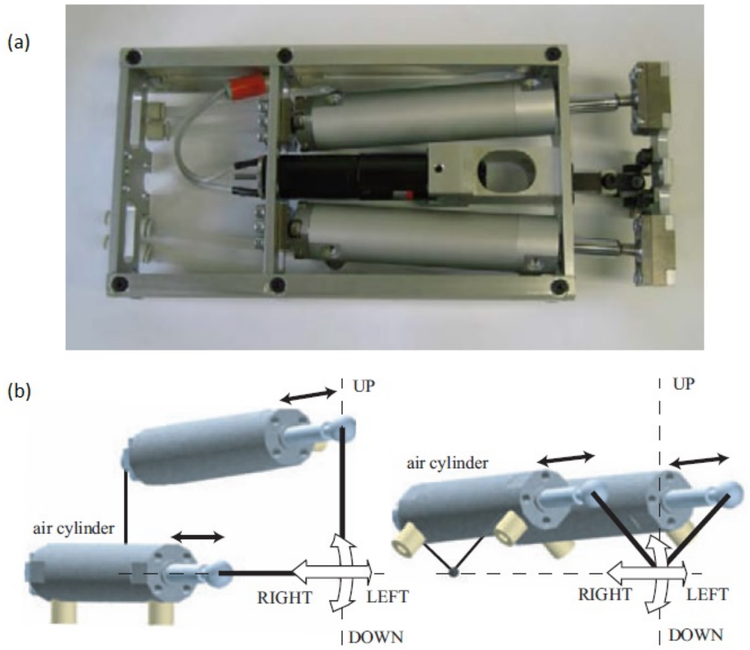

Figure 2.17: (a) MOIRA2 body module [44]. (b) Arrangment of cylinders in MOIRA2 module (right hand side) allows for rotation in 2 DOF, while allowing the structure of the module to be as flat as possible to maintain a low centre of gravity [44].

and a braided fibre mesh [49], which is wrapped around the bladder. When the bladder is inflated it expands. However, because the mesh fibres are inextensible, expansion of the bladder causes the mesh to reduce in length, contracting the actuator in a similar fashion to a natural muscle. This makes it ideal for biologically inspired robots such as Kingsleys cockroach [49] and the Shadow Hand (Figure 2.18) [78]. As well as being lighter than a cylinder they are also capable of producing higher forces for the same diameter, giving a much higher power to weight ratio. However, as well as having a shorter range of motion air muscles can only generate contracting force . If the pressure is lowered the muscle cannot apply force to the mechanism in the opposite direction. They must therefore be used in opposing pairs like a biological system. The force from an artificial muscle dramatically reduces as the muscle contracts, which could be seen as potential issue as well [39]. A further problem with braided muscles is that, due to the braided mesh rubbing on the bladder, fatigue reduces their lifespan.

2.3.4.3 Bellows

Pneumatic bellows are also seen on a number of hypermobile robots, including the OT-4 and the slim slime series of robots [19,39,41,42,71]. The bellow is a softer, more compliant actuator like the air muscle. However, unlike the muscle, when the bellow is actuated

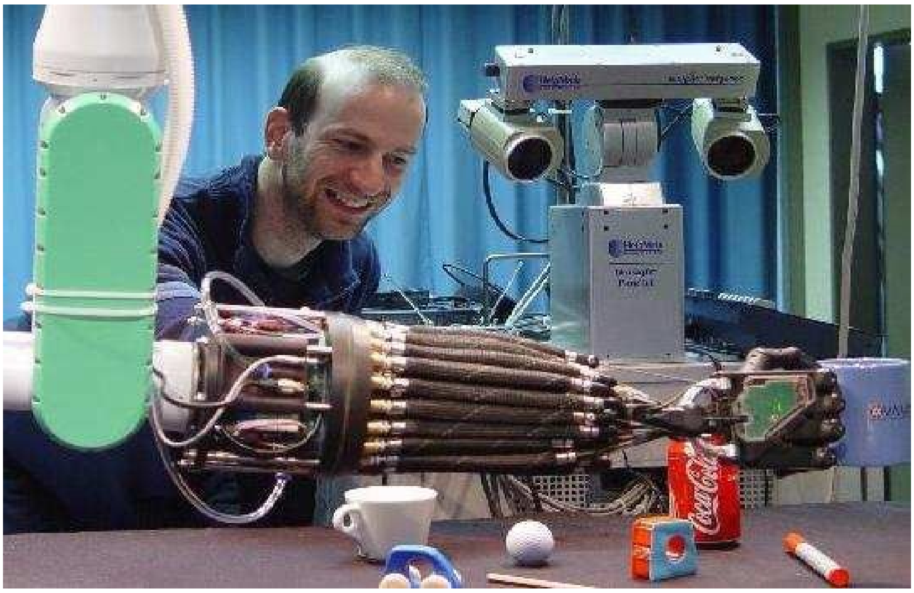

Figure 2.18: The Shadowhand robot makes use of airmuscles to make an accurate artificial representation of a human hand [78].

and the pressure increases, the length increases. This is due to the outer diameter of the bellow being fixed, so the length must increase instead. This produces force performance comparable to pistons. According to Granosik, pneumatic bellows have the advantage of having a much greater actuation strain than other actuators. The compliance that is present in bellow actuators is perfect for hypermobile robots as it means the body can bend easily to adapt to its surroundings, allowing as much of the body to be in contact with the surface as possible. This is important as it relates to the propulsion ratio discussed earlier. Another advantage with bellows is that, while the force from the actuator decreases with actuated distance, the effect is not as extreme as it is in artificial muscles [40]. Bellows, when unactuated, are also compact and take up less space than cylinders and air muscles, as seen in Figure 2.11. OT-4 used four bellows with each universal joint to achieve bending in 2 DOF. Using an external compressor that was able to provide 80psi per bellow, the 13.6kg robot was able to maintain a straight shape when supported only at the two ends.

2.3.5 Smart Materials

Shape Memory Alloys (SMAs) and other smart materials are relatively uncommon in hypermobile robots, but a number of interesting design ideas have been implemented using SMAs [81]. Firstly, the Meshworm uses 2 sets of SMAs to contract the body of the robot and to alter its traveling direction. The latter function is also used in Minetas endoscope [67]. Both these applications take advantage of the fact that both the SMA and its power equipment are small and lightweight. This makes it ideal for remote, untethered use, as shown by the Meshworm [81]. Meshworm has also proved to be very tough and resilient to heavy impact forces, still funtioning after being hit with a hammer and being stepped on, but furthermore it is resistant to corrosion, making it applicable for use in harsh terrains [74]. One of the problems with SMAs lies in how they operate. Contraction is caused by heat, not by electricity. As the flow of current is increased, the temperature of the wire increases too. When a particular temperature is reached, the wire contracts to the austenite stage, where the crystal structure of the alloy changes [74]. The wire then returns to the original martensite structure when the temperature drops past a certain point, reverting the crystal structure to its original layout. These two temperatures are usually not the same, meaning there is a hysteresis loop in its operation. This makes the alloy difficult to control. Additionally, when returning to it martensite state, the wire does not return to its original length on its own and needs additional stress to return it to its original length. Mineta performs this using a spring but even this does not stretch the SMA all the way back to its original state.

SMAs have also been used in hypermobile robots for purposes other than locomotion. SMA wire is used in the US robot as a brake to hold the joints in position [93]. This means that if the robot is stationary, the joint motors can be turned off which in turn saves power. When actuated, the SMA pulls on a pawl lever, interlocking its teeth with a gear fixed to the shaft of the operating motor. This locks it in position. The SMA is then turned off, but doesn't release the pawl. This is because the SMA doesn't automatically revert to its original shape when power is removed. The brake system still holds the joint in position and further saves power. When the opposing SMA is actuated, the pawl lever is released and the motor can move again.

2.4 Methods of Compliance

As it was mentioned in Section 2.2.3, joint compliance is a key characteristic of Wormbot [28]. Therefore it is important to consider potential methods for improving compliance performance. In this section, we will consider the positives and negatives of previously presented solutions as well as some from other applications.

As has been discussed, pneumatic actuation methods have the advantage of naturally occurring compliance within their actuation. This is a large advantage as it means that, with the use of pneumatic actuation, no additional compliance mechanisms are required, potentially reducing weight and space [42]. While pneumatic solutions do not necessarily need to use additional compliance methods, pneumatic devices can be used as purely compliance mechanisms within a motorised system. Whitney et al used pneumatic diaphragms to provide compliance to a motorised system [91]. Two diaphragms are used antagonistically to provide equal performance in both directions; a method used commonly with pneumatic muscles [63, 83]. However, the disadvantage of this is that quantifying the level of compliance could be challenging, due to the number of factors that could affect it, with Whitney listing stretching of components as just one example [91].

The most common solution for providing compliance to a system is by using springs. Linear springs are arguably the obvious choice for the sort of system in question due to being so freely available, though the range of methods they are used in shows their versatility. For example Mathijssen uses an array of springs on sliders around a joint [62]. These springs can be positioned either side of the joint in question to provide compliance in either direction of rotation, as can be seen in Figure 2.19. As there are a number of springs, and the positions of these can be changed, the stiffness of the compliance can be altered, which could be beneficial for adapting the system to a range of applications. However the cost of this is that the system as a whole appears to be quite bulky, and therefore potentially relatively impractical.

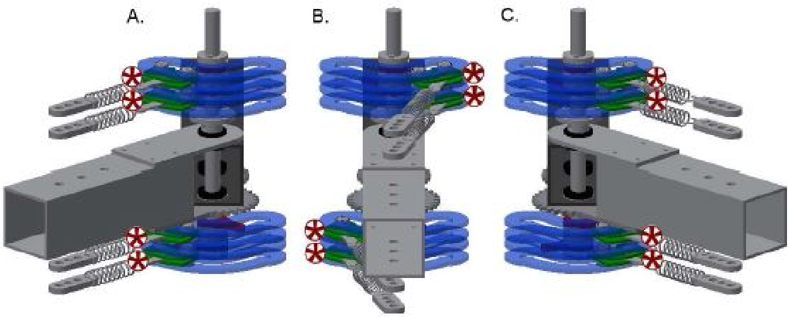

Figure 2.19: Maccepa style sprung joint by Mathijssen. A and C display 2 extreme positions and spring strength. B displays mid point [62].

Another method of producing adaptable compliance was demonstrated by Petit et al at the German Aerospace Center (DLR) [73]. They were inspired by antagonistically positioned actuators (much like a natural muscle pairing) as were others [84]. The DLR however used two motors for a single joint, both positioned at the base of the springs instead of at the joint (Figure 2.20). This means that by altering the position of the motors, the system stiffness can be changed. This can also be performed much more precisely than Mathijssens solution. Additionally, as each motor is bi-directionally fixed to springs, both motors can be used together to result in a stronger actuator. The use of more motors and, once again, multiple springs increases the size of the mechanism, making it oversized for some applications, though using different arrangements and components could improve this at the cost of performance.

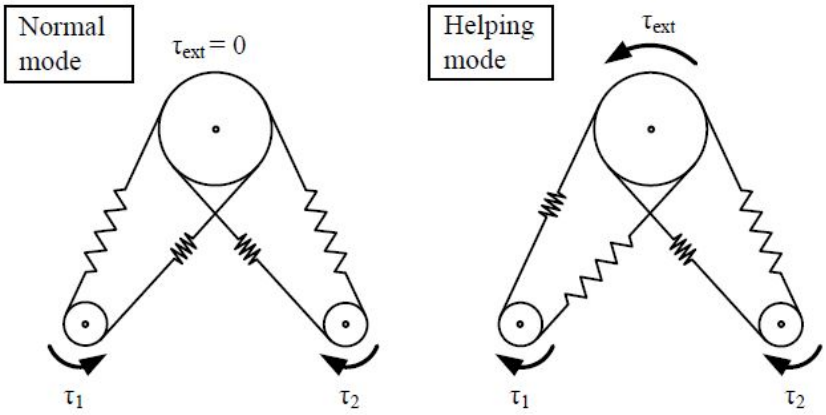

Figure 2.20: Motor spring layout of sprung actuator by Petit et al. Normal mode displays method of increasing/ decreasing spring constant. Helping mode shows torque maximisation [73].

Park et al developed a compliance mechanism for use in devices intended for human interactions [72]. This system can be seen in Figure 2.21. As the end effector is deflected, a cord connected to the sprung slider system is pulled. This compresses a spring positioned 90° to the direction of motion. This has resulted in a system which retains stiffness to a set torque (allowing for a high level of precision), and then beyond that stage will deflect considerably. The performance parameters can also be adapted by changing the initial slider angle, resulting in a highly effective, adaptable system.

One of the downsides of using linear springs with motorised mechanisms is that rotary motion needs to be converted to or from linear motion. This, in a few designs, has included designs which have taken a reasonable amount of complexity. However, one design that combats this is based on a smaller, simpler Series Elastic Actuator (SEA) [89]. This system uses a motor, with a rotary spring element fixed between the motor output and the joint it is powering. This is created with a cylindrical Series Elastic Element (SEE), with 6 springs, arranged in pairs, on 3 spokes. This component means compliance can be achieved in a motorised systems whilst using minimum space.

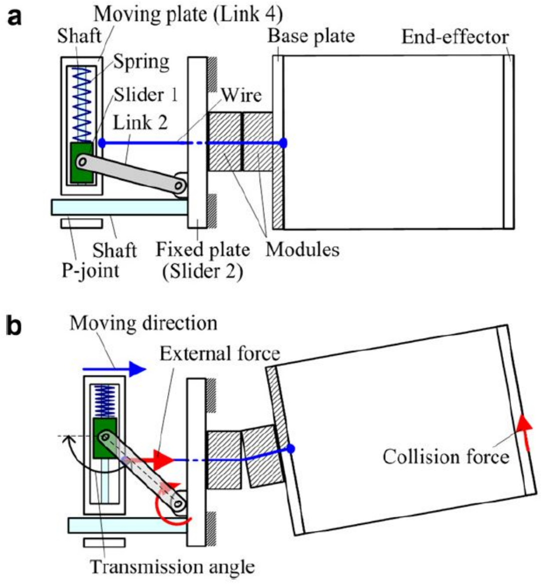

Figure 2.21: Human interation joint. a) Resting position. b) Joint being moved. Notice the spring slider mechanism being contracted [72].

The idea of using SEEs is one that has been applied to a number of occasions, though a number of different methods have been used. Campbell used a simple torsion beam located within the device [31]. Due to the simple yet effective design, the stiffness of this SEE can easily be altered by fitting a different torsion beam. This results in a device which could be easily fitted to a range of machines for different purposes for a low cost.

Using a torsional spring located within the drive system of a joint is a common way of creating compliance within a motorised system, due to being predictable, cheap and commonly available [52, 55]. However, there are a number of devices that make small changes to improve performance. For example, Schiavi et al' wanted to develop a system with a sudden increase in torque per angular movement and their 4 bar linkage system allowed them to achieve that [79]. Sergi et al, on the otherhand, custom built their spring to suit their needs [82]. A spring with specific torque and stiffness requirements was not available commercially, so Finite Element Modelling (FEM) was used to design the SEE to specification, before using Wire Electrical Discharge Machining (WEDM) to produce the part.

In the US robot, mentioned in Section 2.2.3, a custom made SEE was also used, though it was produced using a very different method. The spring component of the SEE is produced from moulded rubber, bonded to two metal plates [77]. Furthermore, the tapered cross-section of the SEE allows for constant strain across the device, as well as control over it's stiffness by altering the dimensions (see Figure 6.1). This would mean you could theoretically produce a SEE, analyse its performance and then produce a new one with slightly changed dimensions for improved performance. However, the downside with moulding SEEs is that to produce a new one, a new mould will need to be produced first, a cost that would not need to be spent in other methods.

Figure 2.22: Cross section of Rubber SEE. Note the tapered shape, providing an even distribution of sheer stress acoss the component [77].

Liljebäck, who created the Anna Konda and Kulko robots talked about in Chapter 2.2.3, followed these up with the MAMBA robot; another snake robot with the potential to swap out certain modules for specialist ones with extra attachments (wheels, flippers etc) [61]. While there is no mechanical compliance mechanism in the robot, the servo motor in each joint is mounted within a strain gauge bracket. The strain gauges are fixed to the bottom of the servo and form a cradle (Figure 2.23). It is possible to imagine the a similar layout with torsion springs instead of strain gauges and providing compliance to the system, though this could have fitting issues within the drive train of a joint if the motor did not move around the axis point.

Based on the literature surveyed, the most prominent methods of providing compliance to a system are by using either springs or using the inherent compliance within pneumatic actuators. However, some alternative methods were discovered. One method used twisted strings to provide stretch [75]. If a piece of string is twisted, when it is pulled from one end it stretches towards its original length, therefore behaving like a spring. If the string is twisted more, the amount of potential compliance is increased. cables have also been used alongside a tensioner, where a joint has movement limited by a piece of string interfering with the joint [87]. As the cable is tightened, it further impedes the point

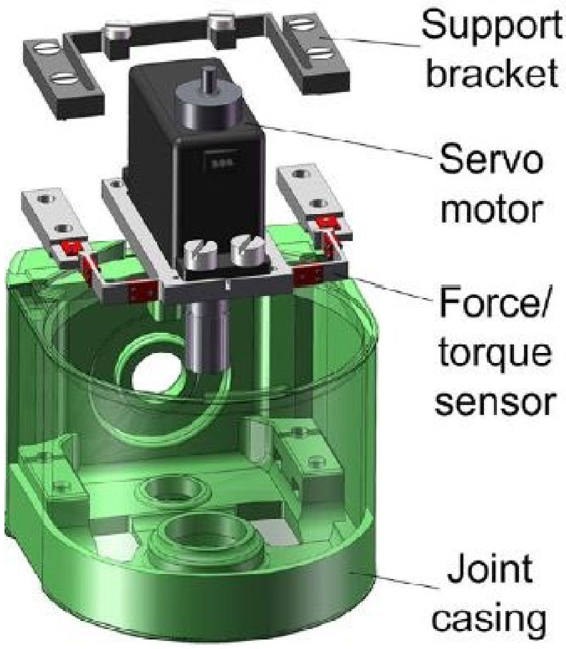

Figure 2.23: Force/ Torque sensor layout for MAMBA. Assembly style could inspire spring fitting for servo motor [61].

movement.

Finally, magnets have also been applied to joint systems for added compliance [86]. Magnets are arranged on a disc so that if a joint moves too far, the magnetic forces resist further movement. Due to the Halbach array assembly that is employed, which can be seen in Figure 2.24, the repelling force gradually increases with joint deflection. However, with this method, if the magnets cannot provide enough resistance, there will be a point when the joint will rotate too far and will be held in the wrong position by the device.

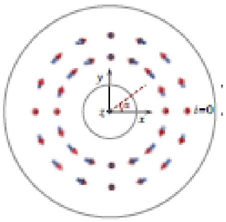

Figure 2.24: Halbach array layout, with arrows indicating field direction of each magnet [86]. Attracting and repelling forces allow device to behave like a compliant element.

2.5 Conclusion

This review has surveyed a number of projects on hypermobile robotics over the last 25 years, from search and rescue robots to surgical endoscopes, with a wide range of design solutions and actuators. A number of these design ideas could become useful in providing inspiration for future joint mechanisms. One of the first points of note is that nearly all the robots that move forward using sinusoidal locomotion use wheels to produce the asymmetrical frictional coefficients required, indicating this is the most feasible current solution. None of the robots use a skin or outer layer to produce this. Therefore if a "skin" was used it could potentially require a large amount of development. Though if using wheels a solution would be needed to stop them catching on potential obstacles in rough environments. One possible solution is to use rollers located around the body of the robot like those used in Perambulator II [96]. However, achieving this allows for a robot to be able to move in environments where a robot using powered wheels or tracks may not be able to travel, such as sand, grease or even potentially deep water [28].

One of the interesting actuators analysed in the review are the bellows used by the Omnitread series of robots [39,41,42]. As well as their high power to weight ratio their are easier to maintain than other options. An additional point is that, when unactuated, then can reduce to becoming almost flat, potentially making them very compact [39]. Another actuator that is worth note is the SMA. It is incredibly small and, as shown with the Meshworm, it is very robust [81]. However, it hasn't been used as an actuator for a robot of a similar size to Wormbot and it would be interesting to see if it could be used in such an application. Motors are also a good candidate for use in hypermobile robots due to the range available to use. In the literature analysed, they have proved to be incredibly versatile, being utilised in a wide range of layouts and arrangements.

Another important area for consideration is the method of providing compliance to the joint. When using pneumatics, compliance is already present, and therefore no additional mechanisms are required to achieve it [42]. However, quantifying the amount of compliance is more difficult. Depending on the type of actuator, the wide and varying range of dimensions and constraints, as well as the pressure within the system could all affect the compliance. Torsional SEE's are found to be a good method for producing compliance within a small contained unit [77,89]. These would be very good for compact machines, specifically those using motorised mechanisms.

Chapter 3

Conceptual Segment Design and Actuator Evaluation

3.1 Introduction

In this chapter a number of design concepts are developed and their feasibility is discussed, building on the information gained in Chapter 2. The actuation methods with the most potential are identified and are incorporated into design proposals as methods of actuating the joints. The force and torques of these designs are calculated using simple theoretical models. Finally, the feasibility of each actuator is discussed, taking into consideration such factors as the cost, power supply, size and implementation complexity, as well as the values calculated previously. Two methods will then be selected for further development.

3.2 Requirements and Specification

For producing a conceptual design for the second version of Wormbot, the obvious starting point is the first version [28]. As we pointed out in Chapter 2, the first Wormbot has the same aspect ratio as an actual *C.elegans* nematode worm. Whilst this aspect ratio should be maintained to match the control method being accurately based on *C.elegans*, the size of the original robot would be very large to be considered in a search and rescue capacity. A number of similar robots are of a length around half the size of Wormbot at approximately 1m long [34, 93, 96, 97]. This would be a reasonable target for downscaling, though the ability to build the robot to a smaller scale should be considered in this chapter. Therefore the main theoretical feasibility analysis will be performed for a robot of length 1m by 0.08m diameter, though analysis should be performed for smaller robots with a view to different environments and applications. It should also be noted that *C.elegans* is not actually cylindrical; it is elliptical. While the aspect ratio of the nematode worm should be kept, the elliptical shape may have to be sacrificed. Many hypermobile robots are modular, as it is the most efficient way to produce such a robot, and as such have a uniform cross-section. This has not been seen to hinder performance in the past so this will be continued.

The *C.elegans* locomotion nervous system can be simplified and modelled as 12 repeating units [28]. A biological *C elegans* worm has 48 muscles per side so each neural unit controls four muscles per side. The first Wormbots structure was based on this control system and thus had 12 segments. Wormbot mk II should follow suit, though this is not essential if there is found to be benefit from having more or fewer segments.

As shown by Berri et al. the amplitude of the sinusoidal locomotion is about 8% of the worms length when travelling on an agar substrate [25]. Therefore, however many segments are in the robot, this amplitude should be achieved. For a 12 segment robot a bending angle of ± 45° per segment is ample to achieve this amplitude, while ± 30° is sufficient (Figure 3.1).

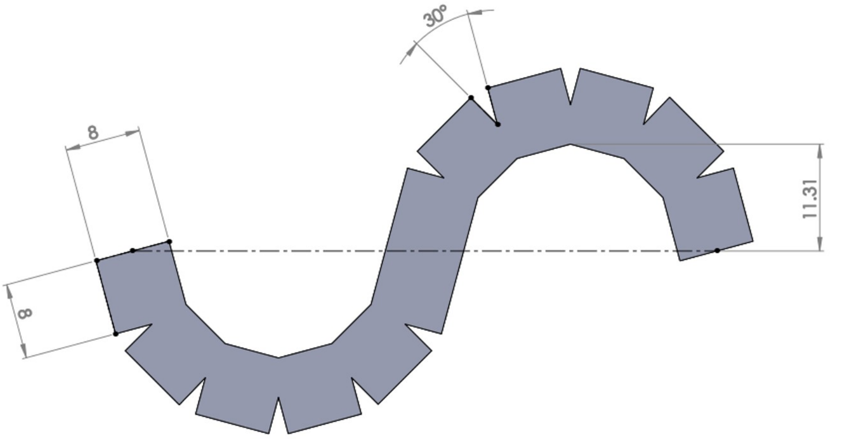

Figure 3.1: Basic Wormbot layout with 12 segments. Note for robot of around 1m in length and maximum joint angle of 30° has a amplitude at 11.31cm, meaning the robot will sufficiently reach *C.elegans*'s body motion amplitude of 8% of it's body length.

Another aspect that was present in the original Wormbot was compliance within the joints [28]. As *C.elegans* doesn't have a skeleton, it relies on a hydrostatic frame, where internal fluid pressure along with the elastic properties of the cuticle (skin) makes the body of the worm compliant. This means that when the rotation of the body is blocked, there is a certain amount of give in the "joint" so it can continue to rotate with the stiffness of the body increasing as more force is applied. This was created by the use of cantilever springs attached to the chain drive of each motor. Any actuator used in the second version must either have in-built compliance or, like the original robot, have the ability to work in series with a compliance mechanism. Progressing from this aspect, it would be interesting to see if a particular amount of compliance would be optimal for a robot such as Wormbot mkII, or if varying amounts of joint "stretch" would be ideal for different tasks. This could be an exciting development, as it could result in customisable robotics that can be tailored for very specific jobs.

One of the requirements for all hypermobile robots relying solely on sinusoidal body motion for locomotion is a difference in friction coefficient in directions parallel and perpendicular to the local body axis [25]. This is apparent in many of the designs featured in Chapter 2. Passive wheels are useful for this as they only roll round one axis. This allows a difference in longitudinal and normal forces to be created (Figure 3.2). It is essential that the next Wormbot has a method of producing this asymmetry.

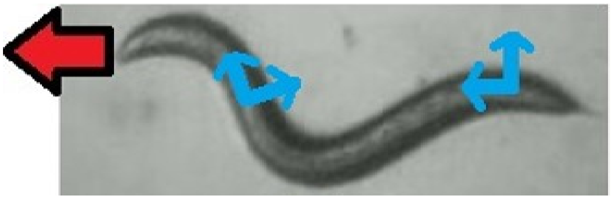

Figure 3.2: Image of *C. elegans*. Red arrow indicates the direction of movement on the longitudinal plane. Blue arrows indicate the local body axis. Normal force acts perpendicular to body.

Considerations also need to be made towards the strength of the joints in Wormbot. We know that the robot needs to be strong enough to overcome the friction of the surface it is moving on, but any indication as to how to quantify that is difficult to obtain. For an indication of what to aim for the Omnitread series of robots could act as a benchmark [39]. Omnitread has the ability to maintain a straight body position when only being supported at both ends of the robot without the body sagging significantly in the middle. Granosik points out that this situation is highly unlikely to occur when the robot is navigating an environment, but this would still be a good indicator of ample strength in a hypermobile robot.

C.elegans worms alter the frequency at which they move according to their environment. When crawling on an agar substrate, *C. elegans* moves with a sinusoidal wave at 0.5 Hz but this increases to 2Hz when swimming in water due to the lower resistance. It may be beneficial to have the ability to change wave frequency to adapt to different environments, although certain speeds may be unfeasible due to mechanical constraints. While swimming amphibot achieves this feat at 1Hz, which it also uses for movement on land [33].

An additional facet that occurs in a number of hypermobile robots is modularity [76, 93]. Modular robotics are a promising method of providing robustness to a system. Robots featuring modular segments have the ability to remove or add segments easily. This has a number of benefits, the first of which is the ability to replace broken segments instead of providing a full robot replacement. Secondly, segments can be added or removed if it benefits the performance of the robot. Additionally, if available, segments with varying designs can be brought in to benefit performance in certain situations (e.g. wheeled segment, finned segment etc.) [61]. Therefore, whilst it isn't a vital requirement, modularity should be a characteristic to be aimed for.

The following table summarises the points stated in this section.

Table 3.1: List of Design Specifications

Area	**Specification**	**Essential?**
Size	Half size of Wormbot (1m x 0.08m)	
	Original *C. elegans* aspect ratio	X
Undulation Frequency	Achieve 1Hz	
	Variable between 0.5Hz & 2Hz	
Segments	12 segments	
	± 30° bending	X
	± 45° bending	
	Modularity	
Forces	Method of producing asymmetric friction	X
Joints	Compliance in each joint	X
Strength	Support own weight from both ends	

3.3 Theoretical Analysis of Actuation Strategies

In this section, potential actuation methods will be put forward and critically analysed. First, layouts will be proposed for specific actuators, then the performance parameters will be arithmetically solved. These will then be compared to find a small number of solutions to take forward to testing.

3.3.1 Design I: Bellows and McKibben Muscles

The principle behind using bellows in a snake like robot is having the ability to work each side in opposition. In this instance, the bellow(s) on one side of a segment would be inflated. When the segment was required to rotate in the opposite direction, the opposing side of bellows is inflated while the first set is vented.

The amount of force that can be generated from a bellow depends on Equation 3.1.

$$F = PA \tag{3.1}$$

where F is the force in Newtons, P is the pressure of the compressed gas within the bellow in Pascals and A is the cross-sectional area of the bellow in metres squared. However due to the shape of the bellow, the cross sectional area can vary (see Figure 3.3). Granosik states that the force generated from a bellow is dependant on the cross sectional area of the inner whorl, or inner fold of the bellow [41]. However, Granosik also states that in OT-4, the inner whorl could expand to the size of the outer whorl, increasing the maximum output force. Therefore in this report, minimum and maximum forces are found depending on which area is used; the inner whorl area or the outer whorl area.

Another factor affecting the force that can be produced is the number of DOF a segment has. If the segment only has to rotate around one axis, half the cross section of the segment can be used for each rotational direction. If the segment must rotate in 2 DOF, it would then need to be broken up into quadrants, meaning significantly less area is available for bellows working in a specific direction when bending in certain directions. To determine which option is best, 5 bellow layouts have been considered, based on space available and size of bellows. These are shown in Figure 3.4.

At this point, it can be seen that all the bellows proposed are circular in cross section. It could be argued that custom designing the bellow cross section to the module's shape could increase the overall area of the bellow, maximising force output. However, when

Figure 3.3: A pneumatic bellow [41]. Each ridge is called a convolute or whorl, with the wider ridges being called the outer convelutes and the narrower ridges being called the inner convolutes.

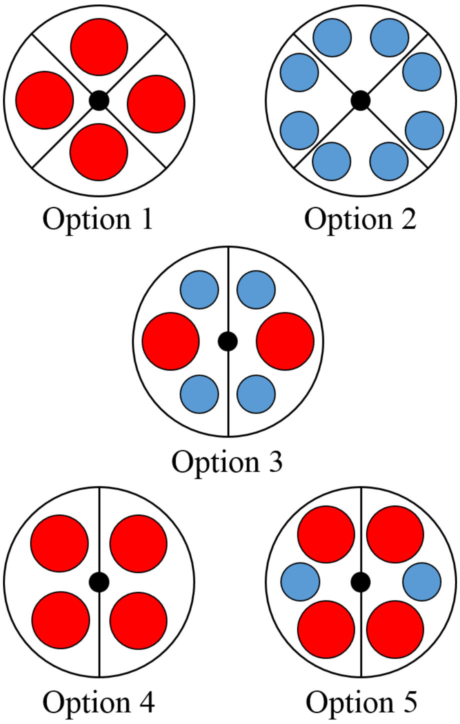

Figure 3.4: Bellow design options. All bellows have convelutes (material between inner and outer whorl) of 5mm. Red circles are bellows with an outer whorl diameter of 25mm. Blue circles are bellows with an outer whorl diameter of 20mm.

actuated the uneven shape would have peak stress points which could result in the actuator failing.

The calculated force is then required to find the torque of the segment. Even though the bellow is a linear actuator and thus provides a force, it is being used to rotate a joint. Therefore the torque result has more of a bearing on the performance of the joint. This is found using Equation 3.2 and displayed in Figure 3.5.

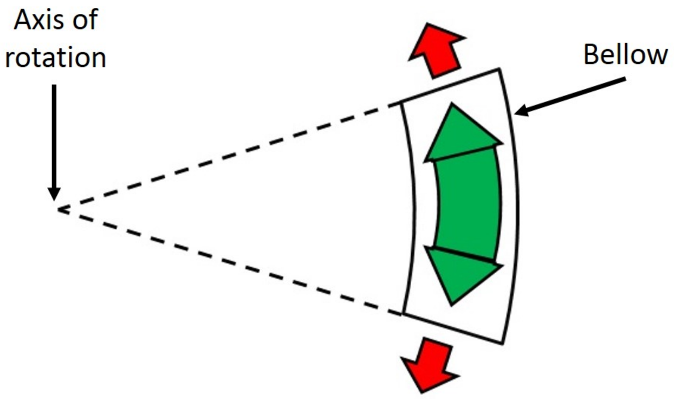

Figure 3.5: Diagram of bellow actuating around an axis. Red arrows equal linear force. Green arrows are torque. Note when forces are applied about a centre point, a torque is imparted.

$$T = Fd\sin\theta \tag{3.2}$$

where T is the Torque in Newton metres, d is the distance from the pivot of the joint to where the force is being imparted in metres and θ is the angle of the force direction in relation to the lever arm. In this case it is 90° so $\sin\theta$ is 1. It can therefore be discarded from the equation for the time being. Table 3.2 shows the minimum and maximum force and torque results, as well as when the body of the robot is straight (indicated by Str), for each design option when the internal pressure is 550kPa, the same used by Granosik et al [39]. The area used is the cross-sectional area of all the bellows used in that segment.

Table 3.2: Theoretical Force and Torque values for proposed bellow layouts

Option		**Area (mm^2)**	**Force (N)**	**Torque(Nm)**
1	Min	176.71	97.19	2.28
	Str	314.16	172.79	4.06
	Max	490.87	269.98	6.34
2	Min	157.08	86.39	2.33
	Str	353.43	194.39	5.25
	Max	628.32	345.58	9.33
3	Min	333.79	183.59	3.73
	Str	667.59	367.17	7.24
	Max	1119.19	615.56	11.93
4	Min	353.43	194.39	3.89
	Str	628.39	345.58	6.91
	Max	981.75	539.96	10.80
5	Min	431.97	237.58	4.79
	Str	805.03	442.77	9.14
	Max	1295.91	712.75	14.90

The distance the bellow needs to expand also needs to be known. As stated in Chapter 3.2, the desired length and width of the robot will be 1m and 0.08m respectively (0.08m of the length will be taken by semi spherical end buffers so segment length will be 0.92m). The minimum angle for each segment to bend through (assuming there are 12 segments) is 30°. These figures lead to the robot being able to perform one 360° loop. This information can be used to find the distance each bellow needs to expand. This is performed by using the maximum and minimum circumferences of Wormbot in a full loop position and uses the number of modules to find the extreme lengths. As this is performed using bellows positioned at the extremities of the proposed module dimensions, this results are assumed to be in Bellow layout option 5. The results are shown in Table 3.3.

It should be noted that in Table 3.3, the minimum and maximum module lengths are found assuming the robot can perform a complete body loop. This allows for for the necessary amplitude indicated in Figure 3.1. The minimum module length uses the inner circumference of this loop while the maximum module length uses the outer circumference. The change in bellow length finds how much the bellow would need to expand/contract assuming it was positioned at the outer limit of Wormbot's body.

Bellows are not the only pneumatic method of actuating joints. McKibben actuators are often used in mechanisms where mimicking natural muscle systems is desirable. This is because, when actuated, McKibben actuators contract like a natural muscle, as can be

Table 3.3: Theoretical Design I dimensions

Modules	**Module Length (m)**	**Angle (°)**	**Min Module Length (m)**	**Max Module Length (m)**	**Bellow Δ L (m)**
10	0.092	36	0.0669	0.1171	0.0502
11	0.083	32.7	0.0608	0.1064	0.0456
12	0.077	30	0.0557	0.0976	0.0419
13	0.071	27.7	0.0514	0.0900	0.0386
14	0.066	25.7	0.0478	0.0836	0.0356
15	0.061	24	0.0446	0.0780	0.0334
16	0.058	22.5	0.0418	0.0732	0.0314
17	0.054	21.2	0.0393	0.0689	0.0296
18	0.051	20	0.0371	0.0650	0.0279
19	0.048	18.9	0.0351	0.0616	0.0265
20	0.046	18	0.0334	0.0585	0.0251

seen in Figure 3.6. This is discussed more in Chapter 2. As these muscles can be built to specification, the performance parameters displayed in Table 3.3 can theoretically be achieved. Equation 3.3 displays the method for finding the theoretical linear force [32].

Figure 3.6: Diagram of McKibbens pneumatic muscle. (a) Relaxed muscle. (b) Actuated muscle [35].

$$F = \frac{\pi {D_0}^2 P}{4}(3\cos^2\theta - 1) \tag{3.3}$$

In this equation, F is linear force, D_0 is braid diameter when braid angle is 90°, P is compressed air pressure within the actuator and θ is the braid angle [32]. It should be noted that the maximum braid angle (angle between the direction of the actuator and the direction of the braid) is 54.7°, which is achieved at maximum contraction when the linear force is zero. Table 3.4 shows the force and torque output of segments using McKibben muscles, assuming the same actuator layouts that were used with Bellows are employed and the same air pressure of 550kPa.

When finding the maximum force and torque, the braid angle used is 30°. Finding an

Table 3.4: Theoretical Force and Torque values for proposed McKibben layouts

Option		Force (N)	Torque(Nm)
1	Min	0.474	0.011139
	Str	152.16	3.58
	Max	337.476	7.931
2	Min	0.608	0.016416
	Str	194.77	5.26
	Max	431.984	11.663
3	Min	1.082	0.02097
	Str	346.93	6.73
	Max	767.444	14.91
4	Min	0.948	0.01896
	Str	304.32	6.09
	Max	674.952	13.499
5	Min	1.252	0.026184
	Str	401.70	8.40
	Max	890.936	18.629

accurate value for minimum braid angle is a difficult task. The minimum braid angle is dependent on how close the strings of the braid are to each other, or how many strings are used for a given area of braid. Using fewer strings allows for a smaller braid angle and thus a greater extension. The downside of this however is that the muscle becomes weaker with fewer braids [70].

The midway angle can be found using Figure 3.7. From this, it is known that l can be found using Equation 3.4. This can be performed for both l_{min} and l_{max}. l_{mid} can be found by taking the average of these, and using arccos finds the angle for this, displayed in Equation 3.5.

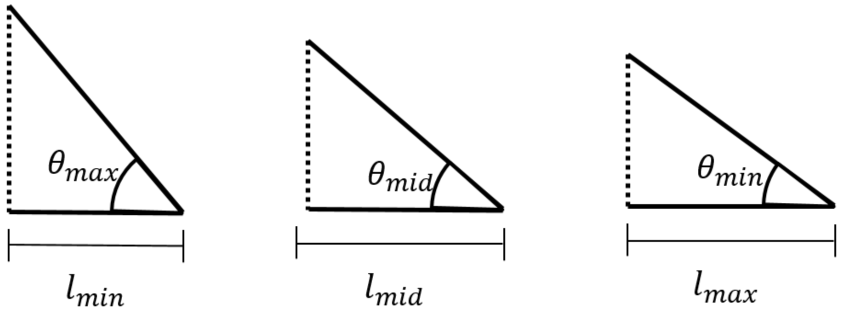

Figure 3.7: Diagram displaying relation of braid angle to actuator length.

$$l = \cos\theta \tag{3.4}$$

$$\theta_{\mathrm{mid}} = \arccos\left(\frac{\cos\theta_{\mathrm{min}} + \cos\theta_{\mathrm{max}}}{2}\right) \tag{3.5}$$

To get a sense of how much of an effect the torque has on the overall system, a free body diagram has been drawn and the theoretical mass of the robot has been calculated. This is performed assuming the robot must be able to support its entire weight when only the ends are being supported; a test used in the performance analysis of OT-8 [39]. This can be seen in Figure 3.8.

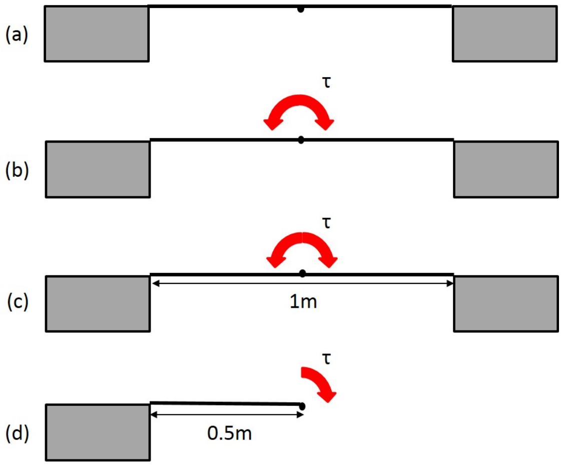

Figure 3.8: System free body diagram. (a) Robot is supported at both ends. (b) Torque applied around centre joint. (c) length labelled. (d) as the system is mirrored, can work from 1 side.

Using Equation 3.2, the force acting down from the centre of the robot can be found. Using Equation 3.6, where g is the acceleration (in this case 9.81ms^{-2} from gravity) the potential maximum mass can then be found. It should be noted that this value should then be doubled, as the free body diagram only represents half the robot.

$$M = \frac{F}{g} \tag{3.6}$$

As the task is to maintain the straight body position, the torque values from when the body is straight will be used, not the maximum or minimum torques. These results can be seen in Table 3.5.

Table 3.5: Theoretical Design I Mass results

Options	**Bellows**		**McKibbens Muscle**	
	Torque (Nm)	Mass (Kg)	Torque (Nm)	(Mass (Kg)
1	4.06	1.66	3.58	1.46
2	5.25	2.14	5.26	2.14
3	7.24	2.95	6.73	2.74
4	6.91	2.82	6.09	2.48
5	9.14	3.72	8.4	3.43

3.3.2 Design II: SMA wire

3.3.2.1 Layout

As seen in Chapter 2, while SMAs are used as a joint brake in the U.S robot, they are not commonly used as a method of actuation for joints in snake-like robots [93]. They have been used more in smaller creations, like the Meshworm robot for peristaltic motion and in small scale continuum robots like endoscope by Mineta [67, 81]. The purpose of Design II is to see whether their use can be feasibility scaled up.

One of the issues with SMA wire is that the difference between its extended and contracted lengths is only 4% [17]. To overcome this limitation, Design II uses a pulley system to utilise the contraction stroke as much as possible. This can be seen in Figure 3.9. The SMA is fixed in one corner, looped around two pivot points and fixed at the corner at the opposite end of the segment. This way the length reduction of 4% of the the total length is only imparted between B and C.

To find out the torque of the system, a selection of equations were derived. Figure 3.10 assists in understanding these equations. Equations 3.7, 3.8, 3.9 and 3.10 explain the geometry of the segment.

$$l = \alpha + \beta = \sqrt{\left(\frac{Diameter}{2}\right)^2 + \left(\frac{L_{\text{mod}}}{2}\right)^2} \tag{3.7}$$

$$SMA_1 = 2(\alpha + \beta \sin\varphi) \tag{3.8}$$

$$SMA_2 = 2(\alpha + \beta \sin\upsilon) \tag{3.9}$$

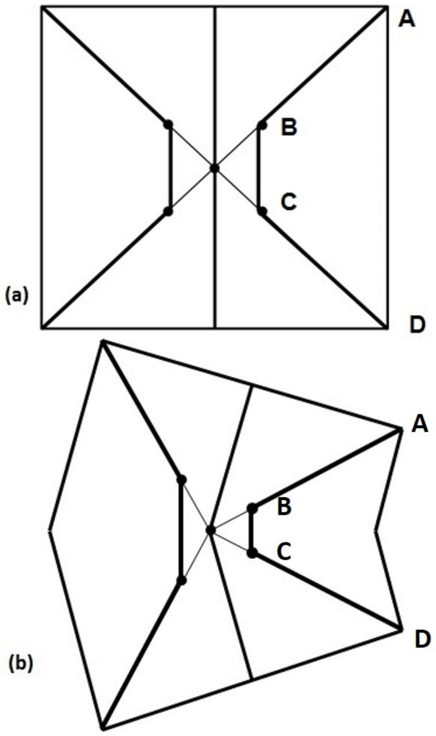

Figure 3.9: (a) Diagram of Design II segment. (b) Design II segment when one side is actuated. Note if pulley points are fixed, the length change of the whole SMA only acts between B and C.

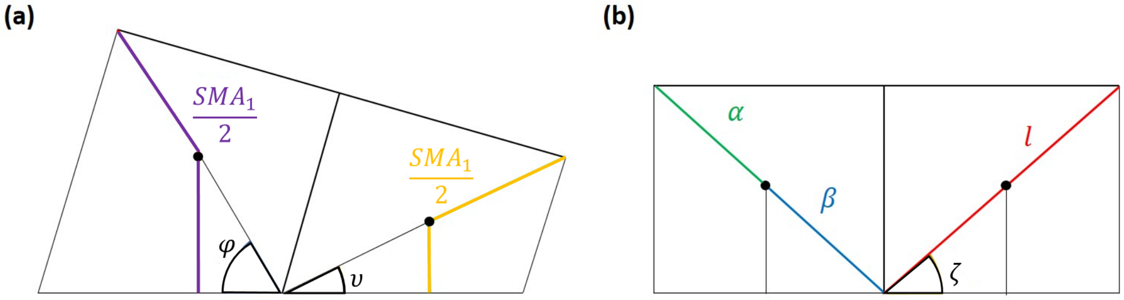

Figure 3.10: Top half of Design II segment, couloured for use in equations. (a) Purple line = $SMA_1/2$, yellow line = $SMA_2/2$, angles = φ, υ. (b) Green line = α, Blue line = β, red line = l, angle = ζ.

$$SMA_1 = 0.96SMA_2 \tag{3.10}$$

Here l is the diagonal length from joint pivot point to the corner of the segment, α is the distance from the pulley point to the corner of the segment, β is the distance from the joint pivot point to the pulley point, SMA$_1$ is the extended length of the SMA wire, SMA$_2$ is the contracted length of the SMA wire, φ is the maximum inside SMA angle, υ is the minimum inside SMA angle and ζ is the resting inside SMA angle. Additionally, 0.96 in Equation 3.10 represents the length of the SMA once actuated, relating to the 4% contraction rate. If Equations 3.8 and 3.9 are substituted into Equation 3.10, Equation 3.11 (shown below) is achieved.

$$2(\alpha + \beta \sin \varphi) = 0.96(2(\alpha + \beta \sin \upsilon)) \tag{3.11}$$

If α is replaced with a rearrangement of Equation 3.7, Equation 3.12 results, which can be rearranged to make Equation 3.13.

$$2((l - \beta) + \beta \sin \varphi) = 0.96(2((l - \beta) + \beta \sin \upsilon)) \tag{3.12}$$

$$\beta = \frac{0.08l}{0.08 + 1.92 \sin \varphi - 2 \sin \upsilon} \tag{3.13}$$

3.3.2.2 Torque & Mass Potential

Now that the equations for this design layout have been identified, it is important to see how effective it would be when using SMA wire. To draw a comparison to the pneumatic solutions used in Design I, the potential torque and mass values for Design II will now be calculated. These will then be compared later in the chapter.

Equation 3.13 can then be substituted into the torque Equation 3.2 as d. If finding the minimum torque, angle θ in Equation 3.2 is 90° - φ, while at the maximum torque it is 90° - υ. This is because, due to the geometry of the design, the torque is at its lowest when the SMA is extended (sine 90° - φ is a smaller value than sine 90° - υ, resulting in a smaller multiplier for Equation 3.2). Table 3.6 displays the results for Design II, where the SMA wire that has been chosen is 0.5mm in diameter (the strongest available from Dynalloy [17]) and can operate with a force of 3560g, or 34.9236N [17].

Table 3.6: Theoretical Design II Dimensions and Torque results

Modules	**Module Length (mm)**	**Angle (°)**	β **(mm)**	**SMA Length (elongated) (mm)**	**Torque (min) (Nm)**	**Torque (straight) (Nm)**	**Torque (max) (Nm)**
10	92	36	5.966	12.0969	0.0814	0.1367	0.1786
11	83	32.7	5.833	11.3951	0.0944	0.1418	0.1769
12	77	30	5.864	10.9351	0.1058	0.1472	0.1793
13	71	27.7	5.859	10.4895	0.1161	0.1528	0.1810
14	66	25.7	5.902	10.1256	0.1258	0.1586	0.1842
15	61	24	5.912	9.7747	0.1346	0.1645	0.1866
16	58	22.5	6.052	9.5589	0.1436	0.1706	0.1920
17	54	21.2	6.093	9.2893	0.1515	0.1767	0.1952
18	51	20	6.205	9.0851	0.1587	0.1828	0.2002
19	48	18.9	6.311	8.8856	0.1678	0.1891	0.2051
20	46	18	6.451	8.7482	0.1753	0.1953	0.2105

While the torque output of these theoretical models seems low, it is hard to put into context how weak the robot is until the potential weight can be seen. Potential mass results of this design concept be seen in Table 3.7.

Table 3.7: Theoretical Design II Mass results

Modules	**Module Length (mm)**	**Angle (°)**	**Torque (straight) (Nm)**	**Mass (Kg)**
10	92	36	0.1367	0.0557
11	83	32.7	0.1418	0.0578
12	77	30	0.1472	0.0600
13	71	27.7	0.1528	0.0623
14	66	25.7	0.1586	0.0647
15	61	24	0.1645	0.0671
16	58	22.5	0.1706	0.0695
17	54	21.2	0.1767	0.0720
18	51	20	0.1828	0.0746
19	48	18.9	0.1891	0.0771
20	46	18	0.1953	0.0796

As can be seen from these potential mass results, a 1m long robot could not weight any more than 80g using SMA wires in the Design II arrangement, assuming it would be able to support its own body weight from fixing both ends. When one considers that many modern smart phones weigh more than 80g, it becomes clear that a 1m long, 80mm diameter worm robot with batteries, framework, compliance systems and more, is an infeasible goal.

3.3.2.3 Consideration to Robot Size and Actuator Thickness

As was discussed in Chapter 3.2, a factor that should be considered in this design process is how changing the robot size would affect the feasibility of each design. Table 3.8 shows how the potential weight of a self supporting robot (see Figure 3.8) would change in respect to the number of modules per robot but also it's length.

Table 3.8: Theoretical Design II Mass results - SMA Diameter = 0.51mm - Extended (kg)

Length (m) / **Modules**	0.2	0.4	0.6	0.8	1
10	0.0557	0.0557	0.0557	0.0557	0.0557
11	0.0578	0.0578	0.0578	0.0578	0.0578
12	0.0600	0.0600	0.0600	0.0600	0.0600
13	0.0623	0.0623	0.0623	0.0623	0.0623
14	0.0647	0.0647	0.0647	0.0647	0.0647
15	0.0671	0.0671	0.0671	0.0671	0.0671
16	0.0695	0.0695	0.0695	0.0695	0.0695
17	0.0720	0.0720	0.0720	0.0720	0.0720
18	0.0746	0.0746	0.0746	0.0746	0.0746
19	0.0771	0.0771	0.0771	0.0771	0.0771
20	0.0796	0.0796	0.0796	0.0796	0.0796

The first of the two main points of note are that the potential weight of the robot does not change in relation with the length of the robot. This was initially very unexpected, but, as we have seen in this chapter, there are a lot of equations that are embedded amongst each other. Therefore, it was decided to reduce the equation for mass to the core inputs, which in this situation are the number of modules and the robot length. The process for this starts with taking Equation 3.6 and incorporating a rearrangement of Equation 3.2 to achieve Equation 3.14.

$$m = \frac{2\left(\frac{\tau}{d\sin\theta}\right)}{g} \tag{3.14}$$

We know that d in this instance is half the length of the robot (see Figure 3.8). Additionally, as the body shape is straight, θ is 90° to the body direction. Therefore $\sin\theta$ cancels down to 1. Next, the equation for finding the torque of a module in the straight position is used to create Equation 3.15.

$$m = \frac{2\left(F_{\mathrm{sma}}\beta \sin\left(90-\zeta\right)\right)\left(\frac{2}{L_{\mathrm{rob}}}\right)}{g} \tag{3.15}$$

Next, Equation 3.13 replaces β to create Equation 3.16.

$$m = \frac{2\left(\frac{0.08 l F_{\mathrm{sma}} \sin\left(90-\zeta\right)}{0.08+1.92\sin\phi-2\sin\upsilon}\right)\left(\frac{2}{L_{\mathrm{rob}}}\right)}{g} \tag{3.16}$$

Equation 3.17 is then formed by replacing l with Equation 3.7.

$$m = \frac{2\left(\frac{0.08F_{\mathrm{sma}}\sqrt{\left(\frac{Diameter}{2}\right)^2+\left(\frac{L_{\mathrm{mod}}}{2}\right)^2}\sin\left(90-\zeta\right)}{0.08+1.92\sin\phi-2\sin\upsilon}\right)\left(\frac{2}{L_{\mathrm{rob}}}\right)}{g} \tag{3.17}$$

To acheive Equation 3.22, φ, υ and ζ are broken down into terms of l_{mod} and diameter.

$$\varphi = \zeta + \frac{angle_{\mathrm{bend}}}{2} \tag{3.18}$$

$$\upsilon = \zeta - \frac{angle_{\mathrm{bend}}}{2} \tag{3.19}$$

$$\zeta = \arctan\left(\frac{l_{\mathrm{mod}}}{diameter}\right) \tag{3.20}$$

$$angle_{\mathrm{bend}} = \frac{360}{N_{\mathrm{mod}}} \tag{3.21}$$

$$m = \frac{2\left(\frac{0.08F_{\mathrm{sma}}\sqrt{\left(\frac{Diameter}{2}\right)^2+\left(\frac{L_{\mathrm{mod}}}{2}\right)^2}\sin\left(90^\circ-\arctan\left(\frac{l_{\mathrm{mod}}}{diameter}\right)\right)}{0.08+1.92\sin\left(\arctan\left(\frac{l_{\mathrm{mod}}}{diameter}\right)+\frac{180^\circ}{N_{\mathrm{mod}}}\right)-2\sin\left(\arctan\left(\frac{l_{\mathrm{mod}}}{diameter}\right)-\frac{180^\circ}{N_{\mathrm{mod}}}\right)}\right)\left(\frac{2}{L_{\mathrm{rob}}}\right)}{g} \tag{3.22}$$

Finally, to reduce the equation to it's basic inputs, Equations 3.23 and 3.24 are employed, resulting in Equation 3.25.

$$length_{\mathrm{mod}} = \frac{length_{\mathrm{rob}} - Diameter}{N_{\mathrm{mod}}} \tag{3.23}$$

$$Diameter = 0.08length_{\mathrm{rob}} \tag{3.24}$$

$$m = \frac{2\left(\frac{0.08F_{\mathrm{sma}}\sqrt{\left(\frac{0.08L_{\mathrm{rob}}}{2}\right)2+\left(\frac{\frac{0.92L_{\mathrm{rob}}}{N_{\mathrm{mod}}}}{2}\right)2}\sin\left(90^{\circ}-\left(\arctan\left(\frac{\frac{0.92L_{\mathrm{rob}}}{N_{\mathrm{mod}}}}{0.08L_{\mathrm{rob}}}\right)\right)\right)}{0.08+1.92\sin\left(\arctan\left(\frac{\frac{0.92L_{\mathrm{rob}}}{N_{\mathrm{mod}}}}{0.08L_{\mathrm{rob}}}\right)+\left(\frac{180^{\circ}}{N_{\mathrm{mod}}}\right)\right)-2\sin\left(\arctan\left(\frac{\frac{0.92L_{\mathrm{rob}}}{N_{\mathrm{mod}}}}{0.08L_{\mathrm{rob}}}\right)-\left(\frac{180^{\circ}}{N_{\mathrm{mod}}}\right)\right)}\right)\left(\frac{2}{L_{\mathrm{rob}}}\right)}{g} \tag{3.25}$$

After reducing Equation 3.6 to the core inputs into Equation 3.25, MATLAB reduces the function to Equation 3.26.

$$m = -\frac{8\,F_{\mathrm{sma}}\sin\left(\arctan\left(\frac{23}{2N_{\mathrm{mod}}}\right)-\frac{180^{\circ}}{2}\right)\sqrt{\frac{{L_{\mathrm{rob}}}^2}{625}+\frac{529\,{L_{\mathrm{rob}}}^2}{2500\,{N_{\mathrm{mod}}}^2}}}{25\;L_{\mathrm{rob}}\,g\left(\frac{48\sin\left(\arctan\left(\frac{23}{2N_{\mathrm{mod}}}\right)+\frac{180^{\circ}}{N_{\mathrm{mod}}}\right)}{25}-2\sin\left(\arctan\left(\frac{23}{2N_{\mathrm{mod}}}\right)-\frac{180^{\circ}}{N_{\mathrm{mod}}}\right)+\frac{2}{25}\right)} \tag{3.26}$$

In Equation 3.26, the length of the robot, L_{rob} appears on the top and bottom of the fraction. These cancel out during calculation, which explains the lack of change in potential mass with respect to robot length in Table 3.8. The second point of note is that the largest potential mass of all the robots is very small. A robot of approximately 80 g is incredibly light regardless of length for a tetherless robot, let alone 57g at the lightest. To give a sense of perspective, using the resistance per metre(RperM) and current (I) values given by Dynalloy, we can find the required voltage (V) for each module with Equation 3.27 [6]. Assuming the strongest SMA is used, with a diameter of 0.51mm, resistance per m of 4.3Ω/m and I of 4A, Table 3.9 displays the potential Voltage with relation to length of robot and number of modules.

$$V = IR \tag{3.27}$$

If we take a 1m long robot with 12 modules, each module requires 1.8768V. Even if we under power it with a 1.5V battery of 8g, the weight of the power supply alone would weigh 96g. When the weight limit for a robot of that specification is 60g, it becomes

Table 3.9: Theoretical Design II Voltage results - SMA Diameter = 0.51mm

Length (m) \ **Modules**	0.2	0.4	0.6	0.8	1
10	0.4161	0.8323	1.2484	1.6645	2.0807
11	0.3936	0.7872	1.1808	1.5744	1.9681
12	0.3754	0.7507	1.1261	1.5014	1.8768
13	0.3603	0.7206	1.0809	1.4412	1.8015
14	0.3477	0.6954	1.043	1.3907	1.7384
15	0.337	0.6739	1.0109	1.3479	1.6849
16	0.3278	0.6555	0.9833	1.3111	1.6389
17	0.3198	0.6395	0.9593	1.2791	1.5989
18	0.3127	0.6255	0.9382	1.251	1.5637
19	0.3065	0.613	0.9195	1.2261	1.5326
20	0.3009	0.6019	0.9028	1.2038	1.5047

apparent that producing a tetherless Wormbot with this design is a difficult challenge. Even with a robot of 0.5m length, a maximum weight of 60g and 0.9384V per module (assuming 12 modules are used), it is a difficult challenge to find batteries to provide power for each separate module (if the robot is to be truly modular). Even if this is achieved the batteries need to fit within a small module. There is also the issue that the 0.51mm diameter wire takes at least 14 seconds to cool, which is required for the SMA to be returned to its extended form. This would result in a very slow moving robot.

While the previous work has been performed with the largest available SMA, there are others available. Tables 3.10 and 3.11 display the maximum mass and voltage per module of a design II type robot using the thinnest SMA wires available, with a diameter of 0.025mm (Resistance per metre = 1425Ω/m, I=4.5mA, Cooling Time = 0.15 seconds) [17].

It can be seen from these tables that the thin SMA is not suitable for a tetherless hypermobile robot. While the cooling time is much more condusive to a faster moving robot, the theoretical potential weight of the robot is less then a gram. Furthermore, the required voltage is actually more then the larger SMA due to the higher resistance of thinner wire, though the required current is much less.

Table 3.10: Theoretical Design II Mass results - SMA Diameter = 0.025mm - (x10^{-3})

Length (m) **Modules**	0.2	0.4	0.6	0.8	1
10	0.1393	0.1393	0.1393	0.1393	0.1393
11	0.1446	0.1446	0.1446	0.1446	0.1446
12	0.1501	0.1501	0.1501	0.1501	0.1501
13	0.1558	0.1558	0.1558	0.1558	0.1558
14	0.1617	0.1617	0.1617	0.1617	0.1617
15	0.1677	0.1677	0.1677	0.1677	0.1677
16	0.1739	0.1739	0.1739	0.1739	0.1739
17	0.1801	0.1801	0.1801	0.1801	0.1801
18	0.1864	0.1864	0.1864	0.1864	0.1864
19	0.1927	0.1927	0.1927	0.1927	0.1927
20	0.1991	0.1991	0.1991	0.1991	0.1991

Table 3.11: Theoretical Design II Voltage results - SMA Diameter = 0.025mm

Modules **Length (m)**	0.2	0.4	0.6	0.8	1
10	1.5514	3.1028	4.6543	6.2057	7.7571
11	1.4675	2.9349	4.4024	5.8699	7.3373
12	1.3994	2.7988	4.1982	5.5975	6.9969
13	1.3432	2.6865	4.0297	5.373	6.7162
14	1.2962	2.5924	3.8887	5.1849	6.4811
15	1.2563	2.5126	3.7689	5.0252	6.2815
16	1.222	2.444	3.666	4.888	6.11
17	1.1922	2.3843	3.5765	4.7687	5.9609
18	1.166	2.3319	3.4979	4.6639	5.8299
19	1.1427	2.2855	3.4282	4.571	5.7137
20	1.122	2.2439	3.3659	4.4878	5.6098

3.3.3 Design III: SMA wire and SMA springs

3.3.3.1 Layout

Design III (Figure 3.11) is a simple design that is applicable to any linear actuator which contracts or expands when actuated. With contrast to Design II where the main variable is the position of the pulley points, the variable with Design III is the distance from the segment midline to the actuator. As the two become closer, the angle range that the segment can perform increases. While Design II optimizes the stroke of the linear actuator, Design III would be easier to construct due to the lack of pivot points. Additionally, the lack of pivot points means that a larger range of linear actuators could be used, such as SMA springs, which have a much larger stroke distance.

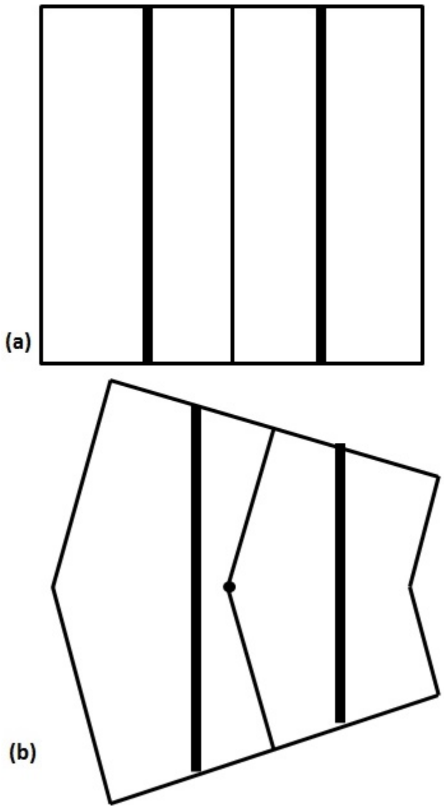

Figure 3.11: (a) Diagram of design III segment. (b) design III segment when one side is actuated. One potential risk in the design is the middle pivot colliding with the outside actuator when bending.

Figure 3.12 assists in explaining the equations derived for finding the output torque from this design layout.

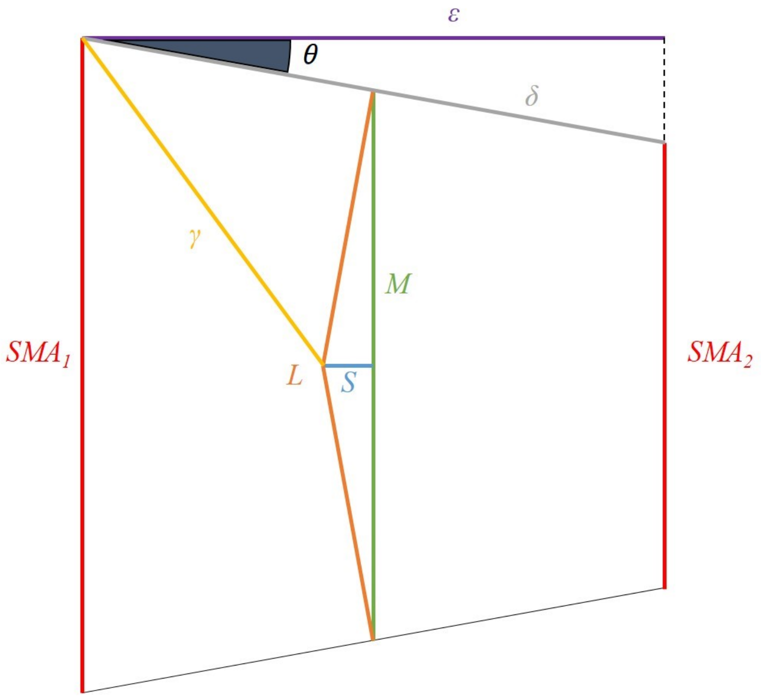

Figure 3.12: Diagram of design III with equation values. Red lines = SMA$_{1,2}$, Grey line = δ, Green line = M, Orange line = L, Blue = S, Purple line = ε, Yellow line = γ, Black angle = θ.

The first aim is to find the actuators extended and contracted lengths (Equations 3.28, 3.29, 3.30 and 3.31). Once these are found, Equation 3.32 can be used to find the distance between the actuators.

$$M = L\cos\theta \tag{3.28}$$

$$S = \sqrt{\left(\frac{L}{2}\right)^2 - \left(\frac{M}{2}\right)^2} = \left(\frac{L}{2}\cos\left(90 - \frac{\theta}{2}\right)\right) \tag{3.29}$$

$$SMA_1 = \frac{M}{1 - \frac{C}{2}} \tag{3.30}$$

$$SMA_2 = \frac{M}{\frac{1-\frac{C}{2}}{1-C}} \tag{3.31}$$

$$\delta = \frac{(\frac{C}{2})SMA_1}{\sin\theta} \tag{3.32}$$

$SMA_{1,2}$ are the maximum and minimum actuator lengths respectively, δ is the distance between the actuators end positions, M is the length of the vertical midline when one actuator is contracted, L is the length of the segment (when straight, L is equal to M), S is the horizontal distance between the pivot point and the vertical midline, C is the contraction ratio and θ equates to half the angle of the joint.

After this, Equations 3.33 and 3.34 need to be used to find the horizontal distance between the actuators ε, and pivot point to actuator corner distance γ. Finally the torque can be found.

$$\varepsilon = \sqrt{\delta^2 - \left(\frac{C}{2}SMA_1\right)^2} \tag{3.33}$$

$$\gamma = \sqrt{\left(\frac{SMA_1}{2}\right)^2 - \left(\frac{\varepsilon}{2} - s\right)^2} \tag{3.34}$$

3.3.3.2 Torque & Mass Potential

Using trigonometry to find the angle the actuator is working at, Equation 3.2 is adapted, then condensed, to produce Equations 3.35, 3.36 and 3.37.

$$\tau_{\min} = F\gamma\sin\left(\arcsin\left(\frac{\left(\frac{\varepsilon}{2} - s\right)}{\gamma}\right)\right) = F\left(\frac{\sigma}{2} - s\right) \tag{3.35}$$

$$\tau_{\text{str}} = F\gamma\sin\left(\arcsin\left(\frac{\left(\frac{\varepsilon}{2}\right)}{\gamma}\right)\right) = F\left(\frac{\sigma}{2}\right) \tag{3.36}$$

$$\tau_{\max} = F\gamma\sin\left(\arcsin\left(\frac{\left(\frac{\varepsilon}{2} + s\right)}{\gamma}\right)\right) = F\left(\frac{\sigma}{2} + s\right) \tag{3.37}$$

ε is the horizontal distance between the two actuators and γ is the distance between the pivot point and the actuator fixing point. The results for using SMA wire of 0.5mm diameter and a contraction rate of 4% can be seen in Table 3.12.

Table 3.13 shows the torque results for Design III with SMA springs with a wire diameter of 0.51, linear force of 243.3g or 2.386N and contraction rate of 56.25% [6].

Table 3.12: Theoretical Design III Dimensions and Torque results (SMA Wire)

Modules	**Module Length (m)**	**Angle (°)**	**δ/2 (m)**	**SMA Length (elongated) (m)**	**Torque (min) (Nm)**	**Torque (straight) (Nm)**	**Torque (max) (Nm)**
10	0.092	36	0.002889	0.0893	-0.4005	0.1009	0.5924
11	0.083	32.7	0.002887	0.0819	-0.3141	0.1015	0.5047
12	0.077	30	0.002932	0.0756	-0.2480	0.1020	0.4469
13	0.071	27.7	0.002939	0.0701	-0.1964	0.1023	0.3964
14	0.066	25.7	0.002952	0.0654	-0.1553	0.1026	0.3568
15	0.061	24	0.002928	0.0612	-0.1221	0.1028	0.3215
16	0.058	22.5	0.002975	0.0575	-0.0948	0.1030	0.2995
17	0.054	21.2	0.002944	0.0543	-0.0722	0.1032	0.2745
18	0.051	20	0.002951	0.0514	-0.0533	0.1033	0.2562
19	0.048	18.9	0.002948	0.0487	-0.0372	0.1034	0.2390
20	0.046	18	0.002964	0.0464	-0.0234	0.1035	0.2279

Table 3.13: Theoretical Design III Dimensions and Torque results (SMA Spring)

Modules	**Module Length (m)**	**Angle (°)**	**δ/2 (m)**	**Spring Length (elongated) (m)**	**Torque (min) (Nm)**	**Torque (straight) (Nm)**	**Torque (max) (Nm)**
10	0.092	36	0.0396	0.1120	0.0560	0.0946	0.1239
11	0.083	32.7	0.0399	0.1027	0.0632	0.0951	0.1194
12	0.077	30	0.0401	0.0948	0.0686	0.0956	0.1160
13	0.071	27.7	0.0402	0.0880	0.0729	0.0959	0.1133
14	0.066	25.7	0.0403	0.0820	0.0763	0.0962	0.1112
15	0.061	24	0.0404	0.0768	0.0791	0.0964	0.1095
16	0.058	22.5	0.0405	0.0722	0.0813	0.0966	0.1081
17	0.054	21.2	0.0405	0.0681	0.0832	0.0967	0.1069
18	0.051	20	0.0406	0.0644	0.0848	0.0968	0.1059
19	0.048	18.9	0.0406	0.0611	0.0861	0.0969	0.1051
20	0.046	18	0.0407	0.0582	0.0872	0.0970	0.1044

At this point it should be noted that, with the spring selected (with the shortest stroke rate for this company's SMA springs), the position of the springs is actually beyond the boundaries of an 80mm diameter robot, and therefore can be seen as unfeasible even before any torque results have been taken into consideration. Even if this was to be disregarded, the theoretical torque results are still very low. The springs could be moved within the boundaries of the frame, which would increase the level of flexibility, though this would be at the detriment of already low torque values. This is the same for design III with using regular SMA wires too (Table 3.12). An additional point that should be noted from the SMA wire results is that all of the minimum torque readings are negative values. This is due to the actuators being positioned very close to the pivot point of the joint to achieve the necessary joint rotation. When the module rotation is at maximum, the end positions of the actuator move beyond the joint midpoint, resulting in actuation applying force in the wrong direction, making this combination of actuator and design an impossible challenge.

Table 3.14 shows the mass results for Design III, using torque readings from when the robot is in a straight position, as in Chapter 3.3.2.2.

Table 3.14: Theoretical Design III Mass results

Modules	**Module Length (m)**	**Angle (°)**	**SMA**		**SMA Spring**	
			Torque (Nm)	Mass (Kg)	Torque (Nm)	Mass (Kg)
10	0.092	36	0.1009	0.0411	0.0946	0.0386
11	0.083	32.7	0.1015	0.0414	0.0951	0.0388
12	0.077	30	0.1020	0.0416	0.0956	0.0390
13	0.071	27.7	0.1023	0.0417	0.0959	0.0391
14	0.066	25.7	0.1026	0.0418	0.0962	0.0392
15	0.061	24	0.1028	0.0419	0.0964	0.0393
16	0.058	22.5	0.1030	0.0420	0.0966	0.0394
17	0.054	21.2	0.1032	0.0421	0.0967	0.0394
18	0.051	20	0.1033	0.0421	0.0968	0.0395
19	0.048	18.9	0.1034	0.0422	0.0969	0.0395
20	0.046	18	0.1035	0.0422	0.0970	0.0396

3.3.3.3 Consideration to Robot Size and Actuator Thickness

As with Design II, Design III should not be immediately discounted because of low torque values when the robot is 1m long. Using different lengths and thicknesses of actuators should be explored. Therefore, as with Chapter 3.3.2.3, Table 3.15 shows how the maximum allowable weight of the robot would change in respect to the number of modules per robot and length when using SMAs, while Table 3.16 displays these results when SMA Springs are used.

Table 3.15: Theoretical Design III Mass results (kg) - SMA Diameter = 0.51mm

Length (m) / **Modules**	0.2	0.4	0.6	0.8	1
10	0.0411	0.0411	0.0411	0.0411	0.0411
11	0.0414	0.0414	0.0414	0.0414	0.0414
12	0.0416	0.0416	0.0416	0.0416	0.0416
13	0.0417	0.0417	0.0417	0.0417	0.0417
14	0.0418	0.0418	0.0418	0.0418	0.0418
15	0.0419	0.0419	0.0419	0.0419	0.0419
16	0.0420	0.0420	0.0420	0.0420	0.0420
17	0.0421	0.0421	0.0421	0.0421	0.0421
18	0.0421	0.0421	0.0421	0.0421	0.0421
19	0.0422	0.0422	0.0422	0.0422	0.0422
20	0.0422	0.0422	0.0422	0.0422	0.0422

Table 3.16: Theoretical Design III Mass results (kg) - Spring Diameter = 0.51mm

Length (m) / **Modules**	0.2	0.4	0.6	0.8	1
10	0.0386	0.0386	0.0386	0.0386	0.0386
11	0.0388	0.0388	0.0388	0.0388	0.0388
12	0.0390	0.0309	0.0390	0.0390	0.0390
13	0.0391	0.0391	0.0391	0.0391	0.0391
14	0.0392	0.0392	0.0392	0.0392	0.0392
15	0.0393	0.0393	0.0393	0.0393	0.0393
16	0.0394	0.0394	0.0394	0.0394	0.0394
17	0.0394	0.0394	0.0394	0.0394	0.0394
18	0.0395	0.0395	0.0395	0.0395	0.0395
19	0.0395	0.0395	0.0395	0.0395	0.0395
20	0.0396	0.0396	0.0396	0.0396	0.0396

Once again, we have found that changing the overall size of the robot has no effect on the maximum potential weight of a robot such as this. To verify this, the same approach is taken once again to reduce the equation for the mass of the robot down to the core inputs; Robot Length, Number of Modules, acceleration (gravity in this case, $9.81ms^{-2}$), Force (of the actuator) and Contraction rate (of the actuator). This is shown in Equation 3.41. We can pick up from Equation 3.14 from Chapter 3.3.2.3. Using Equation3.36 with this, Equation 3.38 is reached.

$$m = 2\frac{\frac{F\delta}{2} / \frac{l_{\text{rob}}}{2}}{g} \tag{3.38}$$

At this point, it should be noted that when the body position is straight, $\varepsilon = \delta$. Therefore Equation 3.32 is used to create Equation 3.39.

$$m = 2\frac{\frac{F\frac{(C/2)SMA_1}{\sin\theta}}{2} / \frac{l_{\text{rob}}}{2}}{g} = \frac{F\frac{(C/2)SMA_1}{\sin\theta} / l_{\text{rob}}}{g} \tag{3.39}$$

Equation 3.30 can then be used to create Equation 3.40.

$$m = 2\frac{F\frac{(C/2)\frac{M}{1-\frac{C}{2}}}{\sin\theta} / l_{\text{rob}}}{g} \tag{3.40}$$

Finally, Equation 3.23 and 3.24 and MDIII are used to create Equation 3.41.

$$m = 2\frac{\frac{F\frac{C}{2}\frac{0.92Length_{\text{rob}}\cos\left(\frac{180^{\circ}}{N_{\text{mod}}}\right)}{N_{\text{mod}}}}{1-\frac{C}{2}} / \frac{\sin\left(\frac{180^{\circ}}{N_{\text{mod}}}\right)}{Length_{\text{rob}}}}{g} \tag{3.41}$$

Using the *simplify* function in matlab reduces this to Equation 3.42.

$$m = \frac{-46CF\cos\left(\frac{180^{\circ}}{N_{\text{mod}}}\right)}{25N_{\text{mod}}g\sin\left(\frac{180^{\circ}}{N_{\text{mod}}}\right)(C-2)} \tag{3.42}$$

As in Chapter 3.3.2.3, the robot length has been cancelled out of the equation for mass, proving that there is no link between the two in this situation. What is found in comparison to Design II is that Design III is not as as strong when using SMAs and even less effective when using SMA Springs. Tables 3.17 and 3.18 show the voltage requirements of Design III with SMAs and SMA springs respectively.

It can be see from Tables 3.17 and 3.18 that the voltage requirements for Design III are generally favourable to those of Design II, with springs requiring a slightly lower voltage

Table 3.17: Theoretical Design III Voltage results - SMA

Length (m) **Modules**	0.2	0.4	0.6	0.8	1
10	0.3071	0.6143	0.9214	1.2285	1.5357
11	0.2817	0.5634	0.8451	1.1268	1.4084
12	0.2599	0.5199	0.7798	1.0398	1.2997
13	0.2412	0.4824	0.7236	0.9648	1.206
14	0.2249	0.4498	0.6747	0.8995	1.1244
15	0.2106	0.4212	0.6318	0.8424	1.0529
16	0.198	0.3959	0.5939	0.7918	0.9898
17	0.1867	0.3735	0.5602	0.7469	0.9336
18	0.1767	0.3534	0.5301	0.7067	0.8834
19	0.1676	0.3353	0.5029	0.6706	0.8382
20	0.1595	0.319	0.4784	0.6379	0.7974

Table 3.18: Theoretical Design III Voltage results - SMA Spring

Length (m) **Modules**	0.2	0.4	0.6	0.8	1
10	0.3298	0.6595	0.9893	1.319	1.6488
11	0.3024	0.6049	0.9073	1.2098	1.5122
12	0.2791	0.5582	0.8373	1.1164	1.3955
13	0.259	0.5179	0.7769	1.0359	1.2948
14	0.2415	0.4829	0.7244	0.9658	1.2073
15	0.2261	0.4522	0.6783	0.9044	1.1305
16	0.2125	0.4251	0.6376	0.8502	1.0627
17	0.2005	0.401	0.6015	0.802	1.0024
18	0.1897	0.3794	0.5691	0.7588	0.9485
19	0.18	0.36	0.54	0.72	0.9
20	0.1712	0.3425	0.5137	0.6849	0.8562

to SMAs. However, the mass that can potentially be maintained is approximately half of that of Design II, which was deemed too weak in the first instance. A potential weight of approximately 40g for a tetherless robot such as this is impossible, considering that would have to include actuators, power supply, micro-controller and the shell of the robot. When a method for implementing compliance within the body has to be included as well, the scale of this challenge becomes overwhelmingly apparent.

3.4 Design IV: Motors

One other actuation method that is possible is the use of motors. From Chapter 2, it is clear to see that this is the most common solution for joint actuation in hypermobile robots. Motors come in a range of sizes and there is often a suitable motor for most needs, though gearboxes can assist if something is not available. For example, Maxon Motor 339154 runs at 10100rpm and works at 30.7mNm, whilst weighing 110g and measuring 43mm long [13]. If a gearbox of ratio 350:1 is used, the torque can be boosted to 10.745Nm; about the same as Design I option 4. At the same time, the rotational speed drops to 28.86rpm. If this is used with a robot that has a 30° max angle, this translates as about 1.44Hz. This is not as much as the *C.elegans* when swimming (2Hz), though Amphibot II is capable of swimming at 1Hz [26,33]. 2Hz can be achieved if the segments have a maximum turn angle of about 21°, which leads to having 17 segments when referring to Table 3.3. This would mean more motors would be required and the robot could become heavier. However this motor is light while it is also relatively small (43mm long and 25mm diameter). Additionally, gearboxes can be designed to save space, with such designs as planetary or harmonic gearboxes, though with larger ratio steps comes heavier components. In comparison to SMAs, while the example motor requires a (much greater) 36V and to provide 20W, the current rating of 0.55A is nearly 16 times less than a pair of SMAs that would be required for the same movement in Design II and III.

Another option would be to use servo motors. Considering the output rotation of a segment joint only needs to rotate ± 45°, a servo motor would be well suited as most have a movement range of 180°. This would mean that a gearbox may not be required, or at least only a very simple one, which could save space and weight. Additionally, servo motors are available with a wide range of specifications, so finding one that would be ideal for our project. For example, a Dynamixel AX-18A is 54.5, has 300° rotation and a maximum torque of 1.8 Nm [5]. If a 3:1 gear ratio is used, the output range would be 100° and a Torque of 5.4Nm could be achieved; comfortably more than the pneumatic options presented in this chapter.

A potential downside of using motors for this application is the lack of compliance within the mechanism. While there is little compliance directly from a motor, there are methods of introducing it into a design. As shown by the original Wormbot, springs are a very common way of employing this [28]. Cantilever springs are fixed to the frame of the robot, with pulleys attaching them to the motors. However other solutions use spring elements connected within the gear train, which could potentially save space but could bring around design challenges if a number of parts are required [31]. Mounting the motor on a spring like component has also been experimented with in the past [61]. This shows that while integrating compliance into a motorised design is an additional challenge, there are many solutions and it shouldn't be a reason to ignore motorised options from further consideration.

3.5 Discussion

Table 3.19 displays the torque values of all previously mentioned design concepts. In this table, the minimum and maximum torque values are displayed, as well as the torque when the joints are straight. Additionally, all results displayed in this section are reached assuming the robot is 1m long, as was declared in Table 3.1.

One of the first points of note is that the torque results for Design I are not affected by the number of modules on a robot. This is because the main determining factor for pneumatic applications isn't the length of the actuator, but the diameter, as can be seen in Chapter 3.3.1. This is also true for SMA based actuator. However, as they are designed to have a set contraction rate, the proportions of the mechanisms in Design II and III must had to change with the changing module length to achieve the correct amount of flexibility. In Chapter 3.3.2 and 3.3.3, it is seen that changing the length of the whole robot had no effect on the torque. This is because as the robot gets shorter, the width of the robot decreses to keep the desired aspect ratio, which appears to result in cancelling out any changes in torque.

For Design I, the 2D and 3D options with the most potential were taken forward. This was option 2 for 3D movement and option 4 for 2D movement. Option 4 was the weakest of the 3 options but the other two options would provide more problems when trying to fit all the components within the segment. One point that should be noted about the

Table 3.19: Collated Torque Results

Modules		10	11	12	13	14	15	16	17	18	19	20
Design I (2D Bellows)	Min	3.89	3.89	3.89	3.89	3.89	3.89	3.89	3.89	3.89	3.89	3.89
	Str	6.91	6.91	6.91	6.91	6.91	6.91	6.91	6.91	6.91	6.91	6.91
	Max	10.80	10.80	10.80	10.80	10.80	10.80	10.80	10.80	10.80	10.80	10.80
Design I (3D Bellows)	Min	2.33	2.33	2.33	2.33	2.33	2.33	2.33	2.33	2.33	2.33	2.33
	Str	5.25	5.25	5.25	5.25	5.25	5.25	5.25	5.25	5.25	5.25	5.25
	Max	9.33	9.33	9.33	9.33	9.33	9.33	9.33	9.33	9.33	9.33	9.33
Design I (2D Muscles)	Min	0.02	0.02	0.02	0.02	0.02	0.02	0.02	0.02	0.02	0.02	0.02
	Str	6.09	6.09	6.09	6.09	6.09	6.09	6.09	6.09	6.09	6.09	6.09
	Max	13.50	13.50	13.50	13.50	13.50	13.50	13.50	13.50	13.50	13.50	13.50
Design I (3D Muscles)	Min	0.02	0.02	0.02	0.02	0.02	0.02	0.02	0.02	0.02	0.02	0.02
	Str	5.26	5.26	5.26	5.26	5.26	5.26	5.26	5.26	5.26	5.26	5.26
	Max	11.66	11.66	11.66	11.66	11.66	11.66	11.66	11.66	11.66	11.66	11.66
Design II (SMA Wire)	Min	0.0814	0.0944	0.1058	0.1161	0.1258	0.1346	0.1436	0.1515	0.1587	0.1678	0.1753
	Str	0.1367	0.1418	0.1472	0.1528	0.1586	0.1645	0.1706	0.1767	0.1828	0.1891	0.1953
	Max	0.1786	0.1769	0.1793	0.1810	0.1842	0.1866	0.1920	0.1952	0.2002	0.2051	0.2105
Design III (SMA Wire)	Min	-0.4005	-0.3112	-0.2491	-0.1971	-0.1558	-0.1214	-0.0957	-0.0724	-0.0531	-0.0362	-0.0234
	Str	0.1009	0.1015	0.1020	0.1023	0.1026	0.1028	0.1030	0.1032	0.1033	0.1034	0.1035
	Max	0.5924	0.5047	0.4469	0.3964	0.3568	0.3215	0.2995	0.2745	0.2562	0.2390	0.2279
Design III (SMA Spring)	Min	0.0560	0.0632	0.0686	0.0729	0.0763	0.0791	0.0813	0.0832	0.0848	0.0861	0.0872
	Str	0.0946	0.0951	0.0956	0.0959	0.0962	0.0964	0.0966	0.0967	0.0968	0.0969	0.0970
	Max	0.1239	0.1194	0.1160	0.1133	0.1112	0.1095	0.1081	0.1069	0.1059	0.1051	0.1044

torque results is that the values given show a constant value, where the force from a bellow varies depending on the length it has expanded, as shown by Granosik [39]. Both Bellows and McKibbens actuators solutions produced similar answers. It is worth noting though that while McKibben actuators also have a greater maximum torque, the minimum torque trends to 0Nm. This implies that as the joint of the robot gets closer to the limit of rotation, the drop off in performance will be severe. Additionally, the "straight" torque value of the bellows solutions are found by assuming the convolute diameter at this point is halfway between minimum and maximum. If the inner convolute were able to expand, it would be conceivable to think that the force output could be higher, as the force is relative to the minimum cross-sectional area of the bellow (see Equation 3.1). This force output could also be increased in both styles of pneumatic actuator by increasing the internal pressure of the system, though this could potentially damage the actuators if they were not strong enough. Additionally, the components required to produce this may need to be stronger and potentially bigger and heavier.

When analysing results from Design II, using SMAs produced much lower torque results than those from Design I; specifically about 25-40 times smaller. The effect of this will become apparent later, but purely from the torque calculations, using this actuator and layout would be vastly detrimental to the performance of the robot. In theory, due to the small diameter of the SMA, multiple actuators could be used in one joint to increase the force output of the joint, though it should be noted that one SMA actuator of the dimensions used here requires approximately 4A; powering multiple SMAs in one module would prove challenging at best. Furthermore, the cooling time for this actuator is 15 seconds, which would make the target of producing a 1Hz frequency of body motion impossible. Thinner actuators can be used to help with the current and cooling issues, though these are even weaker in their force output (see Figure 3.10).

The upside of the layout of Design II is that it utilises the short contraction rate of the SMA, while maximising the potential torque output. This is displayed in Design III, where the positioning of the actuator requires no pivot points. The torque output here is calculated at about half to two thirds of the performance shown in Design II. However the drop in performance is not the only issue. To achieve the required amount of joint rotation, the SMAs have to be positioned very close to the middle of the module. This means that when the joint is fully rotated in one direction, the middle of the opposing SMA moves beyond the midpoint of the joint, meaning that it can only operate in the opposite direction to the one intended, resulting in negative torque results. Using SMA springs in the Design III arrangement has the opposite effect. To achieve the exact amount of rotation demanded, the springs would have to be positioned beyond the body wall of the robot. Changing the width of the robot would mean the aspect ratio required for this robot would not be achieved. If the springs were positioned further in, you could achieve more rotation per joint but the potential torque output would decrease. When this is already as low as around 0.1Nm when the robot is straight, lowering the torque output is not a viable option.

The theoretical results for all the designs are shown in Table 3.20.

As can be seen from Table 3.20, the low torque values for the Design III translate to having a very low threshold of weight for the entire robot. It would be difficult to get a robot of this size built under or even close to 40g. Design II produces results that are not much improved, with a theoretical mass maximum of up to 80g. One point of interest with the design was that as the number of segments increased, the torque increased too. However it is unlikely that with this design that reasonable torque values could be achieved unless each segment was to have multiple sets of SMAs. This however would greatly increase the current within the system. However it was found earlier in Chapter 3.3.2.2 that changing the length of the robot had no effect to maximum weight. Therefore, while it is unlikely that a modular, tetherless robot be produced using SMA's, they would be valuable to other projects of a smaller scale where on-board power is not a concern, which has been seen in other work [67, 81]. The pneumatic solutions presented in Design I show much more promise to the application at hand, with potential masses above 2kg. A further advantage of the pneumatic actuators for this application is the natural compliance that is present in them, meaning that no additional compliance systems need to be built into the design.

3.6 Conclusions

In this chapter, a number of potential segment designs with a range of actuators were proposed for use in the second iteration of Wormbot. These designs were then theoretically analysed to find their suitability for the task. From this process two designs were to be chosen for experimentation. To assist, Table displays the positives and negatives of each design and actuator pairing.

It was noticed that Design III should instantly be disregarded, as with SMA springs

Table 3.20: Collated Mass Results

Modules	10	11	12	13	14	15	16	17	18	19	20
Design I (2D Bellows)	2.82	2.82	2.82	2.82	2.82	2.82	2.82	2.82	2.82	2.82	2.82
Design I (3D Bellows)	2.14	2.14	2.14	2.14	2.14	2.14	2.14	2.14	2.14	2.14	2.14
Design I (2D muscles)	2.48	2.48	2.48	2.48	2.48	2.48	2.48	2.48	2.48	2.48	2.48
Design I (3D muscles)	2.14	2.14	2.14	2.14	2.14	2.14	2.14	2.14	2.14	2.14	2.14
Design II (SMA Wire)	0.0557	0.0578	0.0600	0.0623	0.0647	0.0671	0.0695	0.0720	0.0746	0.0771	0.0796
Design III (SMA Wire)	0.0411	0.0414	0.0416	0.0417	0.0418	0.0419	0.0420	0.0421	0.0421	0.0422	0.0422
Design III (SMA Spring)	0.0386	0.0388	0.0390	0.0391	0.0392	0.0393	0.0394	0.0394	0.0395	0.0395	0.0396

Table 3.21: Comparison Table for Potential Actuation Methods

Design (Actuator)	Positives	Negatives
Design I (2D Bellows)	1. Respectable Torque output 2. Inherant Compliance 3. Lightweight Actuator	1. Large Actuator Cross Section 2. Pressurised Air Supply Required
Design I (3D Bellows)	1. Increased D.O.F 2. Inherant Compliance 3. Lightweight Actuator	1. Large Actuator Cross Section 2. Pressurised Air Supply Required 3. Slightly Reduced Torque
Design I (2D muscles)	1. Higher Torque output than Bellows 2. Inherant Compliance 3. Lightweight Actuator	1. Large Actuator Cross Section 2. Pressurised Air Supply Required 3. Large Torque Drop-off
Design I (3D muscles)	1. Increased D.O.F 2. Inherant Compliance 3. Lightweight Actuator 4.Comparable Torque to 2D Bellows Design	1. Large Actuator Cross Section 2. Pressurised Air Supply Required 3. Large Torque Drop-off
Design II (SMA Wire)	1. Very Small 2. Very Light	1. Very Low Torque 2. Need for additional Compliance System 3. High current rating
Design III (SMA Wire)	1. Very Small 2. Very Light	1. Very Low Torque 2. Need for additional Compliance System 3. High current rating 4. Impossible due to small actuator contraction length
Design III (SMA Spring)	1. Very Small 2. Very Light	1. Very Low Torque 2. Need for additional Compliance System 3. High current rating 4. Large contraction rate results in even lower torque
Design IV (Motors)	1. High Torque 2. Adaptable	1. Need for additional Compliance System 2. Higher Voltage

the geometry resulted in drops in in torque, whilst with SMA wire it proved impossible to produce. In addition, SMA's were found to be very underpowered for this application so Design II was also disregarded. In Design I, two pneumatic actuators are proposed, which benefited from naturally occurring compliance. It has been proved that pneumatic actuators were capable of producing greater torque, and thus support a heavier robot. However the drop off in performance reduced the minimum torque to almost 0. Whilst Bellows were theoretically found to be slightly less powerful, the drop off in torque is much less.

Through these actions, it was decided that pneumatic bellows based design could potentially be a suitable actuator due to their high force output in comparison to other proposed actuators, their potential to be built to a compact size and, as stated in Chapter 2, their natural compliance. The second actuator to be chosen for experimentation was motors. The wide range of motors available, alongside the use of gearboxes make them a very versatile option and one that has been used in many similar applications.

Chapter 4

Pneumatic Bellow Development

4.1 Introduction

As was discussed in Chapter 3, pneumatic bellows are a promising option as they are inherently compliant, a feature that needs to be present for Wormbot to work. They also develop more than adequate force output for the application size and have the potential, depending on the design, to contract to being almost flat [42]. Add to this that the force drop off is much less accentuated than in McKibbens air muscles and you are presented with a light, compliant and powerful actuator.

However, pneumatic actuators are not without their flaws, which were discussed in Chapter 3. Either a tethered air supply or on-board air compressors are required, both of which could hinder performance, whether it be by range of movement or increasing the weight of the robot. Additionally, as the force of the actuator is dependant on the cross sectional area, to achieve the highest power output the actuator can take a reasonable amount of space. When the robot is intended to be 80mm in diameter, care will have to taken to not make the pneumatic bellows too large.

In this chapter, the process behind designing and testing custom made bellows is described. A number of facets to the design process will be discussed, including manufacturing processes, compatibility with existing interfaces and other design features. The design will go through a few iterations before being tested and analysed.

4.2 Bellow Mk I

4.2.1 Design

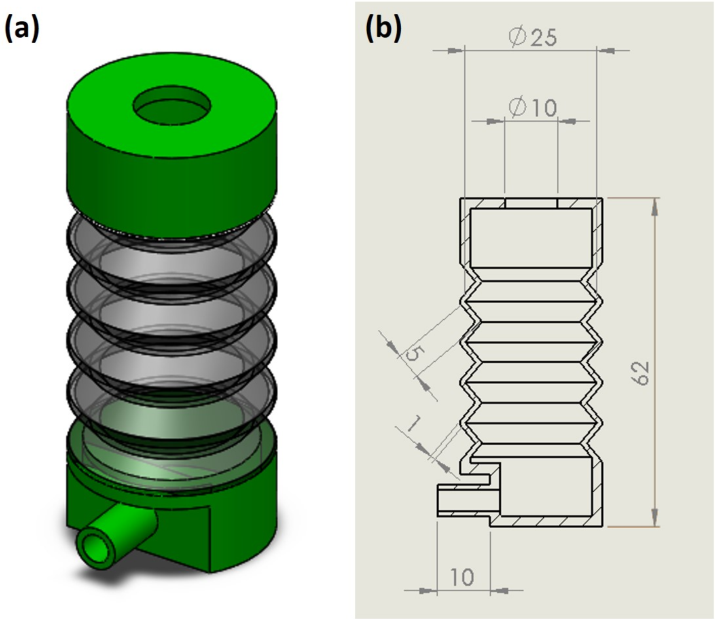

Figure 4.1: (a) CAD model of Bellow Mk I. (b) Cross-sectional drawing of Bellow Mk I.

The first iteration of the bellow design was not designed to be fully functional, but more as a way of testing what could and could not be achieved. As we can see from Figure 4.1(a), There are two end caps with rubber bellows between. There is a 10mm long port, suitable for 6mm pneumatic push fittings, on one end. The bellow could have been designed to have much flatter end caps but then the pneumatic port would have to be fitted to the end of the cap, not the side. A device without flat endings could face additional issues when it comes to fitting the actuator into the robot. Additionally, an outer diameter of 25mm is used, having been suggested in conceptual Design I in Chapter 3.3.1.

Another point of note is the 10mm hole in the upper end cap. This is due to the manufacturing process chosen. Bellows and other soft actuators are often made out of rubber, which can be moulded into shape [22,37]. However, advances in 3D printing mean that 3D printed multi-material parts, including rubber-like materials, can be produced in a single step. This method of production is advantageous for prototyping as 3D printing is a relatively quick process in comparison to moulding. Additionally, the 3D component can be produced in one process, taking CAD assemblies and assigning different materials to the different parts of the assembly. Therefore, a stratasys Objet 1000 has been used to produce the prototype [15]. However, the downside of this process is that a solid part must be produced. Therefore if a part is hollow, it is printed with a soft support material inside, which must be removed. The 10mm hole in the top end cap is there so the support material can be removed.

4.2.2 Analysis

Figure 4.2: 3D printed Mk I Bellow.

Figure 4.2 displays the printed bellow Mk I. Although the device can't be inflated, it can be stretched by hand to 70mm and can be compressed to 39mm, resulting in a range of 31mm. If a 80mm diameter Wormbot was to be used and the full robot was to maintain the scale of *C.elegans*, these actuators would fit in 80mm long segments, of which 12 would construct close to the desired 1m robot.

This Bellow displays that the soft rubber-like material is capable of stretching and flexing as required. However, over time a tear began to appear between the two small black lines in the red circle on Figure 4.2. If Figure 4.1(b) is observed, it can be seen that there is no radius on inside of a bend of each whorl. This could be a point of weakness when it is being extending and contracting. Therefore, convolute corners should be designed with radiuses. However, the outer whorl may need additional measures as it needs to hold its shape and avoid ballooning to retain the outer whorl diameter of 25mm. This could be assisted by either thickening the material around this point or introducing a stronger material.

An additional issue occurred with the pneumatic supply socket. While the diameter was correct for the push fitting, it did not stand proud enough of the end cap and the push fitting was not able to achieve enough purchase. This can easily be solved by extending the port.

4.3 Bellow Mk II

4.3.1 Design

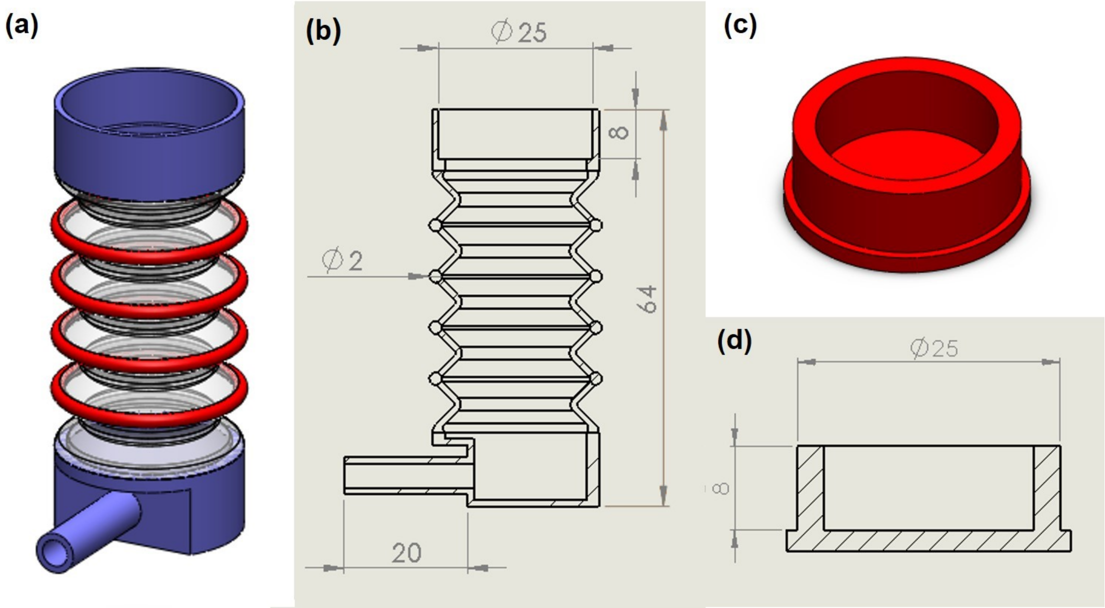

Figure 4.3: (a) CAD model of Bellow Mk II. (b) Cross-sectional drawing of Bellow Mk II. (c) CAD model of Bellow Mk II cap. (d) Cross-sectional drawing of Bellow Mk II cap.

Design II shows the next step towards creating a 3D printed bellow that could be tested. This is displayed in Figure 4.3. The most obvious point of note is the 2mm thick red rings located along the rubber bellow section in Figure 4.3(a). These are intended to provide more structure to the bellow to prevent ballooning and retain the maximum bellow diameter of 25mm. The 3D printer used has the ability to mix two separate materials. The red bands on the model are made of a 50:50 split of the rubber-like material and the standard plastic material used for the end caps. This should provide extra strength while still allowing some flexibility. Additionally, the inside corner of each inner whorl now has radiuses in an attempt to prevent splitting.

The two openings to bellow k I have also been redesigned. As can be seen in Figure 4.3(b), the pneumatic port has been doubled in length to allow the push fitting to gain purchase and create a seal. The hole in the top of the bellow has also been widened. This hole has been designed to have a cap (Figure 4.3(c) and (d)) to plug it once the support material from the print has been removed.

4.3.2 Analysis

Figure 4.4: 3D printed Mk II Bellow.

Figure 4.4 displays bellow a printed Mk II Bellow. When stretched like the previous bellow, the maximum length was 76mm. The compressed length was 43mm, leading to a range of 33mm, similar to Mk I bellow. These would still conform to the segment size discussed in Chapter 4.2.2.

The first area of improvement to be discussed is the adaptations to the pneumatic port and support material removal hole. The increased length of the pneumatic port now allows for the supply push fitting to gain purchase, maintaining a good seal. Additionally, the hole at the top of the bellow is plugged with a cap. Whilst it creates a tight fit, once testing is completed it may be found that a better seal may be required, potentially with the assistance of an O-ring.

Secondly, the rings located on the outer whorl succeed in providing more structure to the bellow. The hybrid material was tougher and less flexible than the standard rubber like material. However, it is unknown how strong the bond between the two materials is. If there is a way of exploring the principle of strengthening the outer whorl whilst minimising material change then, while it isn't vital, it may be beneficial.

The final change that was made is adding a radius to the inside corner of each whorl. This was achieved in the inner whorl but due to the addition of the outer rings this didn't occur there. However, to strengthen the bond between the bellow wall and the rings, radiuses between the two could be added.

4.4 Bellow Mk III

4.4.1 Design

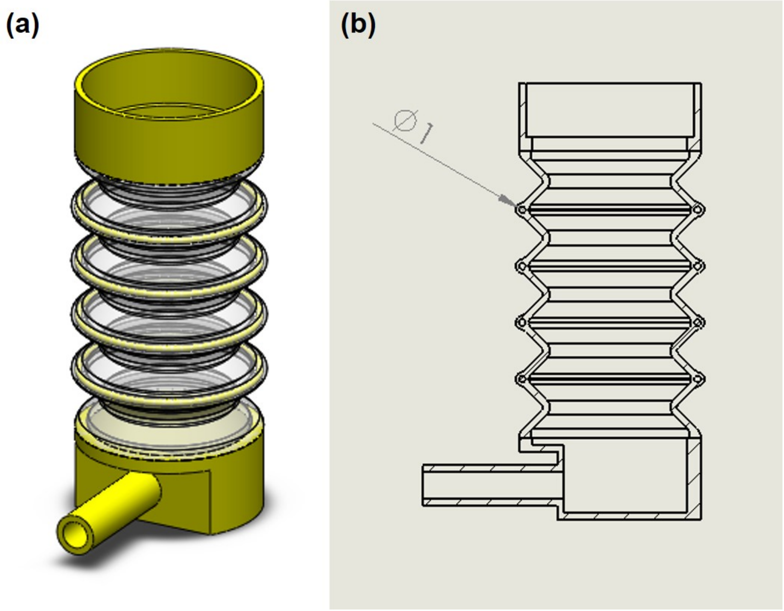

Figure 4.5: (a) CAD model of Bellow Mk III. (b) Cross-sectional drawing of Bellow Mk III.

Bellow Mk III does not differ too much from Mk II in appearance, in that most of the dimensions are the same. The longer pneumatic port remains, as does the cap for the support material removal hole. The only difference between the two different designs lies in the outer strengthening hoops. As can be seen from Figure 4.5 (a) and (b), a 1mm wide strengthening ring is now located within a rubber-like material tube. This is so there is no material change in the convolute at the location of the outer whorl that could lead to any weakness. Additionally, radiuses have been added between the convolute wall and the strengthening rings to provide additional strength (see Figure 4.6 (b)).

4.4.2 Analysis

Figure 4.6: 3D printed Mk III Bellow.

Figure 4.6 shows a 3D printed Mk III bellow. Two versions of the bellow were printed, though they were both identical to look at. The difference between the two was in the structure of the strengthening rings. In the previous iteration, the strengthening ring was made out of a hybrid material; 50% artificial rubber, or “tango plus” material and 50% plastic “vero plus” material [16]. In this version, one bellow was printed with the same mixture, whilst the other was 75% plastic and 25% artificial rubber, to produce a stiffer structure. The stiffer ring would be expected to hold its shape more but it may also be more brittle, which could lead to fracturing.

At this point it was decided that the bellows were suitable for testing. The design has some potential flaws which may cause the bellow to perform less than perfectly. One of these areas is the cap at the top of the bellow potentially requiring an improved design to optimise air retention. Nevertheless, the design of the bellow is at a point where testing can provide a sense of how much more development, if any, would be required produce these to a high enough standard to implement in a application like that of Wormbot.

4.5 Testing

In this sectionr, the process behind testing the effectiveness of the 3D printed bellows is described. Firstly, the method of testing and equipment will be introduced. Following this, the results will be displayed and evaluated.

4.5.1 Method

A very simple method has been devised for this test. Firstly, a pneumatic system will regulate the pressurised air supply. This will then be fed through to the bellow to inflate it. The aim will be to actuate the bellow, then de-activate it. Figure 4.7 displays the pneumatic circuit diagram for this test.

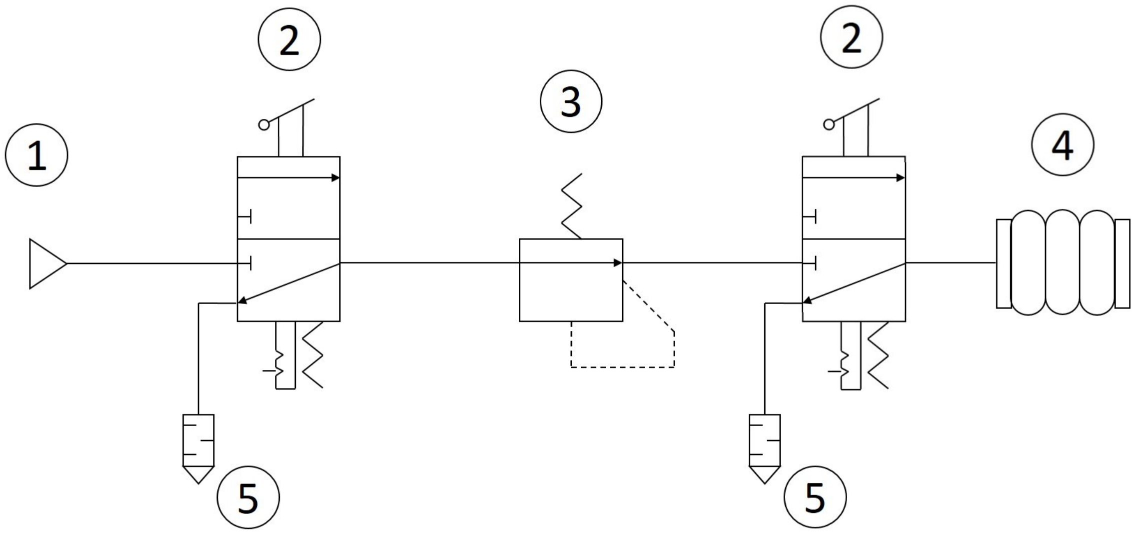

Figure 4.7: Pneumatic circuit digram for bellow testing.(1) Pressurised air supply. (2) 3/2 Manual valve. (3) Pressure regulator. (4) 3D Printed Bellow. (5) Silencer

The first element represents the pressurised air supply to the system. The supply to the system rates at approximately 700KPa. This feeds into the first manual switch, which acts as the main supply switch to the system. A pressure regulator is then used to bring the supply pressure down to 550KPa, the same level as OT-4 [39]. This is followed by another manual switch, which will be used as the operational switch for the 3D printed bellow, which is last in the circuit. Additionally, silencers are fitted to the exhaust port of each manual valve. Figure 4.8 displays the system set out in a lab environement, with the same numbering as Figure 4.7.

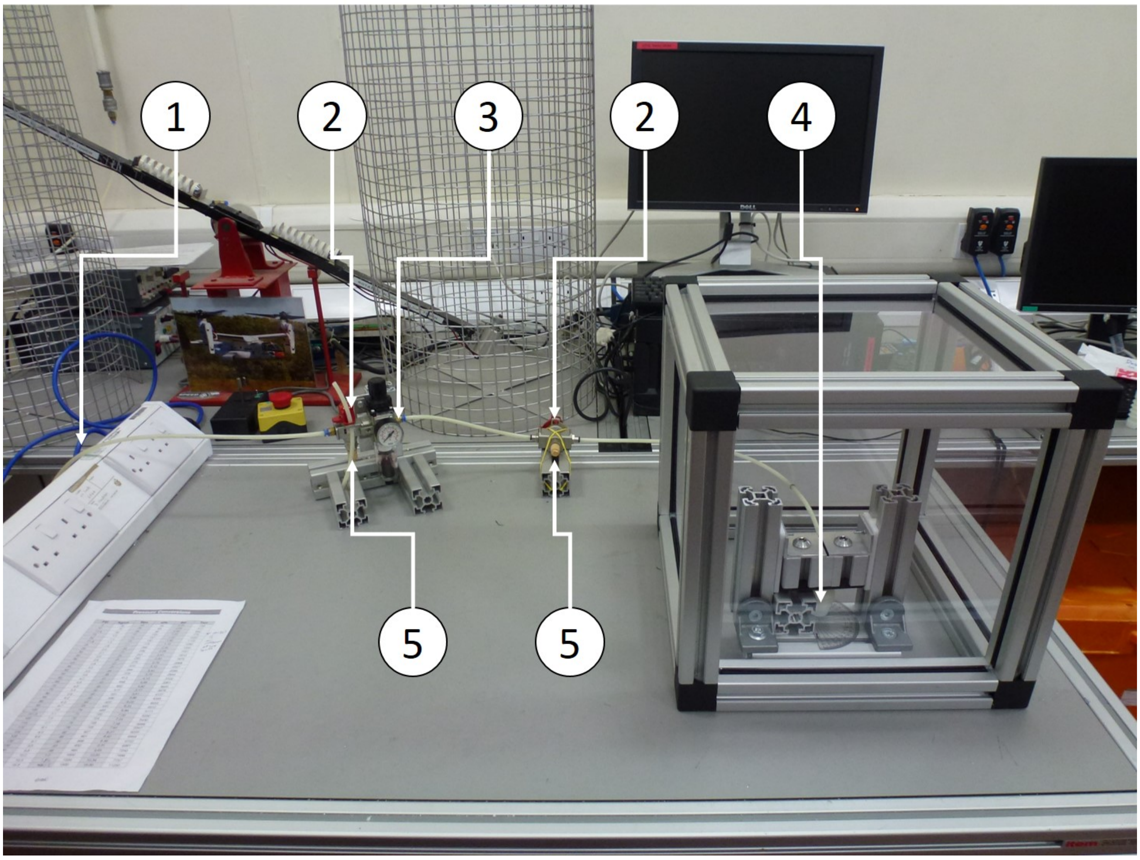

Figure 4.8: Pneumatic system for bellow testing.

As can be seen from Figure 4.8, the main point that catches the eye is the large box that surrounds the bellow. This can be seen in more detail in Figure 4.9. This case was made as a safety precaution in case the bellow or connection parts were to fail. To ensure the effectiveness of the safety box, the walls are made from 2mm polycarbonate. There is a light weight (approximately 300g) on sliders located on top of the bellow to provide a small amount of resistance evenly spread across the top surface. The pneumatic supply is fed through the back of bellow in the image, and the the supply line then feeds out through a small hole in the polycarbonate wall.

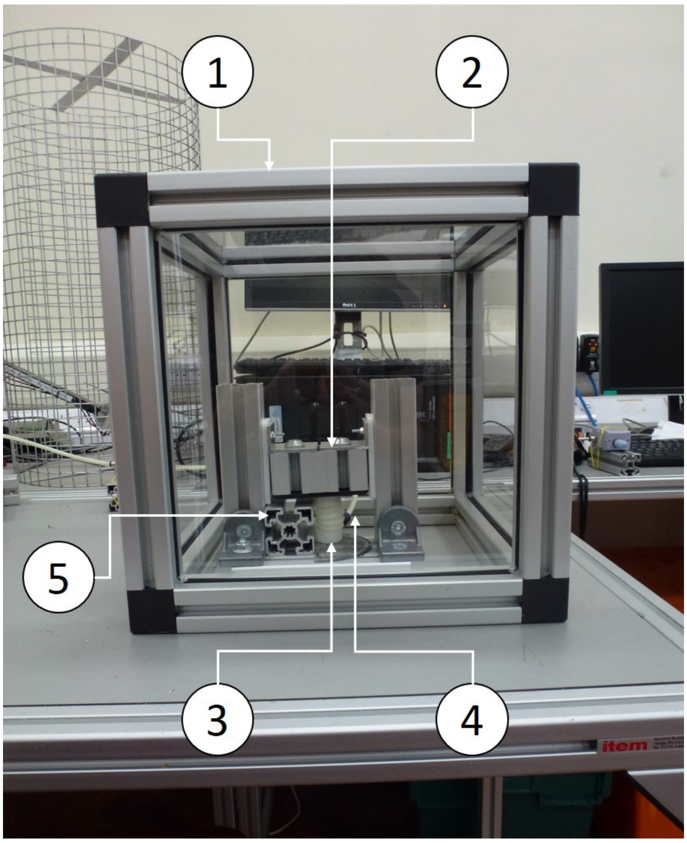

Figure 4.9: Bellow and protective box. (1) Protective box. (2) Sliding weight. (3) 3D printed bellow. (4) Pneumatic supply. (5) Support block to hold weight before test.

4.5.2 Results

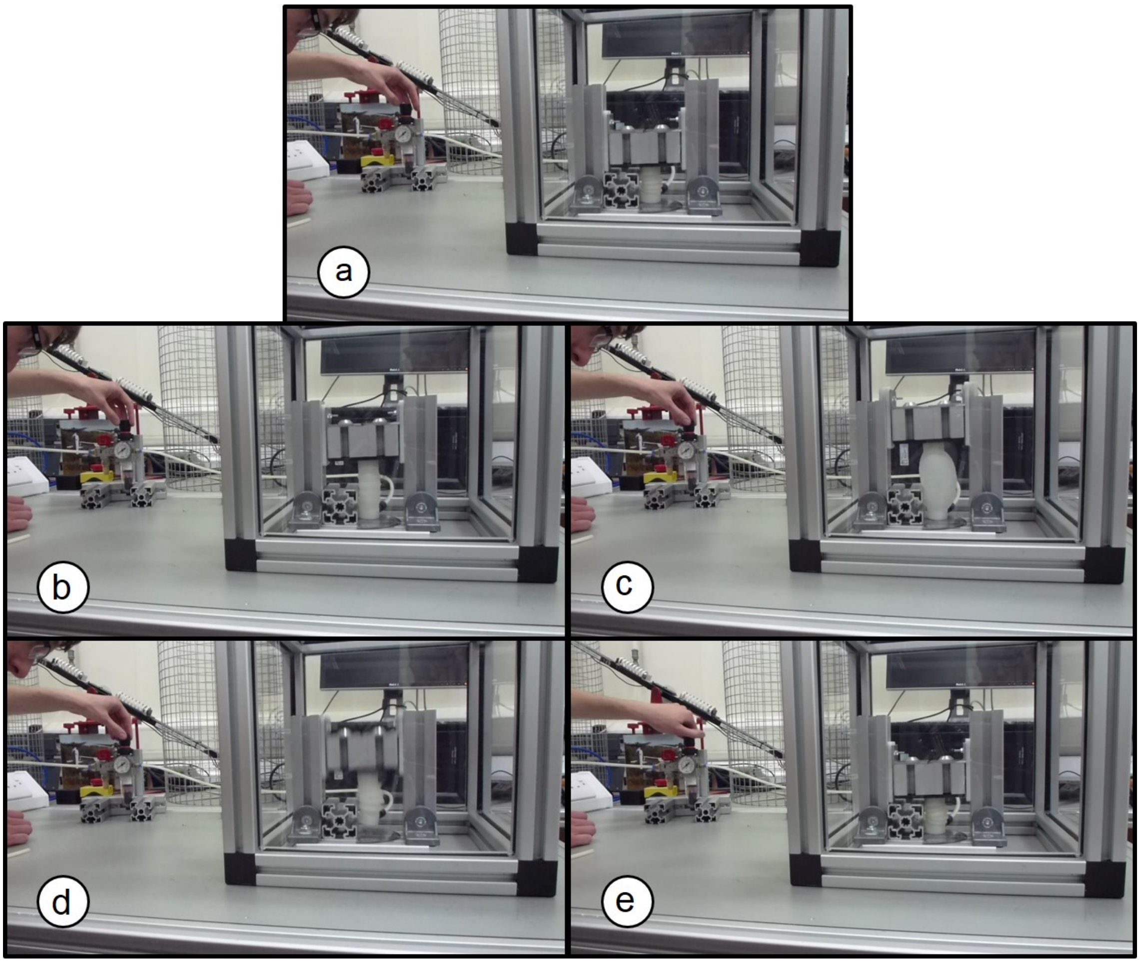

Figure 4.10: Footage of the First Bellow test. (a) Unactuated. (b) Bellow is actuated. (c) Bellow expands further than expected and balloons. (d) Bellow bursts. (e) Bellow can no longer maintain internal pressure and deflates.

Figure 4.10 displays images of the first bellows experiment. As we can see, there are a number of issues with the bellow, the first of which being the failure of the actuator. Figure 4.10(c) shows that the bellow ballooning beyond the limits of the outer strengthening rings, breaking them. Firstly, this indicates that the rubber like material may not be strong enough at 1mm thickness, at least without being supported. This maybe partly due to the inner whorl of the bellow being allowed to expand and nothing to prevent these from expanding further. This may have created additional load on the strengthening rings, causing them to break. Additionally, the bellow expanded further longitudinally as well. The mass used in this experiment was 300g. As there was an additional bellow, the second one was tested with a larger mass of 1.5kg.

Another point that should be noted that in the left of each image, a dial displaying the pressure can be seen. In this experiment, the pressure never read higher than about 100KPa before venting could be heard and the bellow burst. A certain amount of the venting sound will be due to the exhaust on the pressure regulator, but venting from the bellow end cap cannot be ruled out, and may need rectifying in the future.

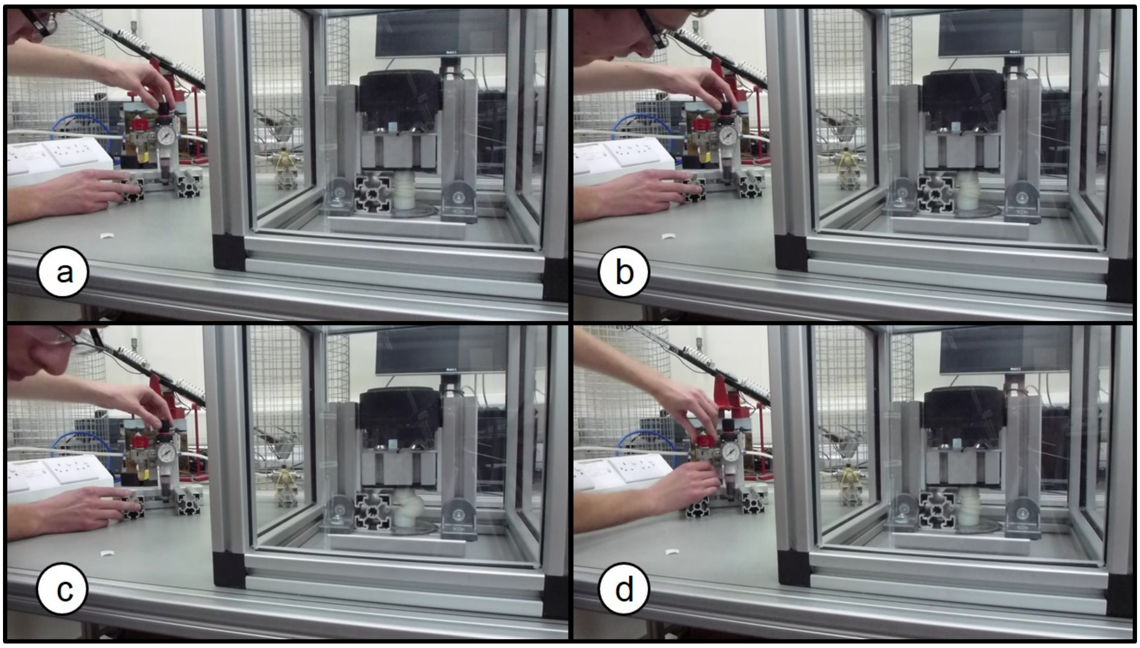

Figure 4.11: Footage of the Second Bellow test (additional weight). (a) Unactuated. (b) Bellow is actuated. (c) Bellow balloons out to side and vents. (d) Bellow is turned off.

Figure 4.11 displays images from footage of the second bellow test. The test was not much more of a success than the first test in that the bellow still failed, though not in the same fashion. When the bellow is actuated, the additional 1.5kg prevents the bellow from expanding longitudinally but expands out to one side. This also occurs in the omni-tread robots [39]. However, on examination it was found that the bellow had still split under the internal pressure, which was very similar to the previous test.

It is also noticeable in Figure 4.11 (c) that the bellow, when actuated, buckles to the side. While this is not ideal, it should not prevent the bellow from actuating successfully, and can be seen in Omni-tread when sustaining a straight body while spanning a gap [39].

4.6 Discussion

This chapter saw the process of designing a 3D printed pneumatic bellow. This went through a number of stages of modifying to try and reduce potential flaws. These were then printed and tested to discover the viability of using such a device. This section will analyse the different stages of this process and discuss positive and negative points, as well as improvements.

Firstly, we look at the design process of the bellows. Chapter 3.3.1 presented a number of potential bellow layout options for use in hypermobile robots. There were also two different sized bellows that were proposed for these. The larger of these was 25mm at its widest and 15mm at its narrowest and could extend 42mm. All of the bellows produced acheived the maximum internal diameter 25mm and minimum internal diameter of 15mm, which theoretically means the 3D printed bellows should be able to produce the required amount of force. While the range of the bellow was measured (albeit by compressing and stretching the bellow by hand) at 33mm, increasing the distance it can stretch could be achieved by increasing the number of whorls.

One of the main issues that was identified during the development of the bellow prototypes was a particular flaw with the manufacturing process of multi-material 3D printing. At this point, 3D printing of this type requires the use of support material and in hollow components, a method of removing the support material must be applied. While a port was needed to be present for the pneumatic supply, it was not large enough to remove all the support material. Therefore a port on top was required to remove the material, with a push fit cap would seal the hole afterwards. This push fit was tight, though there was no guarantee that it was air tight. Test results were also inconclusive as to whether the end caps provided an air tight seal. This could be tested further for by submerging the device in water and watching for air leakage when actuated. This potential issue could be resolved by using O-rings within the design in future. As multi-material printing is being used for this actuator, the O-ring could feasibly be printed into the cap design. Additionally, since the production of these bellows, water soluble support materials have been developed. This means the support material could potentially drain out of the pneumatic port, removing the need for an end cap.

As we saw from Chapter 4.5.2, the bellows failed to be actuate safely and ballooned outwards when actuated. This was supposed to be prevented by the strengthening rings on the outer whorls of the bellows. This was not effective for potentially a number of reasons. Firstly, the original idea was that the strengthening rings would prevent the bellow from expanding further than the outer whorl diameter, whilst the inner whorl was free to expand to that point. In this situation, the inner whorl kept expanding as there wasn't any structure to resist it, and the strengthening rings were not strong enough to resist the expansion. This could be prevented by having a method of retaining the bellows range of movement, preventing it from expanding past a given diameter. The omni-tread series tried this with OT-8, where a mesh was used to prevent ballooning [41].

As well as ballooning outwards, the bellows expanded much further longitudinally than expected, despite being at a seemingly low pressure. However, the intended length was calculated without consideration to the rubber bellows expanding upward. With the bellows inner whorl being designed to stretch outwards, the capability for the bellow wall to stretch longitudinally should have been predicted. This over-stretching may be resolved by using a stronger convolute wall (whether by increasing the wall thickness or by mixing the rubber-like material with a 3D printed plastic). However this will make the bellows stiffer and potentially less efficient. It should also be considered that, when located within a Wormbot module, mechanical constraints may limit this additional extension.

4.7 Conclusion

The aim of this chapter was to explore the viability of 3D printed pneumatic bellows. It was found that, whilst they can be produced, the designs used required a relatively large amount of improvement. This included a method of preventing ballooning and using a much tougher structure or material for the convolutes. Additionally, improving or removing the support material removal port could improve the efficiency.

Additionally, there are other issues with bellows actuation that were not resolved. For example, it is still unknown how to quantify the amount of compliance in the bellow and how much is present in the bellows created for this project.

The 3D printed bellows that have been described in this chapter have still got a lot of development before they can be proved to be effective. After this they would need to be characterised as well to fully understand their performance. As has been outlined in Chapter 3, developing a SEE to compare will allow for direct comparison in performance. However, it would be beneficial to know what sort of performance would be appropriate for a compliant actuator being used in the next Wormbot. Therefore, the next step will be to develop a system for simulating how Wormbot would perform in different environments with varying levels of compliance.

Chapter 5

Development and Implementation of Simulated Testing

5.1 Introduction

As was discussed at the end of the Chapter 4 focus is to be turned to testing and developing a motor-based compliant attachment. One of the advantages of producing a component like this is there is the potential to control the level of compliance, depending on its design. However, it is unknown how compliant a joint in this type of robot should be, or even if different tasks require varying levels of compliance. This could be explored with the use of virtual environment simulations, situating a virtual Wormbot in a range of tests to explore the effectiveness of softer or stiffer joint compliance.

This chapter will describe the process of using simulation software to establish ideal spring constant values for the joints of Wormbot. First, a selection of simulation software will be discussed and compared, one of which will be chosen for further use. After this, the implementation of Wormbot into the virtual environment will be described, as well as the selection of the tests. The results of each of the tests will then finally be displayed and discussed.

5.2 Software Selection

The first task in hand is to identify suitable software for performing all necessary tasks. There are a number of facets that would be required to accurately simulate how Wormbot would behave in a range of environments. The first of these is the ability to build a virtual Wormbot. This would rely on a few different features. The need for compatibility with self-made CAD models is a necessity, and as the Wormbot parts would ideally be made in SolidWorks, compatibility with SolidWorks parts would be preferable. Additionally, for a Wormbot where the compliance of joints will be experimented with, it must be possible within the software to produce customizable sprung joints. Furthermore, it must be possible to have control over material properties, to ensure the properties of the shell of the robot and environment are as they would be in a laboratory situation. If these were incorrect, the resultant performance may result in either a Wormbot that did not move at all or undulated on the spot without any forward momentum.

Another area that is very important for testing Wormbot is the environment in which it will be situated. It is important that the physics engine is able to create realistic collision reactions so the performance of the sprung joints is as accurate as possible. Additionally, the need to produce custom environments is a necessity to the project, as one of the goals is to produce a wide range of test arenas and find how different sprung joint cope with the various challenges.

While it is important that the physical properties of the simulation are as accurate as possible, it is equally vital that the simulated robot moves exactly as Wormbot intended. There must be a way of implementing the control system from prior work on Wormbot into the simulation. As this was originally made in LabVIEW, ideally this method of programming would be able to implement in the simulations, though it is not imperative.

Finally, while this is not a pre-requisite, it would be advantageous if the program used was relatively user-friendly, allowing for many tests to be set up quickly and efficiently. A list of all the criteria is displayed below in Table 5.1.

Table 5.1: List of Simulation Software Specifications

Area	Specification	Essential?
Robot	Can import CAD models	X
	Compatible with SolidWorks	
	Ability to make sprung joints	X
	Controllable material properties	X
Environment	Realistic collision dynamics	X
	Customizable environments	X
Movement Implementation	Method of implementing control algorithm	X
	Compatible with LabVIEW	
Program Performance	User friendly	

5.2.1 LabVIEW Robotics

The first piece of software analysed is “LabVIEW Robotics 2014” [11]. This system works by initially loading up a environment from a small range of pre-made examples (including an open space, a road and an abandoned building). Extra objects, pre-made robots and sensors can then be added after. Using the “Robot Simulation Model Builder”, custom robotics can be developed, as shown in Figure 5.1, where an example Wormbot has been produced. This was achieved by importing CAD models (produced in SolidWorks) and then assigning simple physical models to the model, as well as wheels and motors for each joint.

As well as motorised joints, virtual robots built in the model builder can include springs, which can be defined by a spring constant and a damping constant among other factors such as range limits. However, there are two factors that are hard to define. These are called “fudge factor” and “bounce”, [10]. These properties indicate a certain level of inaccuracy within the software, bringing the reliability of performance accuracy into question. These properties are also present in the motor components.

As can be seen in Figure 5.2, the environments that are provided display a good selection of challenges for testing Wormbot. As can be seen in the bottom left of the image, the material type can be defined. Unfortunately a pre-made arena can only be assigned one material, which allows for little variety. Additional objects may be added to each arena and these may have different materials but this is not much of an improvement. There is a limited number of materials to select from while custom ones can be made, defining the friction of coefficient is unclear [12].

An advantage of using this software is, as it is an add on for LabVIEW, the original *C.elegans* algorithm code can be employed in Robotics 2014. Additionally, LabVIEW Robotics 2014 does not require too much additional learning from the standard LabVIEW package and is relatively well presented and easy to navigate.

5.2.2 V-REP

V-REP is a robotics simulation package from coppelia Robotics [4]. In V-rep, a blank test environment is presented in which objects, landscapes and robots can be added, similarly to LabVIEW. Robots can be built in the environment by importing CAD files and assigning physical meshes to the body. However, unlike LabVIEW, V-rep can fit a mesh

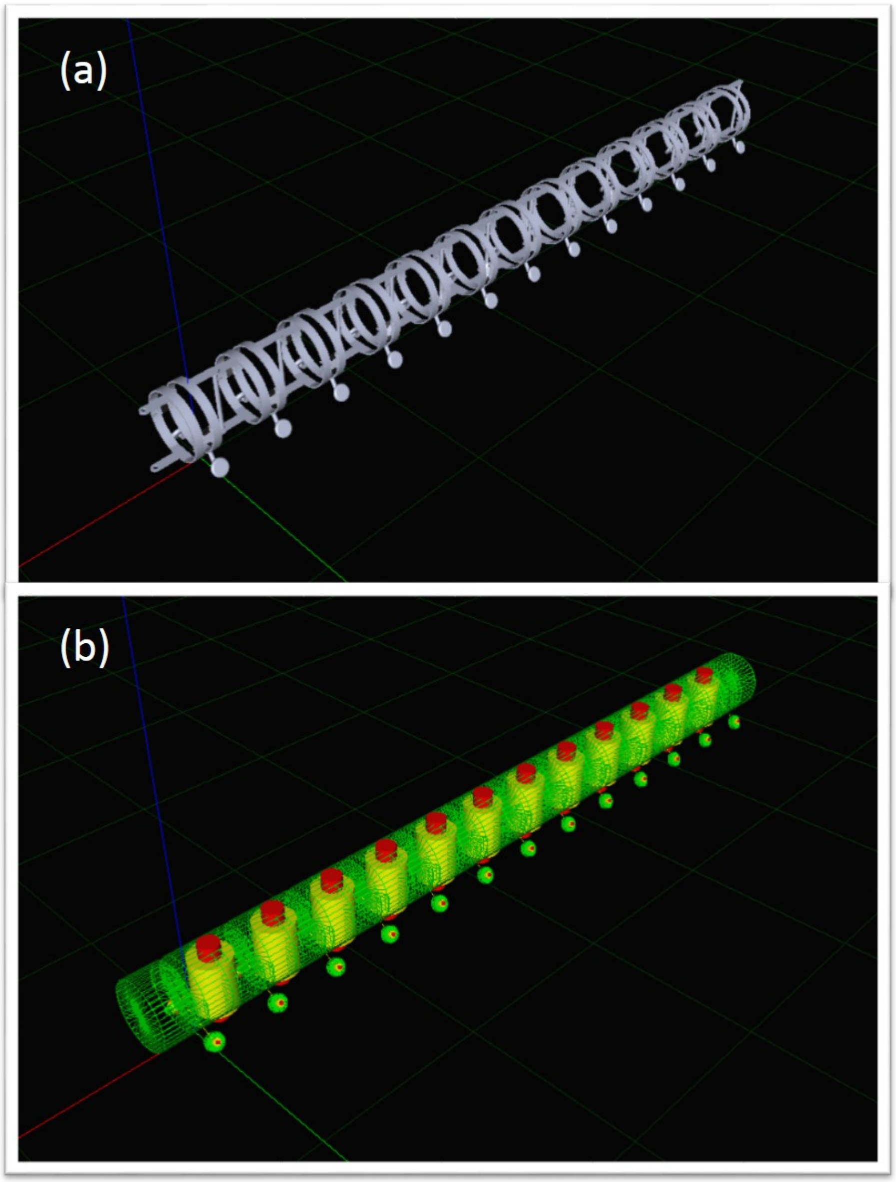

Figure 5.1: (a) Visible model of LabVIEW Wormbot, produced from SolidWorks CAD components. (b) Physical model of LabVIEW Wormbot. Green lines display physical model boundaries, red and yellow cylinders display joints and motors.

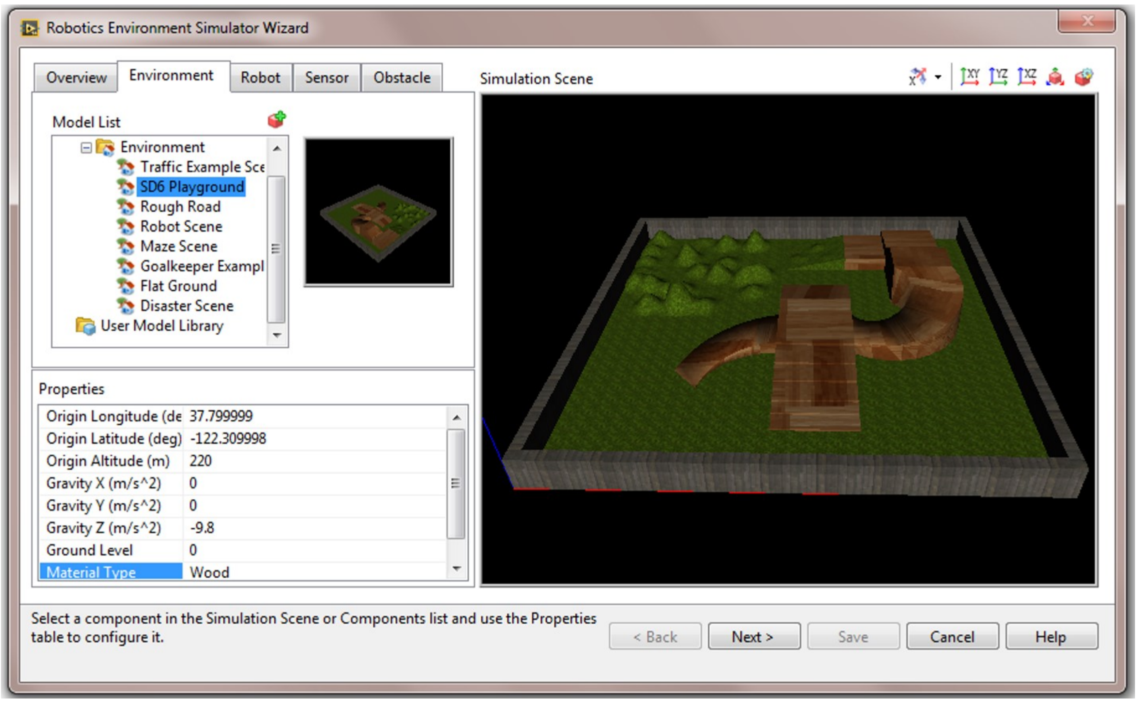

Origin Longitude (de	37.799999
Origin Latitude (deg)	-122.309998
Origin Altitude (m)	220
Gravity X (m/s^2)	0
Gravity Y (m/s^2)	0
Gravity Z (m/s^2)	-9.8
Ground Level	0
Material Type	Wood

Select a component in the Simulation Scene or Components list and use the Properties table to configure it.

Figure 5.2: Menu for creating a test environment in LabView Robotics 2014.

to a part to achieve the most accurate response, though more complicated shapes result in potentially slower running simulations.

Producing sprung joints is similar again to LabVIEW in that a sprung joint can be defined by a spring constant and a damping constant. Using the Newton physics engine that is available in V-rep, the “fudge factor” and “bounce” attributes that were a problem in LabVIEW are not present.

Another positive point for V-REP is the range of materials that can be employed in the software. Producing custom materials is possible, allowing control over static and dynamic friction coefficients as well as other characteristics. The way the friction coefficients are achieved is each material is given a coefficient value. When two materials come into contact, the coefficients are multiplied together to achieve the overall system value. To test the reliability of this, a slope test has been devised to test the validity of the software. This is displayed in Figure 5.3. In this, three blocks of different friction coefficients (static and dynamic coefficients are set equally) are placed on a conveyor feeding them on to a 25° at 0.5 ms^{-1}. The time is then measured for the blocks to reach the bottom of the slope. This time is then compared to the arithmetically found predicted time. These are shown in Table 5.2.

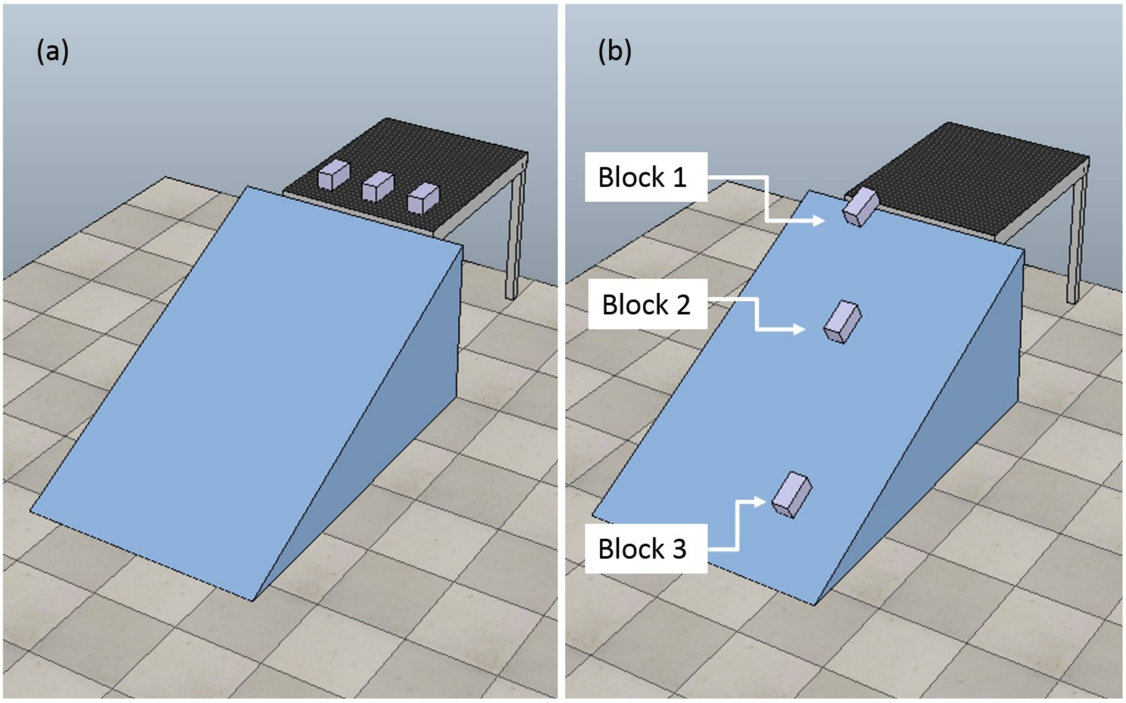

Figure 5.3: (a) Beginning of V-REP test for friction coefficients. (b) V-REP test for friction coefficients in progress.

Table 5.2: Friction Coefficient Validity Test

Block Number	Friction Coefficient (slope)	Friction Coefficient (block)	Friction Coefficient (overall)	Time (theoretical)	Time (V-REP)
1	0.41	1.5	0.615	Invalid (not enough force)	Invalid (not enough force)
2	0.41	1	0.41	1.23	1.23
3	0.41	0.5	0.205	2.17	2.21

As can be seen, the arithmetic and simulation times are very similar. The slight difference in times for block 3 maybe down to the time being taken by hand, pausing the simulation (running slower then real-time) and reading the time on screen when required. This could be improved in the future by recording displacement against time within the program. However, these results display that material properties can be reliably controlled in V-REP. However it was found that the simulation times were more accurate when the time step used is smaller. This was also found for the accuracy of collisions. The downside of this is that the experiments run slower than real time, though this in itself is not essential.

V-REP does not have a wide range of pre made environments. The approach in this software is to start with a blank, 5m x 5m platform. This can be increased or decreased as required. On top of this, there are a number of library components that are available to place within the environment, from terrain mounds to household furniture. As discussed earlier, CAD models can also be imported and simple shapes can be created. This displays the versatility of V-REP to be able to create a wide range of tests and environments for any robot to be simulated in.

Unfortunately, V-REP is not compatible with LabVIEW, which means that the original control code cannot be used, although efforts have been made by a separate company [3]. The main method of operating simulations in this software is through the use of Lua; a programming language based on C. To operate Wormbot, the control code would need to be converted to this different language, though it is a relatively simple programming language so this would not be an large task.

5.2.3 Comparison

Table 5.3 displays a direct comparison between the two simulation packages analysed in this chapter. The main point that seems to be noticeable is that both programs can achieve the essentials of what is required, but for our purposes V-REP performs a number of tasks to a more suitable level. For example, the sprung joints required for Wormbot can be created in LabVIEW Robotics but there are questions over the reliability of some of the joint properties. V-rep appears to have a more reliable physics engine in the Newton engine. The same can be said for control of material properties, as well as arguably collision detection, with greater control over physical models and meshes.

Table 5.3: Comparison of Simulation Software

Ability	LabVIEW Robotics	V-REP
Import CAD Models	Yes	Yes
Solidworks Compatable	Yes, by saving as WRL	Yes, by saving as STL
Sprung Joints	Yes, but physics engine has unclear parameters	Yes, if Newton engine is used
Material Property Control	Yes, but physics engine has unclear parameters	Yes
Accurate Collisions	Yes, simple physical shapes can be linked to visible models	Yes, physical shapes and meshes can be mapped to visible models. More accurate at higher frequency
Customizable Environment	Yes	Yes
LabVIEW Compatable	Yes	Yes, though not through coppelia made package
User Friendliness	Yes if familiar if LabVIEW	Yes

The main area where LabVIEW maintains an advantage over V-rep for our purposes is that the original Wormbot LabVIEW code can be used in conjunction with the simulation package. This can be achieved in V-rep but with a program add on, whereas the amount of time required to adapt the LabVIEW code to be used in V-REP would be relatively short. Therefore, V-rep will be used for producing simulation experiments for Wormbot with varying levels of sprung joints.

5.3 Implementation of Wormbot

5.3.1 SolidWorks Segment

In this section, the implementation of a new Wormbot into the simulation environment will be discussed. Figure 5.4 displays a SolidWorks model of a segment of the simulation Wormbot. The segment is 80mm in diameter and 80mm in length from joint to joint. This to match the segment size used in Chapter 4 and to maintain the same aspect ratio as *C.elegans* and the original Wormbot (though half size) as described in Chapter 3.

The design of the segment involves two structural ribs with longer arms on the top and bottom to extend to the joints between segments. This frame has been designed to allow for ±64.01° between segments so that, while it may not be achieved, the maximum joint

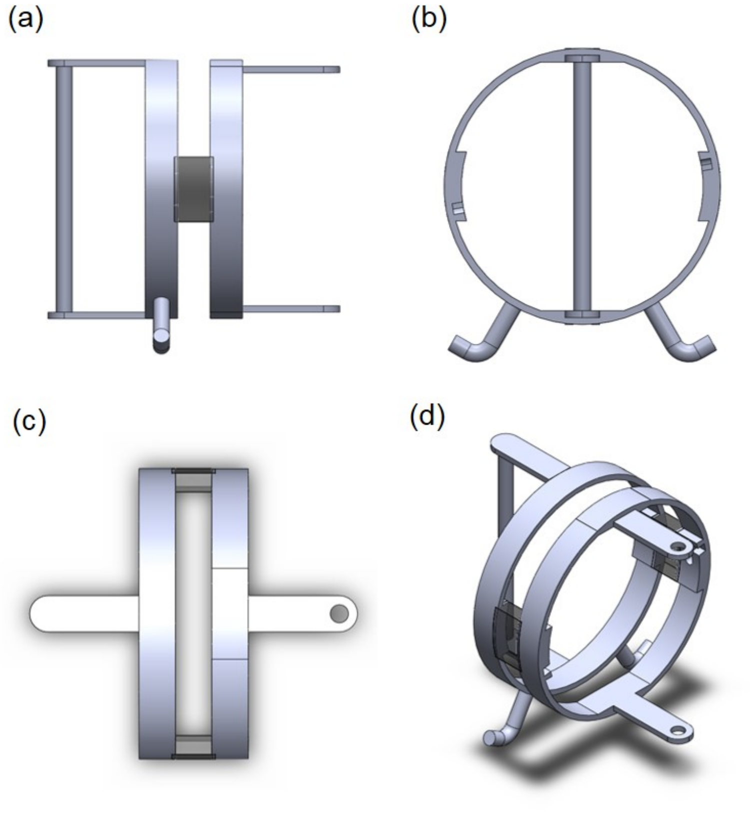

Figure 5.4: Solidworks model of a new Wormbot segment. (a) Side View (b) End View (c) Top View (d) Isometric View

rotation of ± 45° mentioned in Chapter 3 can at least be achieved.

The next point of note is the legs on the segments. These are intended to support the wheels of the robot. It was noted in Chapter 2 that the wheels are the original Wormbot stood too proud of the body. The design presented does not solve this issue, but the role of this chapter is not primarily to solve this issue. Therefore this is not essential at this stage while the compliance is the main issue. However, one potential design feature for Wormbot in the future can be seen most clearly in Figure 5.4a and d. There is a translucent block between the ribs. It was thought that, if the segment were to be 3D printed, these small blocks could be made of a rubber-like material, potentially allowing for a passive vertical degree of freedom, which could be useful in travelling over inclines. However, for the purposes of this simulation, these will be solid.

5.3.2 Importing CAD Segment to VREP

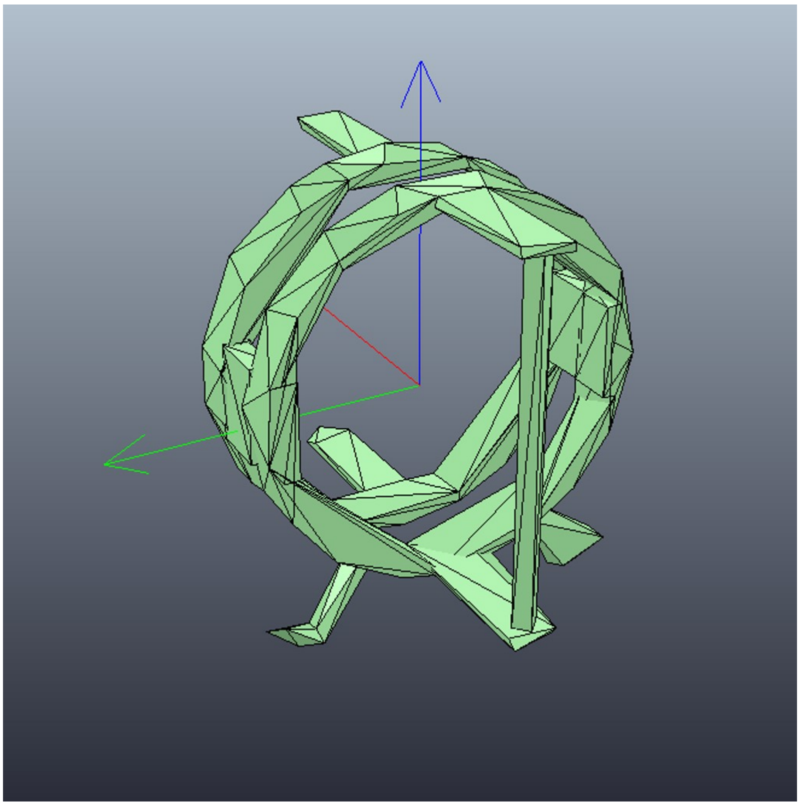

Figure 5.5: Physical model of Wormbot segment when imported into V-REP

Figure 5.5 shows the SolidWorks segment after it has been moved to V-rep and mapped as a physical model, capable of collisions. As can be seen, the model created in V-REP is not a perfect representation of the shape, as it is mapped to reduce the complexity of the part. This is most notable on the wheel supports, where on one side it does not resemble the original shape intended. This would potentially cause problems when trying to mount wheels upon them. This was solved adapting collision details. In V-REP, an object can be set to collide with all objects, with only some objects or even no objects at all. When assembled, the wheels of a single segment and the adjoining segments are set to not collide with the segment in question. This allows movement between adjacent segments to be purely controlled by motor and spring input, and allows the wheels to rotate freely. The final product of this is displayed in Figure 5.6 and 5.7.

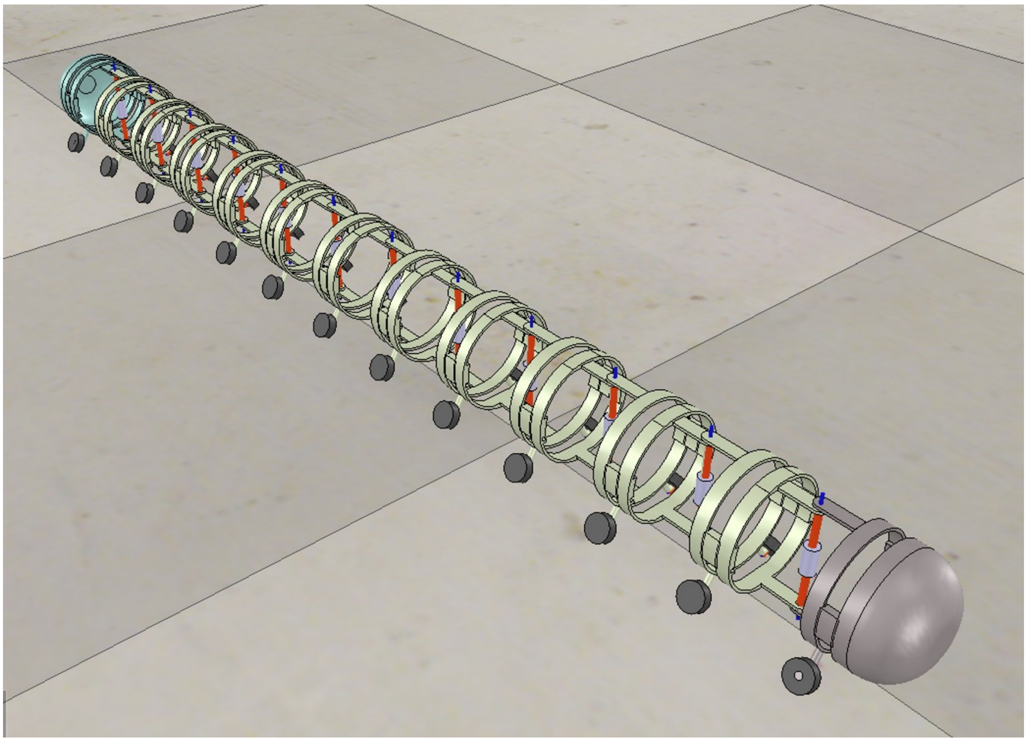

Figure 5.6: Assembled Wormbot in V-REP Simulation Package

The main aspect of the Wormbot simulation is the construction of the joints. This was achieved by using two joints at each segment intersection. The first of these joints is a motorised joint. For this motor, we have assumed the properties of a suitable servo motor. This motor is a Dynamixel AX-18A [5]. As it is, the AX-18A's range of 300° is a lot more than required, as in Chapter 2 the potential joint range of ±45°. However, if a 3:1 geared system was used, this could be reduced to a range of 100°, with the advantage

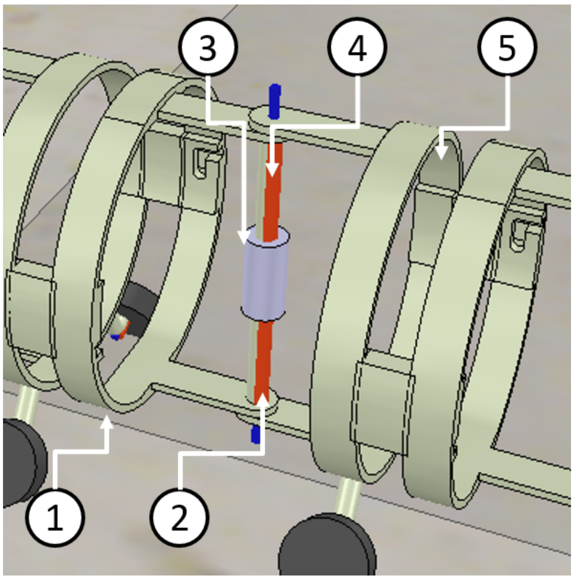

Figure 5.7: Detailed image of Wormbot joint in V-REP. (1) Module 1. (2) Motor. (3) Motor-Sprint Connection Element. (4) Spring. (5) Module 2. Motor and Spring both displayed with orange and blue cylinders. Connection Element required to join Motor and Spring together.

of increasing the torque output. Therefore, the torque output increases from 1.7658Nm (18kg.cm as defined in citation) to 5.3Nm. After this gear ratio, the output speed is 194°/s under no load.

The next part of the joint is the spring component, which is positioned between the motor and the second Wormbot segment. This implies that the spring is acting in series with the actuator as required. In V-REP, two joints cannot be directly connected together, so a spacer component is added between the two that will not collide with any other components or environment. The spring constant (k) of the spring component of the joint can be altered in each experiment, with the aim being to find whether stiffer or softer springs are better suited to particular joints.

The weight of each module in the simulation version is set to 460g. This is an estimation from looking at a number of components that could be suitable when Wormbot is built. The Dynamixel AX-18A previously discussed weighs about 55g, an 11.1V, 1350mAh LiPo Battery from E-flite weighs 114g and, assuming the 3:1 ratio mentioned earlier is upheld, a standard, 36 tooth steel gear weighs about 60g [1, 5, 7]. These three together weight around 230g. While these are the main internal components in each segment, there will also be the weight of the framework, wheels, micro controller (if one is needed for each module), as well as any other components that may be used. While it may be difficult to predict the added weight of these, for the sake of the simulation we will assume the weight is double the known component weight, 460g.

5.4 Selection and Implementation of Tests

Now that the virtual Wormbot has been produced, environments must be developed to test the performance parameters of the robot with varying stiffnesses of spring. There will be five different environments, falling into three different categories, to test the varying performance parameters of Wormbot.

5.4.1 Open Environment Testing

The first environment for simulation testing is a open environment, as seen in Figure 5.8. This is a completely open, 25 metre square. The idea behind this test is to allow the robot to move freely in an environment with no obstacles to analyse the movement speed and direction. The original Wormbot used passive roller blade wheels. These usually made from polyurethane, with Shore A hardness of around 80 [14]. Bringing these into the simulations, the friction coefficient between the wheels and the floor will be 0.65, which is about the same Shore A 80 against steel [2]. This will be maintained throughout all simulations.

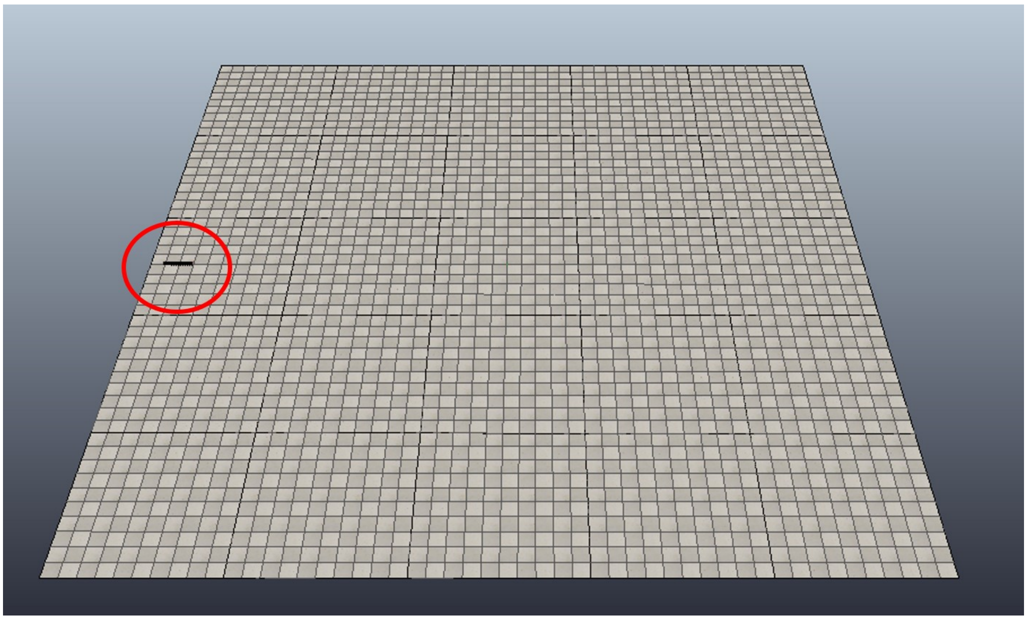

Figure 5.8: Virtual Wormbot in open environment. Wormbot highlighted in red circle.

This simulation will be performed with a wide range of spring constants. These will be k= 5, 10, 15, 20, 25, 30, 35, 40, 80 and infinity (no compliance) Nm/°. The range of 5 to 40 will provide a broad range to find the effects of spring stiffness in tests, with 80 also used to analyse what change in performance a vastly stiffer spring would produce. The use of no spring will also be analysed to act as a indicator to the importance of having compliant elements in such a robot, by providing one with no compliance at all.

From this experiment, the x and y co-ordinates of the head and tail modules will be recorded over the time of the experiment. From this, the robot speed can be determined and the effect of joint complance on this can be analysed. Additionally, angle and torque readings for joints 1, 6 and 12 will be recorded, as these will inform how the system behaves at both ends and the centre of Wormbot. This will provide an insight into how much effect the springs will have on peformance, as well as if sprung elements work more or less depending on their position in the robot.

5.4.2 Constrained Environment Testing

The second type of area is intended to constrain the movement range of the robot, analysing how well the robot can comply to the environment. The first of these is a straight taper, consisting of a pair of walls that get progressively closer, to find how constrained Wormbot can be while still maintaining forward movement, and can be seen in Figure 5.9. This taper is 20m long and reduces from 1m wide to 0m. The friction coefficient between the body of the robot and the tapered wall is kept very low (below 0.03), so the robot's progress is not stopped by friction with the wall, but by the constriction of the body. This will be true of all simulations featuring additional objects.

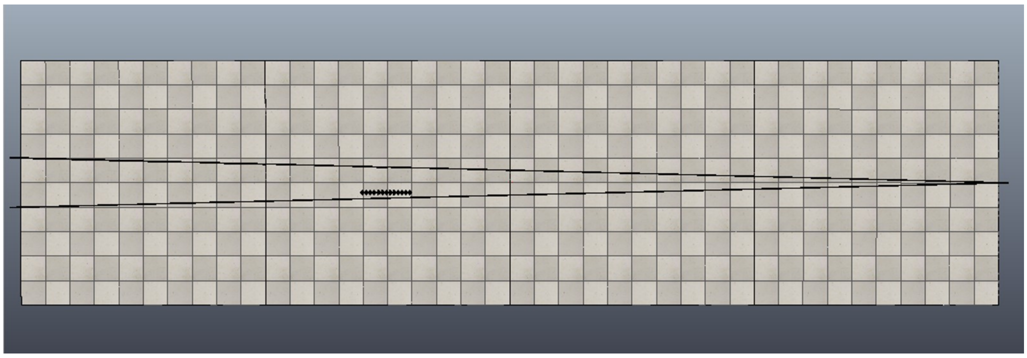

Figure 5.9: Virtual Wormbot in tapered environment

The second test is similar, there are straight channel sections to see if the robot is more efficient when it is is able to maintain a constant amplitude and not being increasingly constrained. This is displayed in Figure 5.10. Each straight segment is long enough for 1 body length. The width of these starts at 0.275m and reduces by 0.025m each time down to 0.15m.

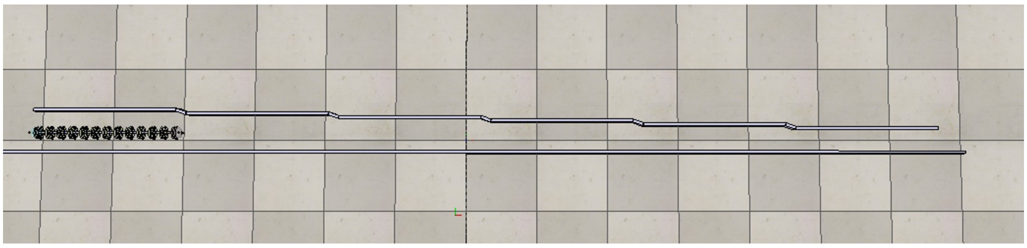

Figure 5.10: Virtual Wormbot in staggered environment

Once again, as in all the simulations forthcoming, the same spring constants will be applied to the simulation as were used in the open test. However, each spring constant will be tested three times, with the robot starting in slightly different positions. This is because the robot could potentially hit an obstacle at different angles and perform differently as a result. It is important to perform the test multiple times to make sure a potentially unique response isn't viewed as being typical. Ideally, one could repeat the tests more times to achieve a better understanding of how Wormbot will behave in different situations, though due to time constraints this was limited to three tests. This however does allow for enough information to understand the variance in performance for each set of parameters.

It is thought that knowing the trajectory of the robot in these two experiments will not be of much use as the robot will be confined in its movement. However, this will give us the maximum distance travelled, which in turn will provide the width at which forward momentum is no longer achievable. Additionally, joint torque and angle will also be analysed to see if spring deflection or stiffness effects the ability to navigate tighter areas.

5.4.3 Maze Environment Testing

The last area of testing is very similar to the testing of the original Wormbot by Boyle [28]. In this, Wormbot was entered into a maze like obstacle course, where a 3x3 grid of cylinders was set up and Wormbot had to navigate the obstacles. The aspect ratio of these cylinders will remain the same (one body width of Wormbot) but the mazes will be remade on a larger scale. Instead of a 3x3 grid, 20x20 grids will be used to provide a more complete test. Additionally, two tests will be performed. The first layout will feature spaces between each adjacent cylinder of 0.16m, as can be seen in Figure 5.11. This is twice the width of the simulated Wormbot.

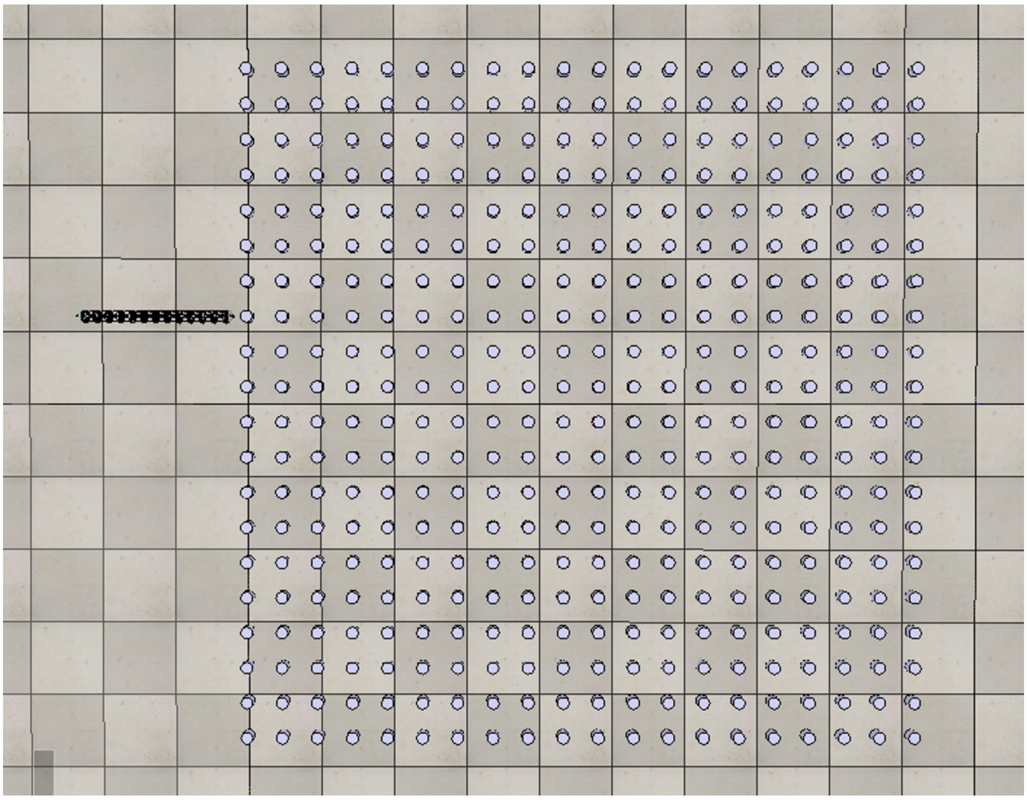

Figure 5.11: Virtual Wormbot in large maze environment

In the second layout, seen in Figure 5.12 this spacing will be reduced to 0.12m, 1.5 times the width of the simulated Wormbot. It is hoped that this experiment may shed light on how effective softer or stiffer compliance are in varying environments, and if there is potential for robot such as Wormbot to be customised for specific tasks.

In these simulations, it will be important to read the position of the head and tail modules against time to identify how quickly the robot can escape the maze. This would be a good indicator as to whether a particular spring is more suited to tighter or more open environments, if there is such a bias in performance.

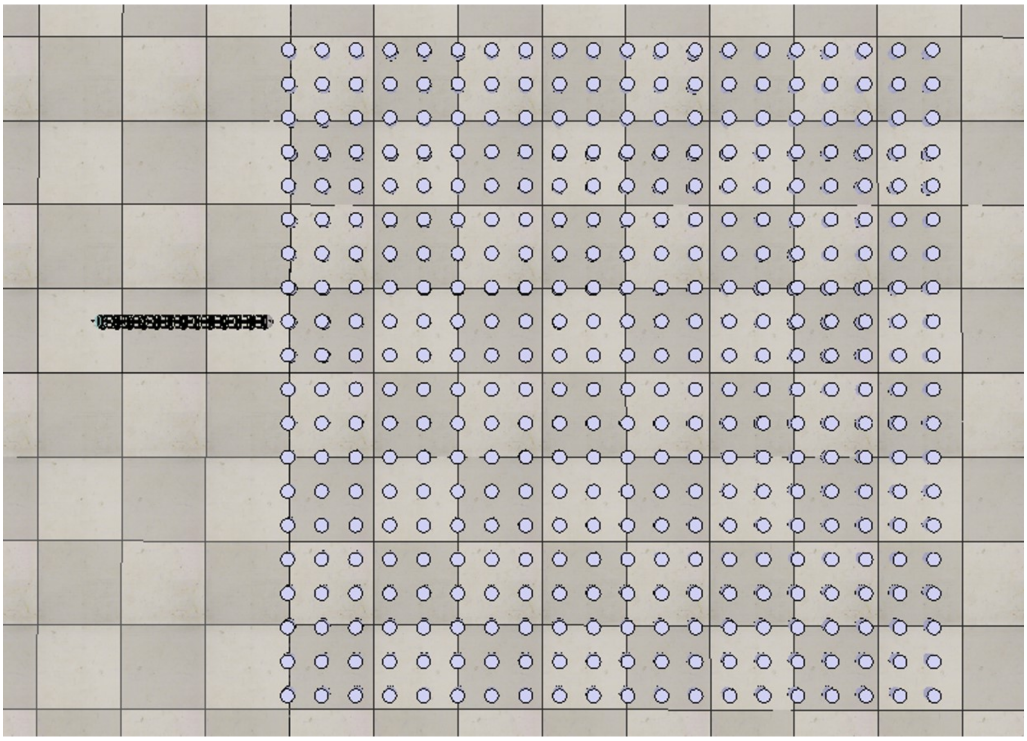

Figure 5.12: Virtual Wormbot in small maze environment

5.5 Results

5.5.1 Open Environment Results

This section displays the results for the open environment tests. For each spring constant, one test is performed, with the virtual Wormbot moving across the test area with no obstacles.

Figures 5.13, 5.14, 5.15 and 5.16 displays the movement of the head and tail module of Wormbot in an open environment at spring constants of 5, 20, 40 and no spring (infinite) respectively. The first point of note is that none of the robots travel in a perfectly straight line. While only four experiments are shown, this is representative of all ten joint spring constants and can be seen in Appendix A (on disc attached).

In these graphs, one of the points of note is the difference in trajectory. It can be seen in Figure 5.13 that the tail module kicks out beyond the path laid out by the head module. As the spring constant increases, this expansive movement reduces, as can be seen in Figure 5.16. This excessive movement in more elastic joins can be seen to have

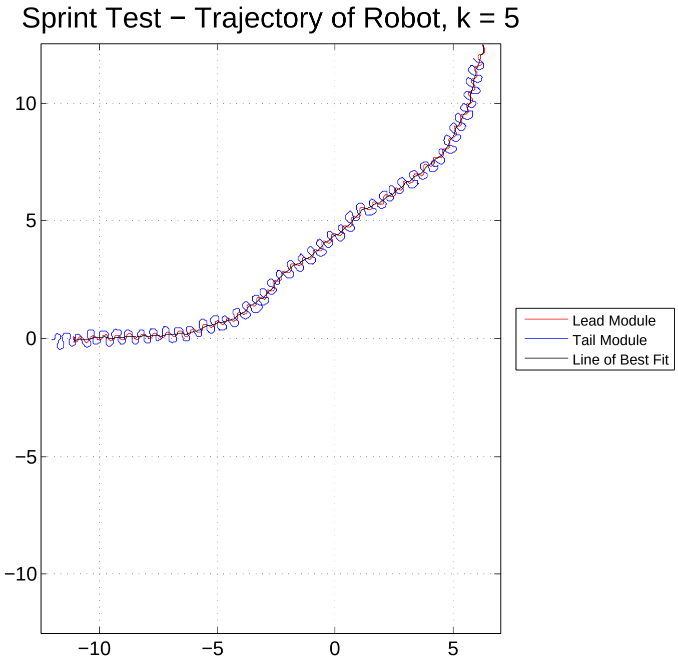

Figure 5.13: Graph displaying trajectory of robot in sprint test when spring constant k = 5.

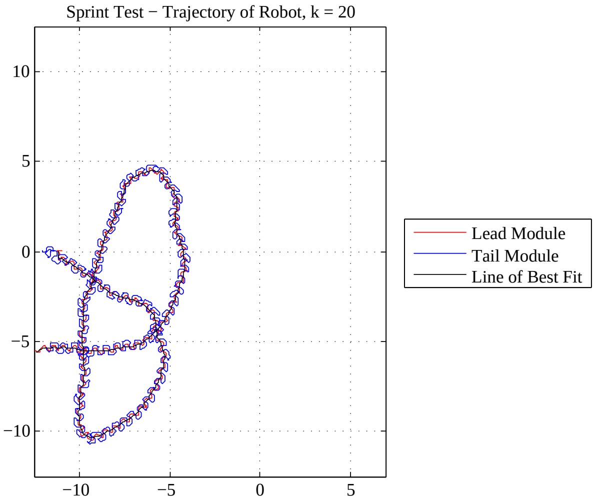

Figure 5.14: Graph displaying trajectory of robot in sprint test when spring constant k = 20.

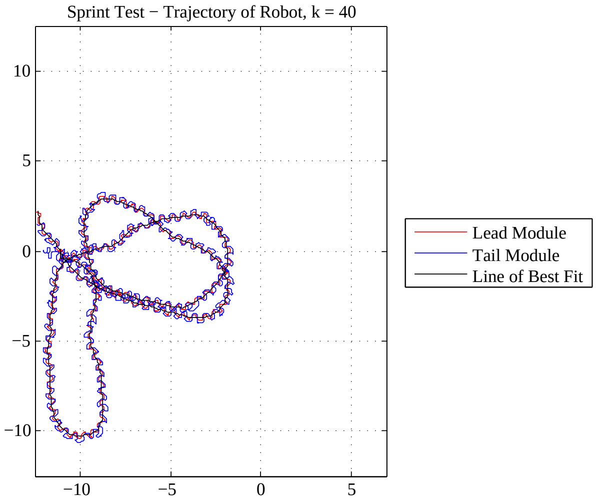

Figure 5.15: Graph displaying trajectory of robot in sprint test when spring constant k = 40.

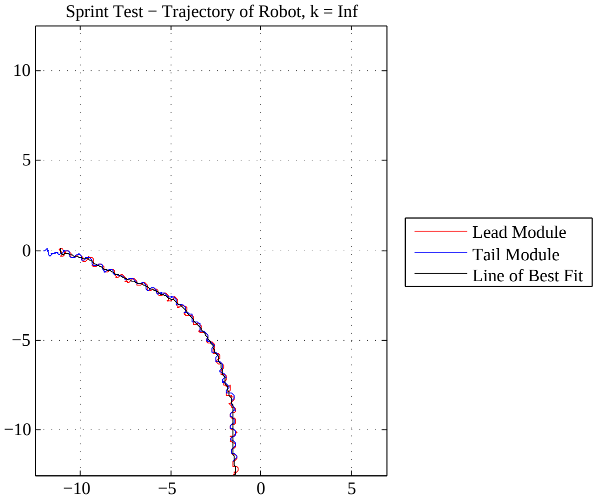

Figure 5.16: Graph displaying trajectory of robot in sprint test when spring constant k = inf.

an effect on the speed of travel in Figure 5.17, where the application of stiffer joints can be seen to result in faster locomotion.

Additionally, it can be seen that when softer springs are implemented, the tail module oscillates much more than the head module. It is assumed that, as this is not an issue when no springs are used, softer springs are not able to counter-act the body motion applied by the body in front of the tail, causing it to overshoot the head modules trajectory.

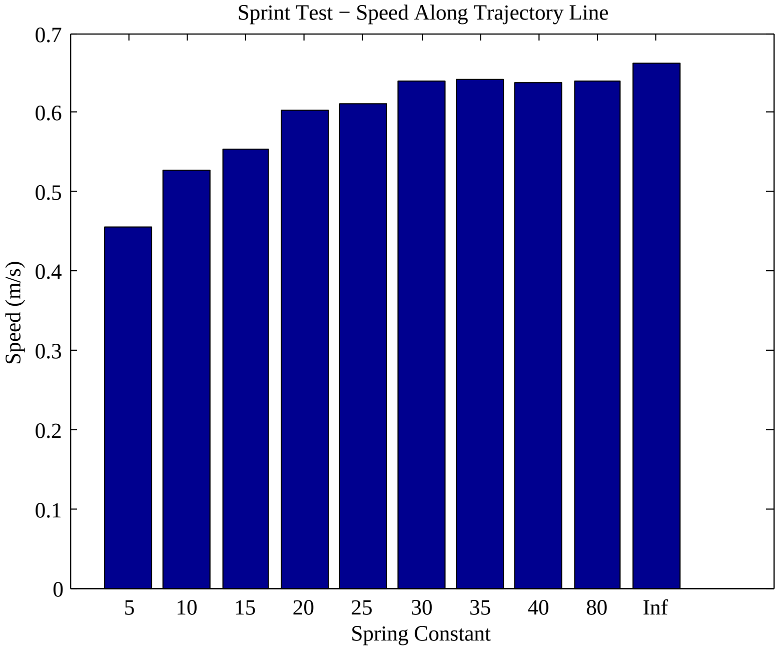

Figure 5.17: Graph displaying speed of robot along trajectory in relation to joint spring constant in sprint test.

We can see from Figure 5.17 that there is a trend of increasing forward speed as the joint springs become stiffer. However this trend appears to level off after around k=30. It should be noted that the speed is found by measuring the the distance of a spline mapping the direction of motion, created using the matlab “csaps” function. This is the divided by the time of travel up to that point.

Next, in Figures 5.18, 5.19 and 5.20, the difference in joint and spring angle deflection across the robot can be observed.

It can be seen in graphs 5.18 and 5.20 that the two end joints deflect as similar amount, with root mean squared (RMS) of spring rotation varying approximately 1.5° (4.34° for

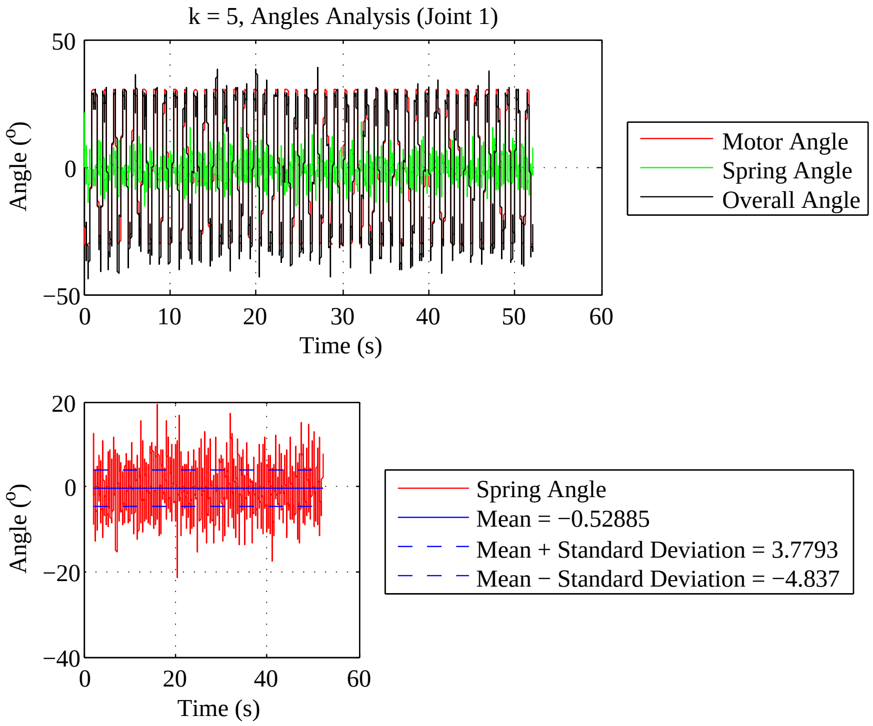

Figure 5.18: Graph displaying angle of first joint in Wormbot when spring constant k = 5 - sprint test.

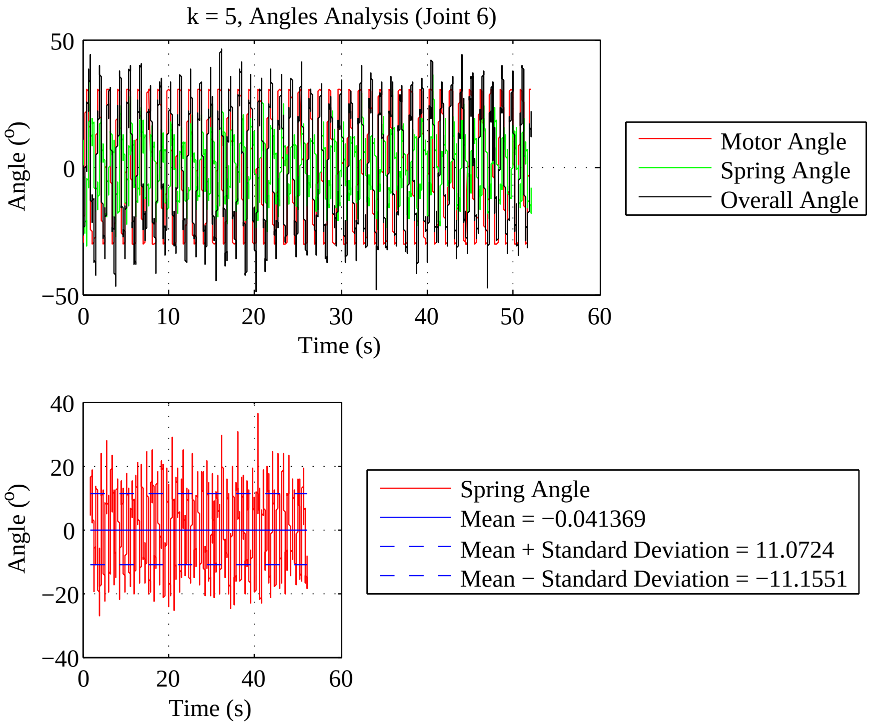

Figure 5.19: Graph displaying angle of sixth joint in Wormbot when spring constant k = 5 - sprint test.

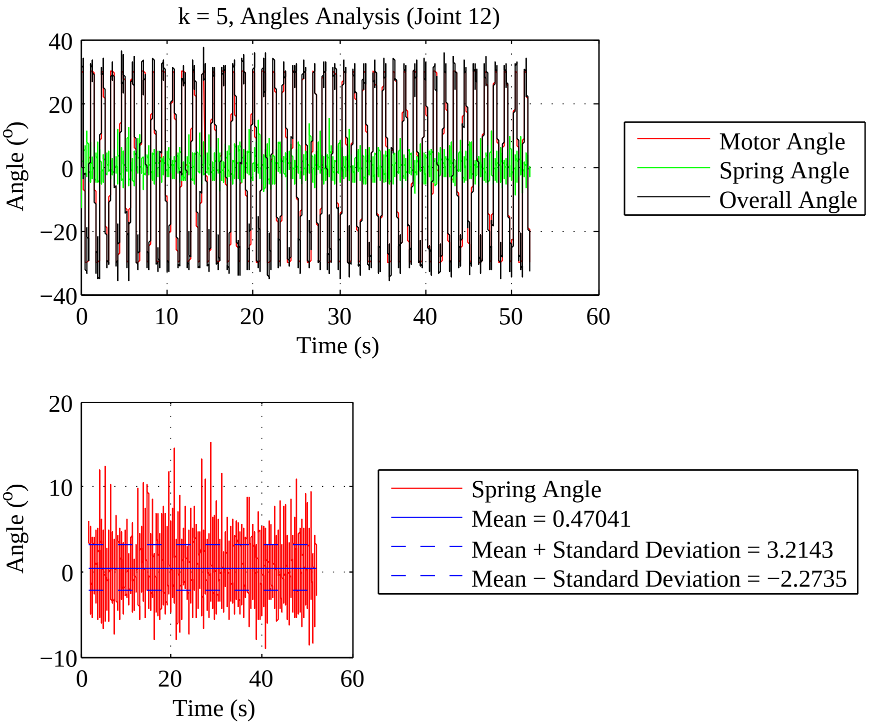

Figure 5.20: Graph displaying angle of twelfth joint in Wormbot when spring constant k = 5 - sprint test.

joint 1 and 2.78° for joint 12). However, Figure 5.19 shows that joint six, located in the middle of the robot, is subject to much higher spring deflections with an RMS value of approximately 11.11°.

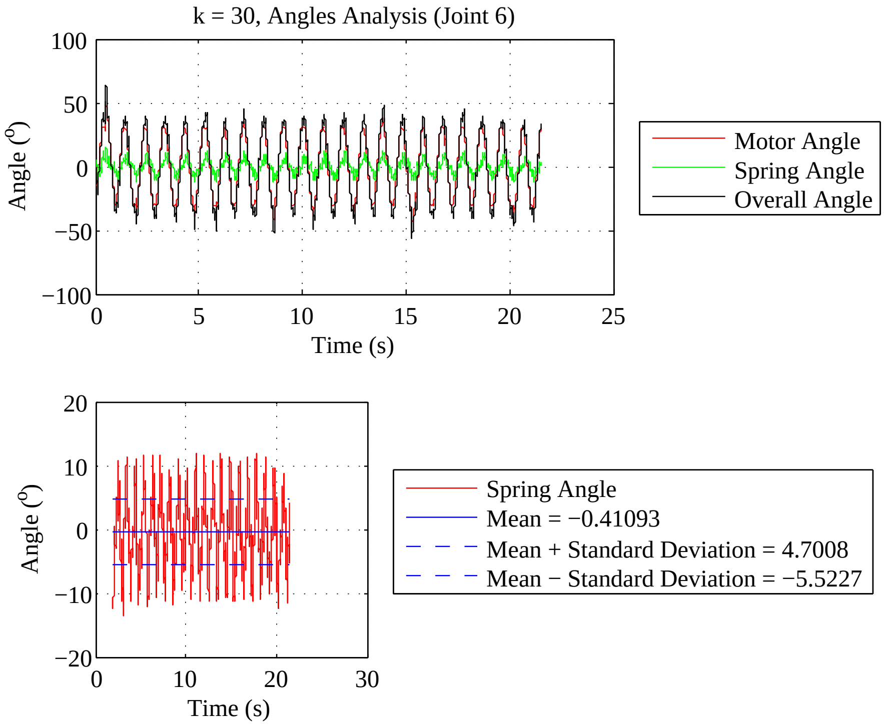

Figure 5.21: Graph displaying angle of sixth joint in Wormbot when spring constant k = 30 - sprint test.

Figure 5.21 displays the joint and spring angles for the sixth joint of Wormbot when it is operating in the open environment when k=30. The RMS of spring movement is a lot less when k=5 as would be expected (5.13° in comparison to 11.11°). One other point that can be noted when comparing Figure 5.21 and Figure 5.19 is that the overall joint output when k=30 appears to occasionally spike beyond what is displayed when k=5.

Figure 5.22 displays the extremes of joint movement in the open environment with the whole range of spring constants. While there doesn't appear to be a strong relationship between the spring constant and the overall joint angle, we can see that there is more joint movement in the middle joint as oppose to the end joints.

Figure 5.23 displays the RMS of spring movement as spring constant increases. This graph also backs up the previous evidence that more deflection occurs in the middle joint

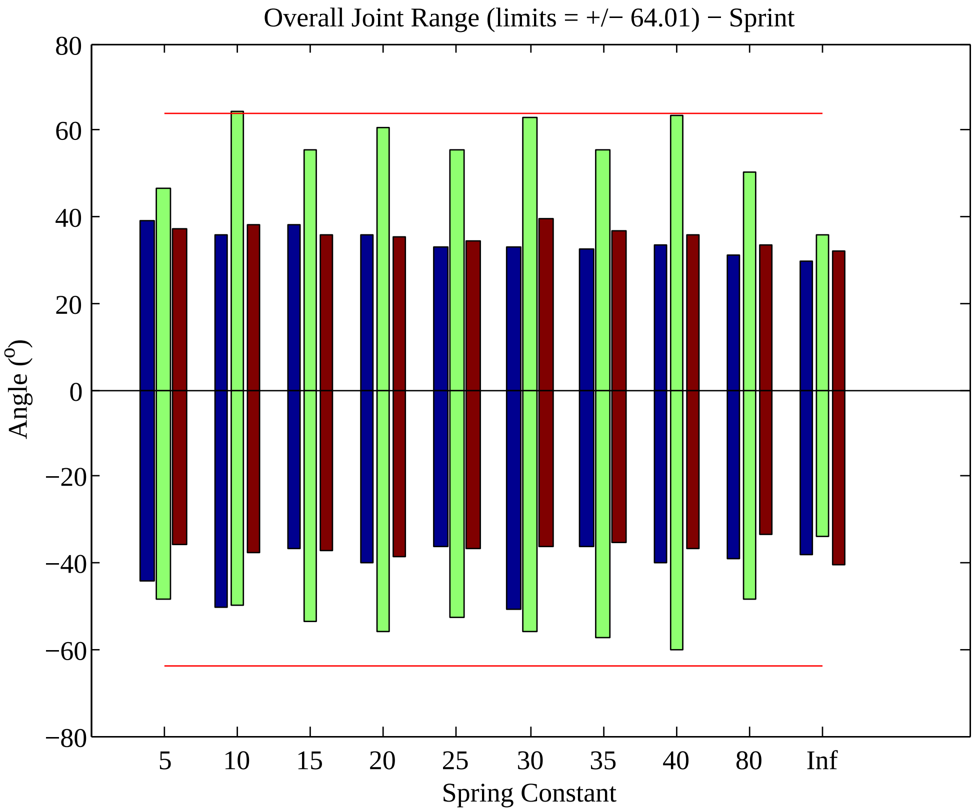

Figure 5.22: Graph displaying the range of joint movement with varying spring constant in sprint test. Blue = joint 1, Green = joint 6, Maroon = joint 12, Red Line = Theoretical limits.

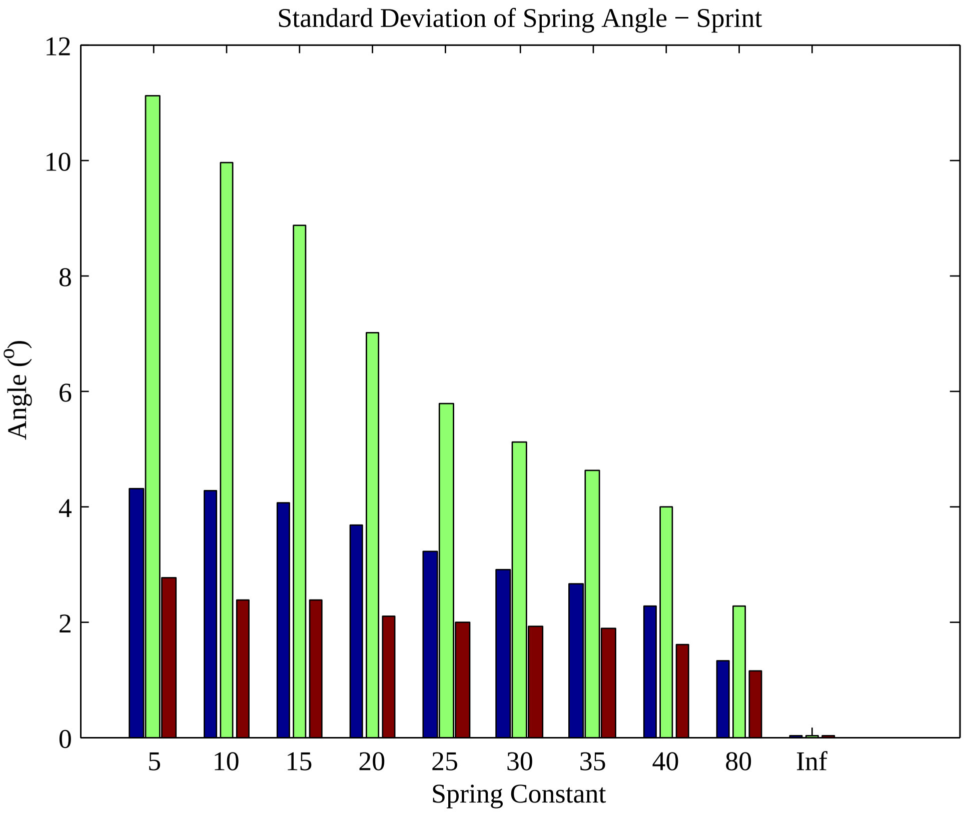

Figure 5.23: Graph displaying the range of spring movement with varying spring constant in sprint test. Blue = joint 1, Green = joint 6, Maroon = joint 12.

of Wormbot, but it can also be seen that there is a negative correlation between spring deflection and increasing spring constant.

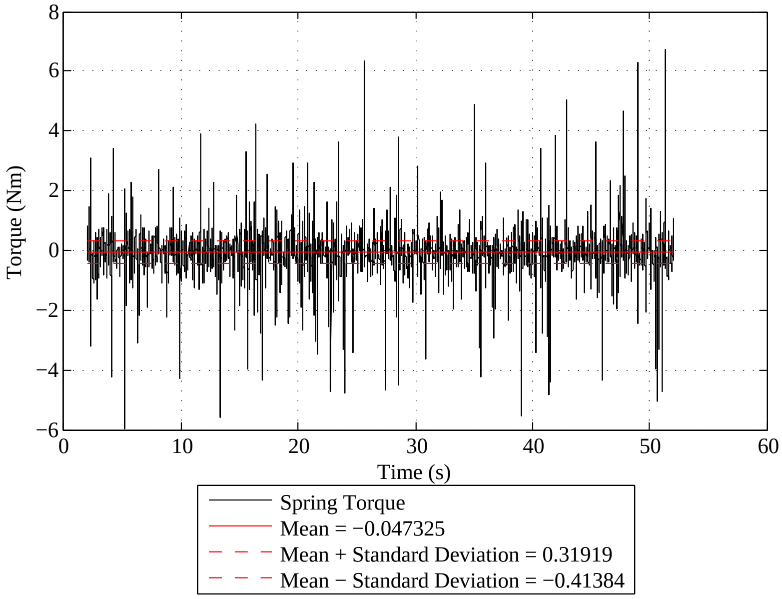

Figure 5.24: Graph displaying torque of first joint in Wormbot when spring constant k = 5 - sprint test.

Figures 5.24, 5.25 and 5.26 display the torque across the springs in joints 1, 6 and 12 respectively. The trend of greater magnitude results occurring in joint 6 is continued here. However, an area of notice is that in each of these graphs there are occasions where the torque readings spike, especially in joint 6. Therefore, Figure 5.27 compares the torque reading to the theoretically calculated torque to see if these are equal, by multiplying the recorded angle with the spring constant.

It can be seen from this graph that, while for the most part the two lines are very similar, the spikes are not present in the calculated torque line, suggesting that this may be some type of error carried across from the simulation software.

Figure 5.28 shows the torque across the springs as the spring constant increases. There is a strong positive correlation between the torque across the spring and the increasing spring constant, an expected result considering the link between spring constant and angle of deflection seen in Figure 5.23.

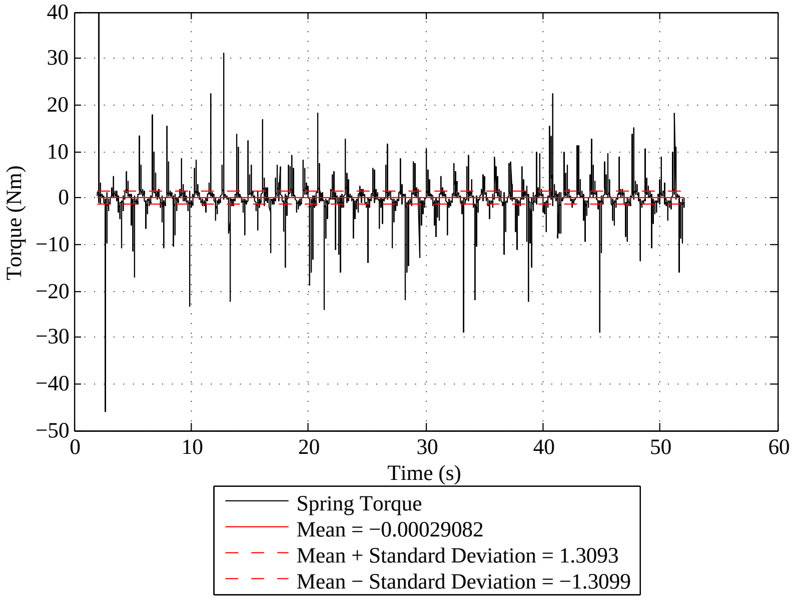

Figure 5.25: Graph displaying torque of sixth joint in Wormbot when spring constant k = 5 - sprint test.

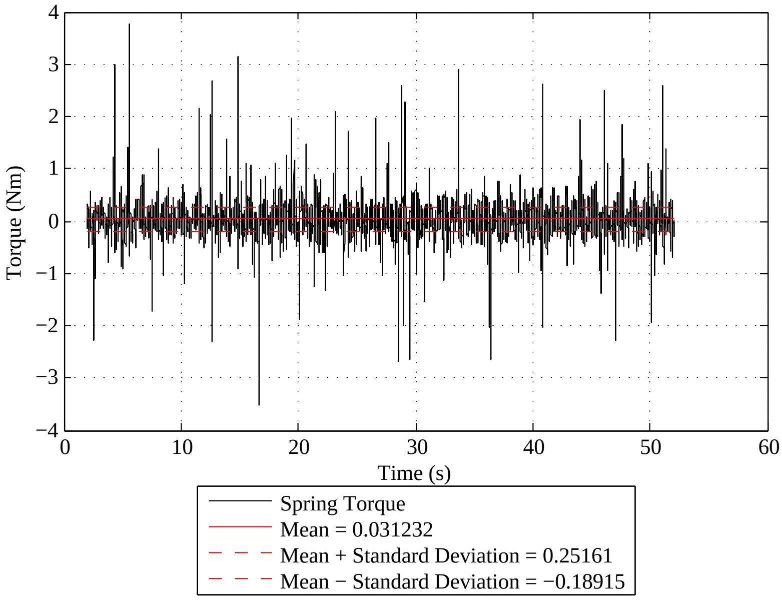

Figure 5.26: Graph displaying torque of twelfth joint in Wormbot when spring constant k = 5 - sprint test.

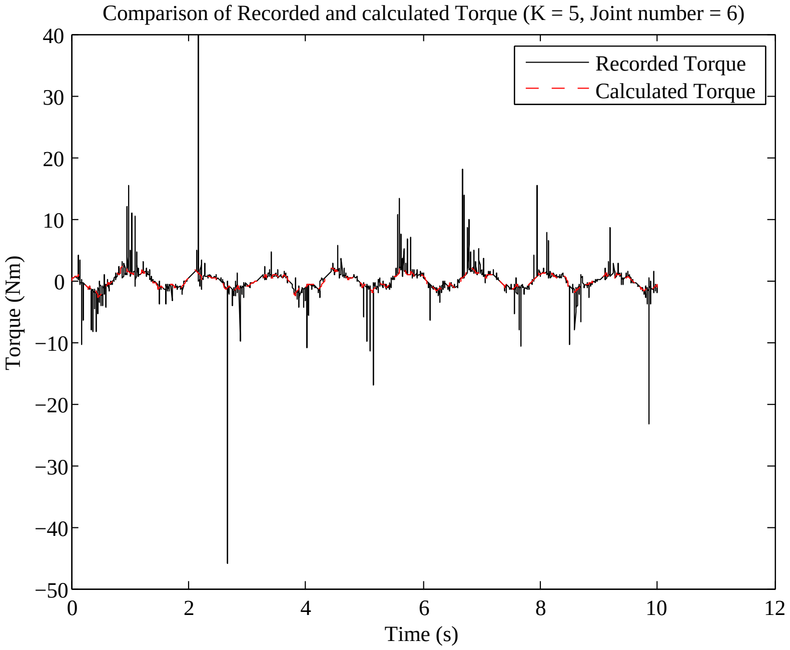

Figure 5.27: Graph displaying comparison between recorded and calculated torque when spring constant k = 5.

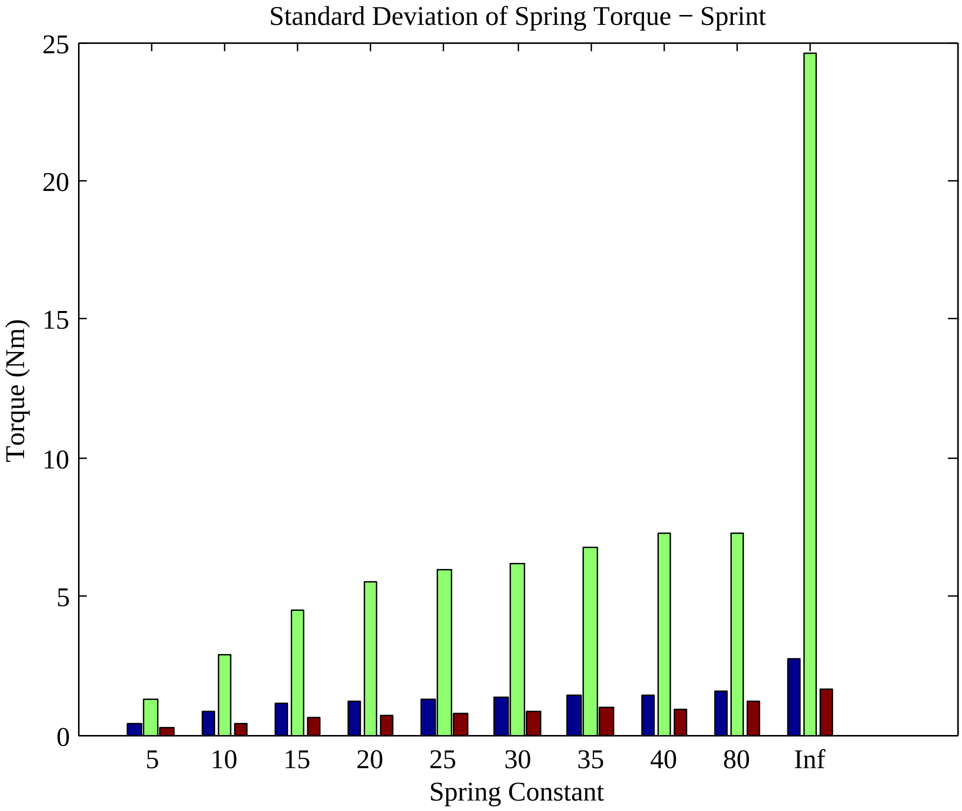

Figure 5.28: Graph displaying torque range with varying spring constant in sprint test. Blue = joint 1, Green = joint 2, Maroon = joint 3.

5.5.2 Constrained Environment Results

This section displays the results for the constrained environment tests. For each spring constant, three tests are performed, with the virtual Wormbot moving down narrowing channels to see how performance is effected by increasing amounts of constraint.

5.5.2.1 Tapered Channel

Figure 5.29 shows the trajectory of the head and tail modules of Wormbot in the tapered environment when k=5. The graphs for the other spring constants are viewable in Appendix A. While it can be seen how constrained the body can be while still moving forward, it would be difficult draw any conclusions from looking at all these in a row. Therefore, Figure 5.30 Shows the mean smallest body amplitude the robot could reach while still travelling. The whisker plots display the range of results across the all 3 tests on each spring constant

In this graph a weak correlation can be seen between the spring constant increasing with the minimum amplitude. However, the mean values of amplitude at k=5 and k=10 don't adhere to this. This indicates that while softer springs allow for more compliance in constrained environments, the results may also be less predictable.

Figure 5.31 shows the spring angle of joint 1 in the tapered environment. It can be seen that on a number of occasions the joint stops moving. However other joints can continue to move to propel the robot.

Figures 5.32 through to 5.37 show the angle range and spring torque across all the spring constants and on each joint recorded. On the whole, most of the previous trends occur in this experiment. The centre joint is loaded with much larger torques and deflections, as well as softer springs are subjected to lower torques.

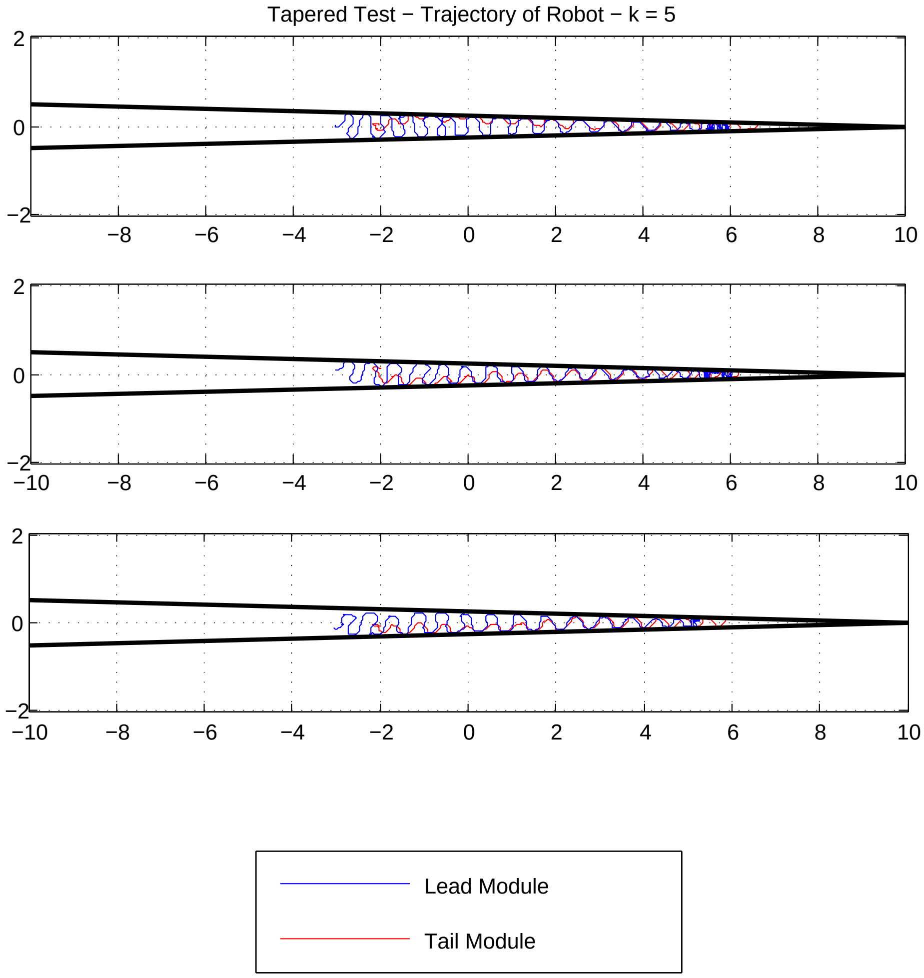

Figure 5.29: Graph displaying trajectory of Wormbot in tapered channel over three tests, where joint spring constant k = 5.

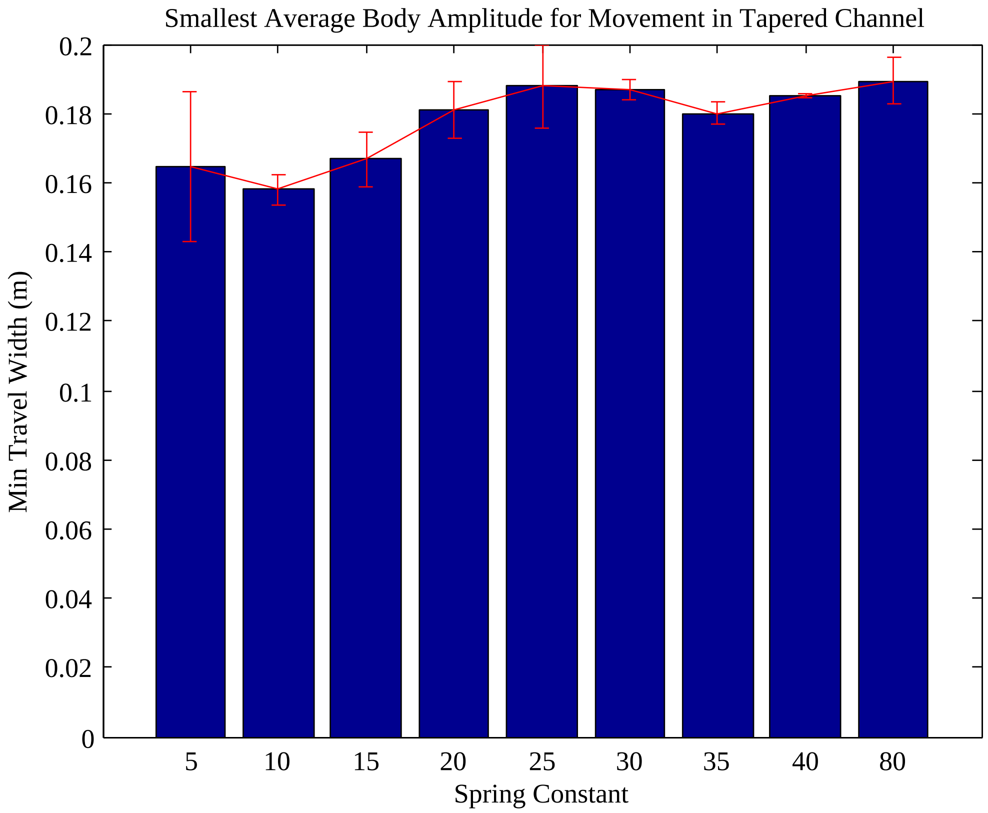

Figure 5.30: Graph displaying average mean narrowest points and reached by Wormbot in tapered channel. Whiskers display range of results

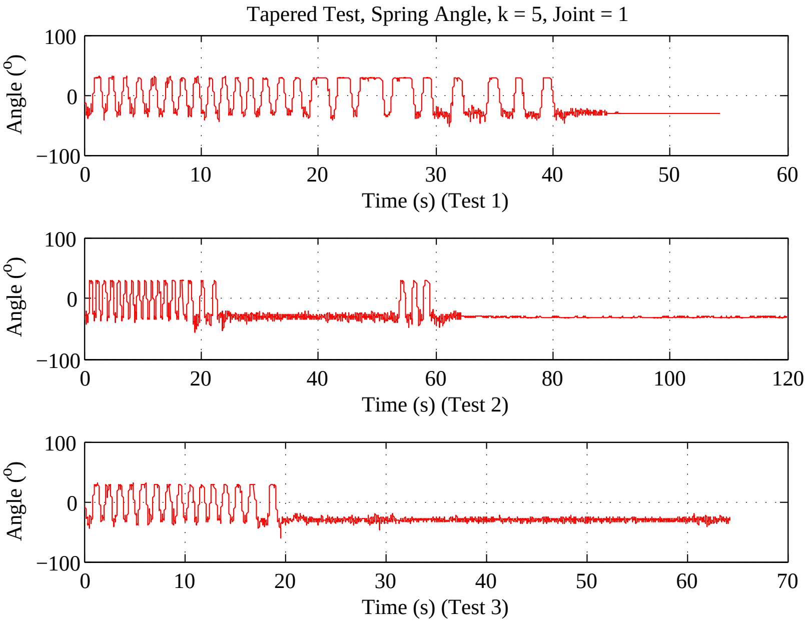

Figure 5.31: Graph displaying spring angle of Wormbot in channel over three tests, where joint spring constant k = 5 and joint number = 1.

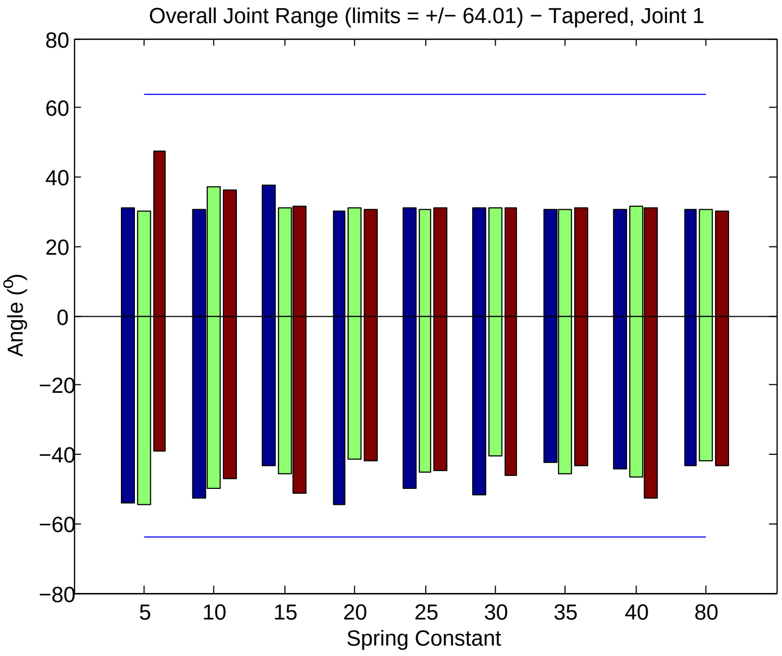

Figure 5.32: Graph displaying maximum displacement of Wormbot Joint 1 in tapered channel. Different colours indicate 3 experiments.

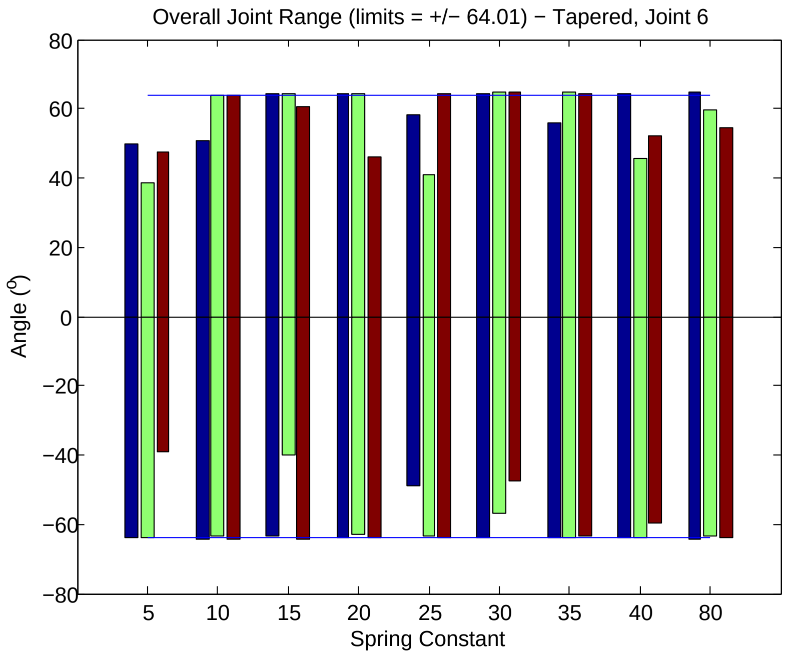

Figure 5.33: Graph displaying maximum displacement of Wormbot Joint 6 in tapered channel. Different colours indicate 3 experiments.

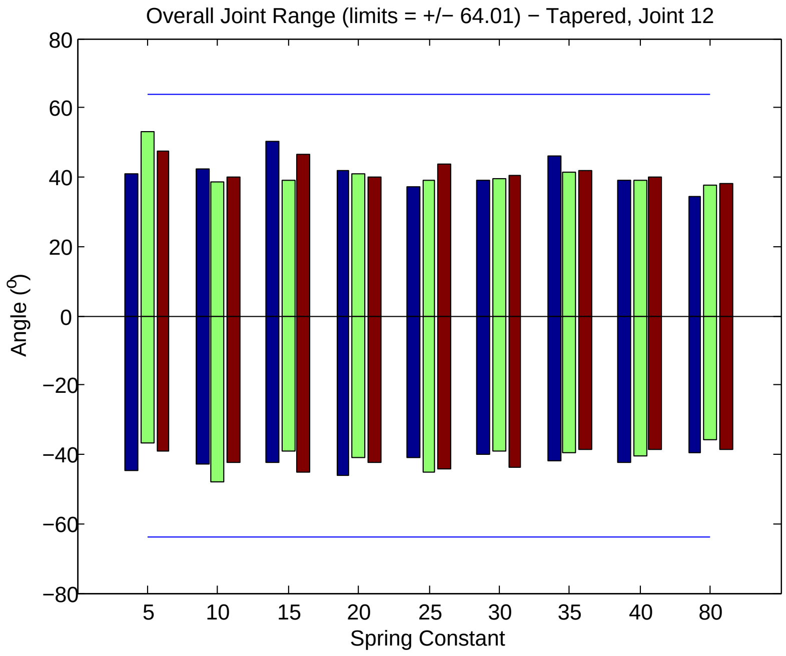

Figure 5.34: Graph displaying maximum displacement of Wormbot Joint 12 in tapered channel. Different colours indicate 3 experiments.

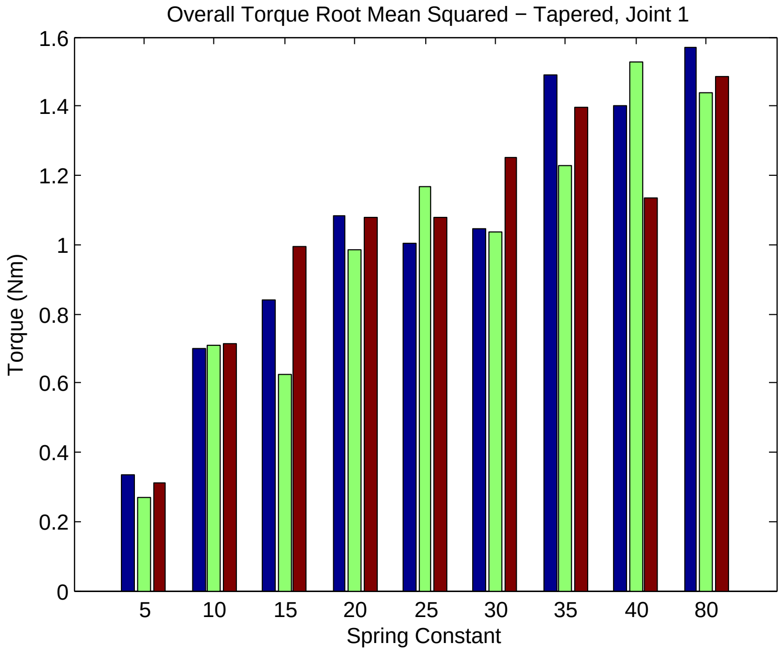

Figure 5.35: Graph displaying maximum rms torque of Wormbot Joint 1 in tapered channel. Different colours indicate 3 experiments.

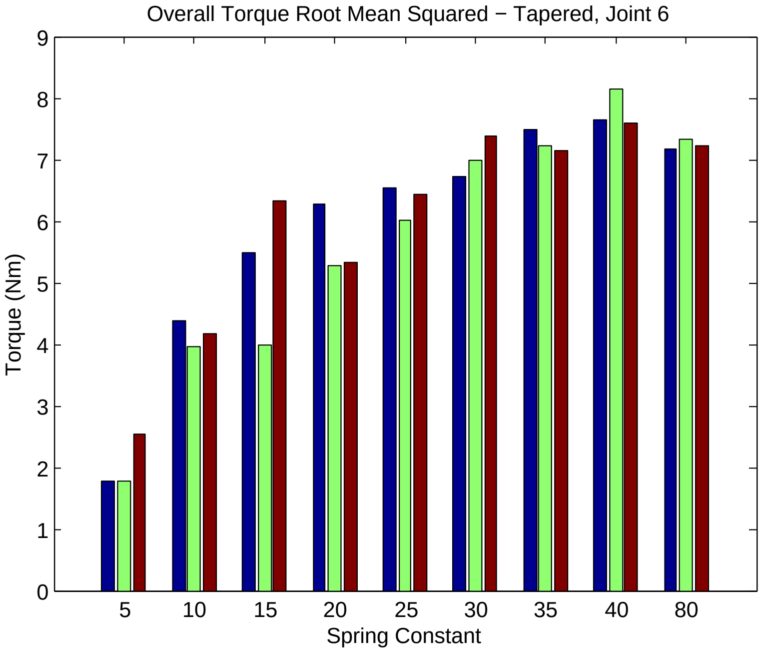

Figure 5.36: Graph displaying maximum rms torque of Wormbot Joint 6 in tapered channel. Different colours indicate 3 experiments.

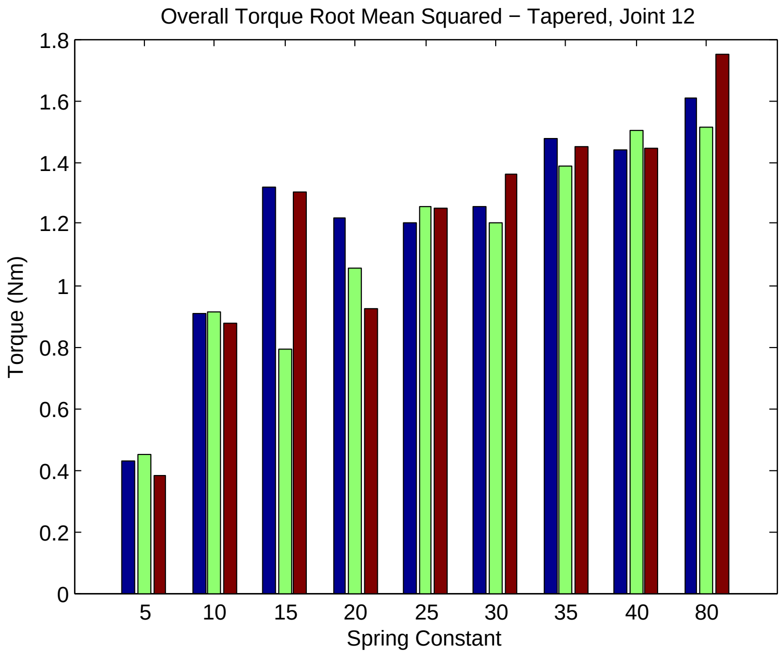

Figure 5.37: Graph displaying maximum rms torque of Wormbot Joint 12 in tapered channel. Different colours indicate 3 experiments.

5.5.2.2 Staggered Channel

Figure 5.38 displays the head and tail module trajectory in the staggered channel when k=5. Figure 5.39 shows the minimum amplitudes achieved by the robot in the staggered channel. It can be seen that the same trend is achieved that was present with the straight tapered channel, though once again the trend is quite weak.

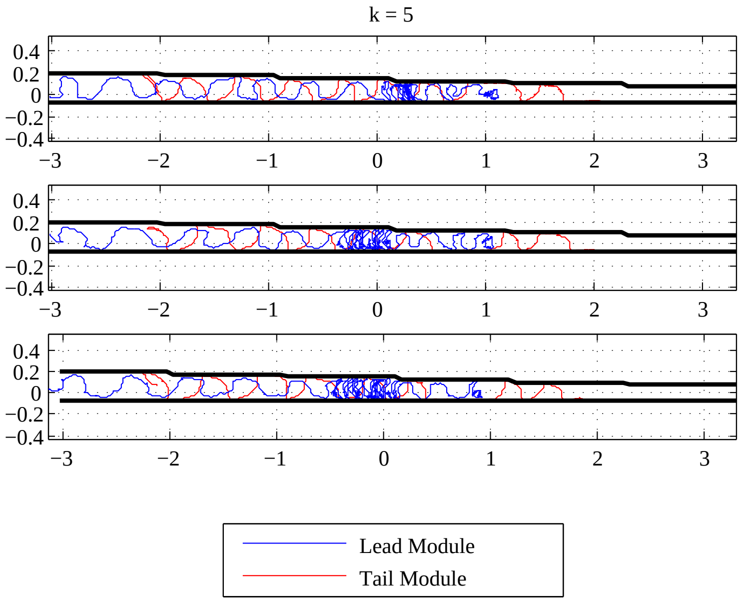

Figure 5.38: Graph displaying trajectory of Wormbot in staggered channel over three tests, where joint spring constant k = 5.

It can also be noted that in Figure 5.38 that the head module became stuck at one of the tapered parts of the staggered channel. This can be expected as at these points, there is a increased level of resistance to forward movement. Overcoming these stages can cause more of an issue if the robot is in contact with them, which becomes more likely as the channel narrows.

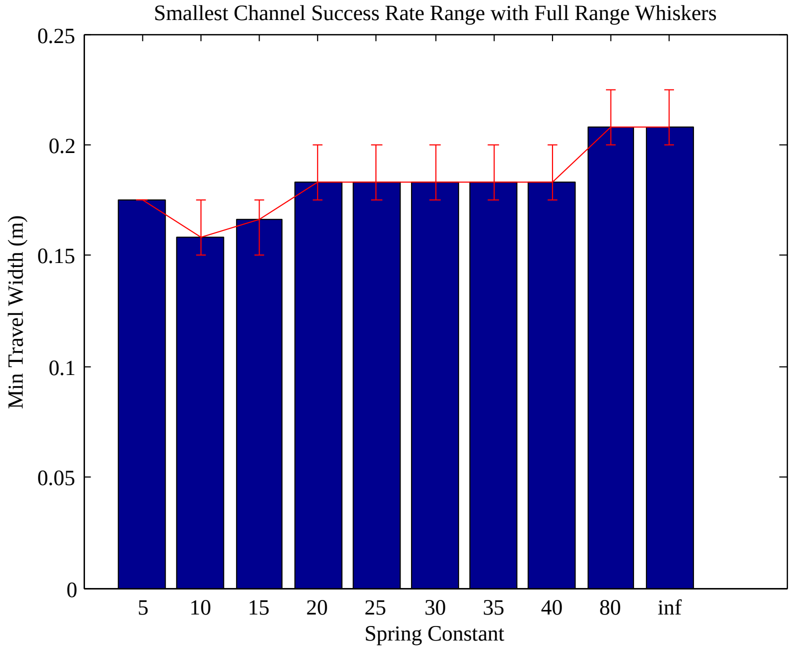

Figure 5.39: Graph displaying average and range of distances reached by Wormbot with range of joint compliances. Red whisker plots display range.

5.5.3 Maze Environment Results

This section displays the results for the maze environment tests. For each spring constant, three tests are performed, with the virtual Wormbot moving across the test area with cylindrical obstacles placed at regular intervals.

5.5.3.1 Large Maze

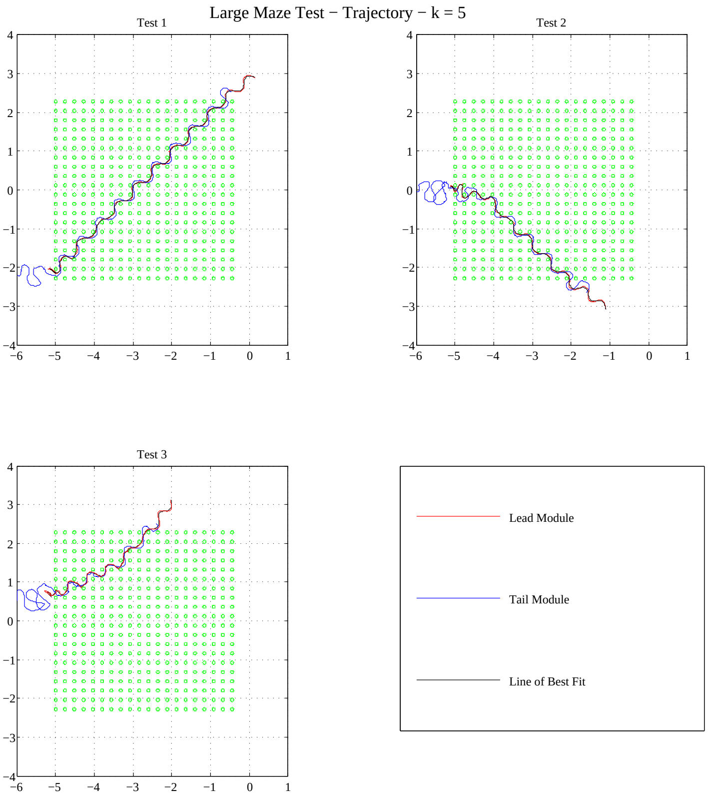

Figure 5.40: Graph displaying the trajectory of Wormbot in the large maze environment over 3 tests, where spring constant k = 5.

Figures 5.40, 5.41 and 5.42 display the trajectory of Wormbot within the large maze environment when k=5, 20 and 40 respectively and Figure 5.43 shows the average speed of the robot travelling through the large maze across all the spring constants tested. It displays that the speed of navigation increase with spring constant until about k=20 when performance begins to level off. The Wormbot with locked springs (k=inf) could not navigate the environment

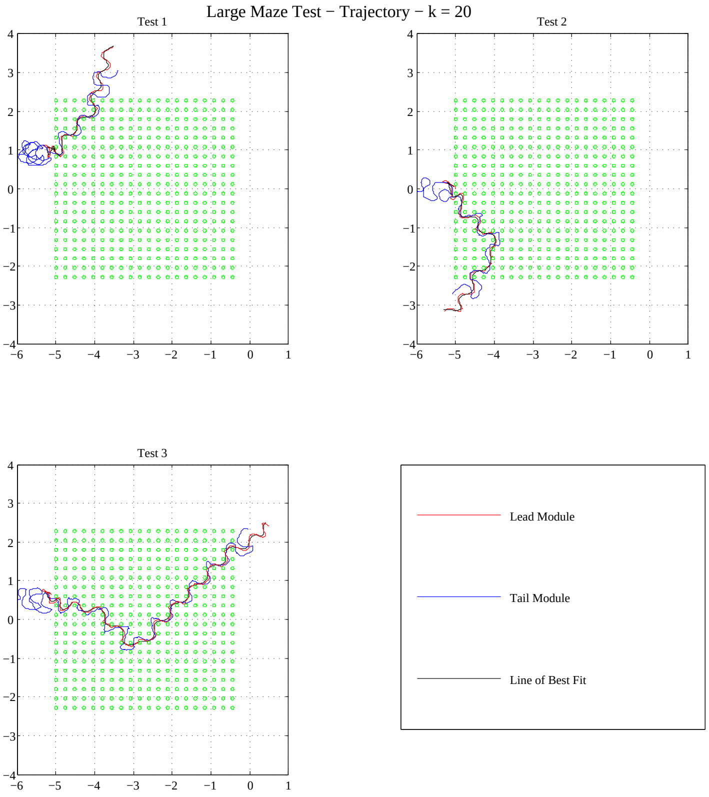

Figure 5.41: Graph displaying the trajectory of Wormbot in the large maze environment over 3 tests, where spring constant k = 20.

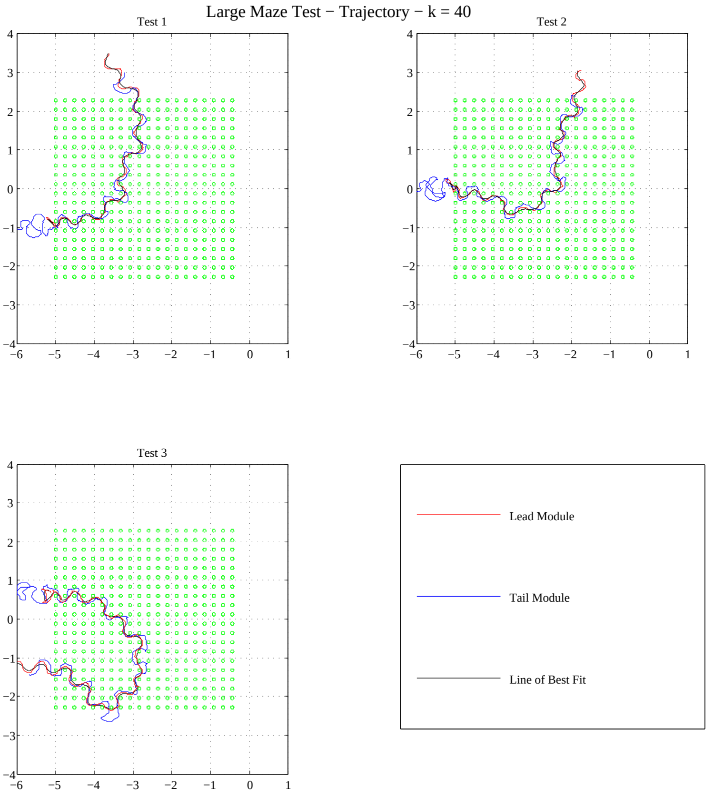

Figure 5.42: Graph displaying the trajectory of Wormbot in the large maze environment over 3 tests, where spring constant k = 40.

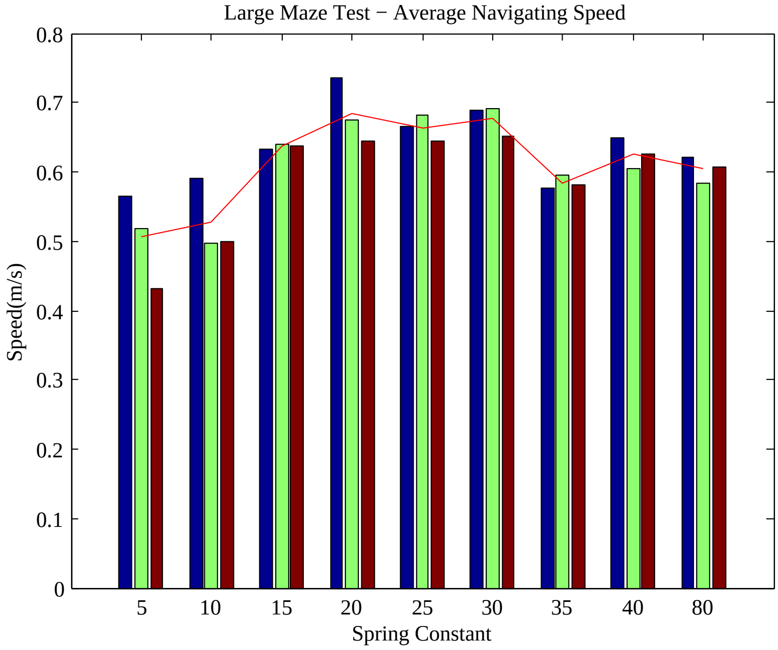

Figure 5.43: Graph displaying the average speed of Wormbot in a large maze environment over a range of spring constants. Blue = test 1, Green = test 2, Maroon = test 3, Red whiskers = Mean and Standard Deviation.

5.5.3.2 Small Maze

Figures 5.44, 5.45 and 5.46 display the trajectory of Wormbot within the small maze environment when k=5, 20 and 40 respectively and Figure 5.47 shows the average speed of the robot travelling through the small maze across all the spring constants tested. The results found in this arena were very similar to those from the large maze environment in that the optimum spring constant appeared to be about k=20 - 30 Nm/°.

5.6 Discussion

The first experiment in this chapter was the open environment; a 25m square open space with no obstacles. The first, and probably most apparent point when observing the experiments is that, as is viewable from Figures 5.13, 5.14, 5.15 and 5.16, is the robot's inability to travel in a straight line. This was thought at one point to be a matter of the coding for the robot potentially having a fault, made when converting the robot's code from LabVIEW to a V-REP compatible form. However, the fact that the robot deviates in both directions suggests that an accidental bias to one side is unlikely. However, the robot

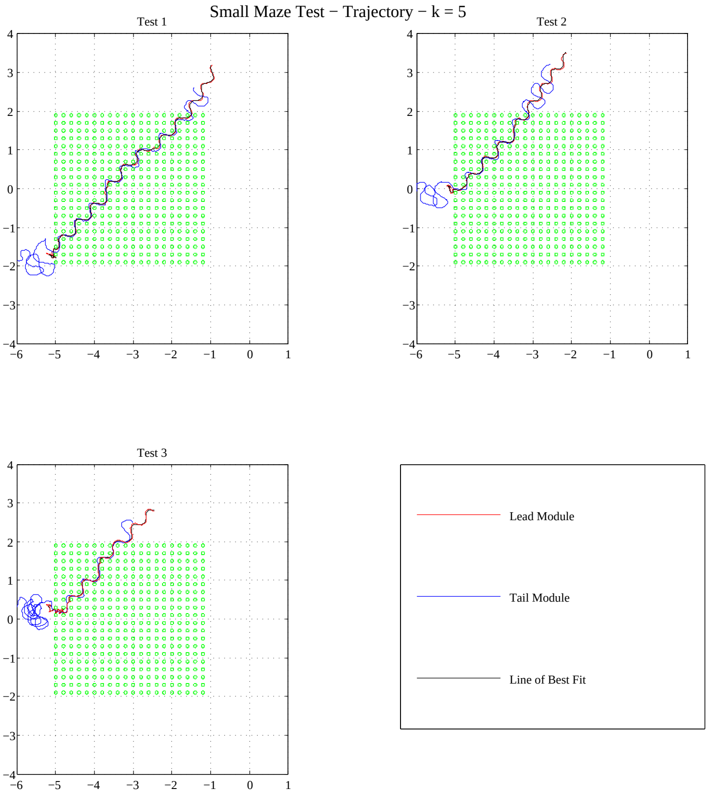

Figure 5.44: Graph displaying the trajectory of Wormbot in the small maze environment over 3 tests, where spring constant k = 5.

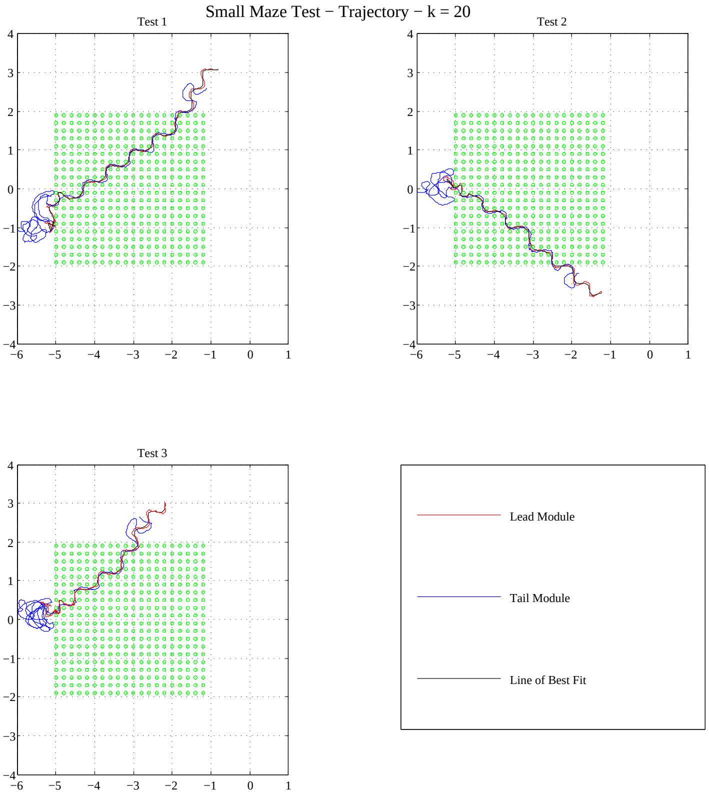

Figure 5.45: Graph displaying the trajectory of Wormbot in the small maze environment over 3 tests, where spring constant k = 20.

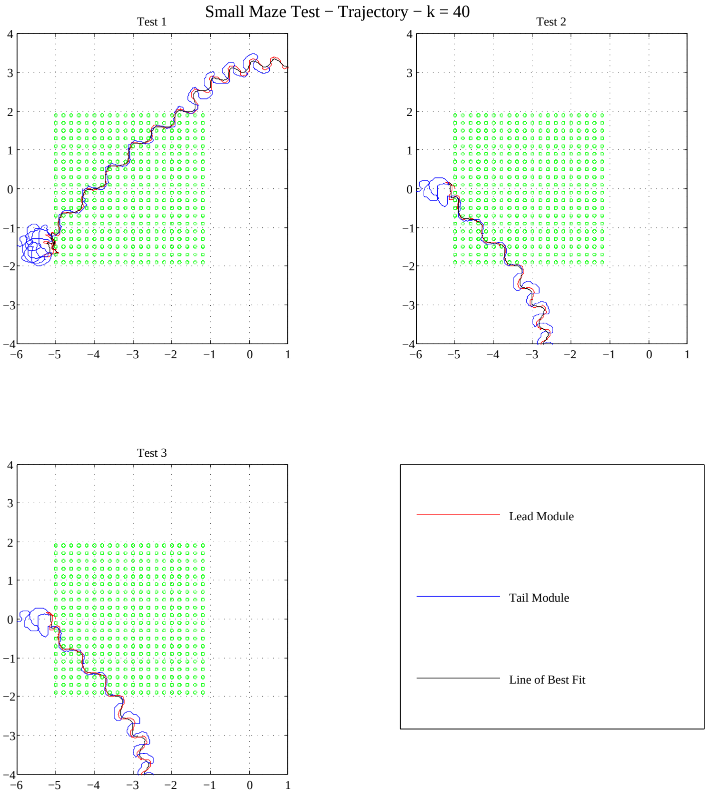

Figure 5.46: Graph displaying the trajectory of Wormbot in the small maze environment over 3 tests, where spring constant k = 40.

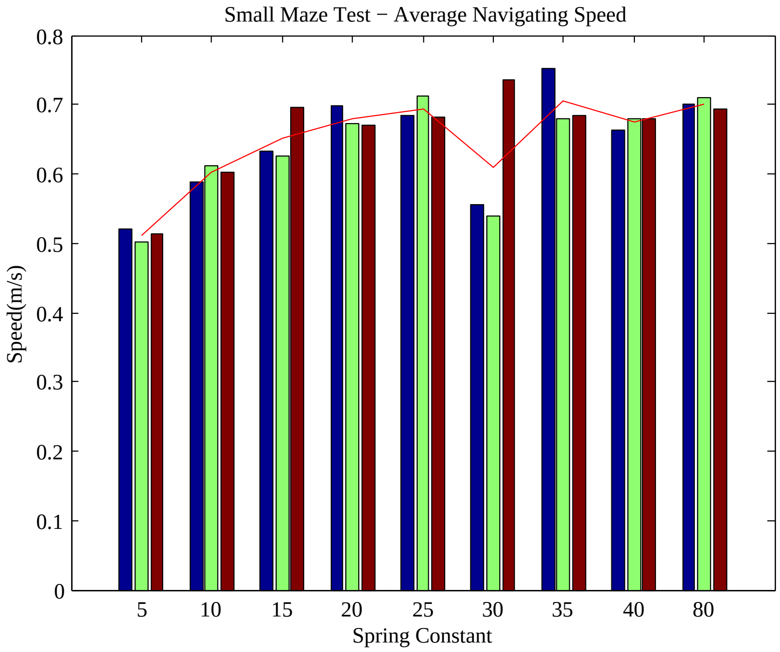

Figure 5.47: Graph displaying the average speed of Wormbot in a small maze environment over a range of spring constants. Blue = test 1, Green = test 2, Maroon = test 3, Red whiskers = Mean and Standard Deviation.

turning a corner with no external force is not something that should provide exceptional duress on the system so it was decided to continue with analysing the data as normal. It is also hoped that, eventually, Wormbot would have a method of steering, probably by applying a bias to turning in one direction over the other. This would mean that any changes of direction would be able to be corrected.

The next point of note is that in Figure 5.13, it can be seen that the tail module overshoots the path of the lead module considerably. It can be seen that this decreases with the joint compliance in Figure 5.14 and Figure 5.15 until, as can be seen in Figure 5.16, the path of the tail module is slightly erratic but does not overshoot the lead modules path; if anything it slightly undershoots it. This trend can be observed in all of the open environment trajectory plots which can be seen in Appendix A. This phenomenon occurs as when the spring is soft, the resistance from the floor alone is enough to deflect the following modules, which cause a kicking out, or flailing, of the tail of the robot. This acts as a hindrance to the robots forward movement and results in the robot travelling slower. This can be seen in Figure 5.17. The speed of the robot is found by using the MATLAB function "*csaps*" to create a spline of the head modules trajectory, then dividing the length of that spline by the time taken in the environment. While stiffer springs seem to result in a quicker robot, this effect seems to stop around k=30, where any change after has minimal effect.

Figures 5.18, 5.19 and 5.20 show the spring angle readings from joints 1, 6 and 12 in Wormbot when k=5. As it was pointed out in Chapter 5.5.1, the magnitude of spring deflection is much larger in the middle joint as it was in the end joints. This is most likely due to joints either side of the joint in question providing additional resistance to motion, which would in turn rotate the spring elements further. This is backed up by the torque data viewable in Figures 5.24, 5.25 and 5.26. When observing Figure 5.21 it can be seen that increasing the spring constant decreases the RMS deflection value. This can be seen more clearly over the full range of k values in 5.23. This is to be expected as the two are inversly proportional. Figure 5.22 however shows the overall joint output doesn't really vary so much in relation to spring constant. This isn't entirely out of the ordinary though as the springs are not being forced out of position by any objects in the envirionment so the motor position will be the main influence behind the entire joint angle.

The torque across the spring increases with the spring constant as can be seen in Figure 5.28, which is expected. However, as was discussed in Chapter 5.5.1, the torque readings from VREP appear to display torque spikes, as can be seen in Figure 5.25. Therefore, Figure 5.28 displays the comparison between the recorded torque and the calculated torque. The calculated torque is found by taking the relevant angle at any time and multiplying it by the spring constant in that test. This found that the spikes could not be recreated with calculated torque. It is therefore assumed that the spikes are brief errors within the simulation software, potentially when 2 physical shapes collide.

On a whole, it was found from the open environment tests that stiffer springs allow for faster travelling speeds when there are no obstacles to Wormbots progress. However, softer springs drastically reduce the load on the actuators.

The next area of testing was in constrained environments, specifically a gradual narrowing channel and a staggered narrowing channel, which can be seen with the k=5 trajectories in Figures 5.29 and 5.38 respectively. The gradual tapered distance results in Figure 5.30 shows that the minimum body amplitude achieved before becoming trapped was lower when the spring constant in the joints is lower. The softer springs would allow the body of the robot to adapt and comply to objects in contact with the body, whereas stiffer joints would lack the flexibility to be able change body shape to fit in narrower passages. This phenomenon appears to level off around about k=20 to k=25. However, the difference in minimum amplitude between k=5 and an infinite spring constant was only about 40mm; half of wormbots diameter, suggesting that the effect is perhaps less than what would have been expected. Considering the torque values with the maximum spring constant are 4 times the amount of the torque at the minimum spring constant (Figures 5.35, 5.36 and 5.37), this isn't necessarily a bad point. This means that weaker motors could be used, which are smaller and less powerful (useful attributes when reducing the size of robots), and performance in constrained environments would not be massively effected.

Furthermore, it appears that the performance of softer springs are more unpredictable, judging by the range whisker plots, suggesting that while improved performance in tighter areas is possible, it is not guaranteed. However, the graph shown displays the experiments where the robot maintained its direction of travel. In one test when k=40 and in 5 different occasions when k=infinite, Wormbot would hit the wall and turn around, eventually heading out of the tapered channel the wrong way. This is why there are no results for infinite spring stiffness with the tapered channel. This could be seen from two points of view. The softer springs allowed the robot to continually travel towards the intended goal, but on the other hand, having no spring component meant the robot avoided becoming trapped. However, if one is trying to reach a goal, it isn't beneficial to have a robot that will not travel towards it due to the environment.

The staggered test was also used to check to see if the same trends occurred when the channels were narrow but parallel. Figure 5.39 shows us that this trend does still occur though it is even less accentuated. This suggests that softer springs will allow for greater ability to access constrained areas, though the trend is not as strong as expected.

The last experiments that were performed were the maze tests. The large and small mazes, with trajectories when k = 5, 20 and 40 can be seen in Figures 5.40, 5.41, 5.42, 5.44, 5.45 and 5.46. Figures 5.43 and 5.47 display the average speed of Wormbot travelling through the large and small mazes respectively. finding the distance traveled involved using the spline function used in the open environment analysis, but in this line is cropped in analysis. The start point for analysing the line begins when the whole robot is within the confounds of the maze and finish when the head module leaves these confounds. When analysing these results, as similar trend emerges to the one seen in the tapered channel test in that the average speed of the robot generally increases with the spring constant until about k=20 in both environments. However, the results in the upper k value differ slightly between the two mazes. In the larger maze, performance seems to dip slightly after k=30 but this is not the case in the small maze. This may be explained by looking at the two sets of trajectories. Figures 5.40 and 5.44, when the springs are soft the robot travels in a relatively straight line, complying to the obstacles around it. In Figures 5.41 and more so in 5.46, Wormbot can be seen to hit obstacles head on in the large maze and, instead of comply to the surroundings, stop and redirect the body, which could take up more time. With the small maze in Figures 5.45 and 5.46, the robot does not suffer from this as the robot seems to be more confined within the maze, which means the robot is not hitting objects square on causing a change in direction.

5.7 Conclusion

In this chapter, the aim was to use simulation software to establish the viability of different strength of springs acting as compliance elements with Wormbot. To achieve this, Wormbot was created using CAD components in VREP simulation software. This software was found to be able to produce realistic physics reactions, particularly with frictional coefficients between materials. One area of concern of this software can be seen however in Figure 5.28, where recorded torque seemed to occasionally spike in comparison to calculated torque. However, these spikes were only incredibly brief (1ms long when recording frequency was 1kHz) and didn't appear to have any other effect on the data, as the recorded and calculated data were almost identical at every other time. If the system was to be improved, some sort of filter could potentially be applied to improve analysing the data.

The results can be split into three groups; open, confined (tapered tests) and mixed (maze tests). It was found that if Wormbot was to be used in an open environment, compliance is found to be a detriment to performance and slows the robot down. It was found that the softest spring constant to achieve maximum speed was approximately k=30. With the tapered experiments, Wormbot was more successful at travelling through more confined environments with softer, more compliant joints. These two findings as were expected before the simulations.

Both maze experiments found that at around k=20, the robot reached around it's maximum speed and that springs softer than this were detrimental to the speed of navigation. However the results were slightly more dubious, as the large maze results suggested that joints stiffer than k=30 were not compliant enough to the environment and would begin to hinder performance. In the smaller maze however, it seemed stiffer springs had little effect to the performance, though this maybe because the were less head-on collisions with obstacles in this arena. However, it can be concluded that spring constants between k=20 and k=30 are a suitable middle ground. Future work with mazes with larger spacing, or even more random spacing may be able to clarify this. It would also be interesting to find the effects of simulating unevenly shaped objects or even uneven ground surfaces, though it would be reasonable to assume that this would require a virtual robot that can at least move passively in a further degree of freedom.

These findings, while being to specific to Wormbot, can benefit the development of many hypermobile robots. There are many factors that can effect the performance of such a robot, like control method, number of segments, robot length and joint torque among other factors. However, this work displays that if compliance is required for the robot to function, a specific level of compliance will be beneficial for performance.

Chapter 6

Development and Implementation of 3D Printed Series Elastic Element

6.1 Introduction

Following the findings of Chapter 5, a method of producing the required spring constant within the Wormbot is required, in the form of a Series Elastic Element (SEE). As discussed earlier in Chapter 3, the wide range of electric motors that are available makes them a very versatile solution. However they do not possess any natural compliance. Series elastic actuation is a method that allows compliance to be introduced to a system, by positioning an elastic element between the motor and the joint, introducing compliance to the system.

In Chapter 2, a solution by Carnegie Mellon University was presented using a torsion spring in the form of a moulded rubber ring between two metal plates and can be seen in Figure 6.1 [77]. This proved to be a capable method of adding compliance to a system by fitting it between the motor and gear train. This proved to be a good solution producing a near linear spring response, although the manufacturing process could be seen to be relatively lengthy, requiring a mould to be produced, the rubber to be moulded, the end plates to be machined and then to be bonded to the rubber component. This process could be streamlined by producing the whole device with multi-material 3D printing, as was used in Chapter 4. This process would also allow for quick alterations to dimensions and hence performance, as this could be changed quickly in a computer aided design (CAD) model and reprinted instead of making a new mould and restarting the long manufacturing process. However, it is unknown whether producing a linear SEE like this could be achieved. Theoretically, altering the dimensions of the rubber element would alter the properties of the spring, which could alter system performance, as seen in Equation 6.1, where T is Torque, k is the spring constant and θ is the angle of rotation.

$$T = k\theta \tag{6.1}$$

Figure 6.1: Cross section of Rubber SEE. Note the tapered shape, providing an even distribution of shear stress acoss the component [77].

As well as experimenting with the feasibility of 3D printing for producing such a device, this chapter will also analyse the potential for producing SEE's with specific performance parameters by altering the cross sectional dimensions, a layout of which can be seen in Figure 6.2. Having experimented in Chapter 5 with varying spring constants within Wormbot's joints, it would be a desirable outcome to be able to perform the same tasks with physical implementations. If this could be achieved with 3D printed SEE's, it would provide a foundation for providing quick, effective solutions to a wide range of applications. For example, two Wormbots could be required to investigate two environments; a relatively open environment and a narrow channelled environment. One could design and 3D print two separate sets of SEE's (stiffer for the open environment one and softer for the channelled one) quickly and have two similar robots custom made for different applications. For this however, characterisation of the device must take place to know how to change the properties of the SEE.

In this chapter, the process behind producing, analysing and optimising a 3D printed SEE will be explored. Firstly, we describe the process behind testing and analysing the device's performance. This will involve step response test analysis. After this, the first SEE test sample will be analysed. As more is learned about the performance of the 3D printed device, further iterations will be produced to improve performance.

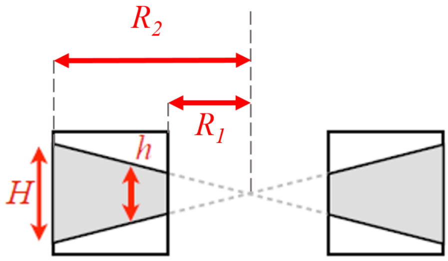

Figure 6.2: Diagram of ideal cross-section of SEE, adapted from [77]. Note how the taper of the SEE meets in the centre.

6.2 Method of Implementation and Analysis

In this section, the process behind analysing the performance and designing the 3D printed SEE will be discussed. This will start with looking at the experimental process and how the device will be tested. Following this, programmatic analysis and design tools will be examined. This will start with the process of characterising the response gained from the sample, and then progress onto using the obtained knowledge to predict how dimension changes should be able to alter the performance of the SEE.

6.2.1 Experimental Approach

The aim of the experimental approach is to be able to produce a set of measurements from which a model can be derived. In this case, the SEE is expected to display some viscoelastic properties as displayed by the original SEE this work is based on [77]. Therefore, a step response will need to be performed to obtain this information. For this, an Instron E10000 material testing instrument is to be used [9]. This machine is capable of torque loading up to 100Nm and capable of ±16 revolutions. The E10000 is designed to hold samples in place using either bolt fittings or pneumatic jaws, though additional frameworks may also be used in addition to these, such as custom made adaptors. Design features will be used to ensure the SEE's are placed centrally so that rotation will occur around the central vertical axis of the component.

To achieve an ideal rotational step response, an instantaneous rotation should occur. This is, practically, impossible to achieve. In these experiments, a preset angle of rotation will be achieved in 0.1 seconds. This will then be held for 20 seconds to allow for any potential viscous property of the component to settle. The test rig will then perform a reverse step response back to zero and hold for 20 seconds. This experiment will be repeated three times per sample and angle of rotation, unless there is a failure of the component. This will be repeated for varying angles of rotation, stepping up each time. The limit at which no more tests will be performed will depend on what each individual SEE has been designed to withstand, or if component failure has occurred. From each test, the time, angle of rotation and torque will be recorded, all the data required to obtain a step response.

6.2.2 Programmatic Approach

Once the data has been collected, a series of Matlab programs are employed to analyse the performance and then take the information learned to predict the design specifications of the next SEE.

The first of these programs starts with importing the time, angle and torque data from each experiment. These are then trimmed from the the time of the highest torque to the end of the response, approximately 18 seconds later. A double exponential curve is then fitted to the curve, which will later be added to the spring constant from the steady-state torque to produce a five-element Maxwell Wiechert model, shown in Figure 6.3, with the related equations shown in equations 6.2 and 6.3 [64]. In this, k represents spring stiffness, C represents viscosity and τ is the time constant. This is performed for both up and down steps of the experiment. After this, the average of each of the Maxwell Wiechert parameters are taken from the 6 samples.

$$k(t) = k_0 + k_1 e^{-t/\tau_1} + k_2 e^{-t/\tau_2} \tag{6.2}$$

$$\tau_i = C_i / k_i \tag{6.3}$$

Once this is completed, these facets are optimised, in case of any imperfections in the step response. This is performed using a function which recalculates the five constants of the model [21]. This is achieved by using a spline of the angle vs time data. The constants of this are then used to find a optimised response line, using the “fminsearch” function in matlab, to produce a simulated model as close to the original torque response as possible.

The second program is designed to take known properties of the SEE and provide

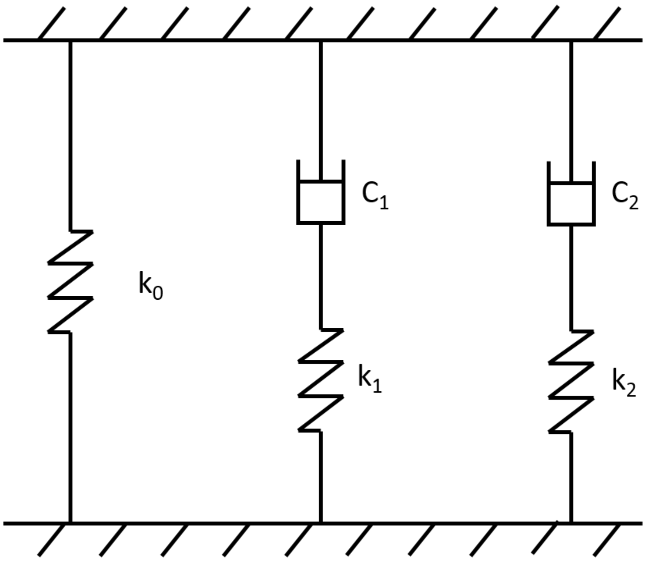

Figure 6.3: Representation of 5-part Maxwell Wiechert Model, adapted from [64]

ideal dimensions for later SEE units, taking intended performance parameters into consideration. This is based on Equation 6.4, which is used by Rollinson et al [77].

$$T = \frac{2\pi R_2 G\theta}{3H}({R_2}^3 - {R_1}^3) \tag{6.4}$$

In this equation, T is Torque, R_1 is the inner radius of the SEE, R_2 is the outer radius of the SEE, H is the outer height of the SEE and G is the shear modulus of the SEE. The dimensions for this are viewable in Figure 6.2. Figure 6.4 displays the Graphical User Interface (GUI) for the program, developed to improve ease of use of the program.

The intended torque, angle, inner radius, maximum allowable outer radius and maximum allowable outer thickness of the SEE are inputs. The final input for Equation 6.4 is the sheer modulus G. This is taken from the first set of experiments, where all other factors are known. These will then be inserted into the rearranged version of Equation 6.4, Equation 6.5. This method does mean that the first iteration will not have a value for G, as there is no data to base it on, and thus will be made with no estimation in performance.

$$G = \frac{3TH}{2\pi R_2 \theta({R_2}^3 - {R_1}^3)} \tag{6.5}$$

Once the inputs are inserted into the GUI, two graphs and four values are returned. The first graph displays a surface plot of the predicted performance, with varying outer

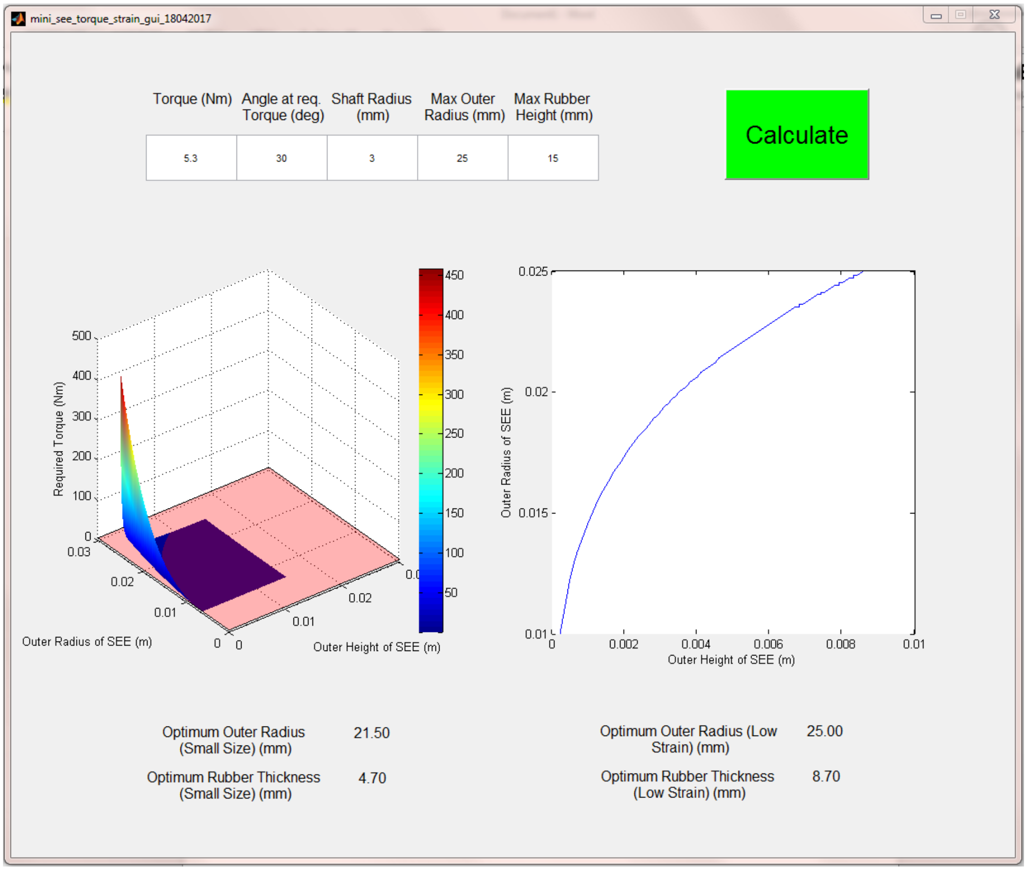

Torque (Nm)	Angle at req. Torque (deg)	Shaft Radius (mm)	Max Outer Radius (mm)	Max Rubber Height (mm)
5.3	30	3	25	15

Optimum Outer Radius (Small Size) (mm) 21.50

Optimum Rubber Thickness (Small Size) (mm) 4.70

Optimum Outer Radius (Low Strain) (mm) 25.00

Optimum Rubber Thickness (Low Strain) (mm) 8.70

Figure 6.4: GUI for MATLAB program for finding ideal dimensions for SEE.

radius, outer height and torque. There is also a plane on the graph indicating the desired torque. A top down view of the plane is visible in the second graph. The values given are two sets of results for ideal height and outer radius. One set of these is the largest to fit within the initial dimension parameters provided. The other set is to provide the smallest SEE possible while being theoretically strong enough to survive testing. This is another facet that cannot be deciphered until the first test has been completed; more specifically when a sample in the first test fails. When a sample fails, the breaking strain can be found. The equation for shear strain in a hollow cylinder can be found in Equation 6.6 [24].

$$\gamma = \frac{r\theta}{l} \tag{6.6}$$

In Equation 6.6, r is the average radius of the hollow cylinder, l is the length of the cylinder and θ is the angle of rotation. Normally, r is the average radius as both ends of the cylinder are parallel, so the equation represents average shear strain. However, as the SEE is tapered, the shear strain is constant throughout the entire device. This means as long as the height and radius relate to the same section of the SEE, they will produce the correct shear strain value. For ease of use, the outer radius R_2 and maximum height H (acting as l) will be used.

Once the strain can be found, it is calculated for the last known point at which the device was still functional. This is then used in the second MATLAB program. The smallest dimensions given will have to produce theoretical strain values that are smaller than the strain threshold point.

A flowchart overviewing the process of developing the 3D printed SEE is displayed in Figure 6.5.

6.3 Development of Series Elastic Element

In this section, the development of the SEE for testing is described. Eventually, it would be hoped that an SEE could be contained in a small enough form to be able to fit within a 80mm diameter Wormbot. However, the first step is to be able to accurately map its performance. This requires the device to be fitted within the Instron E10000. The first stages of development will be affected by this but the designs will adapt to smaller, more encapsulated representations.

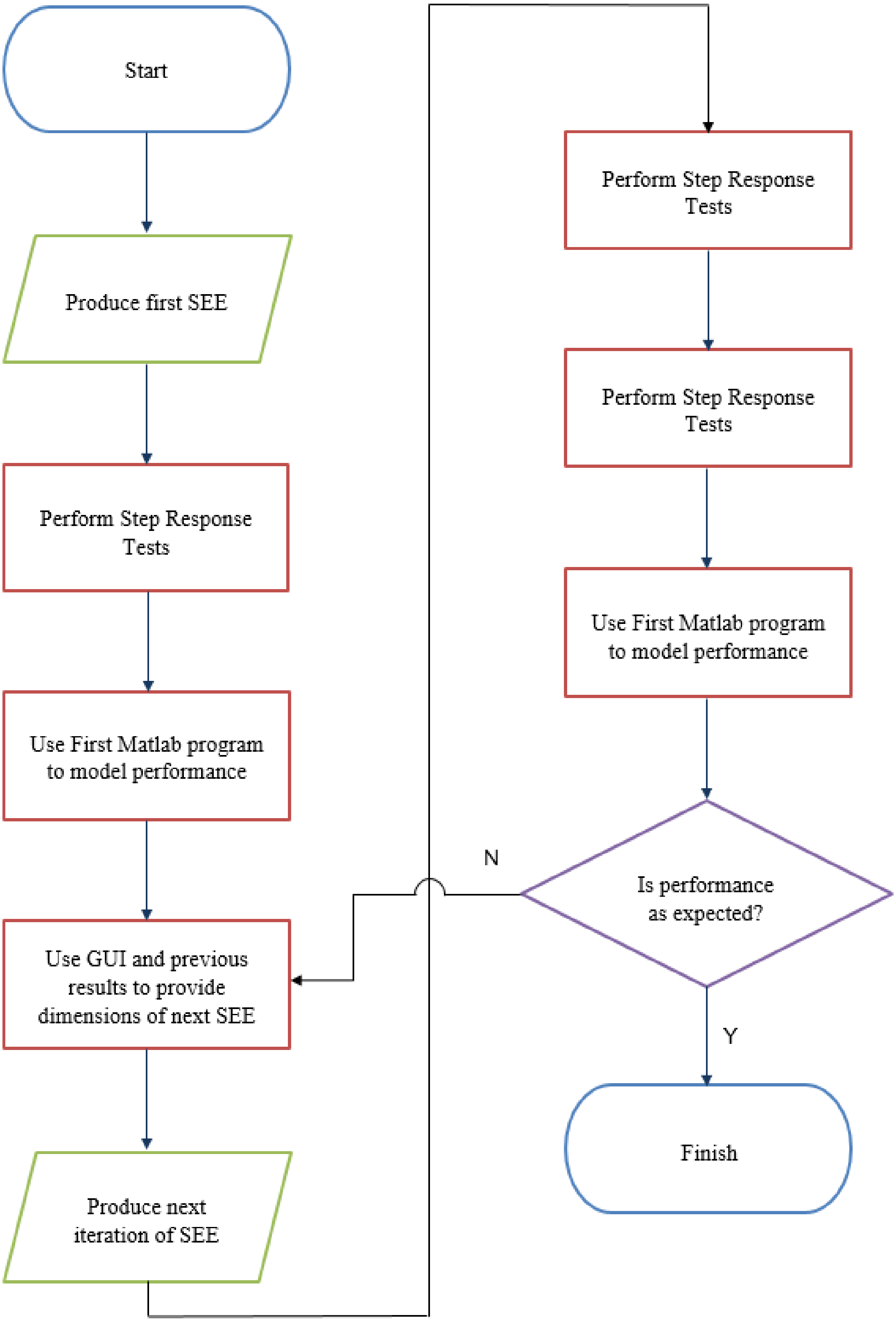

Figure 6.5: Flowchart displaying process of SEE Development

6.3.1 Series Elastic Element Version 1: Arm Fittings

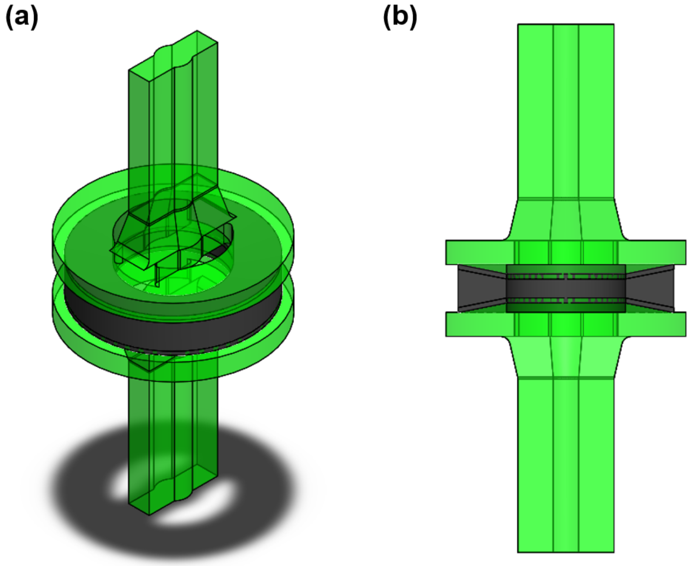

Figure 6.6: CAD model of SEE version 1. (a) Isometric view. (b) Section view.

Figure 6.6 displays the first version of the SEE [21]. The central active ring (grey) is made from the rubber-like 3D printed material(“tango plus” material). The SEE is tapered in shape and solid in structure. Having open spaces or channels printed in to the rubber was considered for a softer spring response but the potential for experimenting with the size and shape of these was limitless. It was decided that it would be much more feasible to analyse a solid component.

The two end components (green) are printed from the 3D printed plastic (“vero plus” material) that was used for the end caps of the pneumatic bellows in Chapter 4. The end components consist of two arms which can fit between pneumatic clamping jaws that can be used to fix the sample. The arms also feature a semicircular ridge along the centre of the arms. This is to centre the SEE in the Instron. The jaws have a groove down the centre of them marking the centreline of rotation. The semi circular ridge on the arm fits in this groove and ensures the sample is centered. Further to this, a radius has been utilised between the arms and the plate on which the rubber component is attached. It was recognised that this would be a potential point of weakness when loading the device, so this point is increased in size though kept small enough to fit in the Instron.

Additionally, it can be seen from Figure 6.6 that there is an overlap between the plastic part and rubber part. This was due to being advised by technicians at the point of manufacture that an overlap of a material creates a stronger bond. Therefore, the 1mm crossover of material was included in the design.

Two sizes of SEE will be employed for this round of tests. The inner and outer radius (R_1 and R_2)will remain constant at 12.5mm and 22.5mm respectively, though the inner and outer heights (h and H) used 6-10mm and 8-12mm. This was implemented to test that the effect of altering dimensions is as expected, although this does mean that the taper of these two samples won't quite have the rubber taper meeting in the middle, like in Figure 6.2, which was an unintentional oversight. This may, according to Rollinson, affect the linear performance of the spring [77]. Two copies will be printed of each design to test the repeatability of performance between prints. Each SEE will be tested at 5° and 10°. This will display the linearity (or lack of) of spring constant over increasing load.

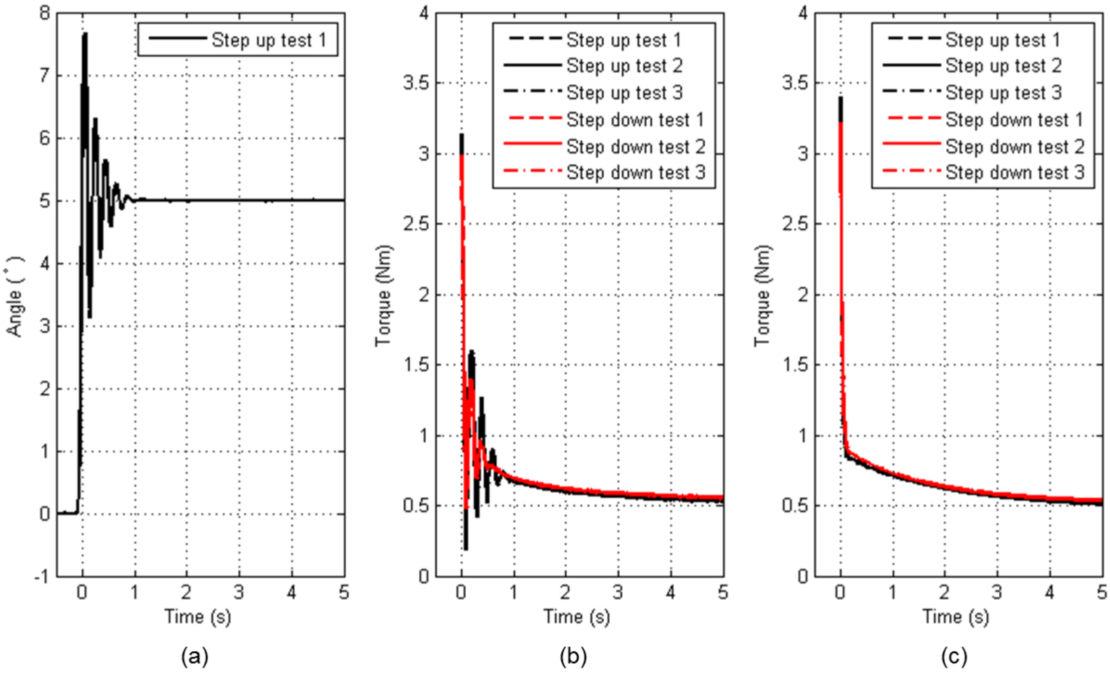

Figure 6.7: (a) 1 sample of angle data from 5° step test. (b) 6 samples of raw data from 3 iterations of 5° step test (1 step up and 1 step down per test) for 10mm thick SEE. (c) Line of best fit for each sample [21].

Part (a) of Figure 6.7 shows the angle input for a 5° step test. It can be seen that the input for the test is not perfect in that the step oscillates before settling at 5°. This means that any raw torque response will feature a certain level of oscillation too, as can be seen in Figure 6.7(b), which displays the raw torque step input for the 3 steps up to 5° and down to 0° (inverted to be easily compared with up-steps). This shows the need for using curve fitting in MATLAB to achieve a 5 part Maxwell Wiechert model, which can be seen in Figure 6.7(c). To achieve the response seen in Figure 6.7(c), the 5 part Maxwell Wiechert model constants are used while assuming a perfect angle step, not the oscillating angle value that was produced by the Instron testing rig.

One point that can be seen from Figure 6.7(b) and (c) is that all the responses are very similar. The steps up feature slightly more oscillation than the steps down but the fitted curves prove to be very similar. This indicates that the performance of a single SEE is repeatable and therefore will perform consistently throughout a single use.

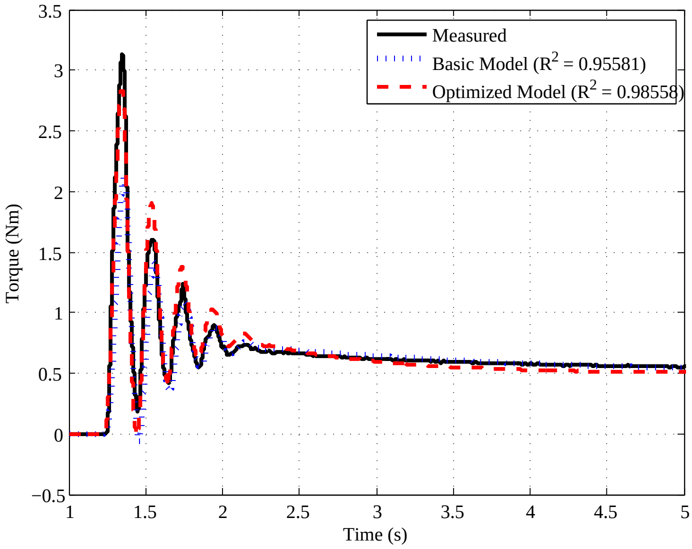

Figure 6.8: Sample of recorded SEE version 1 step test data compared to basic and optimized simulations with thicker SEE rotating 5°.

Figure 6.8 displays the measured torque response against the initial, curve fitted simulation response and the optimised response (All using the recorded angle against time readings). What we can see from this is that, while the original fit model is relatively accurate ($R^2 = 0.95581$), the optimised model is more accurate ($R^2 = 0.98558$). Across all these tests, the improvement in R^2 varies from 0.015 to 0.04. These can be seen in Appendix B (on disc attached).

Figure 6.9 displays the ideal step responses for all SEE's at 5° and 10°, and Table 6.1 shows the constants for each part of the Maxwell Wiechert model. We can see from Table 6.1 that the majority of the constants remain very similar within each size of SEE. There

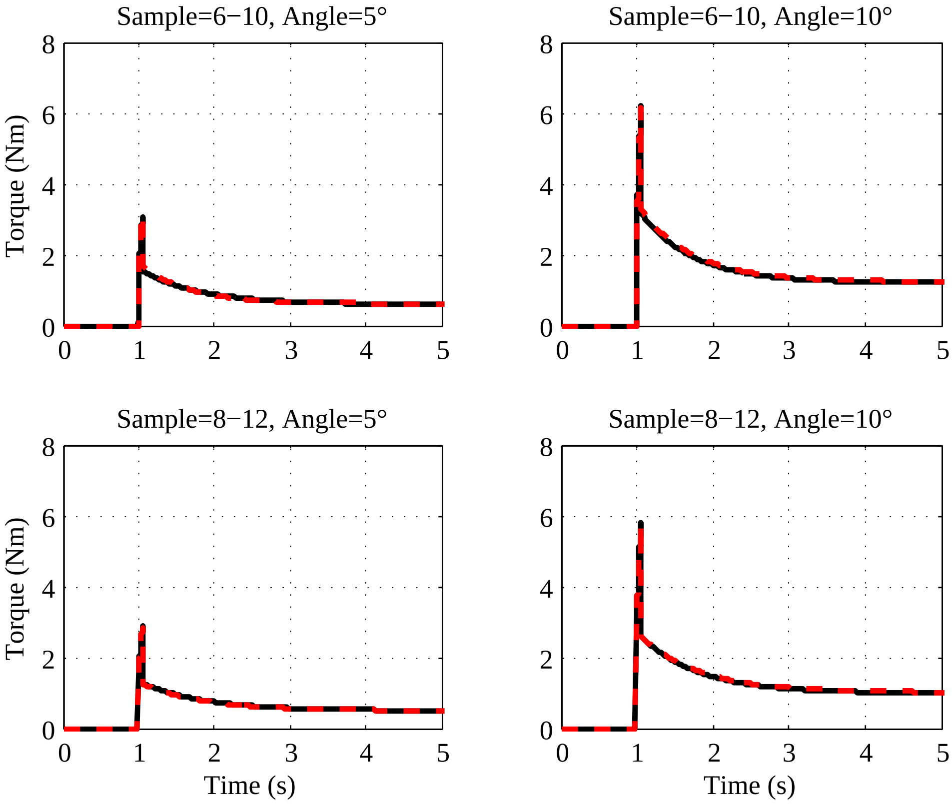

Figure 6.9: Comparison of optimised ideal step responses (different colours indicate different samples) [21]. Notice how thicker SEE's feature a lower resting torque and how resting torque doubles with angle

Table 6.1: Spring and Damping Constants across all Version 1 SEEs. Values given as median ± standard deviation [21].

		6-10				
		k_0	k_1	C_1	k_2	C_2
SEE 1	5°	6.826±0.024	11.18±0.023	8.926±0.099	417.1±71.86	0.863±0.003
	10°	6.918±0.041	11.81±0.087	8.212±0.116	1345±341.5	0.855±0.001
SEE 2	5°	7.062±0.037	12.85±0.182	8.249±0.088	2339±3031	0.810±0.001
	10°	7.080±0.040	12.32±5.835	8.628±4.068	1116±540.0	0.809±2.825
		8-12				
		K_0	k_1	C_1	k_2	C_2
SEE 1	5°	5.672±0.016	9.342±0.072	7.752±0.057	8924±2413	0.907±0.001
	10°	5.670±0.033	9.646±0.054	7.354±0.074	9046±32.76	0.912±0.001
SEE 2	5°	5.703±0.042	9.045±0.399	7.264±0.105	8945±24.70	0.898±0.002
	10°	5.800±0.009	9.511±0.077	7.458±0.049	8945±50.94	0.903±0.001

is some variation in the second small SEE at 10° in comparison to any other constants for smaller SEE's, as can be seen by the standard deviation. This can be explained by viewing Figure 6.10, which displays the corresponding simulation during its third test. It can be seen in that fitting a model in this instance was not as accurate, with an R^2 value much lower than in any other test, which may have biased the results. There is also greater variability in k_2, though it is unknown why this is the case.

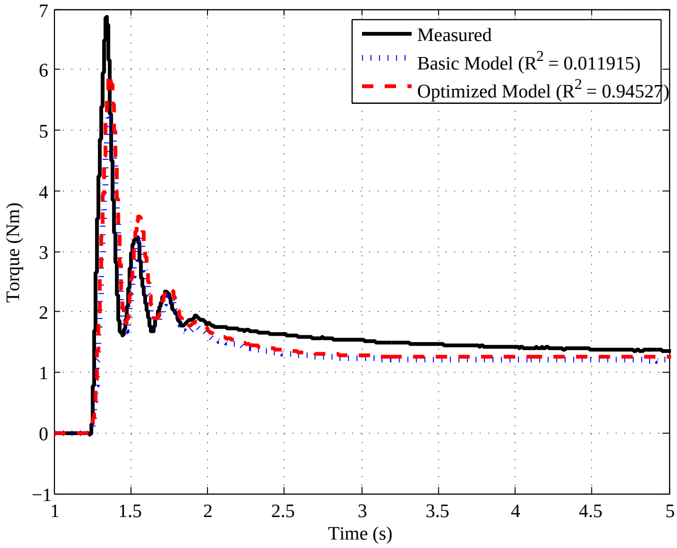

Figure 6.10: Sample of recorded SEE step test data compared to basic and optimized simulations with thinner SEE rotating 10°.

While this looks like a potential flaw, it has had little effect on the ideal step response curves displayed in Figure 6.9, which all show strong correlation between equivalent samples. This indicates that, not only are the SEE's consistent in performance, they are repeatable between prints as well, indicating that the printing process is reliable.

As was mentioned previously, Table 6.1 shows that the constants stay similar when the angle of rotation changes. This indicates that the SEE's are performing linearly, which is ideal as pointed out by Rollinson et al [77]. This means that, if the device is to be rotated twice the original amount, it will require double the torque as indicated by Equation 6.1. This is visible in Figure 6.9, where both the peak and settling torque approximately double when the rotation angle is increased. It can also be seen that the thinner SEEs have a higher initial spring constant, indicating that the spring is stiffer and requires a higher torque when rotating.

6.3.2 Series Elastic Element Version 2: Keyway Fitting

The previous version of the SEE showed the 3D printing technique was effective at producing repeatable devices. However, the arms were designed for attaching the SEE to the Instron and would not be applicable for use in a hypermobile robot. Therefore a method of compressing the design in to a small compact device should be considered. Figure 6.15 displays a CAD model of the second, more compact SEE.

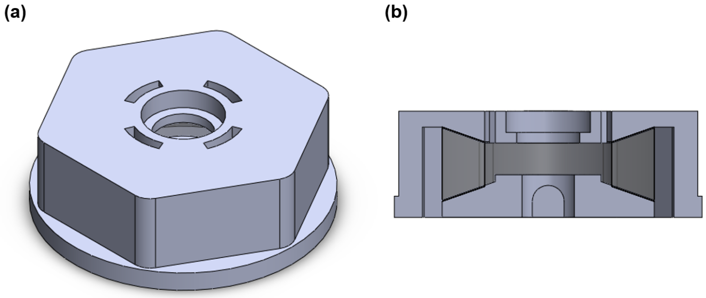

Figure 6.11: CAD model of SEE version 2. (a) Isometric view. (b) Section view.

This design of this SEE is quite different in appearance to the first SEE. This SEE was designed to be able to fit inside a gear to embed the system into the gear train of a joint mechanism, and a number of the features specifically allow for this. The first point of note is that the arms fittings have been removed and the rubber element is encased by a hexagonal wall extending down from the top plate. This wall would allow the SEE to be fitted into a gear, assuming the gear has the same shape cut out, and sit on the lip at the bottom of the hex fitting. The gear used was purchased and then machined to feature a corresponding hole for the SEE [7]. This would allow for a motorised joint mechanism to have compliance introduced with no additional space required. An example of this can be seen in Figure 6.12.

To fix the bottom plate of the SEE, it can be seen in Figure 6.15 (b) that there is a keyway present. This would allow for the bottom plate to be located to a shaft, either from a motor or the joint. There is also a space in the top plate for a bearing, so this shaft will not have any frictional effects on the performance of the SEE.

It can also be seen that there are number of small grooves near the centre of the top and bottom plates. These were produced to allow for the extraction of support material

Figure 6.12: Version 2 SEE located inside gear, indicated by the yellow dashed line.

from the manufacturing process. Effort was made to keep these as small as possible to not impair the strength of the device.

Finally, the rubber component of this SEE is a lot smaller than in the previous version to fit within the confines of the device. While predictions could be made about the performance of this compact SEE, the main idea of this design was to see if it could be produced on a much smaller scale, not to see if the design was precise in its performance. To give a brief overview of expectations, the device is much shallower (in that the height is much lower), which suggests that it will be stiffer in performance. However, the width of the SEE (the distance between inner and outer radius) is low, and it would be reasonable to presume that less material to deflect would produce a softer SEE.

While this device should be suitable for applying to a Wormbot joint mechanism, it also needs to be fitted to the Instron E10000. The parts for this can be seen in Figure 6.13.

This consists of six components; the shaft, the key, the SEE, the bearing, the socket and the fitting bar. Firstly, the shaft will be clamped into the lower jaws of the Instron. A small, 3mm wide key is then used to fix the position of the bottom plate of the SEE. Next, the top plate is fitted within a 25mm socket from a socket wrench set. The square hole in

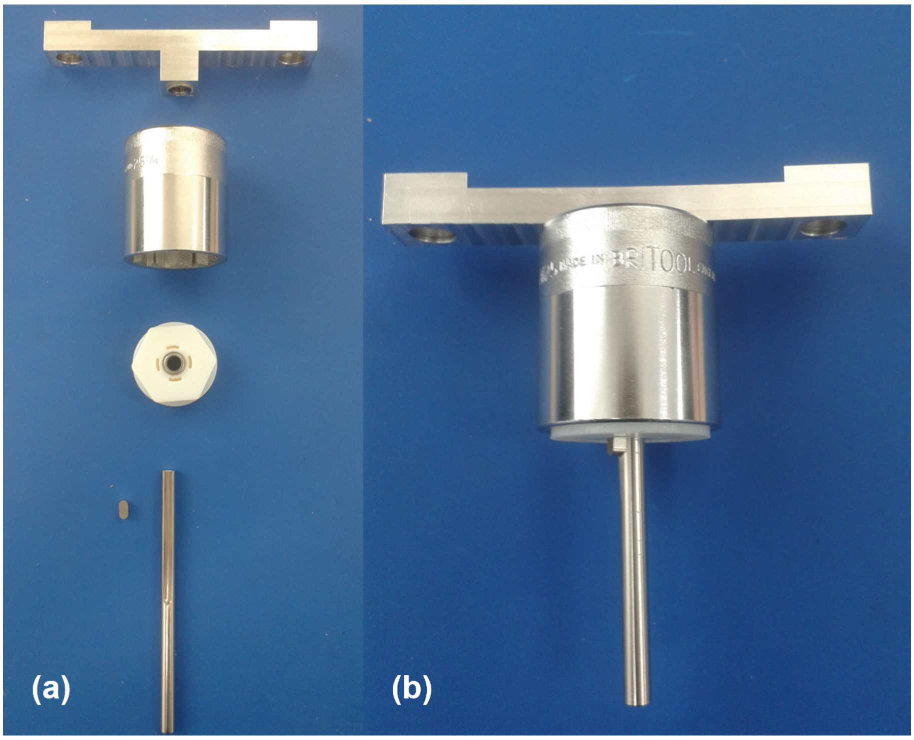

Figure 6.13: Framework used for fixing Version 2 SEE into Instron E10000. (a) Individual components. (b) Assembled.

the top of this will fit into the matching part of the fitting bar. The top of this is designed to use a centering ring from the instron to line it up with the rotating section of the rig, to ensure rotation occurs around the middle. This is then bolted in place.

In this experiment, 3 SEE samples will be tested, at 5° intervals up to 15°. The results will then be analysed to identify any positive or negative characteristics.

Figure 6.14 displays the recorded, simulation and optimised simulation torque response from the version 2 SEE when being rotated. The simulation fit is not as accurate for the compact version 2 SEE as it was original design, partly due to the level of oscillation seemingly rising before settling. Additionally, the settling torque is much lower, settling at approximately 0.5Nm. To examine this further, Table 6.2 shows the constants of the Maxwell-Wiechert model for the SEE.

It can be seen that the initial spring constants are much lower, but also that there is much more variation in all the constants. This indicates that this version of the SEE is not linear, or indeed at all predictable. On analysing the test in process, however it could be seen that the fixing key was able to rotate in the keyway and keyseat. This would mean

Table 6.2: Spring and Damping Constants across Version 2 SEEs. Values given as median ± standard deviation.

		Compact SEE				
		k_0	k_1	C_1	k_2	C_2
SEE 1	5°	0.3112 ± 0.3804	$419.9172\pm1.0384\text{x}10^{8}$	$0.0423\pm5.6603\text{x}10^{6}$	$-0.4929\pm1.0384\text{x}10^{8}$	$-0.0518\pm5.6603\text{x}10^{6}$
	10°	0.3003 ± 0.0096	434.9931 ± 7.3217	0.0438 ± 0.0007	-0.0041 ± 0.0061	0.0831 ± 0.3386
	15°	0.4254 ± 0.0896	458.3693 ± 1.7610	0.0458 ± 0.0002	-0.0998 ± 0.0905	23.2028 ± 10.2138
SEE 2	5°	0.4079 ± 0.0511	394.1806 ± 8.8494	0.0398 ± 0.0013	-0.0010 ± 0.0012	0.0106 ± 0.0198
	10°	0.4561 ± 0.2161	548.8473 ± 15460.6164	315.3325 ± 361.2667	-558.1768 ± 15446.6962	-123.7711 ± 129.6930
	15°	0.0368 ± 0.2010	$1.5774\pm5.1837\text{x}10^{10}$	$498.1053\pm1.2405\text{x}10^{12}$	$-1.5538\pm5.1837\text{x}10^{10}$	$-498.0667\pm1.2405\text{x}10^{12}$
SEE 3	5°	0.4631 ± 0.0104	214.5470 ± 129.2514	0.1936 ± 0.7325	-12.4609 ± 93.4649	-0.1741 ± 0.7391
	10°	0.4488 ± 0.0107	$0.1131\pm2.8866\text{x}10^{8}$	$0.0273\pm9.6932\text{x}10^{6}$	$-2.3402\pm2.8866\text{x}10^{8}$	$-0.2479\pm9.6932\text{x}10^{6}$
	15°	0.4639 ± 0.1754	$2.3664\text{x}10^{8}\pm1.9031\text{x}10^{8}$	$6.8580\text{x}10^{6}\pm8.2781\text{x}10^{6}$	$-2.3664\text{x}10^{8}\pm1.9031\text{x}10^{8}$	$-6.85797\text{x}10^{6}\pm8.27822\text{x}10^{6}$

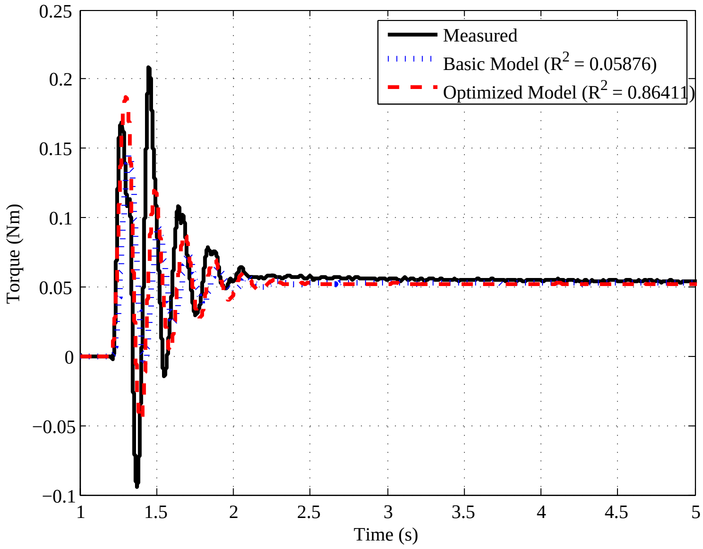

Figure 6.14: Sample of recorded SEE compact version 2 step test data compared to basic and optimized simulations with SEE rotating 5°.

that during every test, only a fraction of the rotation would actually be taken in the rubber component. This would cause huge inaccuracies in the data recorded and it would not be representative of the SEE's characteristics.

6.3.3 Series Elastic Element Version 3: Large Keyway Fitting

It was clear from the previous set of results that the design needed optimising. One of the potential areas of concern was they keyway, which did not completely encapsulate the key when the system was assembled. To overcome this, it can be seen in Figures 6.15(b) and 6.16(b) the version 3 SEE has an encapsulated keyway in an attempt to resist any additional movement that may be taking place. Another change is that the material crossover thickness has been reduced from 1mm to 0.1mm. It is hoped that this may minimise any potential effect the hybrid material may have on performance, while having a period of transition that improves structural integrity.

This version of the SEE has utilised the dimension prediction program. As discussed earlier, this program required the shear modulus, G, found using Equation 6.5. For this we can use results from the last set of tests. These results are not necessarily reliable considering the range of results but this can at least act as a starting point. For the third

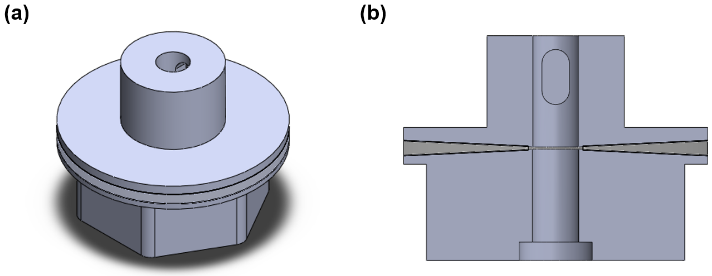

Figure 6.15: CAD model of SEE version 3 (small). (a) Isometric view. (b) Section view.

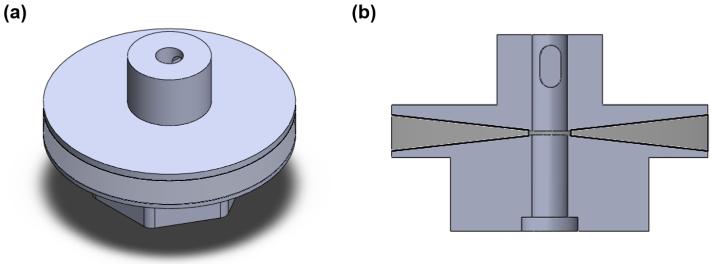

Figure 6.16: CAD model of SEE version 3 (large). (a) Isometric view. (b) Section view.

sample, the settling torque was approximately 0.117Nm at 15°. Using these with the relevant dimensions (R_1=6mm, R_2=10mm, H=7mm), G is found as 190520Pa. A rotation of 15°, with a joint torque of 5.3Nm as was used in Chapter 5, was selected as performance target. Two set of dimensions were selected that would be able to meet the requirements; H= 5mm, R_2=22.5mm and H=1.5mm and R_2=16.6mm. One assumption that was made was that the inner radius, R_1, is 3mm. This is so the rubber component is close to the 2.5mm radius shaft that will be located in the middle of the SEE. This, which can be seen in Figures 6.15(b) and 6.16(b), will reduce the difficulty of support material removal.

Finally, the most notable difference in this third SEE design is that, due to the wider rubber component, it can no longer be enclosed in the hex fitting. This would mean the component would be much more difficult to fit within the next Wormbot, but at this early stage, it was felt it would be more important to produce a reliable device first.

Table 6.3 displays the Maxwell-Wiechert constants for the version 3 SEE's. Five SEE's were tested, two of the smaller and three of the larger version. It should be noted that, while the table indicates that the tests were performed up to 10° as expected, four of these were also tested at 15°, 3 of which broke during testing. In these, on the initial step

Table 6.3: Spring and Damping Constants across Version 3 SEEs. Values given as median ± standard deviation.

		Performance Constants				
		k_0	k_1	C_1	k_2	C_2
Large 1	1°	0.5940±0.1820	329.5040±11.2757	0.0332±0.0013	-0.0358±0.2357	1.4864±17.6042
	2.5°	0.6056±0.0406	317.0280±7.7927	0.0317±0.0009	0.0746±0.0185	0.0867±0.4211
	5°	0.6191±0.0060	0.8872±0.1556	0.1487±0.0212	-2.8316x10^{08}±0.0284	0.0103±0.1512
	10°	0.7915±0.1190	2.1524±0.1067	0.3926±0.0094	0.0602±0.0114	0.2200±0.2144
Large 2	1°	0.8564±0.0373	0.1057±124.3418	0.6326±0.3222	-1.0440x10^{09}±0.0264	0.0149±0.0699
	2.5°	1.8634±0.1032	9.9285±12.4401	0.0010±0.0012	1.7327±0.2019	0.4886±0.0135
	5°	1.1857±0.0427	36.9370±25.6372	0.0064±0.0969	0.7591±0.3665	0.2106±0.1076
	10°	1.8634±0.1032	9.9285±12.4401	0.0010±0.0012	1.7327±0.2019	0.4886±0.0135
Large 3	1°	0.7110±0.2261	0.0604±0.3413	0.3857±0.1475	0.0187±0.0258	0.1407±0.4936
	2.5°	0.6788±0.0372	0.0370±0.0306	0.2444 ±0.5177	-1.0891x10^{08}±0.0017	3.3293x10^{05}±0.0112
	5°	0.6686±0.0681	224.2625±14.9287	0.0224±0.0015	0.1872±0.0515	0.0628±0.7585
	10°	1.0709±0.1059	0.9448±0.4503	0.1883±0.0791	0.8027±0.3402	0.1600±0.0693
Small 1	1°	0.9679±0.0668	256.0303±131.2199	0.0314±0.0044	0.1151±0.0622	0.1393±0.0897
	2.5°	1.1050±0.0716	190.3126±29.3630	0.0190±0.0030	0.4918±0.0681	0.2199±0.0259
	5°	1.6289±0.0890	72.2284±60.9976	0.0150±0.0144	0.7836±0.1174	0.3191±0.0389
	10°	2.0533±0.1792	29.5690±12.6113	0.0030±0.0013	1.5776±0.1829	0.4574±0.0222
Small 2	1°	0.5255±0.5323	0.0845±175.6711	0.0424±0.0289	0.0416±0.5305	130.1883±62.8351
	2.5°	0.7353±0.0318	314.6835±100.3730	0.0317±0.0020	0.0126±0.0251	0.0173±0.0197
	5°	1.3113±0.0800	66.2005±16.9718	0.0067±0.0017	0.8217±0.0491	0.2188±0.0068
	10°	1.7353±0.2206	7.9859±7.9819	0.0008±0.0008	1.7908±0.2126	0.4362± 0.0516

up, an endcap would fracture where the key was forced into the keyway. This can be seen in Figure 6.17.

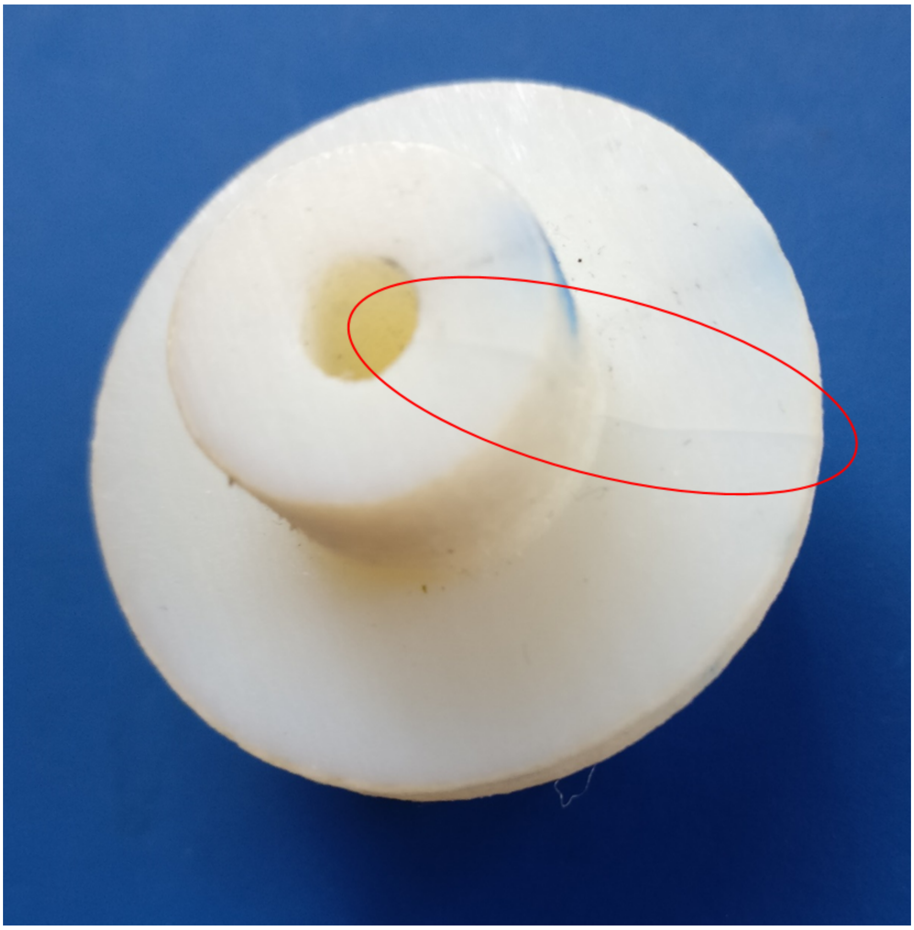

Figure 6.17: Damage to Version 3 SEE during testing. Faint crack in plastic endcap can be located by circle

It can be seen from Table 6.3 that, once again, that the constants are not behaving as expected. k_0 appears to increase as the angle increases. However, it was visible that the keyway end cap was not maintaining its position due to the key moving in the keyway. If the keyway has a set amount of movement before providing resistance to moving, as the overall rotation increase, more rotation will be performed by the rubber component. This could be responsible for the increasing k_0 value as the angle increases. This would also explain the low torque responses in which, if the final torque was the 5.3Nm intended, k_0 would be 30.37Nm/°.

6.3.4 Series Elastic Element Version 4: Hex Socket Fittings

The second version of the SEE seemed to be let down by the performance of the keyway. Therefore, version 4 of this SEE has removed this and replaced it with an additional hexagonal fitting, as shown in Figures 6.18 and 6.19. This version not only avoids the troublesome keyway but is also a lot more robust, which should prevent the same sort of breakages that occurred in the previous version.

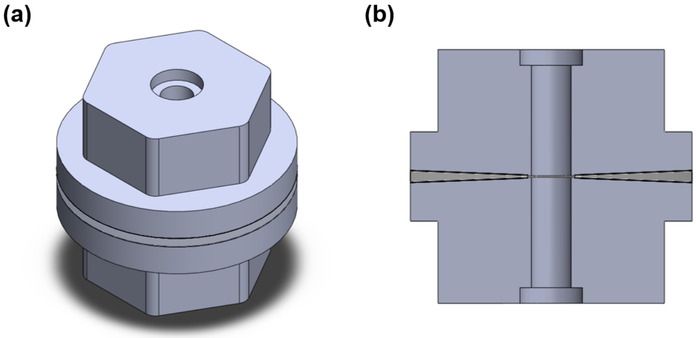

Figure 6.18: CAD model of SEE version 4 (small). (a) Isometric view. (b) Section view.

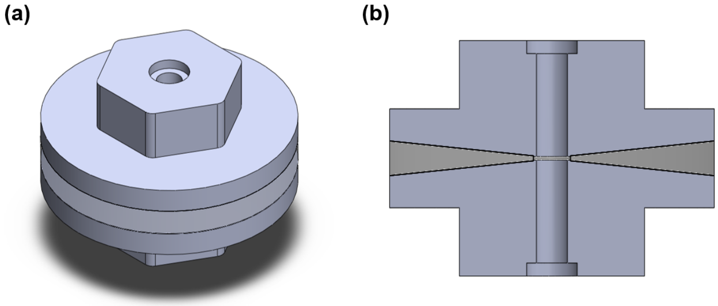

Figure 6.19: CAD model of SEE version 4 (large). (a) Isometric view. (b) Section view.

Using two hexagonal fittings means that a new fitting method is required for one end of the testing rig. This method can be seen in Figure 6.20.

It involves a metal bar with one end shaped to fit into another hex socket for the SEE. The other end is cut to fit between the pneumatic jaws of the Instron, with a central triangular ridge to ensure it is located at the centre of rotation.

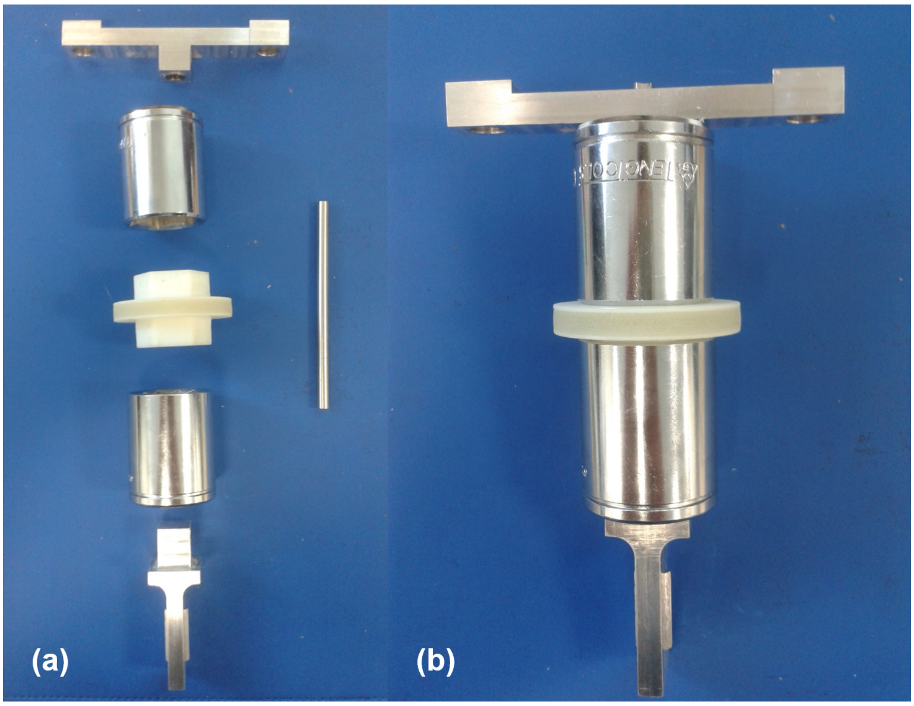

Figure 6.20: Framework used for fixing Version 4 SEE into Instron E10000. (a) Individual components. (b) Assembled.

The dimensions of the rubber component are the same as they were for the last set of tests, which should give a set of results to draw a direct comparison between the two support structures, while having a set of known targets to aim for.

Tables 6.4 and 6.5 display the constants for the Maxwell-Wiechert model for each test, varying the test sample and rotation angle as has been done previously. The constants seem to be more repeatable than for the version 2 and 3 SEE's, indicating that the hex fitting is more efficient at securing the end plates than the keyway mechanism. However it can be seen that k_0 is a lot softer than designed. This can be seen in Figure 6.21, where the resting torque is a lot lower than the target of 5.3Nm at 10°, though the smaller SEE is slightly closer than the larger one (45% of the target torque in comparison to 40%).

Another point of note from Tables 6.4 and 6.5 is that once again, k_0 increases with the angle of rotation. This can be seen when comparing Figure 6.22 to Figure 6.23, where the lower angle test (2.5°) has a proportionally much lower resting torque in relation to the target torque in comparison to the large angle test (15°). This would indicate that there is, as there was with the version 3 SEE, a certain amount of rotation achievable where the

Table 6.4: Spring and Damping Constants across Large Version 4 SEEs. Values given as median ± standard deviation.

		Performance Constants				
		k_0	k_1	C_1	k_2	C_2
Large 1	2.5°	2.5400±0.5797	11.9108±2.5457	1.5091±0.0509	0.2000±0.3322	0.0590±0.7891
	5°	5.5569±0.2923	19.2804±0.9525	2.2298±0.0529	0.7744±0.1132	2.0086±2.1043
	7.5°	9.0247±0.2218	27.9777± 0.2697	3.1741±0.0209	1.3617±0.0606	2.2891±0.2358
	10°	11.5134±0.0433	34.6537±0.4919	3.7522±0.0397	1.9999±0.0348	2.4747±0.0892
	12.5°	12.9528±0.0574	39.1329±0.5512	4.2648±0.0472	2.0088±0.0448	3.4986±0.0579
	15°	14.1250±0.0648	42.3669±0.8113	4.6710±0.3435	2.4733±1.2039	3.5779±3.9383
Large 2	2.5°	2.8608±0.1072	15.6648±1.2786	1.4982±0.0687	0.4064±0.1010	3.6905±1.4748
	5°	6.2838±0.2825	18.6727±1.8993	1.9500±0.0641	1.0762±0.2193	1.1761±0.2115
	7.5°	9.5522±0.1064	24.4933±0.4025	2.7154±0.0303	1.2941±0.0323	2.4947±0.0229
	10°	11.7461±0.0880	30.3953±0.4671	3.3086±0.0393	1.7042±0.0467	3.0766±0.1175
	12.5°	13.2625±0.0486	35.4601±0.5247	3.8362±0.0433	1.9694±0.0384	3.4625±0.0879
	15°	14.3164±0.0702	38.6630±0.7324	4.1702±0.0657	2.0849±0.0550	3.6066± 0.0738
Large 3	2.5°	5.7930±0.3611	12.2648±1.0135	1.3425±0.0206	0.9277±0.1615	2.6215±0.3060
	5°	9.7342±0.0773	18.0347±0.5886	2.0421±0.0499	1.3487±0.0137	2.5956±0.5075
	7.5°	11.9600±0.0969	24.4555±0.4210	2.6127±0.0171	1.7648±0.0383	3.0006±0.0294
	10°	13.5832±0.0484	29.7747±0.1908	3.2127±0.0129	1.9805±0.0165	3.4302±0.0548
	12.5°	14.6535±0.0656	34.6584±0.3576	3.7100±0.0314	2.1301±0.0338	3.6467±0.0730
	15°	15.4638±0.0713	37.8794±0.5103	4.0456±0.0432	2.2055±0.0415	3.8150±0.0452

Table 6.5: Spring and Damping Constants across Small Version 4 SEEs. Values given as median ± standard deviation.

		Performance Constants				
		k_0	k_1	C_1	k_2	C_2
Small 1	2.5°	7.7607±0.5975	10.8155±0.4169	1.2973±0.2232	1.2330±0.6267	4.56853±3.6780
	5°	9.7691±0.1578	15.4290±0.1757	1.7506±0.0109	1.4988±0.0663	3.0680±0.0817
	7.5°	11.4143±0.2185	20.8973±8.9536	2.3680±0.0728	1.7118±9.2793	3.1343±0.4687
	10°	13.1535± 0.0996	26.2557±0.2876	3.0950±0.0234	1.5523±0.0738	3.2749±0.0342
	12.5°	14.9153±0.1010	30.3373±4.4180	3.8117±0.3945	1.4075±3.7791	2.8637±0.8053
	15°	16.5152±0.5864	33.7192±4.2620	4.5478±0.5845	1.1517±3.5597	2.8939±9.1890
Small 2	2.5°	7.6841±0.5093	12.9174±1.0737	1.1675±0.3040	1.5267±0.8968	2.9643±3.6645
	5°	10.7227±0.1244	17.2905±0.2256	2.0159±0.0771	1.5414±0.1846	6.0530±1.4906
	7.5°	12.7905±0.1089	23.0837±0.2817	2.6411±0.0258	1.6515±0.0421	3.2881±0.11333
	10°	14.3474±0.1321	28.2189±0.3804	3.3349±0.0407	1.5737±0.0435	3.1758±0.04372
	12.5°	15.8708±0.1705	32.2354±0.4991	4.0635±0.0551	1.3674±0.0427	3.0044±0.0506
	15°	17.0907±0.8205	29.0840±1.9692	4.2700±0.3062	7.7666±1.5167	1.1422±0.2164
Small 3	2.5°	7.1209±0.7224	8.5861±0.9654	1.3298±0.1731	0.9945±0.7865	1.9375±39.0458
	5°	10.3440±0.1611	13.6995±0.1676	1.4338±0.0127	1.5478±0.0640	2.5519±0.0078
	7.5°	12.1582±0.1471	18.2284±7.8971	2.0666±0.3249	1.7001±7.8131	2.5756±0.3147
	10°	13.8301±0.0589	23.7316±0.0540	2.8319±0.0061	1.5394±0.0132	2.8572±0.0562
	12.5°	15.5156±0.1189	28.4141±0.4348	3.6264±0.0500	1.3354±0.0329	2.4610±0.0632
	15°	17.0824±0.7377	31.7456±5.2069	4.2809±0.5652	1.3272±4.7528	2.5504±0.6075

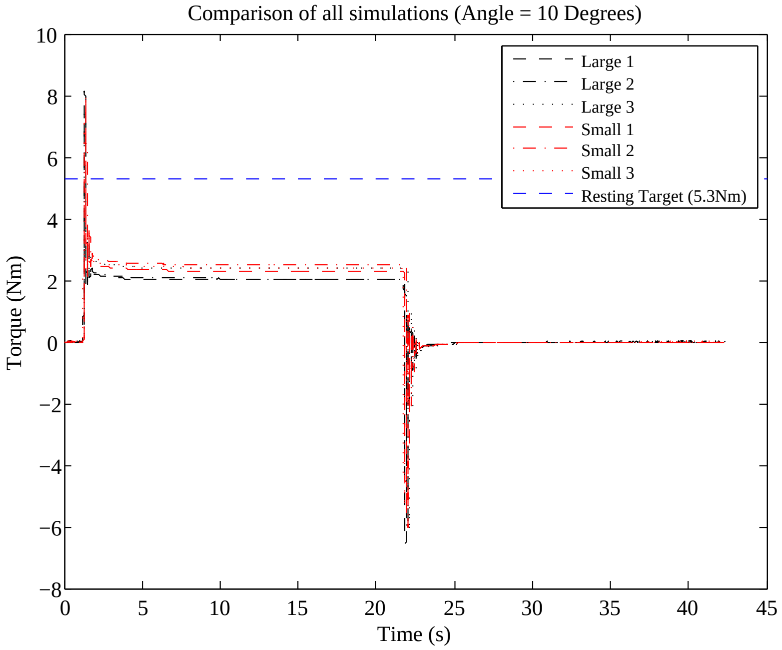

Figure 6.21: Comparison of simulated fits to all Version 3 SEEs when angle = 10°.

two end plates can rotate in their sockets before the rubber element is loaded. However the two plastic hexagonal fittings were designed to have a very tight fit with the sockets that held them. This suggests that the 3D printed plastic used may not be holding it's shape and deforming during tests. It is worth noting that no elastic material is infinitely linear, but there is no doubt that the performance here does not match the behaviour of the version 1 SEE.

It is also worth noting is that each test performed on the smaller SEE at 15° has a slightly lower settling torque (seen in Figure 6.24), potentially Appendix B), and this does not occur when the SEE is tested at 12.5°, as can be seen in Figure 6.25.

This eventuality was discussed in earlier in Chapter 6.2.2 and the potential failure of the device can be used to find the potential highest safest working strain with Equation 6.6. With the highest safe rotation angle of 12.5°, H=1.5mm and R_2=16.6mm, the maximum safe strain measures at 2.41. Considering there may be some additional movement between the plastic hexagonal fittings and the sockets, this safe strain maybe slightly less. In this eventuality, this can be recalculated.

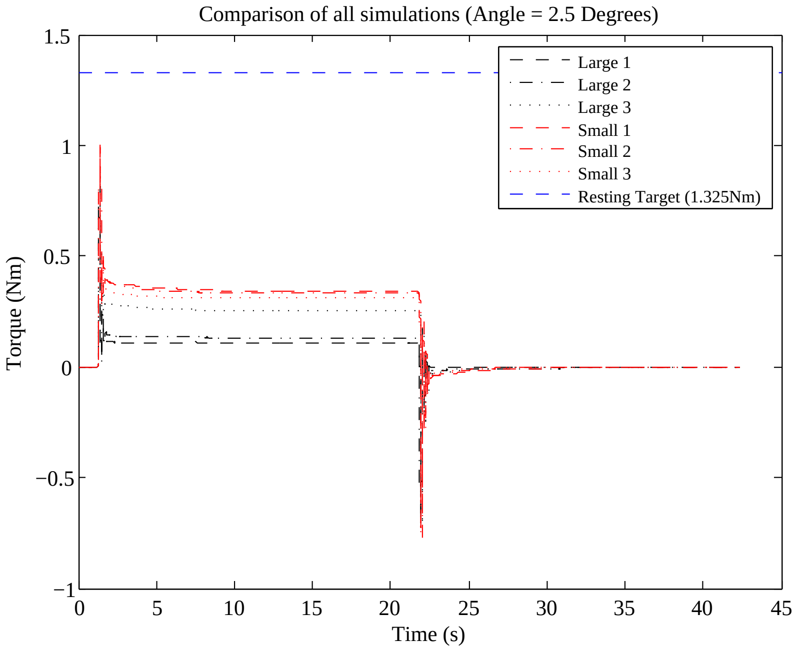

Figure 6.22: Comparison of simulated fits to all Version 3 SEEs when angle = 2.5°.

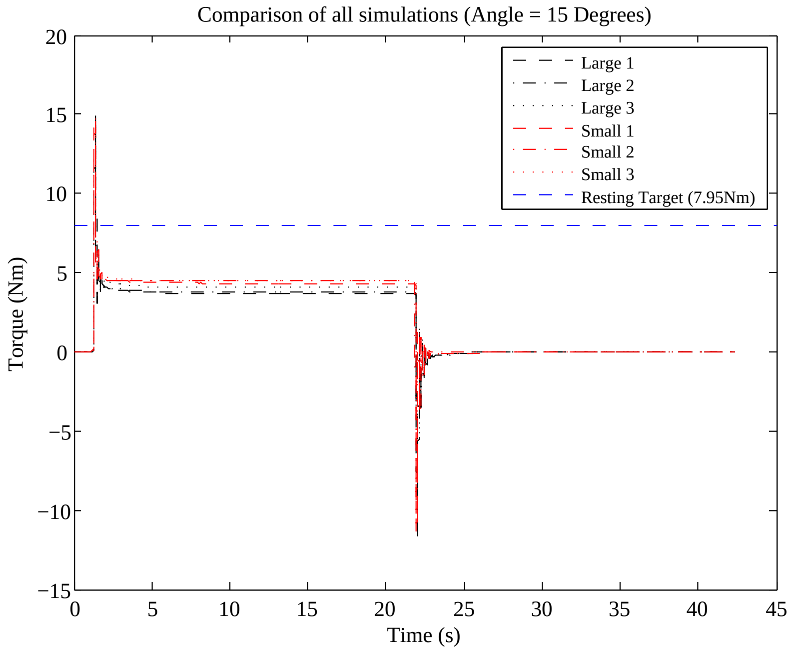

Figure 6.23: Comparison of simulated fits to all Version 3 SEEs when angle = 15°.

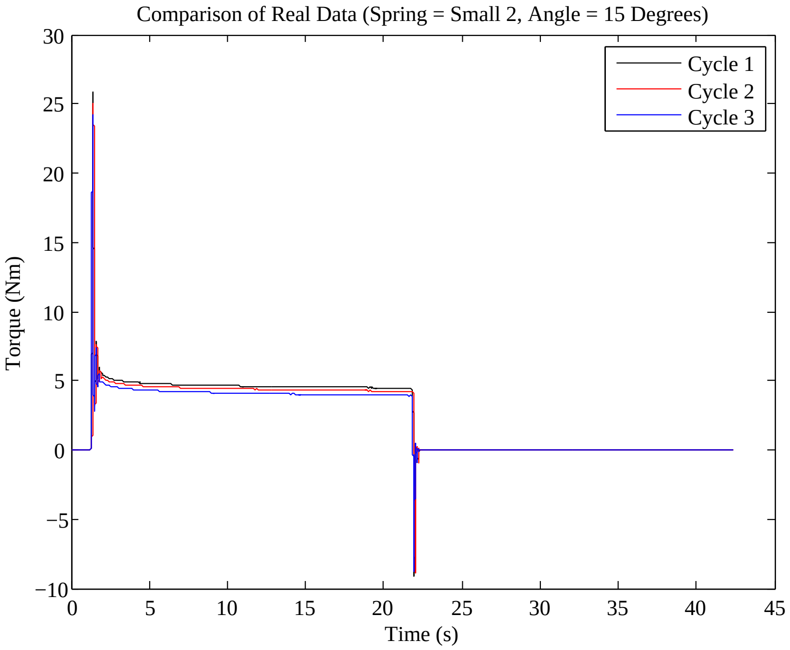

Figure 6.24: Comparison of simulated fits to all Version 3 SEEs when angle = 15°.

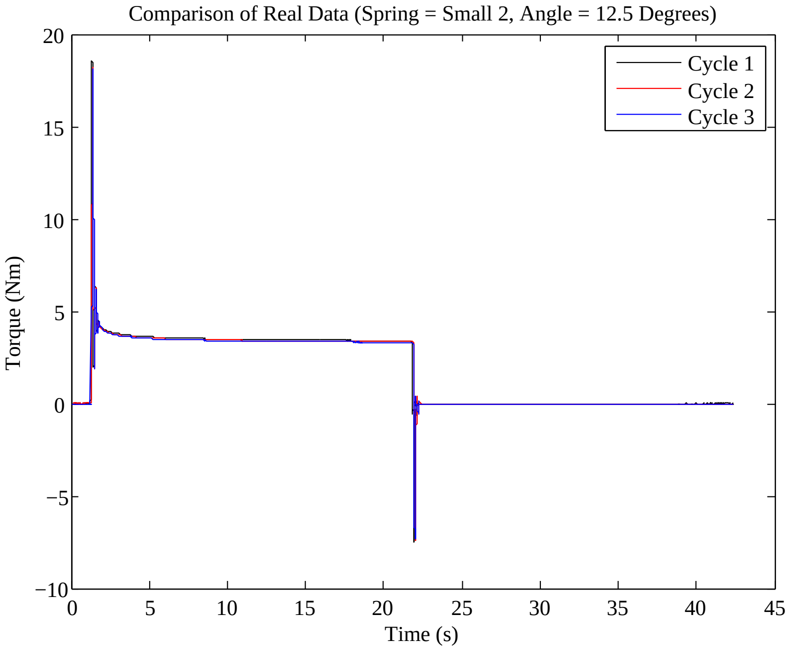

Figure 6.25: Comparison of simulated fits to all Version 3 SEEs when angle = 15°.

6.3.5 Series Elastic Element: Plastic Support Analysis

In both of the previous versions of the SEE, the main spring constant k_0 was often much softer than anticipated. Additionally, the spring constant increased with the angle of rotation, which indicates that the spring is getting stiffer as it rotates more, which goes against the linear spring behaviour found with the first version of the 3D printed SEE. This may be due to the plastic end cap not maintaining a secure connection with the mounting framework, which in turn could be due to a softer plastic than expected. To test this, a 3D printed element was created with no rubber element. The two end plates were fixed to each other, as seen in Figure 6.26.

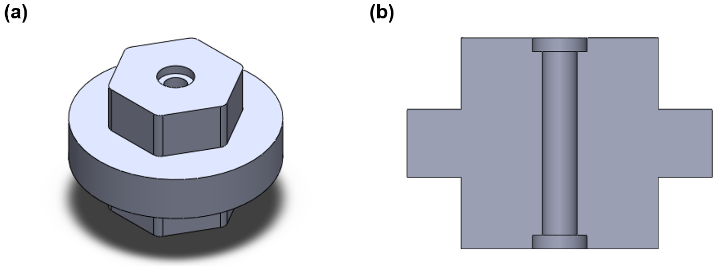

Figure 6.26: CAD model of Solid SEE. (a) Isometric view. (b) Section view.

The solid component will be subjected to the same step tests the standard SEEs undertook, albeit at lower angles of rotation (up to 5°). Theoretically a perfectly stiff material would have a spring constant of ∞. In practice a very high value of k would be expected of the solid device, or for it to fracture during testing. The results of this can be seen in Figure 6.27.

Figure 6.27 displays the torque against angle graph of 3 versions of the test previously described in this section. This test was performed on multiple occasions because it can be seen that the original test performed poorly. It required virtually no torque to rotate the sample up to around 4°, and then the torque only rose relatively slowly with the increasing angle up to 5°. This could partly be due to a softer than expected material, but the period of almost zero torque indicates there may be a loose fitting somewhere in the support structures. Therefore a second test was performed where all connecting surfaces were coated with a thin varnish coating. In Figure 6.27, it can be seen that this was an improvement as the gradient between angle and torque was steeper, though not enough to give the impression that the device was completely rigid. Additionally, there is

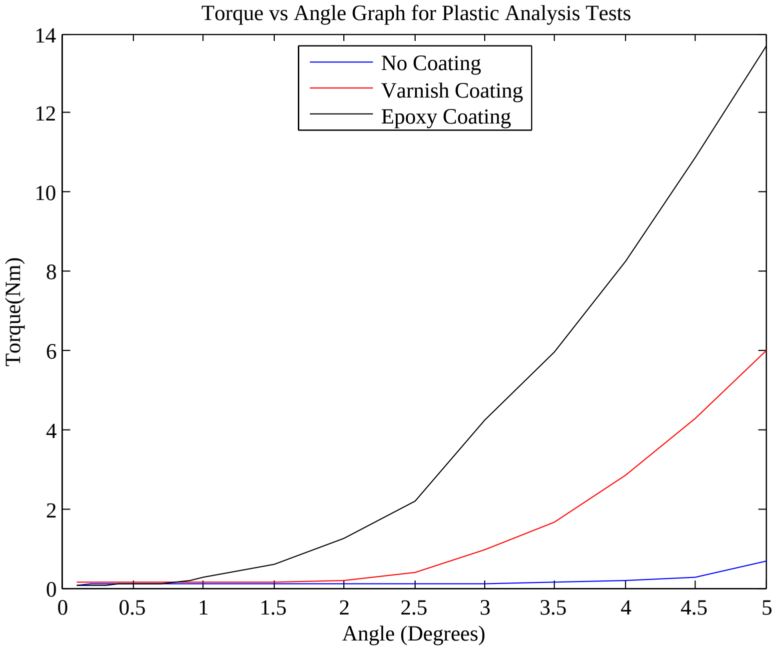

Figure 6.27: Graph displaying the Torque vs Angle relation when testing 3D printed rigid element

still a period of about 1.5° where the torque stays at almost zero. The test was performed one last time but this time using epoxy resin as the coating. This only has a low torque period of about 0.6° and has a steeper torque angle line. These results do back up that the performance of the 3D printed plastic is not as rigid as previously expected.

6.3.6 Series Elastic Element: Arms Characterisation

The finding that the support plates are not behaving as expected is less than ideal for producing a compact linear SEE. It wouldn't be possible to ensure a spring was performing linearly if the support structure holding the device wasn't perfectly solid or performing linearly itself. It is at this point that attention should be brought to the first version of the SEE. Its performance was linear when the two end supports were clamped in position, though there would have been flex in the hard plastic. This will be because there will have been no part rotation between the component and the pneumatic jaws of the Instron testing instrument. Therefore, it was decided that the same process in Chapter 6.3.5 would be performed but with the arms supports instead of the hexagonal fitting. This can be seen in Figure 6.28.

The spring constant of the supports would then be analysed and used as a spring in

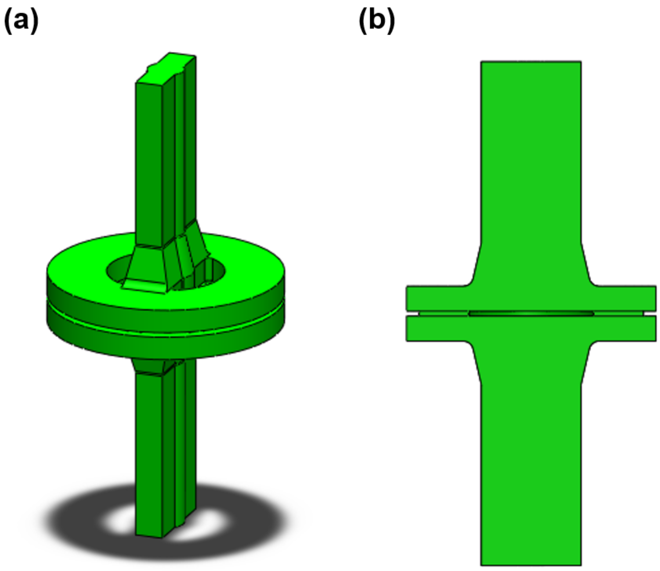

Figure 6.28: CAD model of Solid SEE with arm fittings. (a) Isometric view. (b) Section view.

series with rubber SEE when predicting device behaviour in future. A graph displaying these results can be seen in Figure 6.29.

It can be seen from Figure 6.29 that, while there is a bit of variability at lower angles, the spring constant stayed relatively constant, which makes modelling the whole system easier. The average optimised spring constant was 42.9983.

6.3.7 Series Elastic Element Version 5: Arm Progression

Now that the spring constant of the arms was been taken into consideration, it can be used when predicting the dimensions of the next SEE. The program used is the same, but there is a slight difference when calculating the settling constant. When the user inputs the desired properties, the spring constant should be representative of the whole device. Equation 6.7 displays the equation for calculating the overall spring constant with springs in series.

$$\frac{1}{k} = \frac{1}{k_1} + \frac{1}{k_2} \tag{6.7}$$

In this instance, k is the overall constant defined by the program user, k_1 is the rubber

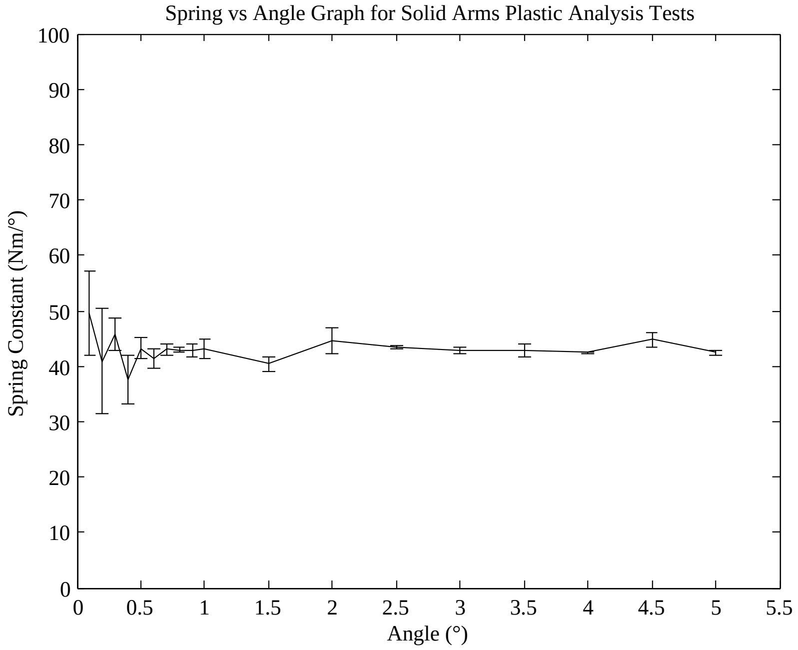

Figure 6.29: Graph displaying the Spring Constant vs Angle relation when testing 3D printed Version 1 rigid element

component and k_2 is the arms. This can be rearranged, as k and k_2 are known, to find what k_1 needs to be. It is this that the program will give dimensions for. Another small alteration that was used was the value of the shear modulus G, which was reverted to the original value found for the Version 1 SEE.

Using the dimension prediction software, it was felt that a settling spring constant, or k_0 in the Maxwell Wiechert model, of 30Nm/° should be aimed for as this was an ideal value found in Chapter 5 . This meant that, at the 5.3Nm of the servo motor selected, the device should be rotating approximately 10°. An SEE with all these attributes fitting within the original sized arms framework whilst keeping below the strain limit established in Chapter 6.3.4 was found to be impossible. Therefore the outer radius (R_2) was extended to 35mm and a outer thickness (H) of 4.2mm. This however meant that the size of the plastic end plate had to expand slightly, as can be seen in Figure 6.30.

Table 6.6 and Figure 6.32 display the spring constant in relation to the angle of rotation and the torque response at each angle respectively. It can be seen from both graphs that, once again, this design of SEE performs linearly within the intended range of operation of 10°. This SEE was tested at 12.5° although the arms supports broke at the base of the arm at this angle of rotation, which can be seen in Figure 6.31.

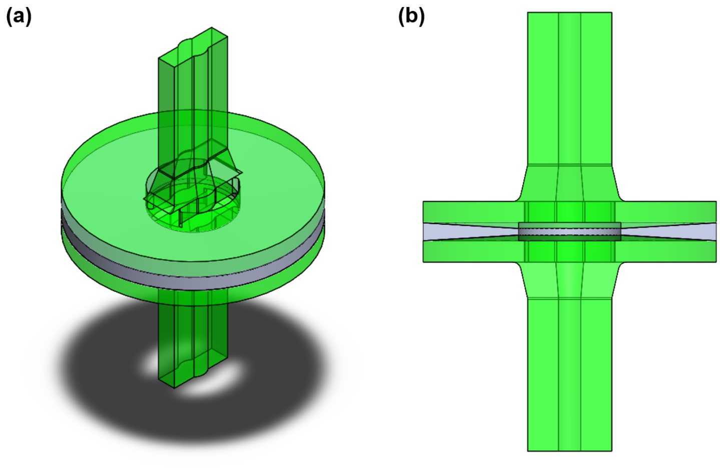

Figure 6.30: CAD model of SEE version 1.1. (a) Isometric view. (b) Section view.

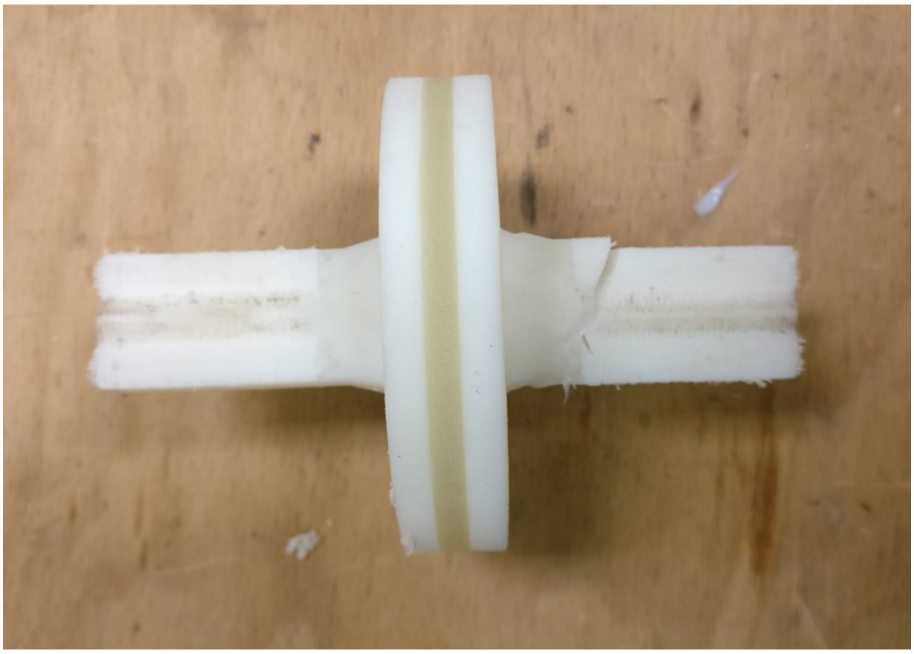

Figure 6.31: Damage to Version 1.1 SEE during testing.

Table 6.6: Spring and Damping Constants across all Version 5 SEEs. Values given as median ± standard deviation.

		Version 1.1 SEE				
		k_0	k_1	C_1	k_2	C_2
SEE 1	2.5°	46.220±1.411	13.333±1.488	13.893±23.369	8.287±3.956	126.537±68.692
	5°	46.611±0.339	15.769±0.952	11.224±0.620	7.358±0.058	94.963±9.691
	7.5°	45.929±0.073	15.047±1.336	10.875±0.839	7.092±0.151	92.237±4.778
	10°	45.079±0.013	14.543±0.866	10.539±0.506	7.025±0.111	92.885±2.712

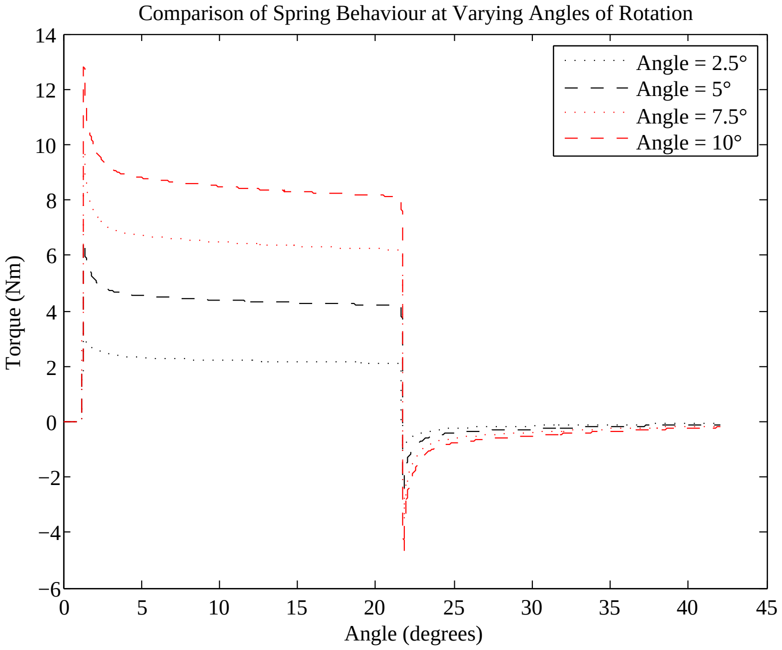

Figure 6.32: Comparison of simulated responses for Version 5 SEE .

Unfortunately, while the linearly performing SEE is positive, the average spring constant is measuring at 46Nm/°, 16Nm/° higher than intended.

6.4 Discussion

SEE version 1 was developed as a method of testing the 3D printed rubber element to see if its performance was repeatable and linear. These were two very important areas as there is little point in being able to change dimensions of a component for a set task when the changes intended are not reliable. Furthermore, the simulation software in Chapter 5 employed a spring constant for the compliant elements at the joints that performed with the spring constant regardless of the angle. If this consistent linear spring performance cannot be repeated then either the performance will not be as predicted, or the complexity of trying to simulate the non linear springs increase significantly.

The initial results indicated that these two characteristics were met. It can be seen from Table 6.1 that the resting torque spring constant, k_0 remained very predictable in both aforementioned areas of importance. With both sizes of SEE, the difference between k_0 of the two samples of the same sized component only varied by 2.2% in the larger SEE and 3.7% in the thinner SEE. Additionally, each spring was able to perform linearly, with the change of k_0 with the increase in angle never being more than 1.7%, indicating a very promising linear performance. The other constants of the Maxwell Wiechert model were generally fairly reliable too, with the exception of k_2 in the thinner SEE, although Figure 6.9 displayed that this had very little effect on the resultant ideal step responses. These initial results indicated that 3D printed rubber-like materials could potentially be used for SEEs. It was also seen in this experiment that thicker rubber SEEs were softer in performance, which was as expected, as there would be greater length of material to rotate.

SEE version 2 was initially an attempt to produce a small, contained SEE that would easily be able to fit within a small gear that could be used in a future version of Wormbot, with an 80mm diameter body. The design, in theory, fit the description, fitting inside a 36mm diameter gear. However, the results proved that the performance of this did not match that of the first version. It was not surprising that the SEE dimensions used produced a much softer element, due to the greatly reduced outer radius. The extent of reduction in k_0 however was a lot more than anticipated, and can be seen in Table 6.2. There was also more variation in results, especially with k_1, C_1, k_2 and C_2. It was felt that these poor results may be due to the keyway of the SEE not encapsulating the key, which may allow unwanted movement in the whole SEE framework, not just the rubber element. However, the next version was not much of an improvement. With rubber elements expected to have k_0 of 30, the highest value was found to be just over 2. Additionally, it was found that the spring constant was lower at smaller angles of rotation. This could be explained by a loose fitting keyway. At lower angles of rotation, the amount of freedom in the keyway will take a greater percentage of the entire movement. As this angle of rotation increases, the keyway freedom accounts for less of the overall rotation, meaning the rubber component is taking more strain, increasing the spring constant.

The third version of SEE was designed to feature a more efficient method of fixing the end plates of device. However Tables 6.4 and 6.5 show that the same problems were still occurring although not as severe. The values of k_0, which were supposed to be 30, only once got above half of the intended value. Once again, the value of k_0 increased with the angle of rotation. To investigate this, a series of tests were performed with a solid version of the device, analysing if stiffer coatings had an effect on performance. Figure 6.27 displayed that this was indeed the case, with the SEE performing much more efficiently with stiffer coatings on all connections. This implies that the coatings have helped create a better fit, but what can also be seen is that when a gradient is formed in each test, the samples with stiffer coatings had more gradual torque-angle lines. This indicates that the plastic is deforming and therefore not behaving adequately.

This finding however influenced the redesign of the original 3D printed SEE layout. If the plastic end caps had behaved like this, the arms in the original design must have too. Therefore these were analysed and given a spring constant, which was then integrated into the design of the final SEE. This, once again, produced a linear performing spring, as can be seen from Table 6.6. However, the overall spring constant of the device was 46, a lot stiffer than the intended 30. This could be down to a few reasons. The plastic end plates are slightly larger than the size tested in Chapter 6.3.7 which could have increased their stiffness. Additionally, the shear modulus used was from a SEE with a slightly different cross section. The tapered design used here matched the cross section of the tapered displayed in Figure 6.2, with the tapered edges coinciding in the centre. The shear modules used was from a experiment where this wasn't quite the case, and the tapers not quite meeting in the centre. This may have also had enough of an effect on the shear modulus not quite being as accurate as it could be. In addition to this, the shear modulus usually refers to a single material, but as this device is being analysed as one unit, the shear modulus relates to the mixture of two materials. As the dimensions of the rubber element change, the percentage of one material in relation to the whole device changes, which will in turn alter the shear modules again.

6.5 Conclusion

The aim of this chapter was to analyse the potential for producing and improving 3D printed SEEs. Fairly early on in proceedings, it was found to be possible to produce repeatable, reliable SEE's for testing purposes, as Table 6.1 showed. However, problems occurred in two main areas. Firstly, reducing the size of the SEE to dimensions that would be usable in the future Wormbot proved to cause issues with inadequate performance. Secondly, while the first version of the 3D printed testing SEE was repeatable, it proved difficult to produce an SEE that could perform to specification.

These two issues boil down to the same issue; the 3D printed plastic used as the plates either side of the rubber element. It was found that the plastic material was compliant in itself, meaning that to accurately define how the SEE as a whole will behave, the plastic parts must be considered in the model as well. This drastically increases the complexity of the device, making it more difficult to accurately predict its performance. Furthermore, if the device has to be downscaled to fit within smaller spaces, the plastic supports need to change shape and become smaller, which makes them thinner and in turn, more compliant. This means that, while the performance of 3D printed rubber like materials may well be suitable for use in reliable, customisable SEEs, the plastic material used to support must also be taken into account in detail.

Chapter 7

Discussion and Conclusion

In this section, the overall results of this research will be discussed, encompassing all of the main areas of the research. The potential for using 3D printing technology for producing compliant actuation methods will be discussed, as well as how using the simulation process in tandem could benefit the field. The original aims and objectives will then be discussed, along with any potential future work that could be undertaken.

7.1 Discussion

7.1.1 3D Printed Compliant Actuators

Modern 3D printing has provided a number of new capabilities in recent years, one of which was the ability to print with more than one material. This meant that 3D printing compliant, flexible components was now a viable option. The aim of this research was to explore whether these developments are viable enough to be considered feasible for use in the field.

The first area of focus in this chapter will be the production of Series Elastic Element, or SEE. The main advantage of 3D printing over the original method of producing this style of SEE was the ease and speed of production. The original device was produced by moulding the central rubber component and then bonding it to two metal plates [77]. The process of production is much quicker with 3D printing and it is also much quicker to alter a design, with no need to produce a new mould.

Initially, the potential for 3D printing this device seemed very positive, with the first test sample proving to behave linearly in tests. Having an ideal linear spring was an area that Rollinson et al aimed for as well [77]. It means that the behaviour of the spring is predictable, which makes modelling the device much easier. Furthermore, this was repeated over multiple prints of the same component, meaning that multiple SEEs could be produced for many joints in the same robot, and each joint would behave almost identically.

Unfortunately, later results were not as positive. Producing smaller SEE's to fit within a smaller version of Wormbot caused a number of problems. Firstly, it was found that the plastic support material was more flexible that expected. This meant that predicting how the device would behave would become drastically more difficult. The original device by Rollinson will have been more effective as two metal plates will have been much more rigid, meaning that the spring constant would purely be controlled by the rubber element [77]. When the end components themselves have some spring like properties, the size of every section of the device affects the performance.

The second problem was trying to create a secure fit between the plastic and any supporting structures This will be in part due to the imperfections of the plastic material used. For example, we could see from Figure 6.17 that when a keyway was used, the plastic material broke before the key itself. This indicates that the plastic structure was weaker than required, and when the load was put through a small key piece, the end plate deformed and cracked. Furthermore, it was noted that when coatings were applied to the plastic, the components performed much more desirably.

These findings have indicated that, while in principle, producing a reliable, linear SEE using 3D printing is achievable, the quality of plastic material that can be used in multi material printing is currently not suitable. If a different, stiffer plastic was available then this concept would become a lot more feasible. Using the stratasys Objet 1000 available for use, there was a higher quality ABS like material available. However, the printer in question can only use two types of material at one time. The ABS material required two different component materials being used together, so using the rubber material together with this was not possible. Potentially, using coatings with the plastic material to produce a stiffer support structure is possible, but one of the benefits of using 3D printing was to cut down on manufacturing time. Applying a coating to each device would increase this time, reducing the benefit of rapid manufacturing.

The alternative device that was produced was the 3D printed pneumatic bellows. These were seen as ideal for larger hypermobile robotic application by Granosik for their high power output and their ability to reduce in size to save space [39]. This was confirmed by the theoretical design work in Chapter 3, where pneumatic solutions were found to have preferable torque potential; potentially greater than the torque output proposed by the servo and gear combination selected in Chapter 5.

3D printing pneumatic bellows has the same benefits as previously discussed, in that manufacturing speed is relatively fast. The ability to alter designs quickly is also advantageous, as it meant that the 3D bellows could be adapted on multiple occasions before being tested. It also meant that features that would otherwise be much more difficult to produce could be made with ease. This includes the strengthening rings that were located within the wall of the third 3D printed bellows, which otherwise would potentially need a break in the wall to fit in the correct position.

While the issue with the 3D printed SEE was the quality of the plastic material, the bellows main issue was the strength of the rubber-like bellows. These, under pressure, ballooned far beyond the intended size parameters and burst open. This could be solved in the future by using a netting or mesh to prevent ballooning, as used by Granosik [41].

It was found during this research that both methods had their flaws, though it was felt that the SEE's had slightly more potential for use in any future version of Wormbot for a number of reasons. Firstly, the use of pneumatic bellows lends itself to designs with a larger cross-section for a greater force output. As the aim is to eventually downscale the size of Wormbot, the potential for using bellows could seem slightly counter-productive, especially since the need for an air supply, pump and regulator amongst other components all need to be considered. Furthermore, while it proved difficult to accurately produce a compact SEE with a particular spring constant, it was possible to produce a larger test SEE. While the bellow could realistically be improved in the future, at the time of testing a working bellow was not achieved. Even if it was, achieving compliance to a specific linear spring constant could be difficult.

7.1.2 Simulating the Ideal Compliant Joint

It was felt that it was one thing to know if a component could be made to behave precisely as designed, but it would be desirable to know how that component would affect the behaviour of the robot as a whole. The idea of using simulation for hypermobile robotics is not new, and it was felt it could greatly benefit the production of 3D printed compliance components [38]. To test the system, a number of environments were constructed to discover how different surroundings would affect the ideal amount of compliance. These were an open environment, two types of narrowing channels designed to constrain movement, and two different sizes of maze.

It was found that for navigating narrow passageways, softer springs were more suited to the task due to the ability to comply to the environment. However, results at this end of the spectrum were also slightly more unpredictable, which can be seen in Figure 5.30. Here, the softer spring also achieved the largest range of results as well as the smallest amplitude. On the other side of the spectrum, in open space softer springs were detrimental to performance, due to the springs deflecting more when it wasn't required, resisting forward movement. However, it was found that beyond k=30Nm/°, there was no improvement in speed of movement, indicating that there would be no need to produce a stiffer compliance mechanism than this. For the mazes, optimal spring constants seemed to be between k=20Nm/° and k=30Nm/°.

These results indicate that there is a requirement for producing components that provide specific amounts of spring compliance. The results show that if you are sending the robot into a very confined space, like a pipe, softer joints will be more suitable. If the test environment is less restraining, a spring constant of k=20Nm/° - 30Nm/° would be more applicable. This lays more weight to the argument that Series Elastic Actuation (SEA) with a motor driven system can benefit from SEEs with interchangeable levels of compliance. This supports the need for 3D printed SEEs. If a robot was needing to be tested or used in an unknown environment, an SEE of k=20Nm/° could be used. If it was then found that certain areas of the environment were inaccessible, new components could be manufactured quickly. With moulded SEE's, the process would take longer. However, while the initial results have given an insight into what is achievable, there is much room for additional research, with the potential to simulate with a wider range of environments where a hypermobile robot could be used.

7.2 Conclusion

This thesis described the process behind researching compliant actuation systems for hypermobile robotics. This section will return to the original aims and objectives, describing how each point was undertaken.

The literature review provided an insight into the world of hypermobile robotics, and the range of different approaches. These ranged from anything from search and rescue robots to continuum arm manipulators. Most applications used either pneumatic or motor driven solutions for joint actuation, though smart materials and hydraulics were also used. Pneumatic bellows feature inherent compliance, giving them an advantage. However, a wide range of solutions had been applied to other actuators, some of which were relatively large and infeasible for the task at hand, but some were small and efficient, from basic springs to cradles for the motor to sit in.

A wide range of solutions were then proposed using theoretical models. These were based around five different types of actuator; pneumatic bellows, pneumatic muscles, SMAs, SMA springs and motors. These took the arrangement of the actuators into consideration, such as with design II for SMAs, where a series of pulley points were used to increase the effectiveness of the small contraction stroke of the actuator. From this work it was found that SMAs and SMA springs were well suited to small applications but were not applicable for hypermobile robots on the scale that was envisioned for this project. Pneumatic solutions were suited to larger applications due to their force output being directly linked to their cross-sectional area. Motors were thought to be suitable for a wide range of applications due to the large range available for purchase. It was decided that, going forward, a motorised solution should be developed for this reason, as well as pneumatic bellows. Bellows were chosen over pneumatic muscles because, despite the slightly lower force output of bellows, the muscles had a steep force drop off in performance when approaching full actuation length.

3D printed solutions for each of these two areas were produced using a stratasys Objet 1000 printer. The first of these was a pneumatic bellow, which included strengthening rings embedded within the wall of the bellow. However, these did not prove to be effective, with the rings fracturing and the bellow wall bursting in low load and higher load tests. On the other hand, the initial tests for the SEE, intended for eventual use with a servo motor, were found to be very positive. It was found that the SEE had repeatable performance across multiple prints that could be characterised using a five part spring-damper model. Both actuators had areas in which to improve, but it was decided that the SEE had more promise, with better initial results and the potential to be able to produce the devices to specific spring constants.

It was at this point that simulation software could be used to analyse how compliance could alter performance of hypermobile robots in different situations. This was especially useful considering the potential for a SEE device that could be made to specific spring constants, although specific damping performance that would match the model for the 3D printed SEEs was still unachievable. This simulation featured a half scale version of the original Wormbot; the intended size for the next version. This was tested in a range of environments, from open surfaces to narrow channels and mazes. It was found that softer springs allowed the robot to adapt to more constricting environments, though the performance is slightly more unpredictable and the robot is not as quick to travel in open spaces. This proved that producing customisable SEE's could benefit the field of hypermobile robotics, by having replaceable components that can tailor a robot for specific tasks.

Unfortunately, producing SEE's to have accurate spring constants proved to be a very difficult task. It was found, through many different design iterations, that the plastic "vero plus" material that was used along side the rubber "tango plus" material did not behave as desired. The material was found to display spring like properties, which increased the complexity of modelling the system. When predicting the dimensions of an SEE for specific spring constants, the behaviour of the plastic had to be taken into consideration. Furthermore, this imperfect plastic behaviour did not help matters when it came to achieving a secure fit between the device and other supporting components, which would be required when locating the device within the next Wormbot.

In answering the main aim of the project, it has been found that it is feasible to produce 3D printed compliant actuation methods by producing SEEs. Furthermore, through the use of simulation software, it has been found that this would be beneficial for producing customisable robots for a range of different applications. However, improvements are required to better the quality of the component before it could be reliable enough to use in the field. These areas are mainly based on improving the quality of the support structures connecting the rubber-like component of the SEE into the drive system of the robot.

7.3 Future Work

7.3.1 3D Printed Bellows

While bellows were found to be the least promising of the two proposed actuation methods for this research, there is still potential for producing 3D printed actuators of this type. These revolve primarily around the redesign of certain aspects before re-testing.

- Increasing the wall thickness, particularly at the location of the inner and outer whorls of the bellow, could help in preventing the device from bursting. Thicker walls may provide additional resistance to stretching in actuation, but the effect of this would be more suitable to consider once the device can actuate successfully.

- Using a form of outer liner, like the type used by Granosik, would prevent the device ballooning while still allowing the inner whorl to expand to increase force output [41].
- Using an end cap with an o-ring seal, or using a form of printing where all printing support material could be removed through the pneumatic supply port, would potentially allow for a more air-tight actuator, increasing the efficiency of the device.

Once these points have been met, the process of testing could restart. This could include using increasing amounts of load and measuring the rate of extension during actuation to see if there is a measurable amount of compliance to the component.

7.3.2 Simulation refinement

Simulated testing provided key information to the performance of compliant hypermobile robots in different situations. However, this was merely the tip of what could be achieved and it could prove highly valuable to the development of a future Wormbot.

- It was found when testing the 3D printed SEEs that they could be modelled using a five part spring damper model, where a spring is in parallel with two spring damper systems. If this more complex model could be applied to the simulation package, a more accurate system could be developed.
- A greater range of maps to test in would provide more valuable information. It was mentioned in Chapter 5 that using a maze with slightly larger spacing would provide more valuable information due to the increased likelihood of a head on collision with an obstacle. A maze with a more random layout, including uneven obstacles would also provide an interesting challenge. 3D environments with uneven terrain could also be developed.
- Wormbot itself could be developed and improved within the software first before testing in the real world. For example, employing a system where an operator could apply bias to the direction of movement could allow for directing the robot towards certain goals if need be. Additionally, giving the robot the potential to move in three dimensions, even if only passively, could be tested within the environment. A

simple concept for this can be seen in Figure 7.1, utilising the 3D printed rubber like material as a means of passively pitching up and down (this can also be seen in Chapter 5). The rubber blocks could be replaced with torsion beams if required.

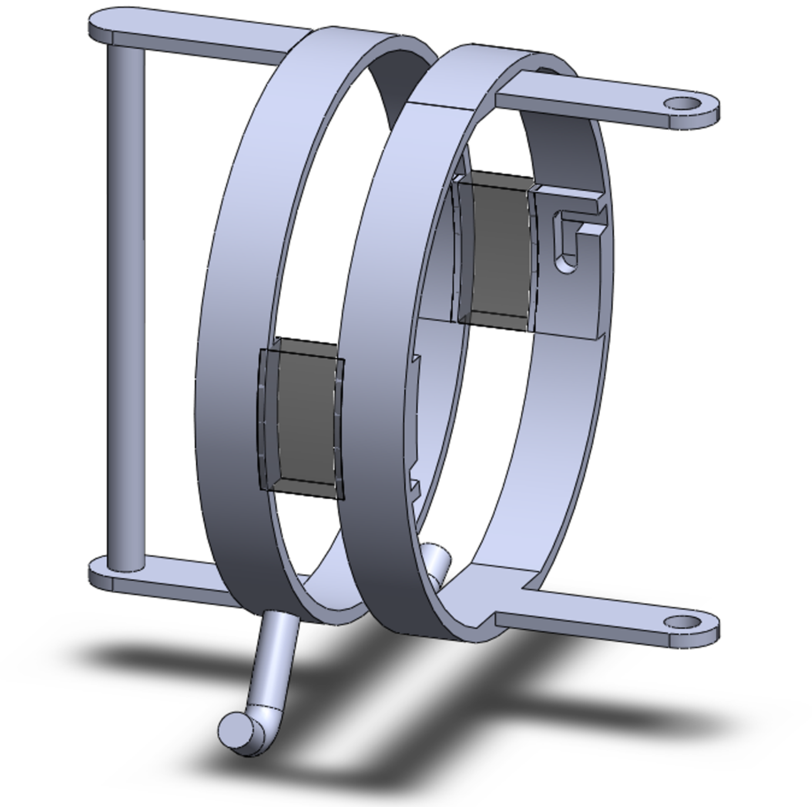

Figure 7.1: Potential Wormbot module skeleton, featuring 3D printed rubber section between the ribs to allow for passive rotation in pitch axis

7.3.3 SEE development

As more materials are developed for multi-material 3D printing, it is important to find whether these materials would have favourable characteristics stiff enough to be used alongside the 3D printed rubber component in the SEE. Until then, the best solution may be to continue where Chapter 6.3.5 left, by using coatings to improve the performance. This would extend the manufacturing process, which is undesirable. However, it does allow for more secure fittings which may improve the performance of the SEE to the point where using it within a small prototype Wormbot is feasible, with producing SEEs with a set spring constant in mind much more achievable. After this, it would be desirable to then focus on producing SEEs where the damping performance could be accurately predicted, as well as the settling spring constant.

Bibliography

[1] 1350mah 3s 11.1v 30c lipo battery details. `http://www.e-fliterc.com/Products/Default.aspx?ProdID=EFLB13503S30`. Accessed 30 June 2017.

[2] Behabelt product catalogue, 2017 - 18. `http://www.behabelt.com/en/downloads/`. Accessed 04 July 2017.

[3] Coppelia forum on linking labview. `http://www.forum.coppeliarobotics.com/viewtopic.php?f=9&t=453`. Accessed 27 June 2017.

[4] Coppelia robotics v-rep. `http://www.coppeliarobotics.com/index.html`. Accessed 22 June 2017.

[5] Dynamixel ax-18a robot actuator at trossenrobotics.com (online). `http://www.trossenrobotics.com/dynamixel-ax-18A-robot-actuator.aspx`. Accessed 10 April 2017.

[6] Flexinol® actuator spring technical and design data (online). `http://www.dynalloy.com/TechDataSpring.php`. Accessed 25 June 2014.

[7] Hpc gears: details on gear pg1-36. `https://shop.hpceurope.com/an/produit.asp?prid=195`. Accessed 30 June 2017.

[8] Ice challenger (online). `http://www.icechallenger.com/icechallenger`. Accessed 04 February 2014.

[9] Instron e10000 product details. `http://www.instron.co.uk/en-gb/products/testing-systems/dynamic-and-fatigue-systems/electropuls-systems`. Accessed 26 July 2017.

[10] Labview® manual: Joint types and functions (online). `https://www.ode-wiki.org/wiki/index.php?title=Manual:_Joint_Types_and_Functions`. Accessed 22 June 2017.

[11] Labview® robotics module (online). `http://sine.ni.com/nips/cds/view/p/lang/en/nid/209856`. Accessed 29 August 2017.

[12] Labview® surface: slip1 property description (online). `http://zone.ni.com/reference/en-XX/help/372983F-01/lvroboprop/lvode_geom_surface_slip1/`. Accessed 22 June 2017.

[13] Maxon motor product information - 339152 (online). `http://www.maxonmotor.co.uk/maxon/view/product/motor/dcmotor/re/re25/339154`. Accessed 25 June 2014.

[14] Online skating magaize, anatomy of an inline skate wheel. `http://www.online-skating.com/articles-761-anatomy-of-an-inline-skate-wheel.html`. Accessed 04 July 2017.

[15] stratasys objet 1000 3d printer (online). `http://www.stratasys.com/3d-printers/production-series/objet1000-plus`. Accessed 24 May 2017.

[16] stratasys polyjet digital materials (online). `http://www.stratasys.com/materials/polyjet/digital-materials`. Accessed 28 August 2017.

[17] Technical characteristics of flexinol® actuator wires (online). `http://www.dynalloy.com/pdfs/TCF1140.pdf`. Accessed 30 May 2014.

[18] Takeshi Aoki and Shigeo Hirose. Study on the brake operation of bridle bellows. In *Intelligent Robots and Systems, 2007. IROS 2007. IEEE/RSJ International Conference on*, pages 40–45. IEEE, 2007.

[19] Takeshi Aoki, Akiyoshi Ochiai, and Shigeo Hirose. Study on slime robot: development of the mobile robot prototype model using bridle bellows. In *Robotics and Automation, 2004. Proceedings. ICRA'04. 2004 IEEE International Conference on*, volume 3, pages 2808–2813. IEEE, 2004.

[20] Masayuki Arai, Yoshinori Tanaka, Shigeo Hirose, Hiroyuki Kuwahara, and Shingo Tsukui. Development of souryu-iv and souryu-v: serially connected crawler vehicles for in-rubble searching operations. *Journal of Field Robotics*, 25(1-2):31–65, 2008.

[21] Andrew Barber, Peter Culmer, and Jordan H Boyle. Development and characterisation of a multi-material 3d printed torsion spring. In *Conference Towards Autonomous Robotic Systems*, pages 44–49. Springer, 2015.

[22] Nicholas W Bartlett, Michael T Tolley, Johannes TB Overvelde, James C Weaver, Bobak Mosadegh, Katia Bertoldi, George M Whitesides, and Robert J Wood. A 3d-printed, functionally graded soft robot powered by combustion. *Science*, 349(6244):161–165, 2015.

[23] Zeki Y Bayraktaroglu. Snake-like locomotion: Experimentations with a biologically inspired wheel-less snake robot. *Mechanism and Machine Theory*, 44(3):591–602, 2009.

[24] Peter P Benham, Roy J Crawford, and Cecil G Armstrong. *Mechanics of Engineering Materials*. Pearson Education, Harlow, England, 1996.

[25] Stefano Berri, Jordan H Boyle, Manlio Tassieri, Ian A Hope, and Netta Cohen. Forward locomotion of the nematode c. elegans is achieved through modulation of a single gait. *HFSP journal*, 3(3):186–193, 2009.

[26] Jordan H Boyle. *C. elegans locomotion: an integrated approach*. PhD thesis, University of Leeds (School of Computing), 2009.

[27] Jordan H Boyle, Stefano Berri, and Netta Cohen. Gait modulation in c. elegans: an integrated neuromechanical model. *Frontiers in computational neuroscience*, 6, 2012.

[28] Jordan H Boyle, Sam Johnson, and Abbas A Dehghani-Sanij. Adaptive undulatory locomotion of a *c. elegans* inspired robot. *Mechatronics, IEEE/ASME Transactions on*, 18(5):439–448, 2013.

[29] Alberto Brunete, Ernesto Gambao, Jose Emilio Torres, and Miguel Hernando. A 2 dof servomotor-based module for pipe inspection modular micro-robots. In *Intelligent Robots and Systems, 2006 IEEE/RSJ International Conference on*, pages 1329–1334. IEEE, 2006.

[30] Alberto Brunete, Miguel Hernando, Jose E Torres, and Ernesto Gambao. Heterogeneous multi-configurable chained microrobot for the exploration of small cavities. *Automation in Construction*, 21:184–198, 2012.

[31] Emma Campbell, Zhao Chad Kong, William Hered, Andrew J Lynch, Marcia K O'Malley, and James McLurkin. Design of a low-cost series elastic actuator for multi-robot manipulation. In *Robotics and Automation (ICRA), 2011 IEEE International Conference on*, pages 5395–5400. IEEE, 2011.

[32] Ching-Ping Chou and Blake Hannaford. Measurement and modeling of mckibben pneumatic artificial muscles. *IEEE Transactions on robotics and automation*, 12(1):90–102, 1996.

[33] Alessandro Crespi and Auke Jan Ijspeert. Online optimization of swimming and crawling in an amphibious snake robot. *Robotics, IEEE Transactions on*, 24(1):75–87, 2008.

[34] Alessandro Crespi, Konstantinos Karakasiliotis, André Guignard, and Auke Jan Ijspeert. Salamandra robotica ii: an amphibious robot to study salamander-like swimming and walking gaits. 2013.

[35] Marc Doumit, Atef Fahim, and Michael Munro. Analytical modeling and experimental validation of the braided pneumatic muscle. *IEEE transactions on robotics*, 25(6):1282–1291, 2009.

[36] Gen Endo, Keiji Togawa, and Shigeo Hirose. Study on self-contained and terrain adaptive active cord mechanism. In *Intelligent Robots and Systems, 1999. IROS'99. Proceedings. 1999 IEEE/RSJ International Conference on*, volume 3, pages 1399–1405. IEEE, 1999.

[37] Grzegorz Granosik. *Pneumatic Actuators for Climbing, Walking and Serpentine Robots*. INTECH Open Access Publisher, 2007.

[38] Grzegorz Granosik. Hypermobile robots–the survey. *Journal of Intelligent & Robotic Systems*, pages 1–23, 2013.

[39] Grzegorz Granosik and Johann Borenstein. Integrated joint actuator for serpentine robots. *Mechatronics, IEEE/ASME Transactions on*, 10(5):473–481, 2005.

[40] Grzegorz Granosik and Johann Borenstein. Pneumatic actuators for serpentine robot. In *Climbing and Walking Robots*, pages 719–726. Springer, 2006.

[41] Grzegorz Granosik, Johann Borenstein, and Malik G Hansen. Serpentine robots for industrial inspection and surveillance. *Industrial Robotics. Programming, Simulation and Applications*, pages 633–662, 2007.

[42] Grzegorz Granosik, Malik G Hansen, and Johann Borenstein. The omnitread serpentine robot for industrial inspection and surveillance. *Industrial Robot: An International Journal*, 32(2):139–148, 2005.

[43] Michael W Hannan and Ian D Walker. Kinematics and the implementation of an elephant's trunk manipulator and other continuum style robots. *Journal of Robotic Systems*, 20(2):45–63, 2003.

[44] Rintaro Haraguchi, Koichi Osuka, Sinobu Makita, and Satoshi Tadokoro. The development of the mobile inspection robot for rescue activity, moira2. In *Advanced Robotics, 2005. ICAR'05. Proceedings., 12th International Conference on*, pages 498–505. IEEE, 2005.

[45] Shigeo Hirose, Akio Morishima, Siniti Tukagosi, T Tsumaki, and H Monobe. Design of practical snake vehicle: Articulated body mobile robot kr-ii. In *Advanced Robotics, 1991.'Robots in Unstructured Environments', 91 ICAR., Fifth International Conference on*, pages 833–838. IEEE, 1991.

[46] Shigeo Hirose and Hiroya Yamada. Snake-like robots [tutorial]. *Robotics & Automation Magazine, IEEE*, 16(1):88–98, 2009.

[47] James K Hopkins, Brent W Spranklin, and Satyandra K Gupta. A survey of snake-inspired robot designs. *Bioinspiration & biomimetics*, 4(2):021001, 2009.

[48] David L Hu, Jasmine Nirody, Terri Scott, and Michael J Shelley. The mechanics of slithering locomotion. *Proceedings of the National Academy of Sciences*, 106(25):10081–10085, 2009.

[49] Daniel A Kingsley, Roger D Quinn, and Roy E Ritzmann. A cockroach inspired robot with artificial muscles. In *Intelligent Robots and Systems, 2006 IEEE/RSJ International Conference on*, pages 1837–1842. IEEE, 2006.

[50] Tetsuya Kinugasa, Yuta Otani, Takafumi Haji, Koji Yoshida, Koichi Osuka, and Hisanori Amano. A proposal of flexible mono-tread mobile tracka new mobile mechanism using one track and spine-like structure. In *Intelligent Robots and Systems, 2008. IROS 2008. IEEE/RSJ International Conference on*, pages 1642–1647. IEEE, 2008.

[51] Bernhard Klaassen and Karl L Paap. Gmd-snake2: a snake-like robot driven by wheels and a method for motion control. In *Robotics and Automation, 1999. Pro-*

ceedings. 1999 IEEE International Conference on, volume 4, pages 3014–3019. IEEE, 1999.

[52] Kyoungchul Kong, Joonbum Bae, and Masayoshi Tomizuka. A compact rotary series elastic actuator for human assistive systems. *IEEE/ASME transactions on mechatronics*, 17(2):288–297, 2012.

[53] Kentarou Kouno, Hiroya Yamada, and Shigeo Hirose. Development of active-joint active-wheel high traversability snake-like robot acm-r4. 2. *J. Robot. Mechatron*, 25(3):559–566, 2013.

[54] Cecilia Laschi, Barbara Mazzolai, V Mattoli, M Cianchetti, and P Dario. Design of a biomimetic robotic octopus arm. *Bioinspiration & Biomimetics*, 4(1):015006, 2009.

[55] Michel Lauria, M-A Legault, M-A Lavoie, and François Michaud. Differential elastic actuator for robotic interaction tasks. In *Robotics and Automation, 2008. ICRA 2008. IEEE International Conference on*, pages 3606–3611. IEEE, 2008.

[56] Man-Cheong Lei and D Ruxu. Geometry modeling and simulation of the wire-driven bending section of a flexible ureteroscope. In *Proc. of the World Congress on Eng. and Comp. Sci*, volume 2, 2011.

[57] Zheng Li and Ruxu Du. Design and analysis of a bio-inspired wire-driven multi-section flexible robot. *Int J Adv Robotic Sy*, 10(209), 2013.

[58] P Liljeback, Kristin Ytterstad Pettersen, and Øyvind Stavdahl. A snake robot with a contact force measurement system for obstacle-aided locomotion. In *Robotics and Automation (ICRA), 2010 IEEE International Conference on*, pages 683–690. IEEE, 2010.

[59] P Liljeback, O Stavdahl, and Anders Beitnes. Snakefighter-development of a water hydraulic fire fighting snake robot. In *Control, Automation, Robotics and Vision, 2006. ICARCV'06. 9th International Conference on*, pages 1–6. IEEE, 2006.

[60] Pål Liljebäck, Kristin Ytterstad Pettersen, Øyvind Stavdahl, and Jan Tommy Gravdahl. A review on modelling, implementation, and control of snake robots. *Robotics and Autonomous Systems*, 60(1):29–40, 2012.

[61] Pål Liljebäck, Øyvind Stavdahl, Kristin Y Pettersen, and Jan Tommy Gravdahl. Mamba-a waterproof snake robot with tactile sensing. In *Intelligent Robots and*

Systems (IROS 2014), 2014 IEEE/RSJ International Conference on, pages 294–301. IEEE, 2014.

[62] Glenn Mathijssen, Raphaël Furnémont, Branko Brackx, Ronald Van Ham, Dirk Lefeber, and Bram Vanderborght. Design of a novel intermittent self-closing mechanism for a maccepa-based series-parallel elastic actuator (spea). In *Intelligent Robots and Systems (IROS 2014), 2014 IEEE/RSJ International Conference on*, pages 2809–2814. IEEE, 2014.

[63] Gustavo A Medrano-Cerda, Colin J Bowler, and Darwin G Caldwell. Adaptive position control of antagonistic pneumatic muscle actuators. In *Intelligent Robots and Systems 95.'Human Robot Interaction and Cooperative Robots', Proceedings. 1995 IEEE/RSJ International Conference on*, volume 1, pages 378–383. IEEE, 1995.

[64] Sébastien Meghezi, Frédéric Couet, Pascale Chevallier, and Diego Mantovani. Effects of a pseudophysiological environment on the elastic and viscoelastic properties of collagen gels. *International journal of biomaterials*, 2012, 2012.

[65] Gavin SP Miller. Snake robots (online). `http://www.snakerobots.com`. Accessed 17 January 2014.

[66] Gavin SP Miller. Snake robots for search and rescue. *Neurotechnology for Biomimetic Robots*, page 271, 2002.

[67] Takashi Mineta, Toshiaki Mitsui, Yoshiyuki Watanabe, Seiya Kobayashi, Youichi Haga, and Masayoshi Esashi. An active guide wire with shape memory alloy bending actuator fabricated by room temperature process. *Sensors and Actuators A: Physical*, 97:632–637, 2002.

[68] Makoto Mori and Shigeo Hirose. Three-dimensional serpentine motion and lateral rolling by active cord mechanism acm-r3. In *Intelligent Robots and Systems, 2002. IEEE/RSJ International Conference on*, volume 1, pages 829–834. IEEE, 2002.

[69] Jun-Ya Nagase, Koichi Suzumori, and Norihiko Saga. Development of worm-rack driven cylindrical crawler unit. *Journal of Advanced Mechanical Design, Systems, and Manufacturing*, 7:422–431, 2013.

[70] Steven C Obiajulu, Ellen T Roche, Frank A Pigula, and Conor J Walsh. Soft pneumatic artificial muscles with low threshold pressures for a cardiac compression device. In *ASME 2013 International Design Engineering Technical Conferences*

and Computers and Information in Engineering Conference, pages V06AT07A009–V06AT07A009. American Society of Mechanical Engineers, 2013.

[71] Hidetaka Ohno and Shigeo Hirose. Study on slime robot (proposal of slime robot and design of slim slime robot). In *Intelligent Robots and Systems, 2000.(IROS 2000). Proceedings. 2000 IEEE/RSJ International Conference on*, volume 3, pages 2218–2223. IEEE, 2000.

[72] Jung-Jun Park, Byeong-Sang Kim, Jae-Bok Song, and Hong-Seok Kim. Safe link mechanism based on nonlinear stiffness for collision safety. *Mechanism and Machine Theory*, 43(10):1332–1348, 2008.

[73] Florian Petit, Maxime Chalon, Werner Friedl, Markus Grebenstein, Alin Albu-Schäffer, and Gerd Hirzinger. Bidirectional antagonistic variable stiffness actuation: Analysis, design & implementation. In *Robotics and Automation (ICRA), 2010 IEEE International Conference on*, pages 4189–4196. IEEE, 2010.

[74] José L Pons. *Emerging actuator technologies: a micromechatronic approach*. Wiley. com, 2005.

[75] Dmitry Popov, Igor Gaponov, and Jee-Hwan Ryu. Towards variable stiffness control of antagonistic twisted string actuators. In *Intelligent Robots and Systems (IROS 2014), 2014 IEEE/RSJ International Conference on*, pages 2789–2794. IEEE, 2014.

[76] Mathieu Porez, Frédéric Boyer, Auke Ijspeert, et al. Improved lighthill fish swimming model for bio-inspired robots-modelling, computational aspects and experimental comparisons. *International Journal of Robotics Research*, pages 1–34, 2014.

[77] David Rollinson, Steven Ford, Ben Brown, and Howie Choset. Design and modeling of a series elastic element for snake robots. In *ASME 2013 Dynamic Systems and Control Conference*, pages V001T08A002–V001T08A002. American Society of Mechanical Engineers, 2013.

[78] Frank Rothling, Robert Haschke, Jochen J Steil, and Helge Ritter. Platform portable anthropomorphic grasping with the bielefeld 20-dof shadow and 9-dof tum hand. In *Intelligent Robots and Systems, 2007. IROS 2007. IEEE/RSJ International Conference on*, pages 2951–2956. IEEE, 2007.

[79] Riccardo Schiavi, Giorgio Grioli, Soumen Sen, and Antonio Bicchi. Vsa-ii: A novel prototype of variable stiffness actuator for safe and performing robots interacting

with humans. In *Robotics and Automation, 2008. ICRA 2008. IEEE International Conference on*, pages 2171–2176. IEEE, 2008.

[80] K-U Scholl, V Kepplin, K Berns, and R Dillmann. An articulated service robot for autonomous sewer inspection tasks. In *Intelligent Robots and Systems, 1999. IROS'99. Proceedings. 1999 IEEE/RSJ International Conference on*, volume 2, pages 1075–1080. IEEE, 1999.

[81] Sangok Seok, Cagdas Denizel Onal, K Cho, Robert J Wood, Daniela Rus, Sangbae Kim, et al. Meshworm: A peristaltic soft robot with antagonistic nickel titanium coil actuators. 2012.

[82] Fabrizio Sergi, Dino Accoto, Giorgio Carpino, Nevio Luigi Tagliamonte, and Eugenio Guglielmelli. Design and characterization of a compact rotary series elastic actuator for knee assistance during overground walking. In *Biomedical Robotics and Biomechatronics (BioRob), 2012 4th IEEE RAS & EMBS International Conference on*, pages 1931–1936. IEEE, 2012.

[83] Dongjun Shin, Irene Sardellitti, Yong-Lae Park, Oussama Khatib, and Mark Cutkosky. Design and control of a bio-inspired human-friendly robot. *The International Journal of Robotics Research*, 29(5):571–584, 2010.

[84] Ernesto C Martinez-Villalpando SM. Agonist-antagonist active knee prosthesis: A preliminary study in level-ground walking. *Journal of rehabilitation research and development*, 46(3):361, 2009.

[85] Hermann Streich and Oliver Adria. Software approach for the autonomous inspection robot makro. In *Robotics and Automation, 2004. Proceedings. ICRA'04. 2004 IEEE International Conference on*, volume 4, pages 3411–3416. IEEE, 2004.

[86] Angelo Sudano, Nevio Luigi Tagliamonte, Dino Accoto, and Eugenio Guglielmelli. A resonant parallel elastic actuator for biorobotic applications. In *Intelligent Robots and Systems (IROS 2014), 2014 IEEE/RSJ International Conference on*, pages 2815–2820. IEEE, 2014.

[87] James S Sulzer, Michael A Peshkin, and James L Patton. Marionet: An exotendon-driven rotary series elastic actuator for exerting joint torque. In *Rehabilitation Robotics, 2005. ICORR 2005. 9th International Conference on*, pages 103–108. IEEE, 2005.

[88] Kousuke Suzuki, Atsushi Nakano, Gen Endo, and Shigeo Hirose. Development of multi-wheeled snake-like rescue robots with active elastic trunk. In *Intelligent Robots and Systems (IROS), 2012 IEEE/RSJ International Conference on*, pages 4602–4607. IEEE, 2012.

[89] Nikolaos G Tsagarakis, Matteo Laffranchi, Bram Vanderborght, and Darwin G Caldwell. A compact soft actuator unit for small scale human friendly robots. In *Robotics and Automation, 2009. ICRA'09. IEEE International Conference on*, pages 4356–4362. IEEE, 2009.

[90] Robert J Webster and Bryan A Jones. Design and kinematic modeling of constant curvature continuum robots: A review. *The International Journal of Robotics Research*, 29(13):1661–1683, 2010.

[91] John P Whitney, Matthew F Glisson, Eric L Brockmeyer, and Jessica K Hodgins. A low-friction passive fluid transmission and fluid-tendon soft actuator. In *Intelligent Robots and Systems (IROS 2014), 2014 IEEE/RSJ International Conference on*, pages 2801–2808. IEEE, 2014.

[92] Rainer Worst and Ralf Linnemann. Construction and operation of a snake-like robot. In *Intelligence and Systems, 1996., IEEE International Joint Symposia on*, pages 164–169. IEEE, 1996.

[93] Cornell Wright, Austin Buchan, Ben Brown, Jason Geist, Michael Schwerin, David Rollinson, Matthew Tesch, and Howie Choset. Design and architecture of the unified modular snake robot. In *Robotics and Automation (ICRA), 2012 IEEE International Conference on*, pages 4347–4354. IEEE, 2012.

[94] Cornell Wright, Aaron Johnson, Aaron Peck, Zachary McCord, Allison Naaktgeboren, Philip Gianfortoni, Manuel Gonzalez-Rivero, Ross Hatton, and Howie Choset. Design of a modular snake robot. In *Intelligent Robots and Systems, 2007. IROS 2007. IEEE/RSJ International Conference on*, pages 2609–2614. IEEE, 2007.

[95] Hiroya Yamada and Shigeo Hirose. Study of a 2-dof joint for the small active cord mechanism. In *Robotics and Automation, 2009. ICRA'09. IEEE International Conference on*, pages 3827–3832. IEEE, 2009.

[96] Changlong Ye, Shugen Ma, Bin Li, Hongjun Liu, and Hequan Wang. Development of a 3d snake-like robot: perambulator-ii. In *Mechatronics and Automation, 2007. ICMA 2007. International Conference on*, pages 117–122. IEEE, 2007.

[97] Shumei Yu, Shugen Ma, Bin Li, and Yuechao Wang. An amphibious snake-like robot: design and motion experiments on ground and in water. In *Information and Automation, 2009. ICIA'09. International Conference on*, pages 500–505. IEEE, 2009.

[98] Houxiang Zhang, Wei Wang, Zhicheng Deng, Guanghua Zong, and Jianwei Zhang. A novel reconfigurable robot for urban search and rescue. *International Journal of Advanced Robotic Systems*, 3(4):359–366, 2006.